THE FINITE ELEMENT MODELLING OF THE DYNAMIC BEHAVIOUR OF A TRANSMISSION LINE CONDUCTOR

Thesis completed in partial fulfilment of the requirements for the degree of
Master of Science in Engineering

at the

University of Cape Town

by

Günther Carl Kruse
BSc.Eng (Cape Town)

October, 1996

Für Jenni

ACKNOWLEDGEMENTS

I would like to thank the following people for their assistance:

- Dr Howard Pearce, my thesis supervisor, for his assistance and advice
- Dr Dzevad Muftic, Claudio Ravera, Mike Korber, Logan Pillay and Bertie Jacobs, all of Eskom, for their assistance and for providing me with required information
- Mr Lothar Möcks, of Richard Bergner GmbH + Co., Germany, for sending me numerous useful documents and data
- Dr Konstantin Papailiou, Switzerland, for sending me a copy of his thesis
- My fellow post-graduate students and the staff members in Cerecam and the Department of Mechanical Engineering who gave me advice and assistance in completing the project

SYNOPSIS

The problem of conductor motion has been of concern to transmission line engineers for many years. This thesis describes the application of one of the most powerful and useful tools of modern engineering, the finite element method, to the problem of modelling the dynamic behaviour of conductors.

In modelling the conductor, the assumption that it may be treated as a solid continuum is made. Due to the construction of a conductor, however, the bending stiffness and internal damping of the conductor are non-linearly related to a number of factors. The results of a study on these factors are discussed in this thesis, and have been used where necessary in defining the material behaviour of a conductor.

Four types of conductor motion are modelled, namely aeolian vibration, wake-induced vibration, bundle pinch (resulting from short-circuit currents) and the motion of a section of a transmission line after a conductor breaks. Finite element models have been developed specifically for each of these types of conductor motion, and the details of these are presented. The effects of various options in the finite element modelling, on the results obtained from the simulations, are also discussed. The finite element models are implemented by means of the finite element package, ABAQUS.

Algorithms which have been developed and implemented by means of user-defined subroutines for the simulation of vortex shedding loads (in the case of aeolian vibration), electromagnetic forces (due to short circuit currents) and the loads experienced by a conductor in the wake of another, are discussed in the thesis. In the case of wake-induced oscillations, the fluid flowing over two conductors is simulated with the aid of SPECTRUM, a finite element package with fluid flow modelling capabilities. Drag and lift coefficients for a conductor in the wake of another are obtained from these simulations, and together with data obtained from literature, are used in applying the loads on the downwind conductor for wake-induced vibration.

Where data is available, results obtained from the finite element simulations are compared with existing data from literature and are found to agree favourably, thus verifying the finite element models developed.

The main objective of the finite element simulations carried out, and the results obtained from them, is to demonstrate the capabilities of the finite element models. A number of useful observations are however also made from the results, some which are relevant to the accuracy of the finite element models, and others which demonstrate the effects of various properties of a transmission line, such as the tension and spacer separation, on the behaviour of the conductor.

It is envisaged that the models which have been developed during the course of this project and which are described in this thesis will be useful not only for further research purposes, but also in the design of transmission lines.

TABLE OF CONTENTS

LIST OF FIGURES

LIST OF TABLES

GLOSSARY

ACSR - type of conductor: *A*luminium *C*onductor *S*teel *R*einforced

bundle - an arrangement of two or more conductors which are bundled together by means of spacers. A conductor bundle is used for each phase of a transmission line operating at very high voltages

CFD - Computational Fluid Dynamics

far-field - the part of a span not in the direct vicinity of the suspension points

mesh - in the context of a mesh for a conductor, this is comprised of a number of line (beam or truss) elements connected end on end to model the continuous conductor

near-field - the part of the conductor or span in the direct vicinity of the suspension points

spacer - used to maintain the spacing between the individual conductors in a conductor bundle

spacer damper - a spacer which has damping capabilities due to the inclusion of an elastic material (such as rubber) at joints in the spacer

sub-conductor - the individual conductors in a conductor bundle

sub-span - the section of a conductor bundle between two successive spacers

vibration damper - a mechanical damping device attached to the conductors at the ends of a span to reduce the severity of vibration at the conductor's suspension points

1. INTRODUCTION

1.1 AN OVERVIEW OF THE PROBLEM

Conductors of a transmission line are fairly unique in terms of engineering structures. Their length and flexibility make them susceptible to various types of motion, most of which are bound to cause damage to some component of the transmission line either within a few hours, or over a period of years. Numerous studies have thus been carried out over the past few years with the aim being to gain a better understanding of the different types of conductor motion, and the consequences thereof. A better understanding of the dynamics of a conductor will aid not only in improving the reliability of transmission lines by designing them to cope with the types of motion they are likely to encounter, but also in cost savings by not over-designing.

The dynamic characteristics of a conductor are very much dependent on various factors, which include the conductor type, span length, conductor tension, spacer locations and characteristics of adjacent spans, amongst others. Existing data on the dynamics of a line is thus often valid only for very specific types of transmission lines, namely those with similar characteristics to the lines from which the data has been obtained. This is where a general model of a transmission line, on which the dynamic behaviour of a particular transmission line or section thereof can be simulated and studied, would be useful to a transmission line engineer.

The finite element method is ideally suited to a problem of this nature. Once a recipe of element types, solution procedures and material models is available, a model of any particular section of a transmission line can be generated, and the dynamic behaviour of a specific line can be studied. The costs and time involved in generating a finite element model of a transmission line are considerably less than constructing experimental test lines and rigs. Even though some of the finite element simulations do take up a fair amount of computer time, the reduced manpower, space and facilities required make finite element simulations a more viable option than experimentation. Once a finite element model has been constructed and verified, it can be used an endless number of times to study the behaviour of different transmission lines.

1.2 OBJECTIVES

The main objective of the work reported on in this thesis is to investigate the modelling and simulation of the dynamic behaviour of a transmission line conductor using the finite element method. The four different types of conductor motion which are of concern and are simulated using the finite element technique are aeolian vibration, wake-induced vibration, the motion during and after the occurrence of a short-circuit fault, and the motion of a section of a transmission line following the breaking of a conductor. A commercially available finite element package, ABAQUS, is used to simulate the problems.

This thesis presents and discusses various factors which must be considered when simulating these events. It discusses various problems encountered in the generation of the models and the effects that various choices of elements and other variables have on the solution. In some cases, a decision of the number of elements used, the amount of damping in the conductor and the choice of boundary conditions have a significant effect on the results.

Different methods have been used in the past to estimate the dynamic stresses experienced in a conductor during aeolian vibration. An improved method which estimates the stresses from the change in bending curvature of the conductor, which is obtained directly from the finite element simulations, is presented.

Where appropriate, algorithms to simulate the loads on the conductors which cause the motion have been developed, and the implementation of these algorithms by means of user-defined loading subroutine in ABAQUS is described.

The results of typical analyses are also compared with existing experimental and other numerical data from literature, where available, to verify the models. Apart from these verification examples, a number of parametric studies have been carried out with the aim of demonstrating the capabilities of the models. Due to time constraints, no further in-depth studies have been carried out as part of this project.

In most cases, the number of simulations has been limited by the amount of CPU time required to simulate problems. A typical simulation may take anything from a few minutes, in the case of the simulation of a conductor breaking, to 2 or 3 days, as required for some of the simulations of aeolian vibration and the dynamics following a short-circuit. These times refer to the amount of CPU time required by an IBM RISC 6000 system. The real time required may be anything from 2 to 6 times as long, depending on the number of users of the system.

1.3 STRUCTURE OF THE THESIS

Before discussing the various aspects of the project in any detail, a brief and general discussion on the dynamics of a transmission line conductor and a short note on some aspects of a conductor's mechanical properties are included in this introductory chapter.

The next two chapters discuss the bending stiffness and internal damping of a transmission line conductor respectively. In the following four chapters, the various aspects involved in the finite element modelling of aeolian vibration, wake-induced oscillations, short-circuit induced conductor motion and the response of a transmission line resulting from a conductor breaking are discussed.

Each of these chapters introduces the specific problem with a literature review and a discussion of the phenomenon being dealt with in the chapter. The details of the finite element model are then given and the various options discussed. The last section in each chapter presents and discusses various results obtained from the finite element simulations.

In the penultimate chapter, the most important conclusions which are drawn from the study and from the results are presented, while the closing chapter makes a number of relevant recommendations.

In the appendices, the equation of motion of a taut cable is presented, the method used to calculate the original length of a tensioned conductor is discussed, and the field results for aeolian vibration are given. The FORTRAN codes for the various user-defined loading subroutines, example problem input files for ABAQUS and SPECTRUM and a graph of the power dissipated by a vibrating conductor are also given.

1.4 AN INTRODUCTION TO THE DYNAMICS OF A TRANSMISSION LINE CONDUCTOR

As mentioned earlier, the nature of a transmission line conductor makes it unique in terms of it's dynamic behaviour. The main types of motion which a conductor might experience, and which could lead to damage, are aeolian and wake-induced vibrations, galloping, motion resulting from large short-circuit current induced electromagnetic forces and the response of a transmission line section which follows the failure of a conductor.

The first of these, namely aeolian vibration, is a relatively high frequency vibration, encountered in low to moderate winds, typically 1 to 7 m/s (Doocey et al, 1979). It occurs in the 3 to 150 Hz frequency range, with the typical peak to peak amplitude of vibration being 0.01 to 1 times the diameter of the conductor. The alternate shedding of vortices from the downwind side of the conductor is the cause of aeolian vibration. Due to the high frequency, low amplitude nature of the vibration, fatigue and fretting damage are of concern in conductors that

undergo aeolian vibration, with the period of time to severe damage typically being a number of years.

Wake-induced vibration is less commonly encountered on transmission lines and is restricted to conductor bundles. As the name implies, this type of vibration is caused by the motion of a conductor in the wake of another conductor in the bundle. It occurs in moderate to high winds, typically 4 to 18 m/s (Doocey et al, 1979; Cigrè Study Committee 22 - working Group 01, 1989). The range of frequencies encountered is typically 0.15 to 10 Hz, corresponding usually with the fundamental or one of the first few modes of vibration of the span or sub-span. The peak to peak amplitude of vibration is anything from 0.5 to 20 conductor diameters for the sub-span mode of oscillation, and 0.5 to 80 diameters for the so called rigid-body modes. These different types of wake-induced oscillation are discussed in more detail later on. Wake-induced vibration is generally the cause of accelerated wear of components and clashing of the conductors in a bundle (Doocey et al, 1979). A few months of wake-induced oscillation are usually required before severe damage occurs.

The third type of oscillation, galloping, is of concern in areas where the formation of ice on the conductors under certain climatic conditions occurs. Ice on the conductor may give the conductor cross-section an unstable aerodynamic shape, and cause large amplitude vibration, typically in the order of 5 to 300 conductor diameters (Doocey et al, 1979). The frequency of vibration usually corresponds to the fundamental of the span, typically 0.08 to 3 Hz. The range of wind speeds in which conductor gallop might occur is 7 to 18 m/s. As mentioned in the Cigrè report (Cigrè Study Committee 22 - working Group 01, 1989), conductor gallop is not very frequently encountered, as it is restricted to areas in which icing under favourable conditions occurs. When it does occur, however, significant dynamic loads are imposed on various components of the transmission line, and damage to the hardware can normally be expected within a few hours. This is the only type of conductor motion mentioned here which is not modelled as part of this project, as it is a problem not commonly encountered in Southern Africa.

Short-circuit fault currents in a conductor give rise to large attractive electromagnetic forces between the conductors of a bundle. These forces pull the conductors together, and may cause them to clash quite severely. Damage to the surface of the conductor due to the clashing, large bending loads imposed on the conductors in the vicinity of spacers, and large compressive forces in the spacers are the main consequences of this type of motion. Damage to other hardware is similar to what would be expected from wake-induced oscillations or galloping, and the damage to the strands of the conductors reduce their resistance to fatigue damage (Möcks, 1972).

In the event of a component of the transmission line breaking, the loads imposed on the remaining hardware or towers could cause further damage or failure. Of major concern are the loads imposed on the hardware and suspension structures after the severance or breaking of a conductor close to the suspension point on a tower. The cause of failure of the conductor or other hardware could be the

result of any of the types of motion discussed above, including conductor failure. The dynamic loads imposed on the tower, as the insulator string swings upwards to form part of the catenary of the adjacent span, may result in failure of the tower or its components. The worst case scenario is the cascading failure of a number of adjacent towers, and thus of a whole section of a transmission line.

1.5 A NOTE ON THE PHYSICAL NATURE OF CONDUCTORS

Due to the construction of a transmission line conductor, the properties of a conductor when treated as a continuum are quite complex. An ACSR *Zebra* conductor for example consists of 61 strands in five strand layers, each strand (except the core strand) being helically wound around an underlying strand layer. As can be imagined, it would be impractical to model each individual strand of a 400 metre length of such a conductor using finite elements, and as such the conductor must be approximated as a continuum.

The two main problems encountered when making the assumption of a continuum are that as the strands in the conductor slide over one another, the bending stiffness of the conductor is reduced, and additional damping is introduced in the conductor. The damping would be expected to have a significant effect on the behaviour of a conductor undergoing small amplitude oscillations, while the choice of bending stiffness is of considerable importance when determining the behaviour of the conductor in the direct vicinity of boundaries, such as at a suspension clamp.

2. THE BENDING STIFFNESS OF CONDUCTORS

One of the biggest problems encountered over the years by engineers when modelling conductor motion and behaviour, has been in deciding what value to use for the bending stiffness of the conductor. Various experiments have been performed on conductors not only to find acceptable values for the stiffness in bending of a conductor, but also to determine why and how the bending stiffness of a conductor changes.

The sections below discuss the information and results obtained from literature and describe the behaviour in bending of a conductor. A description of the method used to calculate the bending stiffness is followed by a section describing the implementation of the non-linear bending stiffness, together with the problems experienced with the implementation. Next, the results of an example problem are used to demonstrate the effect of the non-linear as opposed to constant bending stiffness on a simple cantilever. The last section in this chapter compares the dynamic stresses calculated using the method employed in this thesis (according to Papailiou, 1995a) with methods used in the past.

2.1 LITERATURE REVIEW AND DISCUSSION OF THE PROBLEM

For convenience, the literature review and the discussion of the problem relevant to the bending stiffness of conductors are combined in the following sections.

2.1.1 The Maximum and Minimum values of EI

Being composed of individual strands which are helically twisted together, the behaviour of a conductor in bending depends on the interaction of the individual strands with one another. If the assumption is made that the strands act together as a single unit, i.e. no relative motion occurs between the individual strands, a maximum value can be calculated for the bending stiffness (EI_{max}) using equation 2.1 below. The stiffness of each of the strands about the central axis (corresponding to the origin of the global x-y co-ordinate frame in Figure 2.1) of the whole conductor is calculated and summed to obtain the bending stiffness of the conductor.

$$EI_{\max} = \frac{\pi}{8} \cdot \sum_{i=1}^{layers} E_i n_i d_i^2 \left(\frac{d_i^2}{8} + R_i^2 \right) \cos\beta_i \qquad (2.1)$$

where
- n_i = number of strands in the layer
- R_i = perpendicular distance from the neutral axis of the conductor to the centre (in cross section) of a strand in the i-th layer.
- d_i = diameter of strands in the layer
- E_i = Young's Modulus for the layer
- β_i = lay angle of the layer

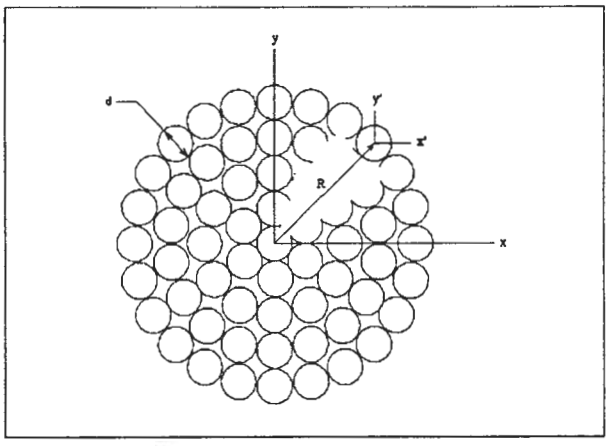

Figure 2.1: *The cross-section of a zebra conductor showing the notation used in equations 2.1 and 2.2*

On the other extreme, a minimum value for the stiffness in bending (EI_{min}) may be calculated by assuming that each individual strand is completely free to slide relative to any adjacent strands (Papailiou, 1995b). The stiffness of the conductor is obtained by summing the bending stiffness of each strand about it's own central axis (x'=0; y'=0) i.e.

$$EI_{\min} = \frac{\pi}{64} \cdot \sum_{i=1}^{n_{tot}} E_i d_i^4 \cos\beta_i \qquad (2.2)$$

where n_{tot} is the total number of strands in the conductor.

The $\cos\beta_i$ term takes into consideration that the strands are helically wound about the underlying layer. The formulae given in the EPRI Handbook (Doocey et al, 1979) neglect the term for the lay angle, effectively making $\beta_i = 0$, i.e. $\cos\beta_i = 1$. The difference in the values obtained for EI_{min} by this simplification is negligible for typical lay angles of ACSR conductors, with a difference being less than 0.2%.

2.1.2 Assuming a Constant Value for EI

In practice, the bending stiffness of a specific conductor type will fall in the range between EI_{min} & EI_{max} with the actual value depending firstly on the type of motion the conductor undergoes, and secondly on the severity with which the motion occurs. As EI_{max} and EI_{min} may vary as much as 70 to 1 (Doocey et al, 1979), it is clear that the value chosen for the bending stiffness in a model of a conductor is a very important consideration.

The EPRI handbook suggests that the value used should be $\frac{1}{2}EI_{max}$, a value obtained by comparing calculated values with values obtained experimentally by Sturm (1936). The values obtained by Sturm, however, are for a short span, 1.1m to 1.8m in length, with a single point load being applied in the middle of the span. Assuming a relationship for the displacement as a function of the

point load, which included the stiffness of the conductor, Sturm estimated the bending stiffness by comparing the displacements and point loads.

Experiments carried out by other researchers, have yielded different results. McConnell and Zemke (1980) conducted 3 different types of experiments on a number of different conductor types. Each of the 3 experimental methods had a different point load and moment loading configuration. The assumption was made that the bending stiffness was constant along the 7.32m conductor span. In the case of the ACSR *Cardinal* conductor (the same type of conductor as used by researchers mentioned below), the stiffness was found to be in the 28.7Nm^2 to 57.7Nm^2 range.

Seppa (1995) prepared a short report in which experimental results obtained by Papailiou (1995a) are compared with experimental results obtained by himself for the ACSR *Cardinal* conductor type. The value obtained for the bending stiffness of the first 50mm from the point of attachment at the end of a test section ranged from 1120 Nm^2 to 1300 Nm^2, according to Papailiou, while Seppa obtained a value of 1050 Nm^2. In the free field, the value obtained by Seppa was 1370 Nm^2, compared to a value of 1780 Nm^2 by Papailiou. Seppa obtained his data for a 40m span which was excited with a constant bending angle (see equation 3.4) of 7.5 minutes. Papailiou's results on the other hand were obtained for a 360 mm length of conductor, set up as a cantilever, with a prescribed vertical displacement and an axial tensile load at the free end.

The difference in these experimentally obtained values shows that the assumption of a constant value, such as $\frac{1}{2}EI_{max}$ (which would equal 900 Nm^2 for a *Cardinal* conductor) for the bending stiffness would be unsuitable in a realistic model of a conductor. As can be seen from the different results obtained for different experiments, the value obtained for the bending stiffness depends on the position in the span, and the span arrangement. This can be explained by the fact that the bending stiffness depends on the bending curvature of the conductor, as described below, and that the curvature varies with the position along the span, and vibration amplitude.

2.1.3 The Dependence of EI on the Bending Curvature

Scanlan and Swart (1968) found that the bending stiffness during vibration varies with the position in the span. The values reported by Seppa and Papailiou also indicate a definite dependence of the bending stiffness on the position in the span.

Papailiou (1995a) found the bending stiffness of a section of a conductor to vary non-linearly as a function of the bending curvature, κ of the conductor, a theory supported by Raoof and Huang (1992). Papailiou suggests that for small bending curvatures, the bending stiffness is a maximum corresponding to EI_{max}, while for large bending curvatures the stiffness approaches the value of EI_{min}. This is due to the fact that under slight bending, the friction between adjacent strands prevents relative motion with respect to one another, so that the strands essentially act together as a single unit.

As the bending increases though, the fact that each of the strands is helically wound about the underlying layers, means that the sections of a strand on the one side of the conductor will be axially tensioned, while the sections on the other side will be compressed. The conductor will continue bending as a single unit until the stage is reached at which the difference in axial stresses in a specific strand (or strand layer) is great enough to overcome the frictional forces. As soon as sliding between adjacent strands occurs, the stiffness of the conductor is reduced.

This variable bending stiffness is accommodated in a set of equations, developed by Papailiou, which govern the bending stiffness of a certain conductor as a function of the bending curvature. These are described in more detail later on.

At the points of support, i.e. at the ends of the span where the conductor is clamped, the conductor usually experiences a greater intensity of bending than in the free field (Seppa, 1995). This means that the change in curvature in the near field is significantly larger than that of the free field, resulting in the reduced stiffness nearer to the ends of the span, as reported by Scanlan and Swart (1968) and Seppa.

Regarding the movement within a conductor, Scanlan and Swart postulated that while the inner layers of a conductor acted as a unit, the strands in the outermost layer were free to slide relative to one another during vibration. This theory is supported by Seppa who concluded from his experimental results that the bending model could be satisfactorily derived, for a conductor strung to 20-30% of its Rated Breaking Strength (RBS), by making this assumption.

The equations developed by Papailiou show that the strands in the outermost layer are the first to slip, followed one by one by the underlying layers as the bending curvature increases.

Raoof and Huang reported that the stiffness for an axially pre-loaded cable could be significantly higher for small vibration amplitudes, than for larger disturbances, due to the fact that small disturbances did not induce inter-strand slippage. McConnell and Zemke concluded from their experimental results, that the bending stiffness in static bending was closer to the value obtained for EI_{min}, while it approached EI_{max} for dynamic bending during vibration of the test section. These findings support the theory that the bending stiffness of a section of a conductor is dependent on the curvature, or change in curvature of the conductor section.

2.1.4 Dependence of the Bending Stiffness on the Conductor Tension

McConnell et al (1980) found a dependence of the bending stiffness on the axial tension, with the stiffness increasing almost linearly with an increase in the tension. This relationship was also noticed by Diana and Claren (1969).

Using Papailiou's (1995a) equations, the bending stiffness vs curvature relationships have been shown for different axial tensions of an ACSR *Zebra* conductor in the graphs of Figure 2.2. The increase of the bending stiffness with an increase in tension is clearly visible.

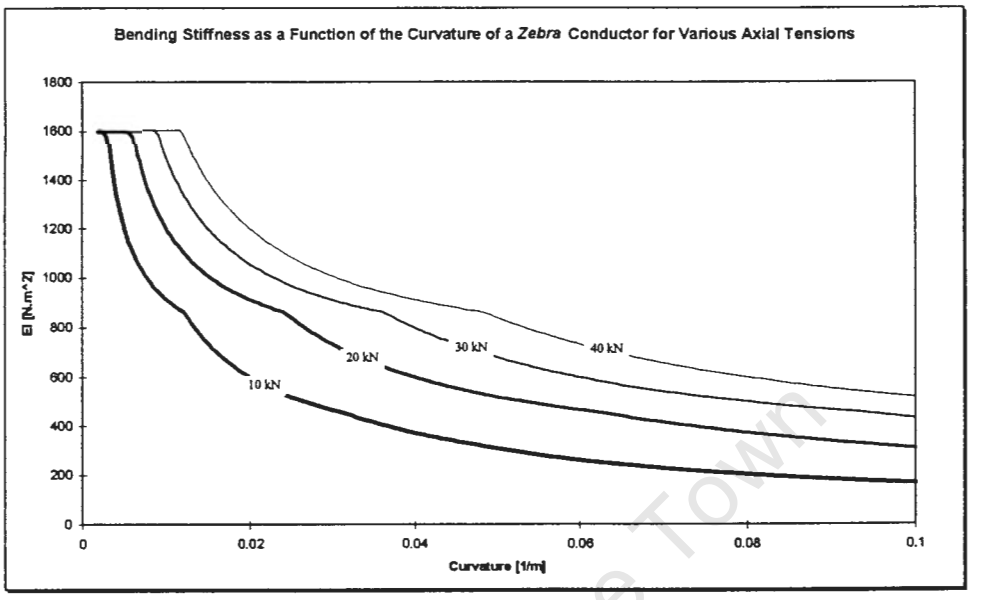

Figure 2.2: *The bending stiffness (EI) of a zebra conductor vs curvature (κ) for different axial tensions as calculated using equation 2.22*

2.2 CALCULATING THE BENDING STIFFNESS OF THE CONDUCTOR USING PAPAILIOU'S METHOD.

The method used for the calculation of the bending stiffness, and the equations used are presented below. The original equations may be found in Papailiou's thesis (1995a).

MATHCAD, a commercially available symbolic mathematics manipulator is used to implement the equations, and the resultant stiffness-curvature relationships are included in the input data for the finite element model in the form of bending moment-curvature tables as required by ABAQUS (Hibbitt Karlsson & Sorensen Inc, 1994b). The data is converted to this format using equation 2.12.

The reason for choosing Papailiou's method as a basis for calculating the variable bending stiffness, is that it does not restrict the analysis by assuming a constant bending stiffness, but rather allows a more accurate implementation of the behaviour of a conductor in bending. Papailiou's experimental results also agree very favourably with his theoretical model, as can be seen from Figure 6.7 on page 109 of Papailiou's thesis (1995a). A cantilevered 1m long section of *ACSR Cardinal* conductor is loaded at the free end by a vertical load of 4kN, and an axial load of 40kN. The difference in the experimental and theoretical data is negligible for the whole length of the test specimen. The only discrepancy in the results is that the theoretical model underestimates the deflection for the first 15 mm from the fixed end of the specimen.

2.2.1 Papailiou's Equations (Papailiou, 1995a)

The stress experienced by a strand in a conductor as the conductor is subjected to bending moment M can be written as the sum of two components:

$$\sigma_w = \sigma_w^{min} + \sigma_w^{add} \qquad (2.3)$$

where σ_w^{min} is the stress experienced in the wire due to it being bent about it's own neutral axis, and σ_w^{add} is the stress experienced by a strand due to frictional forces between it and adjacent strands as the conductor is bent. The former can be calculated as follows:

$$\sigma_w^{min} = E_i \kappa \cdot y \qquad (2.4)$$

where y is the distance from the neutral axis of the strand, and κ is the bending curvature.

The second term, σ_w^{add} is calculated using one of two equations, depending on whether the wire slips or not:

no slip: $$\sigma_w^{add} = \sigma_w^{stick} = E_i r_i \sin(\phi)\cos^2(\beta_i)\kappa \qquad (2.5)$$

slip: $$\sigma_w^{add} = \sigma_w^{slip} = \frac{Z_w^{slip}}{A_i} \qquad (2.6)$$

A_i is the circular cross-sectional area of the strand, and Z_w^{slip} is the tensile force in the wire after slipping, which is calculated using equation 2.8. The angle ϕ defines the position of the wire in the conductor cross-section, as shown in Figure 2.3, and r_i is the distance from the neutral axis of the conductor, to that of the strand.

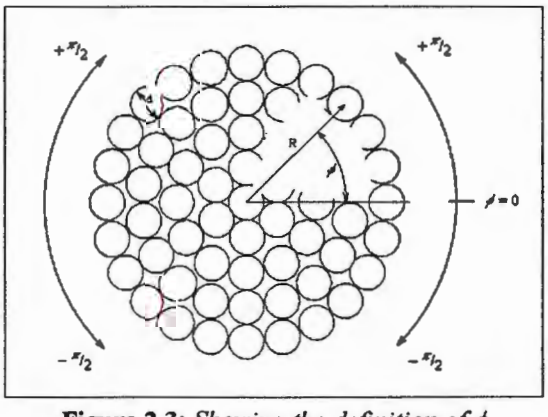

Figure 2.3: *Showing the definition of ϕ*

The tension Z_i^T in a strand of the layer i which arises due to an axial load T on the conductor, can be calculated as follows:

$$Z_i^T = \frac{E_i A_i \cos^2(\beta_i)}{\sum_{all\_wires}\left[E_j A_i \cos^3(\beta_j)\right]} \cdot T \qquad (2.7)$$

The value for the tension in the wire after it has slipped, Z_w^{slip} , can then be calculated from the following equation:

$$Z_w^{slip}(\phi) = \left(Z_i^T + S_i\right)\left(e^{\mu \sin(\beta_i)\phi} - 1\right) \qquad (2.8)$$

The term S_i, calculated using the equations below, considers the contribution during bending of the adjacent layers to the tension in the wire. (See Papailiou (1995a/b) for a more detailed discussion).

$$S_i = \frac{C_i^z}{\mu \sin(\beta_i)} \qquad (2.9)$$

with

$$C_{i-1}^z = \left(2 \cdot Z_{T_i} \mu \sin(\beta_i) + C_i^z\right)\left[\left(\frac{l_{i-1}}{l_i}\right) \cdot \left(\frac{n_i}{n_{i-1}}\right)\right] \qquad (2.10)$$

l_i being the lay length of the layer, and n_i the number of strands in the i'th layer.

The lay length l_i is the distance along the axis of the conductor after which the strand has completed one helix spiral around the underlying strand layers. The lay angle β_i and l_i are related as follows:

$$l_i = \frac{\pi \cdot d_i}{\tan \beta_i} \qquad (2.11)$$

For the core strand and the outermost layer the value for S_i is zero. In the first case this is as a result of the lay angle being zero, so the C^z term is zero, and in the case of the outermost layer the contribution is zero as it's radial motion is not restricted as in the case of the inner layers.

The bending moment M acting on a length of a conductor is related to the curvature as follows:

$$M = EI(\kappa) \cdot \kappa \qquad (2.12)$$

where EI is the bending stiffness of the conductor, dependent on κ. For equilibrium, the external bending moment must be balanced by the sum of the internal bending moments in each strand:

$$M = \sum_{all\_wires} M_w = EI(\kappa) \cdot \kappa \qquad (2.13)$$

where M_w is the internal moment in a strand. Two alternatives exist for the internal moment in the strand, for the stick and slip cases respectively.

$$M_w^{stick} = \int \sigma_w^{min} \cos(\beta_i) y dA + \int \sigma_w^{stick} \cos(\beta_i) r_i \sin(\phi) dA \qquad (2.14)$$

$$M_w^{stick} = \int \sigma_w^{min} \cos(\beta_i) y dA + \int \sigma_w^{slip} \cos(\beta_i) r_i \sin(\phi) dA \qquad (2.15)$$

Substituting σ_w^{min}, σ_w^{stick} and σ_w^{slip} in equations 2.14 and 2.15 with the expressions of equations 2.4 to 2.6, the following expressions are obtained for the bending stiffness:

$$EI_w^{min} = E_i \frac{\pi \cdot d_i^4}{64} \cos(\beta_i) \qquad (2.16)$$

$$EI_w^{stick} = E_i A_i \left(r_i \sin(\phi)\right)^2 \cos^3(\beta_i) \qquad (2.17)$$

$$EI_w^{slip} = \frac{Z_w^{slip} r_i \sin(\phi) \cos(\beta_i)}{\kappa} \qquad (2.18)$$

Assuming that all the strands in a specific layer start slipping at the same instant, or rather for the same curvature, the curvature at which a layer *(i)* will start slipping can be obtained from equation 2.19.

$$\kappa_i^{slip} = c \frac{EI_i^{slip} \cdot \kappa}{EI_i^{stick}} \qquad (2.19)$$

where

$$EI_i^{stick} = \sum_{w=1}^{n_i} EI_w^{stick} \qquad (2.20)$$

$$EI_i^{slip} = \sum_{w=1}^{\bar{n}_i} EI_w^{slip} \qquad (2.21)$$

The number of strands per layer is n_i. In the calculation of κ_i^{slip}, the κ term cancels out, making κ_i^{slip} independent of the curvature. The constant c of equation 2.19 takes on a value of unity for once-off bending with no reversal of the direction of bending. For repeated bending, however, $c = 2$, accounting for the fact that the curvature at which a layer slips has to be doubled to account for the reversal of friction forces (Papailiou, 1995b).

The effective bending stiffness of the conductor as a function of curvature is then obtained by comparing κ and κ_i^{slip}. If $\kappa > \kappa_i^{slip}$, the i'th layer has slipped, and the layer's contribution to the total bending stiffness of the conductor section is obtained using equation 2.23. If, however $\kappa_i^{slip} \geq \kappa$, the frictional forces between the layer and the adjacent layers are too large to allow slipping

of the layer, and the contribution to the stiffness is calculated using equation 2.24 .

$$\text{i.e.} \qquad EI^{tot} = \sum_{all\_layers} EI_i \qquad (2.22)$$

$$\text{where} \qquad EI_i = EI_i^{slip} \quad \text{if } \kappa > \kappa_i^{slip} \qquad (2.23)$$

$$\text{or} \qquad EI_i = EI_i^{stick} \quad \text{if } \kappa \le \kappa_i^{slip} \qquad (2.24)$$

To ensure the above equations had been correctly implemented, the construction details of the *ACSR Cardinal* conductor used by Papailiou were obtained from his thesis, and entered into MATHCAD. A graph of the calculated bending stiffness as a function of bending curvature was generated, and compared with that presented by Papailiou in his thesis. The curve for the stiffness obtained compared exactly with the original, proving that the equations had been correctly implemented.

2.2.2 Implementing the Variable Bending Stiffness in the Finite Element Model

The equations given by Papailiou are written as a function of the actual curvature of the conductor section. For an initially straight conductor the equations can thus be applied directly.

Consider a conductor section which has a slight curvature in its equilibrium position, such as a span sagging under its own weight. Assuming that creep (for example) over a period of time has eliminated any frictional stresses between the individual strands, and the stress state between the strands is similar to that which would be expected for a straight conductor, the change in bending stiffness would be more accurately described as a function of the change in curvature from the rest position as opposed to the actual curvature.

The equations for the bending stiffness-curvature relationship given above may be modified by substituting for the curvature κ with the change in curvature $\Delta\kappa$ where relevant, to accommodate this modification.

This modification can however not be implemented in the finite element model. The beam behaviour model in ABAQUS allows for a variable bending stiffness which changes with κ, but makes no provision for a dependence on $\Delta\kappa$. The user provides a table relating the bending moment to the corresponding curvature of the beam, with one requirement of the data being that it pass through the origin, i.e. the bending moment must be zero for zero curvature.

In the case of the aeolian vibration model for example, the beam elements making up the conductor, after being subjected to the gravitational load, have a non-zero curvature which is fairly large at the ends of the span. If the variable bending stiffness is then given as a function of the conductor curvature, so that the stiffness decreases with increasing curvature, the bending stiffness when it is

in the gravitationally displaced position will be quite small, as is to be expected from an initially straight conductor. However, in the real situation, effects such as creep will have caused the internal stresses to be eliminated, and the stiffness will once again be a maximum, and any change in bending stiffness will now be as a function of the change in curvature from the static curvature. This change in the bending stiffness-curvature relationship can however not be implemented in the finite element model using the existing facilities. The result is that if the original variable bending stiffness implemented in the ABAQUS model is now used in the aeolian vibration simulation, the beam elements will have a bending stiffness which is considerably less than in reality. The results obtained from the model would thus be an inaccurate representation of the real situation.

The correct behaviour could probably be implemented by means of an algorithm similar to that used in modelling the plastic behaviour of materials, however this would be a considerable project in itself, and is thus not implemented as part of the current project due to time constraints. Instead, alternative methods are employed to accommodate the variable bending stiffness for each of the relevant models as described in the chapters dealing with each specific load type.

2.3 CANTILEVER EXAMPLE PROBLEM

The results for the displacement profile and curvature along a section of a *Zebra* conductor, modelled as a cantilever, are presented in this section. The conductor is 1 metre in length, and is modelled with fifty 2-noded cubic elements.

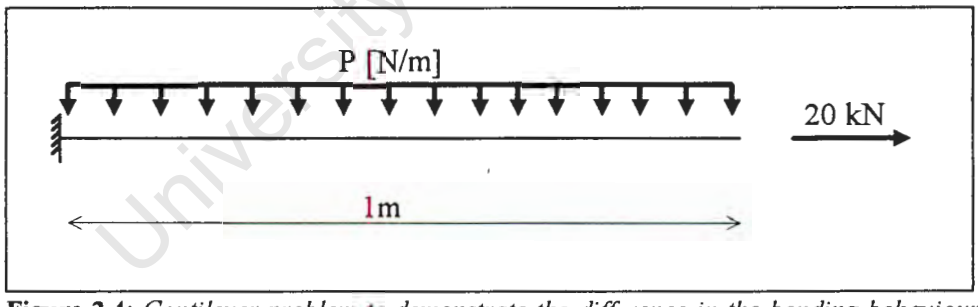

Figure 2.4: *Cantilever problem to demonstrate the difference in the bending behaviour for the constant and variable bending stiffness of a conductor.*

The loads applied are a 20 kN end load, and a uniformly distributed load P (Figure 2.4) along the length of the conductor. The deflection and curvature along the length of the cantilever are shown in Figure 2.5 and Figure 2.6, and show the results for P equal to 25 and 50 N/m respectively. The value used for the constant bending stiffness is the maximum, i.e. EI_{max} = 1605 Nm^2 for a *zebra* conductor. The variable stiffness implemented is that for an axial tension of 20 kN as shown in Figure 2.2.

As is to be expected, the displacements are larger for the variable bending stiffness, than for the constant. Even though a difference in the results for the displacements is clearly evident, they are not as pronounced as the difference in

the results for the curvature. As the transverse loads are increased, the curvature predicted by the constant stiffness model increasingly underestimates the real curvature, and thus when estimating the maximum stresses in the individual strands of the conductor (which are proportional to their curvature), the values predicted by the constant stiffness become more and more inaccurate with an increase in the loads.

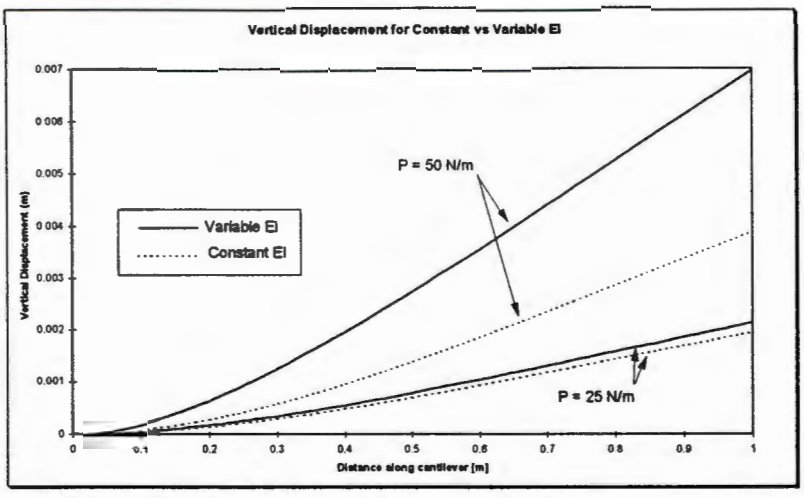

Figure 2.5: *Displacement profile of the conductor cantilever for constant vs variable bending stiffness.*

What is also clearly evident from Figure 2.6, is the threshold curvature that has to be exceeded before slipping of the strands, and therefore a reduction in the bending stiffness, occurs. The kinks in the curvature plots for the variable bending stiffness indicate the curvature levels at which the different strand layers slip. As mentioned above, the assumption is made that all the strands in a strand layer start slipping simultaneously.

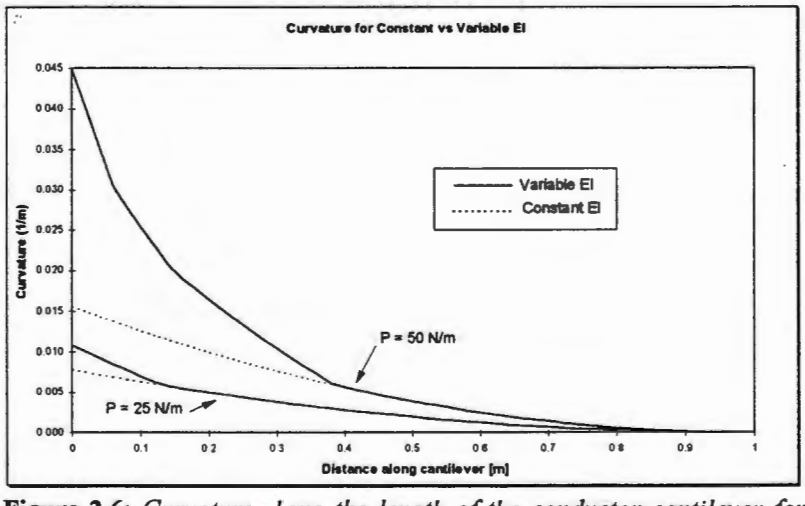

Figure 2.6: *Curvature along the length of the conductor cantilever for constant vs variable bending stiffness.*

2.4 COMPARISON OF DIFFERENT METHODS USED TO CALCULATE THE BENDING STRESSES IN A VIBRATING CONDUCTOR.

In this section, the method used to calculate the alternating bending stresses in the conductor adjacent to the suspension clamp, which will be referred to as Papailiou's method, is compared with the stresses predicted using the Poffenberger-Swart and EPRI equations. The latter is a fairly simple approach illustrated in the EPRI handbook (Doocey et al, 1979), while the Poffenberger-Swart formula is one which is often encountered and referenced in papers dealing with bending stresses due to aeolian vibration and the fatigue of conductors (Cigrè Study Committee 22 - working Group 04, 1988; Papailiou, 1995a; McGill & Ramey, 1986; Ramey et al, 1986). The Poffenberger Swart Formula has been compared by various authors with their experimental results, as discussed later.

The process of determining the alternating bending stresses in the conductor can be divided into two levels of calculation, which are described below. The first involves the assumptions made in calculating the bending curvature during vibration, and the second uses the calculated bending curvature to estimate the maximum stress to be expected in a strand of the conductor.

The three different methods of determining the alternating stresses are compared using the simulations for different boundary conditions as described in chapter 4 dealing with the aeolian vibration simulations.

2.4.1 Calculating the Bending curvature

EPRI Method

The EPRI equation assumes the bending curvature to be linearly related to the amplitude of vibration in the free span as shown by equation 2.25.

$$\kappa = 2\pi\sqrt{\frac{m}{EI}} \cdot fA \qquad (2.25)$$

The frequency of vibration is given by f, m is the mass per unit length of the conductor, and A is the amplitude of vibration far from the span ends.

Poffenberger-Swart Method (P-S)

The second approach on which the well known Poffenberger-Swart (P-S) formula (equation 2.26) is based, relates the bending curvature in the conductor to the deflection of a point on the conductor 89 mm from the last point of contact with the clamp.

$$\kappa = \frac{p^2}{e^{-px} - 1 + px} \cdot y_x \qquad (2.26)$$

where

$$p = \sqrt{\frac{T}{EI}} \qquad (2.27)$$

with $x = 0.0889$ m, and y_x the deflection at this point.

Papailiou's Method

For Papailiou's equation, the curvature used in calculating the stress is obtained directly from the finite element analysis. As the curvature in a finite element is only available at the integration points, the curvature at the last point of contact with the suspension clamp must be estimated. This is done by fitting a quadratic curve to the curvature values for the four integration points at the end of the conductor as a function of the distance from the last point of contact with the clamp. This is done by means of the least squares method, and the curvature at the end of the conductor is then estimated from this relationship.

To verify this procedure, the elements making up the conductor at the end were refined, so that the four integration points were closer to the end of the conductor, and to one another, by a factor of ten. The curvature estimated at the end of the conductor was very similar to that obtained with the coarser mesh, verifying this method of estimating the curvature.

What is clearly evident for the first two equations is that, all other variables being easily determined and constant, the choice made regarding the bending stiffness *EI* will have a significant effect on the results. The value used may vary from the minimum value of $EI_{min} = 26\text{Nm}^2$ to a maximum value of $EI_{max} = 1605\text{Nm}^2$ for a *Zebra* conductor, depending on the assumptions made on the amount of slipping between adjacent strands in the conductor.

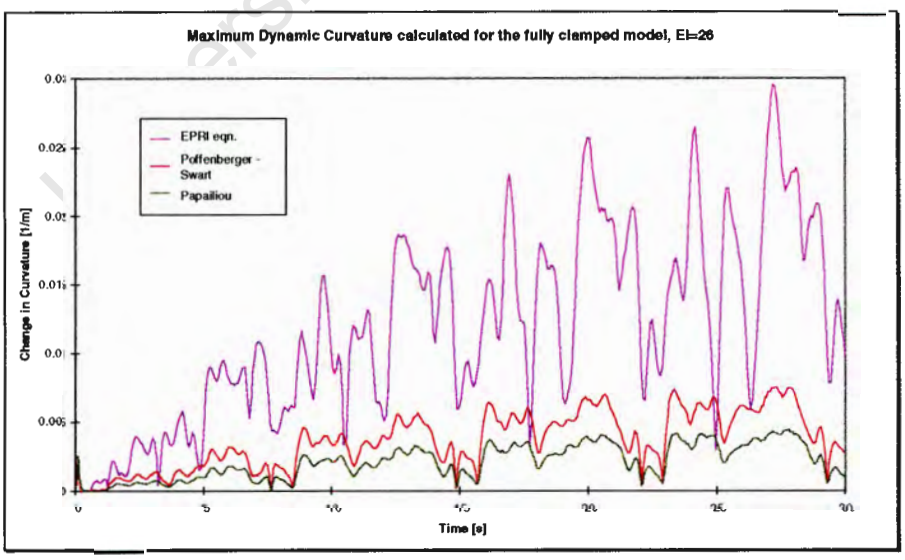

Figure 2.7: *Showing the different methods of calculating the amplitudes of the bending curvature using a bending stiffness of* EI_{min}.

According to the EPRI handbook (Doocey et al, 1979), the value for the bending stiffness most commonly used in conjunction with the P-S and EPRI equations is the minimum value (EI_{min}), which assumes all strands are free to

slip relative to one another. As can be seen from Figure 2.7 which compares the bending curvature obtained using equations 2.25 and 2.26 to that obtained from the analysis, the curvature is exaggerated slightly by the P-S relationship, and very much so for the EPRI equation, when using a bending stiffness of EI_{min}.

Figure 2.8 below shows the values obtained for EI = 1605 Nm^2, and as can be seen this value for the bending stiffness gives values which agree more with that obtained for the finite element analysis, and in the case of the curvature calculated using the P-S formula (equation 2.26), the results agree quite favourably with the finite element analysis. Even though the results for the other boundary conditions are not shown, the correlation for the curvatures predicted by the different methods is virtually the same.

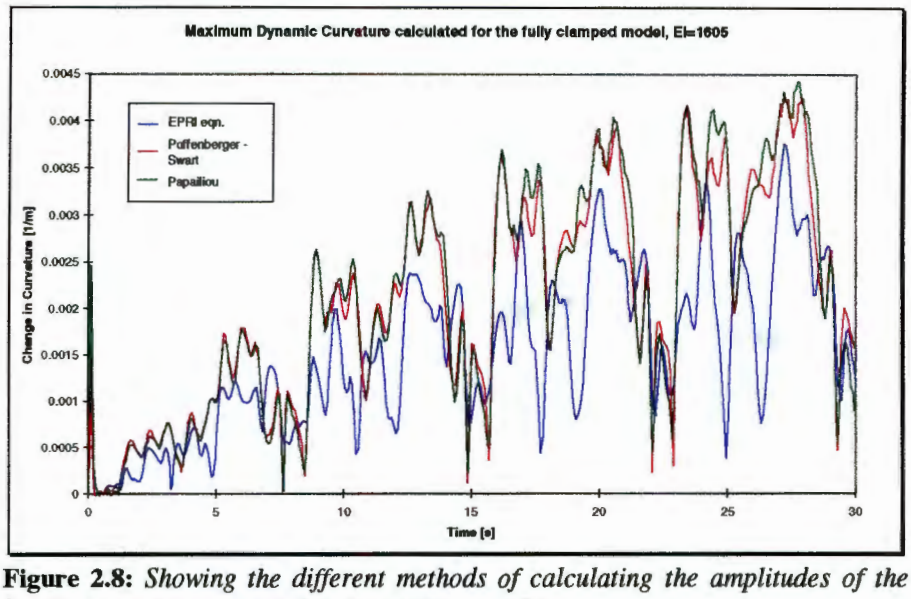

Figure 2.8: *Showing the different methods of calculating the amplitudes of the bending curvature using a bending stiffness of* EI_{max}.

The value used for the bending stiffness in the finite element analysis is the maximum of 1605 Nm^2, as the change in bending curvature is less than that required for inter-strand slipping to occur for any of the strand layers, according to equation 2.19 .

2.4.2 Calculating the Alternating Stress from the Bending Curvature

To calculate the bending stress from the curvature, a fundamental difference exists between the EPRI and P-S methods, and the method given by Papailiou. The assumption made for the first two methods is that full slipping has occurred, and thus the value for the bending stiffness is the minimum corresponding to EI_{min}. From section 2.2, it can be seen that the bending stiffness changes gradually with an increase in the curvature. For this reason, Papailiou has written the stress in the strand as consisting of two components, a minimum, corresponding to the bending of the strand about its own axis, and a second term, which depends on whether the strand is slipping or not. In the case of no slipping occurring, such as is the case for the small amplitude aeolian vibration encountered in this project, an additional stress component is introduced due to the bending of the strand about the axis of the conductor (see

section 2.2). In the case of the other two methods, the stress is assumed to consist solely of the first term.

The equations used to calculate the maximum dynamic stresses during bending in a strand on the top of the conductor, in the outer layer, may thus be written as follows:

EPRI Method: $$\sigma_a = E_a d\pi \sqrt{\frac{m}{EI}} \cdot fA \qquad (2.28)$$

Poffenberger-Swart: $$\sigma_a = E_a \frac{d}{2} \frac{p^2}{e^{-px} - 1 + px} \cdot y_x \qquad (2.29)$$

Papailiou: $$\sigma_a = E_a \left(r \cos^2(\beta_i) + \frac{d}{2} \right) \kappa \qquad (2.30)$$

where d is the strand diameter, and E_a is the modulus of elasticity of the strands in the outer layers of a conductor. In the case of ACSR conductors, this is the elastic modulus for aluminium.

The stresses calculated using the three approaches are compared in the graphs below, for different boundary conditions.

The value used for EI for the EPRI and Poffenberger-Swart formulae is the minimum value of EI_{min} = 26Nm^2, as required for the assumption of full slippage between strands.

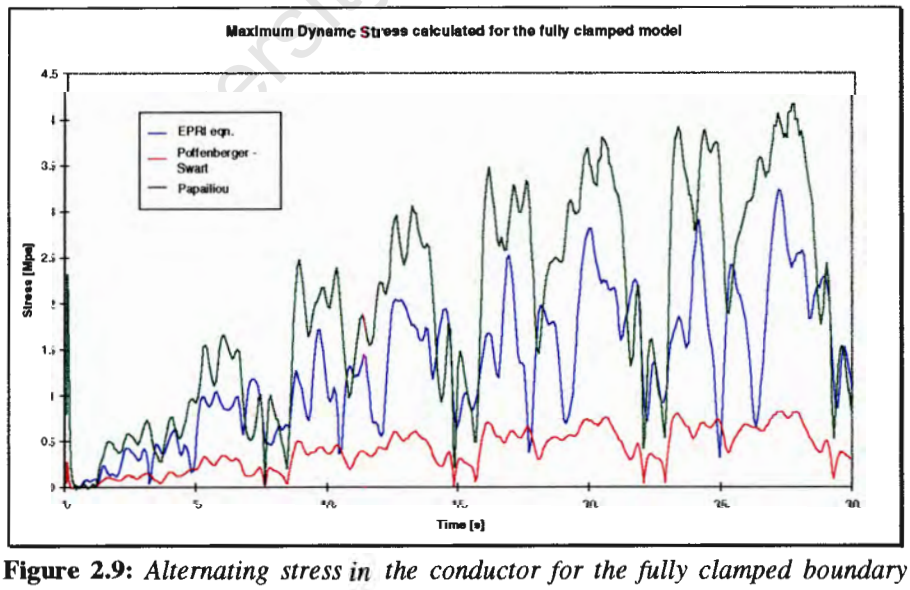

Figure 2.9: *Alternating stress in the conductor for the fully clamped boundary condition, calculated using the three different methods.*

For the fully clamped boundary, the alternating stress predicted by the Poffenberger-Swart and EPRI equations is less than that using Papailiou's equation. As can be seen in the results for the other two boundary conditions, the alternating stress amplitude predicted by the P-S equation is significantly

less than that predicted by the other two equations. This agrees with what other authors have found. Claren and Diana (1969), reportedly obtained values for the maximum alternating stress amplitude which varied from 14% less to 73% more than that predicted by the Poffenberger-Swart equation. As shown by Papailiou, the Poffenberger-Swart equation underestimates the dynamic stresses for small amplitude vibrations, and exaggerates them for larger displacements (Papailiou, 1995a).

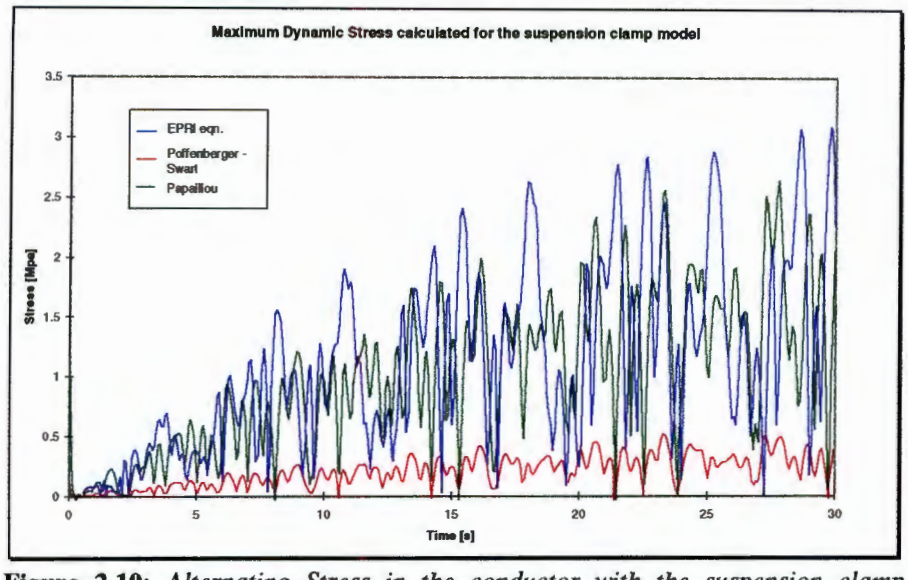

Figure 2.10: *Alternating Stress in the conductor with the suspension clamp modelled.*

What is quite interesting and maybe a little surprising from these results, is the fairly good agreement of the alternating stresses using the EPRI equation and a bending stiffness of EI_{min} with those predicted by Papailiou's equation, considering the different values of EI on which the different methods are based.

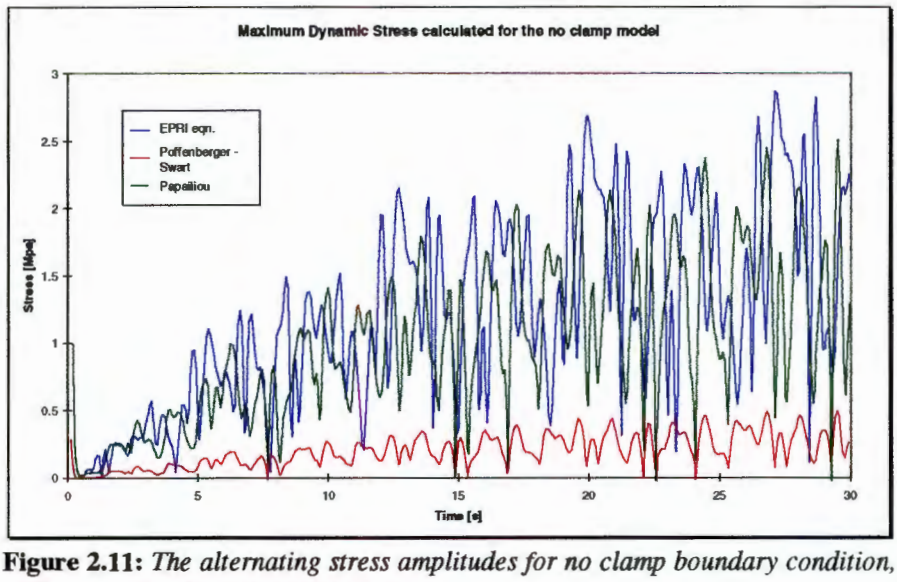

Figure 2.11: *The alternating stress amplitudes for no clamp boundary condition, with unrestricted rotation at the supports.*

3. THE SELF-DAMPING OF CONDUCTORS

Decisions on the inclusion of damping in any dynamic model may have a considerable effect on the results obtained from the model. In the case of a model for small amplitude, high frequency vibration, such as aeolian vibration, the inclusion of material damping may have a significant effect on the results. This chapter describes the modelling of the internal damping of a conductor and it's implementation in the aeolian vibration model.

A short discussion of the information obtained from the literature is followed by a description of the Rayleigh method used to implement the damping in the finite element model. The available data is then discussed, and the method used to convert it from a power dissipation format to a damping ratio is then described. The procedure employed in obtaining the Rayleigh damping coefficients from the damping ratio is then explained, while the last section deals with the assumptions made about the vibration amplitude in calculating the internal damping for the aeolian vibration simulations.

3.1 LITERATURE REVIEW

The internal damping experienced by a vibrating conductor is made up of two components. The first is the small amount of damping caused by friction between the molecules of the material of the conductor. The second is as a result of the frictional losses due to inter-strand slippage, which occurs when the bending curvature exceeds the minimum curvature for slipping of one or more strands to occur. When the curvature of the conductor is less than that required for any slipping, the internal damping will be as a result of material damping on a molecular level only.

According to Noiseux (1991), the internal damping losses of a conductor are an essential element in any model dealing with aeolian vibrations. Timoshenko et.al. mention in their book (1974) that in systems being subjected to a forcing function close to a natural frequency of the system the damping is of primary importance, even if it is small. They also advise that damping should be included in a vibration analysis until its effect on the solution has at least been established.

Hagedorn (1982) states that the internal damping is considerably less than that provided by external sources such as vibration dampers, and as such could be considered negligible when such devices are included. Following the advice of Timoshenko and his colleagues, a more complete and accurate model should however probably include the internal damping, even when the model includes external damping devices, at least until the effects have been ascertained.

Another factor which supports the inclusion of the internal damping, is that Hagedorn bases his assumption on a more global approach. He says that for a system as a whole the amount of energy absorbed by the vibration dampers is much greater than that absorbed by the conductors. Considering that for a 400m span, for

example, a maximum of two dampers would be used at each span end, it might be that the small amount of internal damping has a fairly significant effect on the behaviour of the sections of the conductor furthest from the dampers, such as in the middle of the span. The behaviour of the middle section of the conductor, could in turn have a significant effect on the motion of the system as a whole.

3.2 RAYLEIGH DAMPING

The method most commonly used to introduce material damping in a direct integration vibration analysis is one known as Rayleigh or proportional damping (Cook et al, 1989). The damping matrix **[C]** describing the damping of the system, is written as a linear combination of the mass and stiffness matrices, **[M]** and **[K]**, respectively, i.e.

$$[\mathbf{C}] = \alpha\,[\mathbf{M}] + \gamma\,[\mathbf{K}] \qquad (3.1)$$

where α is the mass proportional constant, and γ is the stiffness proportional constant. The Rayleigh constants, α and γ, are related to the fraction of critical damping (ξ) by

$$\xi = \frac{1}{2}\left(\gamma\omega + \frac{\alpha}{\omega}\right) \qquad (3.2)$$

where ω is the frequency of vibrations in rad/s. The fraction of critical damping, or damping ratio is described as

$$\xi = \frac{c}{c_{cr}} \qquad (3.3)$$

with c_{cr} being the critical damping, and c the actual damping, for the system.

The following section describes the data on internal damping that is available, and how the data required for the analyses is obtained from it.

3.3 AVAILABLE DAMPING DATA

The experimentally obtained results for the power dissipated in a zebra conductor are obtained from the German company, Richard Bergner GmbH and co. in the form of a chart. The chart is given in the appendix and shows the power dissipated in the conductor as a function of vibration frequency. Three curves are given for vibration angles of β = 5, 10 and 20 minutes respectively, with the vibration angle β defined as follows:

$$\beta = \frac{2\pi A}{\lambda} \qquad (3.4)$$

where λ is the wave length, and A is the amplitude of vibration. The vibration angle β is in fact the rotation of the conductor at a node (in the sense of a wave node, i.e. the

point in a wave that does not experience any transverse displacement), as shown in Figure 3.1

As the bending angle expected in the finite element simulations is estimated to be considerably less than that for which the data is available, the internal losses for the range of vibration angles expected are estimated from the data available.

The following empirical formula has been found empirically to describe the power dissipated internally by a conductor, for different tensions (T), vibration angles and frequencies (Hagedorn et al, 1991, Möcks, 1984):

$$P_{dissipated} = C \cdot f^{n} \beta^{m} L \frac{T_{UTS}}{T} \qquad (3.5)$$

where C, n and m are experimentally determined constants, L is the span length, f the frequency of vibration, T_{UTS} the ultimate tensile strength of the conductor, and T the tension in the conductor.

Agelink (1981) reports from his experimental results that the value for m varies between 2 and 3, with the average value being 2.2 .

Equation 3.5 can be rewritten for a particular frequency as

$$\overline{P}_{dissipated} = \frac{C_2 \cdot \beta^{m}}{T} \qquad (3.6)$$

where $\overline{P}_{dissipated}$ is the internal loss per unit length of the conductor. Equation 3.6 is clearly valid only for constant frequency and for the same conductor type, for which the ultimate tensile strength is constant.

To implement the Rayleigh damping, the power dissipated in the conductor for the highest active vibration frequency, corresponding in this case to the frequency of the aeolian excitation, must be determined.

For the purpose of this project, the five frequencies of aeolian vibration considered are 15Hz, 22.5 Hz, 30Hz, 37.5Hz and 45Hz respectively, and as such equation 3.6 is evaluated for each of these frequencies. This is done by obtaining the value of the power dissipated at the specific frequency, for each of the three vibration angles available, and fitting a graph of the form given by equation 3.6, using a commercially available curve fitting package, to the data. Instead of trying to estimate a value for both constants m and C_2, from only three data points, a value of m = 2.2 (according to Agelink, 1981) is used, enabling the unknown C_2 to be determined with more accuracy.

Table 3.1 below shows the values of C_2 obtained for each of the five loading frequencies.

Frequency (Hz)	15	22.5	30	37.5	45
C_2 (W.N/m)	0.576	2.16	6.26	12.49	26.11

Table 3.1: *The values of the constant C2 in equation 3.6, obtained for each of the aeolian vibration frequencies modelled.*

As the internal loss must be expressed as a damping ratio, the data is converted to the required format as described in the next section.

3.4 CONVERTING THE POWER LOSS TO A DAMPING RATIO

The damping ratio, kinetic energy and power dissipated in the conductor are related as follows (Noiseux, 1991):

$$\xi = \frac{1}{2} \cdot \frac{P_{dissipated}}{\omega \cdot KE} \qquad (3.7)$$

where KE is the kinetic energy of the conductor. If the kinetic energy in a half wave length at any point in time is denoted by $KE_{\lambda/2}$, and the wave length by λ, the previous equation can be rewritten as

$$\xi = \frac{1}{4} \cdot \frac{\overline{P}_{dissipated} \cdot \lambda}{\omega \cdot KE_{\lambda/2}} \qquad (3.8)$$

Assuming the displaced shape of the conductor during aeolian vibration to be sinusoidal in nature (Figure 3.1), and the displacement at any position along the conductor to vary periodically, the transverse displacement for a point in the conductor can be described by equation 3.9.

$$w(x,t) = A \cdot \sin(\omega t) \cdot \sin\left(2\pi \frac{x}{\lambda}\right) \qquad (3.9)$$

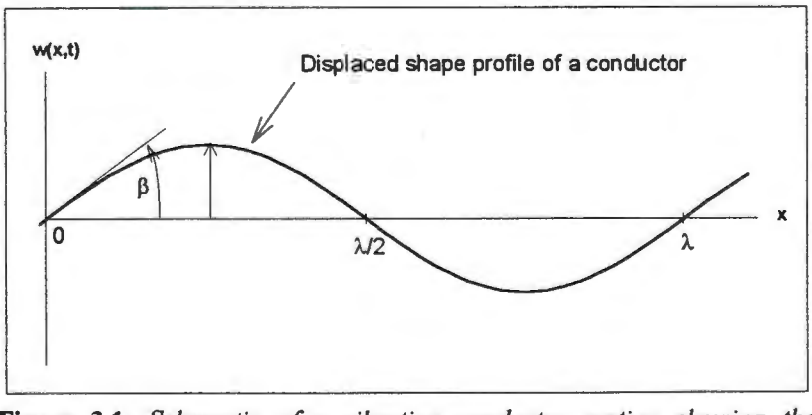

Figure 3.1: *Schematic of a vibrating conductor section showing the notation used*

The velocity of the point in the conductor is then given by

$$v(x,t) = \frac{\partial w(x,t)}{\partial t} = A \cdot \omega \cos(\omega t) \cdot \sin\left(2\pi \frac{x}{\lambda}\right) \qquad (3.10)$$

If the mass per unit length of the conductor is $\overline{m}$, the kinetic energy per unit length for a point located at x, at time t will be

$$\overline{KE}(x,t) = \tfrac{1}{2} \cdot \overline{m} \cdot v(x,t)^2 \qquad (3.11)$$

Integrating equation 3.11 from $x = 0$ to $x = {}^{\lambda}/_{2}$, over one complete cycle, and dividing the result by the period of vibration, will give the average kinetic energy for a half wave per cycle, i.e.

$$KE_{\lambda/2}^{ave} = \frac{\omega}{2\pi} \int_0^{\frac{\lambda}{2}} \int_0^{\frac{2\pi}{\omega}} \tfrac{1}{2} m \left(A \cdot \omega \cos(\omega t) \cdot \sin\left(2\pi \frac{x}{\lambda}\right) \right)^2 dt dx \qquad (3.12)$$

Substituting the value obtained for $KE_{\lambda/2}^{ave}$, along with the appropriate values for λ, ω and $\overline{P}_{dissipated}$ into equation 3.8 gives the desired damping ratio for the problem. This ratio is then used to obtain the mass and stiffness proportional damping constant respectively, as described below.

3.5 OBTAINING VALUES FOR THE RAYLEIGH DAMPING

Once a damping ratio has been established, the values α and γ are determined by substituting the damping ratios (ξ_1 and ξ_2), for two different frequencies (ω_1 and ω_2), into equation 3.2, and solving the resultant simultaneous equations. The frequencies used to determine the constant should be chosen so that $\omega_1 < \omega < \omega_2$ for all the frequencies of vibration which may be expected in the analysis (Cook et al, 1989). Thus ω_1 will usually correspond to the fundamental frequency of vibration of the system, and ω_2 to the highest frequency of loading. In the case of aeolian vibration ω_2 will correspond to the frequency of the vortex shedding loads the conductor is subjected to during aeolian vibration. In the case of the models for this project, the first natural vibration mode of the 400m span is in the region of 0.1Hz. As can be seen from the chart of the damping in the appendix, the lowest frequency for which data is available is 10 Hz.

As damping data is not available at the fundamental frequencies of the span, the assumption that $\omega_1 = 0$, with a corresponding damping ratio of zero, is made instead. The damping introduced at the higher frequencies is considerably greater than at the fundamental frequency and thus the values of α and γ are almost totally dependent on the data at the upper frequency (ω_2), and any error introduced by this assumption is negligible.

Making the assumption that $\omega_1 = 0$ introduces problems with singularities when evaluating α and γ and substituting $\omega = 0$ into equation 3.2. The assumption that

$\omega_1 = 0$ requires that the mass proportional damping is zero, i.e. $\alpha = 0$. To determine the validity of this assumption, consider the following example.

Assume that the damping ratio of a *Zebra* conductor at a frequency of 15 Hz is 1.E-4, and the damping ratio at a frequency of 0.1 Hz is 5.E-7, i.e. $\omega_1 = 0.2\pi$ rad/s, $\zeta_1 =$ 5.E-7, $\omega_2 = 30\pi$ rad/s and $\zeta_2 =$ 1.E-4. This assumes that the damping at 0.1 Hz is less than that at 15 Hz by a factor of 200. Studying the trend of the damping curves of the chart in the appendix and making the observation that they follow a logarithmic trend, it is safe to assume that the factor of 200 is a conservative one, and that the damping at 0.1 Hz would be even less than 5.E-7.

The values obtained for the Rayleigh constants using this data are $\alpha =$ -2.1E-7 and $\gamma =$ 2.1E-6 respectively. The Rayleigh damping, along with the mass and stiffness proportional contributions to the damping are plotted in the graph of Figure 3.2 below. At the lowest mode of vibration, 0.1 Hz, the damping predicted by the stiffness proportional component is 77% of that predicted by the Rayleigh damping, and at frequencies of 0.2 Hz and above, the difference is negligible. The difference in the values obtained for γ is less than 0.001% if ω_1=0 instead of $\omega_1 = 0.2\pi$ is used.

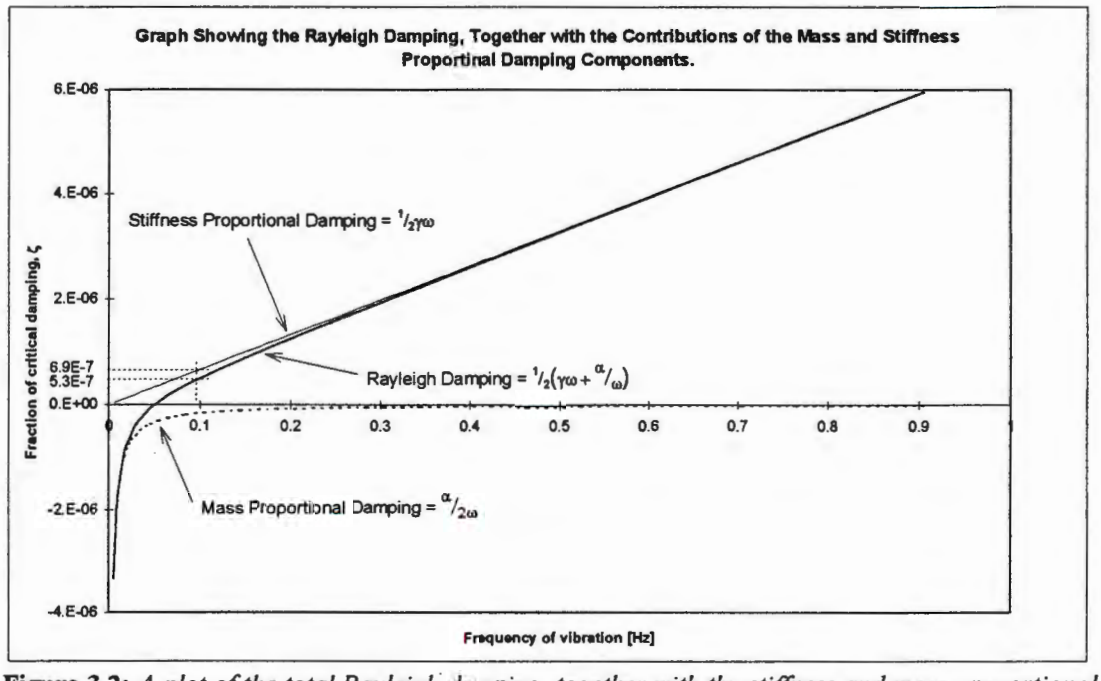

Figure 3.2: *A plot of the total Rayleigh damping, together with the stiffness and mass proportional contributions as calculated for a vibration frequency of 15Hz. Note that the plot only shows the lower frequency range of interest and that the total damping and Stiffness proportional factor are virtually identical above the fundamental frequency of the span corresponding to ≈ 0.1 Hz.*

This example shows that the mass proportional component is negligible, and that the Rayleigh constants can be considered dependent only on the loading frequency (ω_2).

3.6 Dependence of the Damping Ratio on the Vibration Amplitude

As can be seen from the aeolian vibration results presented later, the amplitude of vibration of a specific point along the span varies with time. The amplitude of vibration is also dependent on the position in the span. From equations 3.6 and 3.12, it can be seen that the internal loss and kinetic energy of the conductor, and therefore the damping ratio, are dependent on the vibration angle, which depends on the vibration amplitude. Hence the damping of a section of the conductor should strictly speaking be dependent on the current amplitude of vibration of the section. As no facilities are currently available to accommodate this however, a simpler alternative must be used.

Figure 3.3 below shows the dependence of the damping ratio on the amplitude of vibration as calculated using the equations above. As shown in the graph of Figure 4.30, showing the vibration amplitude during aeolian vibration 100m from the end of the span, the amplitude of vibration of the conductor varies typically from 0.25 to 1 mm. For the finite element simulations, the damping ratio is calculated for A = 0.5 mm and used in the analyses. The graph below shows that the damping ratio does not change drastically over the range of typical vibration amplitudes. It is thus reasonably fair to assume that the damping ratio calculated for the chosen value of A= 0.5 mm is a fair approximation for the range of vibration amplitudes expected.

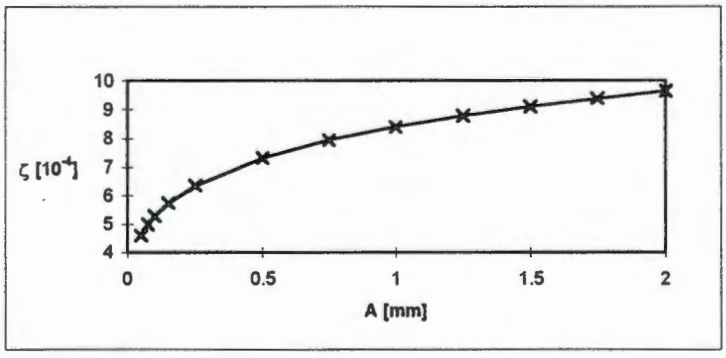

Figure 3.3: *Dependence of the damping ratio on the amplitude of vibration.*

4. AEOLIAN VIBRATION

One of the most commonly encountered types of conductor motion is aeolian vibration. This chapter describes various aspects of the modelling of aeolian vibration on a conductor. The first section mentions the works in literature which have been found useful and relevant to the study, while the following section describes the phenomenon of aeolian vibration. Where appropriate, the information from literature is discussed in more detail in this second section. The method used to simulate the aeolian loading in the finite element model is then described, followed by the details of the finite element model. A discussion on the effect of the choice of boundary conditions on the results is followed by the verification of the finite element model. The last section in the chapter presents and discusses the results of a number of different finite element simulations of aeolian vibration.

4.1 AVAILABLE LITERATURE

A substantial amount of work has been done in the past on vortex shedding and aeolian vibration. Most of the work which is relevant to the subject of aeolian vibration of conductors and which was available at the time, is included in a book compiled by the Electric Power Research Institute (EPRI), entitled "Wind Induced Conductor Motion" (Doocey et al 1979).

A large portion of the work deals with the interaction between a fluid and a vibrating cylinder in the path of the fluid. One of the papers most frequently referred to is that compiled by Diana and Falco (1971) which deals with the forces transmitted to a vibrating cylinder. Other works dealing with vortex shedding and the forces experienced by the cylinders as the vortices are shed include those of Chi and Vossoughi (1985), Sarpkaya and Kline (1982), Goswami et al (1993), Chilikuri(1987), Staubli (1983), Hurlbut et al (1982) and Feng (1968). In most cases the forces on both vibrating and stationary cylinders are studied. Motion of the vibrating cylinder is usually accommodated by mounting the cylinder on a system of springs.

Numerous papers have also been published on the aeolian vibration of conductors in particular. These include the work of, amongst others, Oliviera & Freire (1994), Simmons and Cleary (1980), Sturm (1936), Möcks (1986), Schäfer (1986) and Du Plessis (1994). Apart from the EPRI reference book mentioned above, another publication which has been compiled as a general design and research reference is the report on aeolian vibration by a working group of Cigrè's study committee 22 (Cigrè Study Committee 22 - working Group 01, 1989).

4.2 THE PHENOMENON OF AEOLIAN VIBRATION

The phenomenon of aeolian vibration is named after the ancient Greek God of Wind, Aeolus. It refers to the high frequency vibration of a slender structure in a moving fluid.

Aeolian vibration occurs as a result of the alternate shedding of vortices from the top and bottom of the cable respectively. These vortices, which have opposite spin to each other, cause pressure fluctuations perpendicular to the direction of flow of the fluid as they break away from the fluid boundary layer around the structure. The periodically shed vortices are carried away from the rear of the cylinder, forming what is known as a von Karmen vortex street.

As shown by the results of the experiments on an elastically mounted cylinder inside a wind tunnel, carried out by Diana and Falco (1971), the pressure around the cylinder, and therefore the lift force on the cylinder varies periodically and can be assumed to be sinusoidal.

The vertical displacement of the cylinder, which is also periodic in nature, follows the lift force by a certain phase angle. This angle varies between 0 and π radians (Diana & Falco, 1971), depending on the ratio v/v_s, where v is the free stream velocity of the fluid, and v_s is the Strouhal velocity, obtained from equation 4.4. The phase angle is discussed in more detail later on.

In the case of aeolian vibration of a conductor, many different factors play a role in determining firstly the possibility of onset of vibrations, and secondly the severity at which they occur (Doocey et al, 1979). These factors include the turbulence of the wind flowing over the conductor, which in turn is dependent on the topography and vegetation of the surroundings. Laminar wind is more conducive to vortex shedding, thus the likelihood of aeolian vibration increases as the turbulence in the wind decreases. The diameter of the conductor, wind velocity, tension at which the conductor is strung and the roughness of the surface of a stranded conductor (as opposed to a smooth cylinder) are all contributing factors and these, along with any other significant factors are described in the sections that follow.

4.2.1 Frequency of Vortex Shedding

The frequency at which vortices are shed from a cylinder in a laminar fluid was investigated by Vincent Strouhal (Douglas et al, 1986) and was found to be governed by the relationship:

$$f = Str \cdot \frac{v}{D} \qquad (4.1)$$

where
- f - frequency of vortex shedding (Hz)
- Str - Strouhal number
- v - free stream fluid velocity (m/s)
- D - diameter of cylinder (m)

Strouhal empirically related the Strouhal number to the Reynolds number as follows:

$$Str = 0.198 \cdot \left(1 - \frac{19.7}{\mathrm{Re}}\right) \quad \text{for} \quad 250 < \mathrm{Re} < 2 \cdot 10^5 \qquad (4.2)$$

where Reynolds number is given by

$$\mathrm{Re} = \frac{\rho v D}{\mu}, \qquad (4.3)$$

ρ and μ being the density and dynamic viscosity of the fluid respectively.

Rearranging equation 4.1, the Strouhal velocity v_s can be determined for a specific frequency, i.e.

$$v_s = \frac{f \cdot D}{Str} \qquad (4.4)$$

The Strouhal velocity and the actual free stream velocity may differ from one another, due to the phenomenon of lock-in as described below.

The dependence of the frequency of vortex shedding on the fluid velocity results, in the case of a long conductor, in the possibility of more than one natural mode of vibration being excited on the same span at any one time, due to the fact that the wind velocity may vary along the length of a single span.

Regarding the magnitude of the Strouhal number, Diana and Falco (1971) found a constant value of $Str = 0.19$ for $2\times10^3 < \mathrm{Re} < 6.5\times10^4$. Feng reportedly measured a value of $Str = 0.198$ for $\mathrm{Re} = 2\times10^4$, while Staubli (1983) found a value of $Str = 0.18$ at $\mathrm{Re} = 6\times10^4$. The EPRI handbook (Doocey et. al. 1979) recommends an average value of $Str = 0.185$ for use with conductors, and the reader is referred to Figure 1-2 of the handbook which gives the Strouhal number for a range of Reynolds numbers. The report compiled by Working Group 01 of the Cigrè study committee no. 22 on Overhead Lines (Cigrè Study Committee 22 - working Group 01, 1989), states that the Strouhal number for a conductor lies between the values of 0.18 and 0.22.

4.2.2 Lock-in

For a stationary cylinder, the vortices are shed randomly along its length. However, when, in the case of an elastically mounted cylinder, it starts vibrating in the plane perpendicular to the fluid flow, the vortex shedding becomes synchronised with the motion of the cylinder. This leads to the phenomenon known as "lock-in" whereby the cylinder will continue vibrating at the natural frequency, at which it was originally excited by the shedding vortices, even if the velocity of the fluid deviates by as much as 10% from the original excitation velocity (Doocey et. al. 1979).

In the case of a conductor, this means that once it is excited at a certain frequency, it may continue vibrating at that frequency even if the wind velocity deviates from the original by up to 10%.

4.2.3 Forces on the Conductor Due to Vortex Shedding

Chi and Vossoughi (1985) state in their paper that a rigorous analysis of the fluid-structure interaction, which occurs in wind-induced excitation of slender beams, would include the integration of the Navier-Stokes equations, and matching of the pressures and displacements at the fluid-structure boundary.

This would require that not only the conductor, but also the fluid region around the conductor be modelled using finite elements along the whole length of the span. Due to the small diameter of a typical conductor when compared to its length in, for example, a 400m span, the large number of elements required to model the problem with any accuracy makes such a simulation impractical. If a 0.5×0.5 metre cross-section of fluid were modelled around the conductor, the number of elements required per unit length of the conductor would be about 1000. Translating this to a 400 metre span would result in a problem in which the fluid region alone consists of approximately 400 000 elements. Due to the large amount of CPU time required to model a problem of such proportions in which a sufficient period in real time is modelled to capture the response accurately, such a simulation is impractical.

As an alternative, empirical data from experiments may be used to simulate the fluid structure interaction, thus eliminating the need to model the fluid domain, and substantially reducing the amount of CPU time. This involves certain assumptions about the interaction between the fluid and the structure, such as the nature of the force exerted by the vortices on the structure. In general, all these assumptions have been validated by experimental data, such as the assumption that the force on the conductor is periodic in nature. The experimentally obtained results of Figure 9 in the paper by Diana and Falco (1971) show the periodic nature both of the force acting on an elastically mounted cylinder and of it's displacement.

As shown by the results of Hurlbut et al (1982), the fluctuation in the drag force is small compared to the change in the lift force during vortex shedding. The drag force is thus assumed to be constant, while the lift force varies periodically. If the latter is assumed to vary sinusoidally, the lift force acting on a cylinder undergoing aeolian vibration can be written as follows:

$$F_L = F_{L0} \sin(\omega \cdot t + \phi) \qquad (4.5)$$

with ω being the vortex shedding frequency [rad/s], t being time [s] and ϕ [rad] the phase angle. F_L is in units of force per unit length.

The amplitude of the lift force (F_{L0}) per unit length is written as follows: (Doocey et al, 1979; Diana and Falco, 1971; Sarpkaya and Kline, 1982)

$$F_{L0} = 0.5\rho D C_L v^2 \qquad (4.6)$$

where ρ is the density of the air, D the diameter of the cylinder, C_L the lift coefficient, and v the free stream velocity of the fluid.

In the case of a conductor, which is considerably longer than the cylinders typically used in wind tunnel experiments, the displaced shape of the conductor at any point in time consists of a number of standing waves along its length. This is due to the natural mode, or combination of natural modes in which the conductor vibrates as a result of the vortex shedding. To maintain the phase angle between the force and displacement along the whole length of the conductor in the span, the lift force must vary along the conductor's length. The variation of the force is accounted for by an additional term in the equation for the lift force acting on the conductor, β_i which is dependent on the displacement (u_i) of any specific point i along the length of the conductor. The lift force acting on the conductor at a point i is thus given by the following equation:

$$F_{L_i} = F_{L0} \sin(\omega \cdot t + \phi + \beta_i) \qquad (4.7)$$

4.2.4 Phase Angle Between the Force and Displacement

As mentioned previously, the phase angle by which the lift force acting on the cylinder leads the cylinder's displacement is dependent on the ratio $r = v/v_s$ (Diana et al, 1971). The ratio of the distance between the two vortex trails, shed on either side of the structure, to the distance between two successive vortices shed from the same side of cylinder is written as h/l (Figure 4.1) and was found by von Karmen to be constant, and equal to $\sinh^{-1}(1)/\pi \approx 0.281$ (Sayers, 1992).

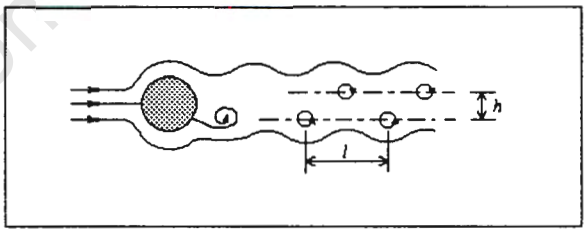

Figure 4.1: *Showing the von Karmen vortex street behind a cylinder in a fluid.*

As described by Diana and Falco (1971), the width of the vortex street depends on the instant at which the vortex breaks away from the boundary layer. If the vortex breaks away above the cylinder when it's upward displacement is maximum, or similarly when it breaks away below the cylinder at the maximum downward displacement, the vortex street will be widest and the lift force will lead the displacement by 180°. If, however, the vortex breaks away above, when the cylinder is at its maximum downward displacement, the vortex street will be at its narrowest, and the lift force and displacement will be in phase.

For $r > 1$, the distance l will increase. To maintain the constant ratio for h/l, the distance h also has to increase, forcing the phase difference to approach 180°. Conversely, for $r < 1$, l and therefore h decreases, forcing the phase difference to its minimum. For a ratio of $r = 1$, the natural frequency of vibration and the Strouhal frequency of vortex shedding will coincide, and the phase angle, relating to maximum power transfer from the wind to the vibrating object, is 90°.

4.2.5 The Lift Coefficient

The values reported for the lift coefficient vary between 0.3 and 0.84 and are given either for specific ratio's of A/D, where A is the amplitude of vibration and D is the diameter of the cylinder, for a range of Reynolds numbers, or both. The table below summarises the values reported by different authors, along with their dependence on the Reynolds number or A/D ratio.

Source	C_L	A/D	Re
Diana et. al (1971)	0.45	0.1	2E3 - 6E4
"	0.7	0.2	"
"	0.8	0.3	"
"	0.84	0.5	"
Sarpkaya et al (1982)	0.3 - 0.4	?	1.6E4 - 3.3E4
Chilikuri (1987)	0.4	0.1	144
Hurlbut et al. (1982)	0.3	0.14	80

Table 4.1: *Showing the lift coefficient due to vortex shedding as obtained from various sources.*

A dependence of the lift coefficient on the ratio of the vibration amplitude to the cylinder diameter, rather than on the actual diameter of the cylinder, is evident from the experimental results (Diana et al, 1971). The results are thus valid for any cylinder diameters. It is evident from the results above and for the range of data shown that the lift coefficient increases with A/D.

As mentioned in the chapter dealing with the self-damping of conductors, the maximum amplitude of vibration is in the order of 1 mm. For a *zebra* conductor, this translates to a ratio of $A/D < 0.1$. From the data above and a few test simulations carried out, a value of 0.3 seems to be an appropriate value for this ratio, and is the value used in simulating the loading due to aeolian vibration.

4.2.6 Drag Loading on the Conductor and Drag Coefficient.

According to the EPRI handbook (Doocey at al, 1979), aeolian vibration normally occurs for wind velocities of between 1 and 7 m/s. For a conductor of 30 mm diameter and a value of 1.5E-5 for the kinematic viscosity of air at 20°C (Douglas et al, 1985), this translates to a range of Reynolds numbers from 2.E3 to 14.E3 . The drag coefficient for a smooth cylinder for this range of Reynolds numbers varies slightly between 1 and 1.2 (Sayers, 1992). Figure 5-8 of the EPRI handbook shows that the drag coefficient of a *Chukar* conductor (similar

to the *Zebra* conductor, with an additional layer of aluminium strands on the outside) for this range of Reynolds numbers is very similar to that of a smooth cylinder.

When including drag in the finite element analyses, it is noticed that with a drag coefficient of 1 for the conductor, the bending curvature and therefore also the bending strains imposed on the span due to drag are negligible in comparison with the gravity loading. Drag is thus neglected when modelling aeolian vibrations.

4.3 SIMULATION OF AEOLIAN VIBRATION ON THE CONDUCTOR

As described above, the force* acting on a cylinder leads the cylinder's displacement by a phase angle (ϕ). In the case of a conductor, where the displaced shape of the conductor consists of a number of standing waves at any point in time, the force acting on any specific half wave length of the conductor would lead the displacement of that section of the conductor by ϕ.

The algorithm developed in this thesis for the simulation of the forces which arise due to vortex shedding, is based on the assumption that if the displacement of a certain load integration point along the conductor is monitored, the periodic force acting on that specific load integration point can be reset at pre-specified intervals to lead the point's displacement by the chosen angle ϕ. As the algorithm is called by the finite element program for each load integration point in the mesh, the load and displacement of each individual nodal point in the finite element mesh are separated by the angle ϕ, as required by the phenomenon of lock-in and the nature of vortex shedding.

The angle ϕ may also be specified uniquely for each element, so that the case where the wind speed varies along the conductors length may be simulated.

The following sections discuss the resetting procedure, and the implementation of the procedure in the finite element program respectively.

4.3.1 Details of the Resetting Procedure for the Simulation of Vortex-Induced Loading.

Figure 4.2 is an example of the type of displacement history for a point on a conductor which might be expected at some location along a span during aeolian vibration. The displacement is composed of a number of different modes of vibration of the span, with the highest corresponding to the frequency of aeolian vibration. If the contribution to the displacement of the highest mode of vibration of the conductor (referred to here as the aeolian displacement), at some point *i*, is assumed sinusoidal, it may be written as follows:

* Unless otherwise stated, in this section *force* and *displacement* refer to the *lift force* and *vertical displacement* respectively.

$$u_i^{aeol}(t) = A\sin(\omega t + \beta_i) \qquad (4.8)$$

with A the amplitude of aeolian vibration, β_i the reset angle (rad) which is used to reset the force according to the displacement, as illustrated below, and ω is the frequency of aeolian vibration (rad/s).

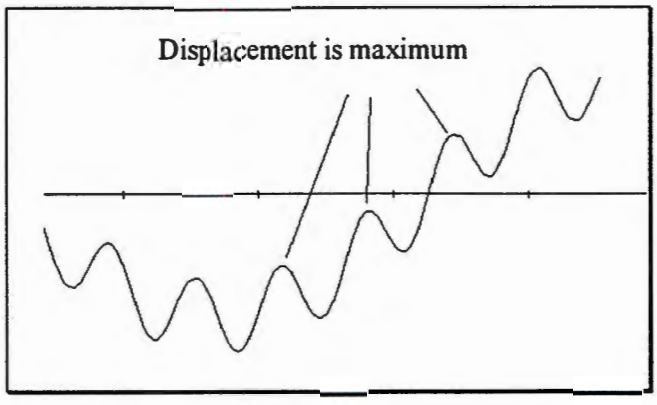

Figure 4.2: *Typical displacement history of a point along a conductor, showing the maximum amplitude during each cycle at which the loading is reset.*

If the pressure force acting on a unit length of the conductor, for a specific load integration point (i) is denoted as F_{L_i}, the force can be given as a function of time (t) as follows:

$$F_{L_i}(t) = F_0 \sin(\omega t + \theta_i) \qquad (4.9)$$

where

$$F_0 = 0.5\rho D C_L v^2 \qquad (4.10)$$

and

$$\theta_i = \phi_i + \beta_i \qquad (4.11)$$

with

ρ - density of fluid (kg/m^3)
D - conductor diameter (m)
C_L - lift coefficient
v - free stream fluid velocity (m/s)
ϕ_i - phase angle

If the aeolian displacement of a load integration point is monitored, F_{L_i} can be updated each time the displacement reaches a maximum so that the phase angle between the displacement and aeolian loading is maintained. The aeolian displacement is a maximum when $\sin(\omega t + \beta_i) = 1$, i.e. when $\omega t + \beta_i = \pi/2$. The reset angle can then be written as:

$$\beta_i = \tfrac{\pi}{2} - \omega t \qquad (4.12)$$

and thus

$$\theta_i = \phi_i + \beta_i = \phi_i + \tfrac{\pi}{2} - \omega t \qquad (4.13)$$

This value for θ_i is then used for the next n cycles of displacement to calculate F_{L_i} for the section, where n is chosen by the user to determine how often the force is reset.

4.3.2 Implementation of the Resetting Procedure.

The procedure to reset the loading, as described above, is implemented in a FORTRAN 77 coded algorithm. This algorithm, which is referred to in the ABAQUS manuals (Hibbitt Karlsson & Sorensen Inc., 1994) as a user-defined loading subroutine, is called by the finite element program for each load integration point along the conductor in the section of the model being subjected to the loading. This is obviously repeated for each equilibrium iteration and increment in the analysis during which the aeolian loading is applied.

The algorithm is represented by a flow chart as shown in the diagram of Figure 4.3 below. When the subroutine is called by the main program, the current co-ordinates of the integration point, amongst other data (See the ABAQUS User Manuals) are passed into the subroutine. The current change in displacement, $du_1 = u_1 - u_0$ is calculated (where the subscripts 1 and 0 refer to the current and previous increments respectively). A check is then made to see if the previous displacement was a maximum, which it will have been if the previous change in displacement, du_0 was positive, while du_1 is negative.

If the previous displacement was a maximum, a counter (*count*), which keeps track of the number of times a maximum has occurred since the last reset, is updated. A check is then made to see whether the counter value equals the value prescribed by the user (*freq*).

If the previous displacement was not a maximum, or the counter value is less than the prescribed value (i.e. $count < freq$), the angle θ_i remains unchanged. If the previous displacement was a maximum and the counter value and the prescribed value coincide, the counter is reset to zero and the angle θ_i is updated using a modified version of equation 4.13 above, which includes a fraction, μ, of the time step dt as follows:

$$\theta_i = \phi_i + \beta_i = \phi_i + \frac{\pi}{2} - \omega \cdot (t - \mu \cdot dt) \qquad (4.14)$$

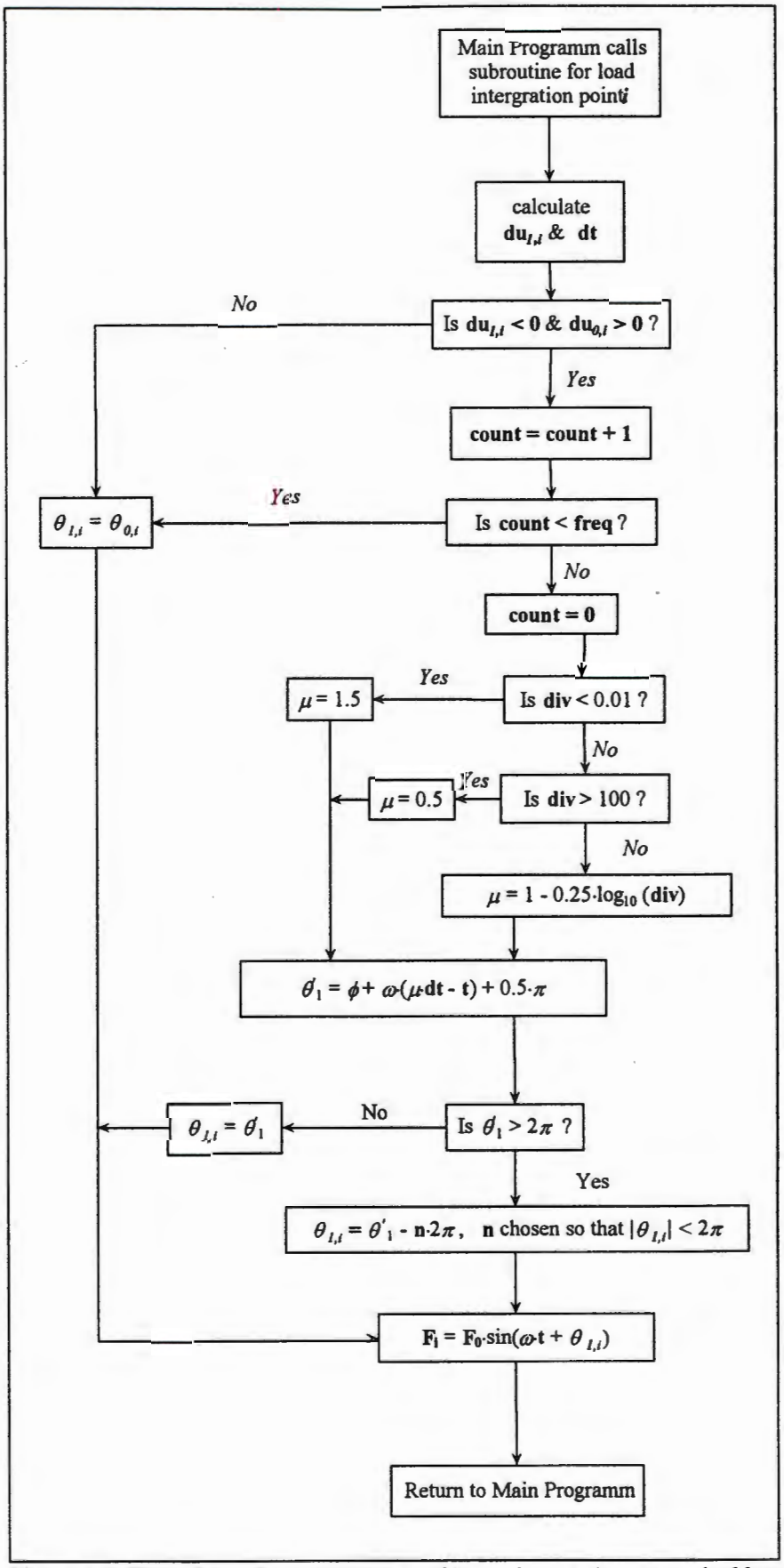

Figure 4.3: *Flow chart of the algorithm used to implement the vortex shedding loading on the conductor. The subscripts 0 and 1 refer to the previous and current increments respectively*

The purpose of the additional term $\mu \cdot dt$ is explained, with the help of Figure 4.4.

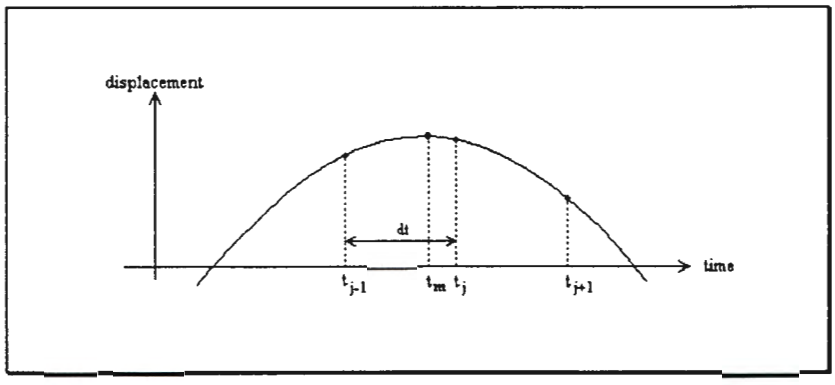

Figure 4.4: *showing the implementation of the additional term $m \cdot dt$ of equation 4.14 to account for the difference in the increment time at which the loading is reset and the time at which the maximum displacement occurs.*

Consider the displacement of a point along the length of the conductor, corresponding to a load integration point. If the real displacement traces a sinusoidal path, the displacement path given by the finite element analysis will consist of a number of discrete points u_j calculated at time t_j . These u_j will lie on the real displacement path.

If the maximum displacement occurs during a certain time increment, of length dt, between times t_{j-1} and time t_j , unless the t_j corresponds to the exact period in time at which the real displacement is a maximum, the displacement u_j will be less than the maximum. In other words, the time t_m at which the real displacement is a maximum will lie somewhere between the range $t_{j-1} < t_m < t_j$. As a result, when updating the angle θ_i during the next time step, t_{j+1} , the fact that t_m does not correspond to one of the discrete times in the finite element analysis must be taken into account. This is done by including the additional term $\mu \cdot dt$ in equation 4.14 .

To explain how the value of μ is determined, consider the following three cases. The quantity div is defined as the ratio of du_{j+1} to du_j , where du_j and du_{j+1} are the change in displacement for the previous and current increments respectively. The time increment dt is assumed to be equal in both increments.

case: (i) $|div| = 1$: t_m and t_j are exactly equal, thus $\mu = 1$.

(ii) $|div| \Rightarrow 0$: $t_m = \frac{1}{2} \cdot (t_j + t_{j+1})$, thus $\mu = 1.5$

(iii) $|div| \Rightarrow \infty$: $t_m = \frac{1}{2} \cdot (t_{j-1} + t_j)$, thus $\mu = 0.5$ (4.15-a,b,c)

$$\text{with} \quad div = \frac{du_{j+1}}{du_j} \qquad (4.16)$$

Cases (ii) and (iii) represent the two extremes, with the possible values of μ thus ranging from 0.5 to 1.5 . The relationship between the ratio du_{j+1} / du_j and the value for μ is implemented by writing μ as a logarithmic function of du_{j+1} / du_j as follows:

$$\mu = \left(1 - \frac{\log_{10}(div)}{4}\right) \qquad (4.17)$$

In determining the above equations, values of 0.01 and 100 are chosen, to replace zero and infinity respectively, as the limits approached in cases (ii) and (iii) above. These values for the limits are used after comparing them with the sets of values of 0.1; 10 and 0.001; 1000 respectively, and have been found, by means of a small test programme written for this purpose, to give the best results for resetting of the phase angle.

4.3.3 Verification of the Loading Subroutine

To verify that the loading specified by the user-defined subroutine, as implemented in ABAQUS, is in fact correct, the load and displacements of various integration points are monitored and written to a file from within the subroutine.

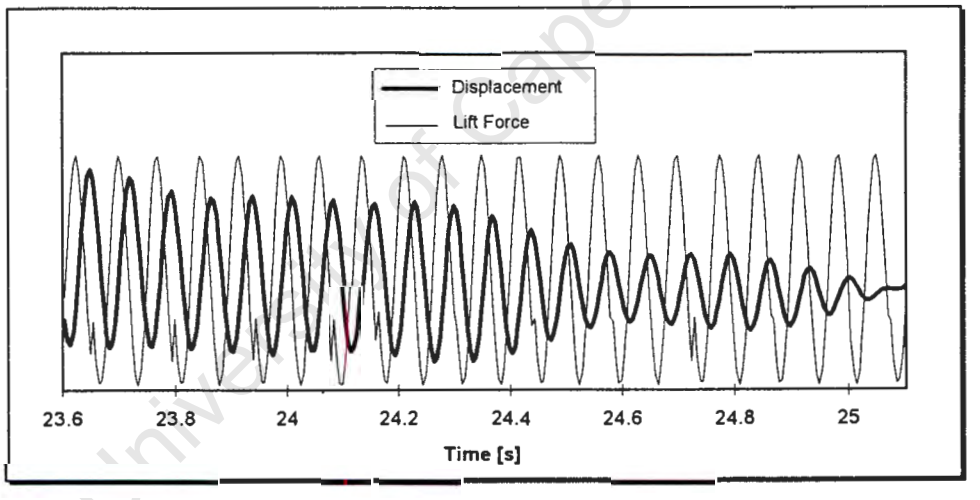

Figure 4.5: *The vertical displacement and lift force on a section of conductor undergoing aeolian vibration at a frequency of 15 Hz.*

The graph of Figure 4.5 above shows the load and the displacement of an integration point for about 21 cycles of vortex shedding, at a frequency of 15 Hz. The points in time at which the phase angle is reset and corrected can be seen in the load history graph as the slightly irregular peaks which appear on the curve of the lift force. As can be seen from the results, a phase difference (ϕ) of approximately 90 degrees, the value specified by the user in this case, is maintained throughout the history.

4.4 DETAILS OF THE FINITE ELEMENT MODEL

The details of the finite element model of the transmission line for aeolian vibration is discussed in this section. The types and sizes of elements used to model the conductor and the modelling of the suspension clamps and vibration dampers are discussed. An explanation of the method used to model additional spans is followed by a discussion of the analysis procedure, and other specific details of the model.

4.4.1 Element Types

The two classes of elements available in ABAQUS which may be used to model the conductor are truss and beam elements. Before discussing the elements used for the aeolian vibration finite element model, the different types of elements available are briefly described below.

i.) Truss Elements

These elements are based on the assumption that they can only transmit axial forces, and not moments. They thus have only translational degrees of freedom, with the end nodes being pinned. Since no moments can be transmitted, no rotational degrees of freedom exist.

A cable is very flexible in bending relative to its axial stiffness, thus when considering the section of a cable away from it's support points, the truss assumption is quite valid. The situation is significantly different closer to the points of support however, where a long cable experiences a significant bending moment due to the weight of the cable in the span.

In the case of a conductor on a transmission line, the sections of the conductor closest to the points of support and those at which additional hardware such as external damping devices are connected, are those sections which are most likely to fail due to fatigue. As shown in the results given later, the alternating stresses in the strands of the conductor which arise from the bending are considerably larger than the axial stress fluctuations. The assumption that the bending effects could be neglected is thus invalid, and the bending stiffness must be taken into account. This is done by making use of beam elements.

ii.) Beam Elements

Two beam theories are generally used in the formulation of beam type finite element, namely the Euler-Bernoulli, and the Timoshenko beam theories. For each of the element types available, a hybrid version, where the axial and shear (if relevant) forces are treated as additional independent degrees of freedom, is also available. These options are described below:

Euler-Bernoulli Beam Elements

Euler-Bernoulli beam theory assumes that any cross-sectional plane, which is initially normal to the beams axis, remains normal to the beam's axis, and is undistorted. It therefore does not account for any transverse shear

deformation. This assumption is usually valid for long, slender beams, where the distance between support points is much greater than the cross-sectional dimensions of the beam, with a ratio of 15:1 or more (Hibbitt Karlsson & Sorensen Inc., 1994a). In ABAQUS, the Euler-Bernoulli theory is implemented in the 2 noded elements with a cubic interpolation function.

The main short-coming of these elements, is that they experience convergence problems for large rotations.

Timoshenko Beam Theory

The Timoshenko beam theory, unlike Euler-Bernoulli theory, allows for transverse shear deformation. Thus it is a more favourable option when modelling thicker beams. In this case, the assumption that a cross-section which is initially plane, remains plane is also made, however the normal of the plane is allowed to deviate from the normal of the beam's axis.

In the elements available for ABAQUS, Timoshenko beam theory is used in the formulation of the elements having linear and quadratic interpolations, for 2 and 3 noded elements respectively. These elements are capable of modelling large rotations more effectively than the Euler-Bernoulli beams (Hibbitt Karlsson & Sorensen Inc., 1994a).

Hybrid Beam Elements

The hybrid, or mixed-formulation, beam elements available in ABAQUS are designed for long slender beams, where the ratio of the beam length to thickness is of the order of 10^3. To improve convergence, the axial force, and in the case of Timoshenko beams, also the shear force, is introduced as an independent degree of freedom. The hybrid version is available for all the beam elements in ABAQUS.

For a 400 metre conductor span, the distance between the ends of the spans, and therefore the distance between successive supports, is in the order of 10^4 times larger than the cross-sectional dimensions of the conductor. The obvious first choice of elements for such a slender beam, as discussed above, are thus those based on Euler-Bernoulli theory. In ABAQUS these are the two noded beam elements which use a cubic interpolation function. The rotations experienced at the ends of the span are however larger than can be accommodated by these elements, and as such the solution does not converge when these elements are used to model the whole length of the conductor.

To accommodate this problem, the mesh for the aeolian models is modified by using a combination of Timoshenko and Euler-Bernoulli beam elements. The first metre at the end of each span is modelled using quadratic Timoshenko beams, and the remainder of the span, where the rotations are much less severe, is modelled using the preferred Euler-Bernoulli beams. Regarding the choice of Timoshenko beams at the ends, the quadratic beams are preferable to linear elements, as they are more adept at modelling bending curvature. As shown

later, the curvature is important in determining the stresses experienced in the conductor at the ends of the span.

The use of the hybrid versions of the beam elements reduces the computational time significantly, as they converge easier than their non-hybrid counterparts. In testing the hybrid versus non-hybrid elements, the displacement histories obtained when modelling aeolian vibration are virtually identical.

4.4.2 Number of Elements

The number of elements used in a model must be capable of modelling a sufficient number of modes so that simulation will give a good approximation of the true response of the system. Bathe (1982) advises that if the finite element model is capable of modelling the mode corresponding to at most four times the highest frequency of loading, an accurate response can be expected. In most cases, he states, the highest mode that needs to be considered can be considerably lower than four times the highest loading frequency.

To choose the minimum number of elements which could be used for an accurate model of the conductor during aeolian vibration, while keeping the solution as cheap as possible in terms of CPU time, two test problems are simulated using different numbers of elements to model the conductor.

In the first test, a 20 metre long conductor section as shown in Figure 4.6 is modelled. The static loads imposed on the conductor are a tensile load of 20 kN and a gravitational distributed load corresponding to 2g. The conductor is then subjected to aeolian loading at a frequency of 15 Hz.

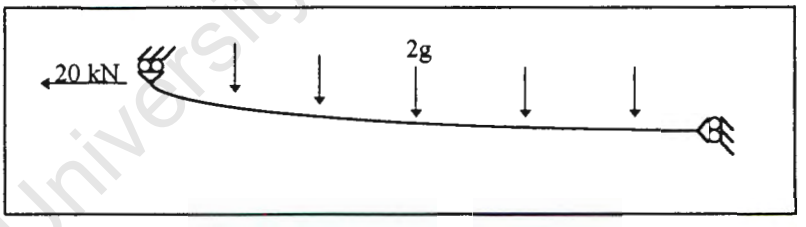

Figure 4.6: *Showing the arrangement of test1 to ascertain the effect of the mesh density on the solution.*

The response of the system is found to be virtually identical when using 30, 50, 100 and 200 elements to model the conductor. The displacement of the conductor, 90mm from the end of the span, is shown in Figure 4.7 for each of the simulations.

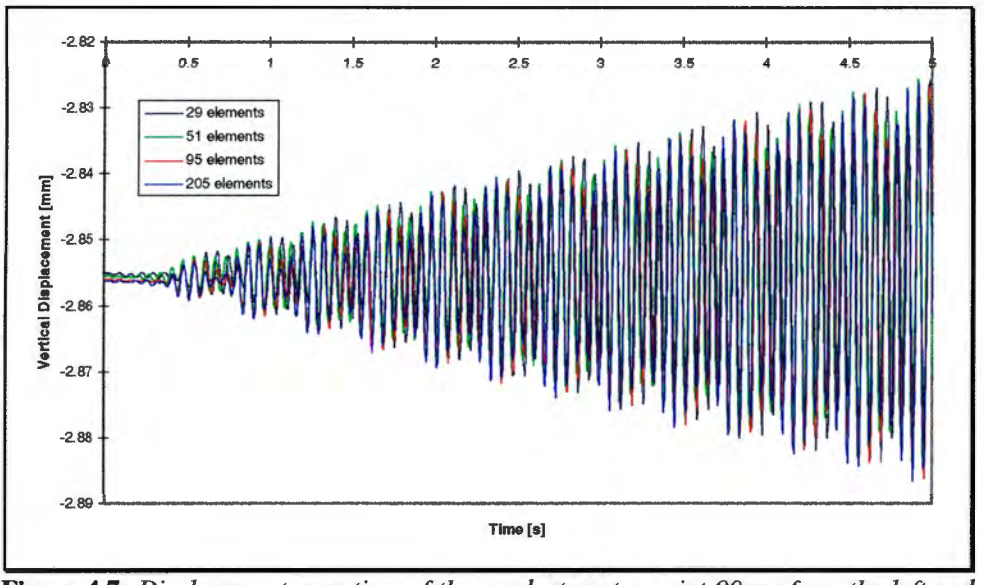

Figure 4.7: *Displacement over time of the conductor at a point 90mm from the left end of the span of* Figure 4.6

The details of the second test, carried out on the model for aeolian vibration on a 400m span, are as follows:

The static load consists of a gravitational load of 1g, while an axial tension of 20 kN is applied. The aeolian excitation is applied once again at a frequency of 15 Hz. As the results for the displacement at a point 90mm from the end of the span show (Figure 4.8), there is a notable difference in the response when the conductor is modelled using 442 elements, than when it is modelled using 792 and 1192 elements.

Using Bathe's advice of modelling the mode corresponding to four times the highest frequency of loading, in this case 60 Hz, with sufficient accuracy, one would have to make provision for the accurate modelling of a wavelength of about 2.3 metres, as calculated using equations (A.14) and (A.17). The minimum required of four elements per wavelength is satisfied in the 792 and 1192 element models.

The wavelength for the 15 Hz vibration mode is approximately 7.6 m. This translates to about 8, 15 and 23 elements per wavelength in the 442, 792 and 1192 element models respectively.

Studying the graphs of Figure 4.8, it can be seen that even though the displacement of the 442 element simulation seems to lag that of the other two mesh densities, the pattern of vibration (over the time period modelled) seems to approach that of the other two as the simulation proceeds. There are two possible explanations for the initial difference in the response. Firstly, if the number of modes of the system modelled is not sufficient, the response of the system will not be accurately modelled, as mentioned above. The second possible explanation is that the number of load integration points is not enough

to model the aeolian loading along the length of the conductor with sufficient accuracy for the 442 element model.

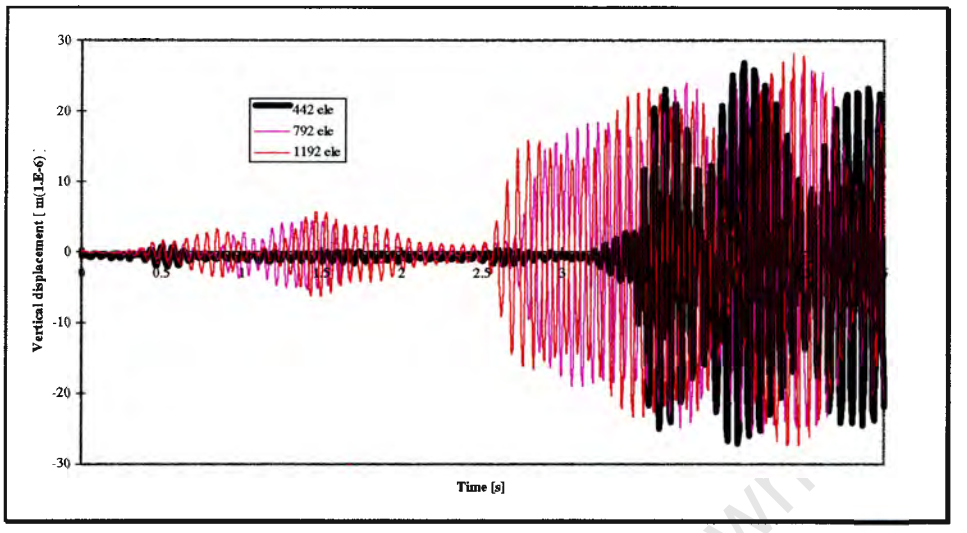

Figure 4.8: *The displacement history at a point 90mm from the end of a 400m span, showing the effect of different mesh densities on the solution for a vibration frequency of 15 Hz.*

Whatever the reason though, it does seem fair to assume that the response due to the 772 and 1192 element models are fairly similar, with the likely explanation for the small difference in the results being the difference in the number of points at which the aeolian loading is applied over the length of the conductor. As the behaviour of the conductor is very non-linear, any small difference in the load at any point in its history would be expected to have an effect on the history of the conductors motion, even though the general response should follow a similar pattern.

This is similar to what would be expected in the real case. If the behaviour of a conductor were to be monitored during aeolian vibration over a specific period of time at a constant frequency, the histories for two different periods would be unlikely to be exactly the same, even though the overall pattern of vibration would be expected to be similar.

Based on the results of the two test above, it may be assumed that 15 elements per wavelength are adequate to obtain a sufficiently accurate simulation of the aeolian vibration of a conductor.

4.4.3 Properties of the Conductor

i.) Damping

The damping included in the finite element model to simulate the internal self-damping of the conductors is in the from of Rayleigh damping, as is discussed in the earlier chapter dealing with the internal damping of conductors.

Table 4.2 shows the damping details for all the aeolian vibration simulations, with the data calculated and obtained as discussed in chapter 3. The wavelengths are estimated from equations A.14 and A.17.

f	T	λ	β	$KE_{\lambda/2}^{ave}$	$\overline{P}_{dissipated}$	ζ	γ
[Hz]	[kN]	[m]	[minutes]	[J·10^{-6}]	[W/m]	[10^{-3}]	[10^{-6}]
15	20	7.6	1.42	1.72	62.3 E-6	.73	15.5
15	25	8.4	1.28	1.91	39.8 E-6	.47	9.91
15	30	9.2	1.17	2.08	27.3 E-6	.32	6.79
22.5	20	5.2	2.08	2.65	540 E-6	1.9	26.6
30	20	4.0	2.67	3.66	2.72 E-3	4.0	42.3
37.5	20	3.4	3.22	4.74	8.2 E-3	6.2	52.2
45	20	2.9	3.72	5.91	23.6 E-3	10.2	72.4

Table 4.2: *Details of the internal conductor damping for the aeolian vibration simulations and other information used in calculating the damping constants*

ii.) Bending Stiffness

As explained in chapter 2, the variable bending stiffness can only be defined in ABAQUS as a function of the actual curvature, as opposed to a change in curvature. The assumption of a constant bending stiffness must therefore be made.

In the aeolian vibration model, the maximum bending stiffness of EI_{max} is used. The only discrepancy obtained in the curvature for the static sagging of the conductor under gravity, using the value of EI_{max} in comparison with the variable bending stiffness, is in the section of the conductor directly adjacent to the suspension clamps. This means that the curvature only exceeds that required for slipping to occur (when $\kappa > \kappa_i^{slip}$) in the direct vicinity of the suspension points.

The displacement profiles for the first metre of the conductor, using the constant vs variable bending stiffness respectively, are shown in Figure 4.9. As can be seen, the difference in curvature of the conductor is only evident for the first 0.5 metres.

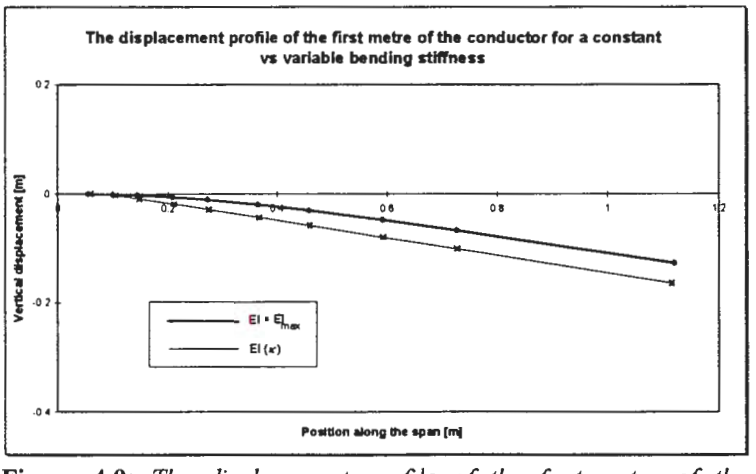

Figure 4.9: *The displacement profile of the first meter of the conductor of a 400m span under gravity loading, for constant and variable bending stiffness.*

During the aeolian vibration simulations, the bending curvature of the conductor stays well within the no slipping curvature range. This implies that even though the static displacement profile differs slightly from the real profile as a result of the assumption of a constant EI for the conductor, the behaviour of the conductor during aeolian vibration with respect to the static sag profile is correctly modelled, as the bending stiffness of the conductor does in fact corresponds to EI_{max} when nc slipping occurs.

Even though the difference in the displacement profile is evident in the vicinity of the suspension points, it is small enough to assume that the effect on the mode of vibration and the behaviour of the conductor during vibration is negligible.

When estimating the fatigue life of a conductor under certain aeolian vibration conditions, the static stresses in the conductor can be calculated using the curvature dependent relationship. The alternating stresses experienced during aeolian vibration can then be obtained using a constant value for the bending stiffness and superimposed on the static stresses obtained with $EI(\kappa)$.

iii.) Other Properties

The other relevant properties of the *Zebra* conductor are as shown in the following tables.

No of layers:	5
Steel Strands:	1+6 = 7
Aluminium Strands:	12+18+24 = 54
Strand Diameter:	3.18 mm
Conductor Diameter:	28.62 mm
Mass per unit length:	1.63 kg/m
Axial Elasticity:	73.2 GPa
EI_{max}:	1605 N.m^2
EI_{min}:	26 N.m^2
Friction coefficient between strands[†]:	0.5
Ultimate Tensile Strength:	133 kN

Table 4.3: *Properties of an ACSR Zebra conductor(Obtained from the catalogue of conductors manufactured by Aberdare Cables (Pty) Ltd, South Africa, unless stated otherwise).*

Table 4.4 shows the material for the strands in each layer, the number of strands in each layer, and the range of allowable lay lengths (l_i) for each layer[‡].

[†] Papailiou, 1995a

[‡] Information obtained telephonically from USKO Ltd., South Africa.

Layer:	1	2	3	4	5
Steel/Al:	Al	Al	St	St	St
no of strands:	1	6	12	18	24
lay length (mm):	-	124-267	159-270	222-356	286-400

Table 4.4: *Details of the strand layers of a Zebra conductor*

4.4.4 Modelling the Suspension Clamp

The construction of a typical suspension clamp, used to connect a conductor to the insulator string on a suspension tower (see section 4.5.1) is shown in Figure 4.10. The conductor is tightly clamped inside the body of the clamp, the inside which may contain cross-grooves to restrict the slipping of the conductor inside the clamp. The movement of the section of the conductor inside the clamp is thus totally restricted, and the section can be treated as being rigid.

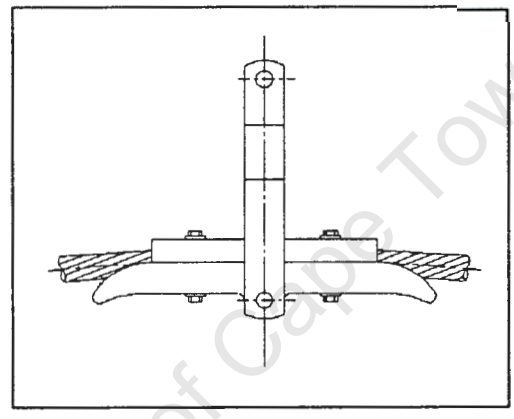

Figure 4.10: *Sketch of a typical suspension clamp.*

Two different methods of modelling the restriction of the clamp on the conductors motion were attempted, as described below.

i.) Modelling the Suspension Clamps using MPC's

The first method involves a set of Multiple Point Constraints (MPC's), a facility available in ABAQUS whereby the degrees of freedom at certain nodes are restricted or linked in a specific way to the degrees of freedom of another node or set of nodes (Hibbitt Karlsson & Sorensen Inc., 1994b).

The four types of MPC's described below are used in combination to model the pivoting clamp:

Pin: The translational displacements of one node are restricted so that they are the same as those of a second node, while the rotational degrees of freedom of the nodes are totally independent.

Slider: The displacement of a node is modified so that it always lies along a straight line defined by two other nodes. The rotation of the node is independent.

Link: This modifies the displacements of one node relative to the other so that the distance between the two nodes remains constant. The rotation at either node is once again independent of that at the other.

Tie: Makes all the degrees of freedom at two nodes equal.

The MPC's are used in conjunction with one another as shown in Figure 4.11.

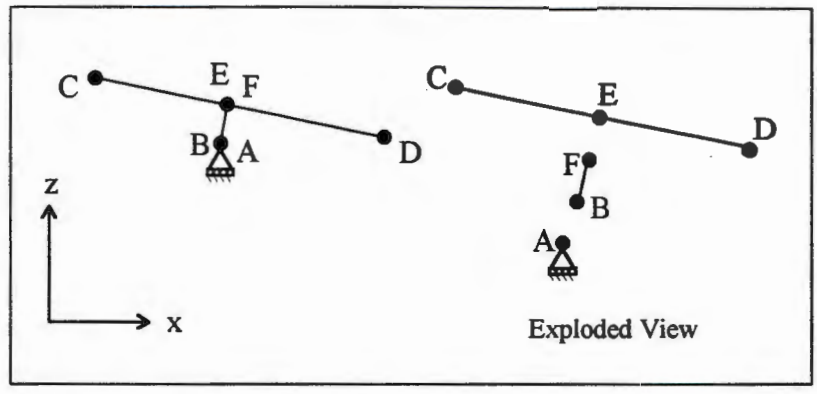

Figure 4.11: *Showing the modelling of the suspension clamp using Multiple Point Constraints (MPC's). The sketch on the right is an exploded view.*

Referring to Figure 4.10 and Figure 4.11 above, node A corresponds to the centre of the pin about which the bottom of the clamp, modelled by node B, pivots. Nodes C and D are the last points of contact between the clamp and the conductor, and node E is the section of the conductor midway between C and D. The node F is coincident with E.

Node A is free to move along the x-axis, but is restrained vertically. Node B is pinned using the *Pin* option to node A, and a constant relative distance between nodes B and F is maintained by means of the *Link* option. The lines described by BF and CED are perpendicular to one another. This is implemented by the *Tie* option, used to tie nodes E and F together. The motion of node E is restricted by using the *Slider* option, which is thus free only to move along the straight line defined by nodes C and D. Section CED is part of the conductor, and is thus modelled using beam elements, as is the remainder of the conductor.

The stability and viability of using this method of modelling the clamp was tested by setting up a finite element of the above arrangement. Loads of 20 kN were applied on nodes C and D in the negative and positive x direction respectively. In the next step, a variety of combinations of vertical loads (z-direction) were applied to these two nodes, and the solutions converged immediately in each case.

The model was then extended to a model of two adjacent spans of conductors, joined in the middle by the suspension clamp arrangement. A tensile load was applied to the free end of one span to provide axial tension in the beam elements before applying any transverse loads. The node at the other was fixed for all degrees of freedom to prevent the occurrence of any rigid body modes. In the next step, a gravitational load was applied to the two spans, and once again the solution converged without difficulties. When the arrangement was implemented in the model for aeolian vibration, however, the solution diverged as soon as any gravitational loads were applied.

This problem seems to arise from the use of the relatively short beam elements required to accurately model the behaviour of the conductor at the span endings. The large bending moments at the span ends cause significant rotations in the elements at these points, and each of the shorter beams elements are subjected to rotations which are relatively large. Longer beam elements at the ends, such as those used in the test model mentioned in the previous paragraph and which were 20 times longer, are not capable of modelling the significant bending at the end of the span, and as such the elements are not subjected to the large rotations, and allow the solution to converge without difficulty. To obtain a convergent solution, an alternative method of modelling the suspension clamp is thus used, as described below.

ii.) Modelling the Suspension Clamp using a Combination of Stiffer Elements and MPC's

The second method used to model the suspension clamp is based on the same principals as those used above. The main difference being that instead of modelling the sections BF and CED (referring to Figure 4.11 above) using MPC's the same restrictions are implemented using beam elements with much greater stiffness than the remainder of the conductor. The nodes E and F are tied using the *Tie* MPC, and node B is pinned to node A. The motion of node A is restricted to the horizontal translational and rotational degrees of freedom.

This arrangement also leads to convergence problems when the gravitational loads are applied. The large moments experienced at the top end of the BF section seem to cause numerical problems in the form of singularities which prevent convergence.

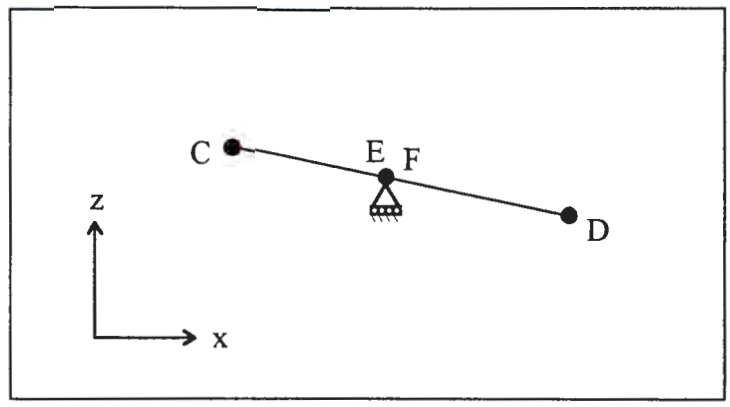

Figure 4.12: *Showing the modelling of the suspension clamp in the aeolian vibration models. Section CFD consists of a stiff beam element, which is free to pivot about node E. Node E is free to translate along the x-axis.*

A simplified version of this arrangement, where CED pivots about node F is found to converge, and as such this arrangement, which is shown in Figure 4.12, is the one used in the aeolian vibration model.

4.4.5 Mesh Refinement at the End of the Span

To enable the stress in the conductor at the point of last contact with the clamp, and the displacement at the standard distance of 89 mm from this point to be obtained with a sufficient degree of accuracy, the mesh of the conductor is refined towards the ends of the spans (Figure 4.13).

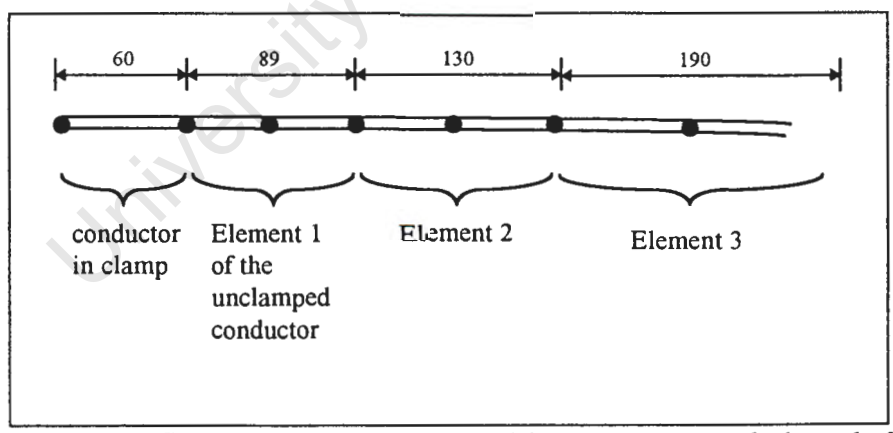

Figure 4.13: *Showing the mesh refinement of the conductor towards the end of the span. All dimensions in mm.*

As shown in the figure above, only one quadratic beam element is used to model the first 89mm of the conductor. To test the validity of using only one element for this section, the results of a small test model are shown below. A 0.5m section of a conductor span is modelled using 4 and 40 quadratic beam elements respectively. The left side is fixed, and the loads applied are as shown in Figure 4.14

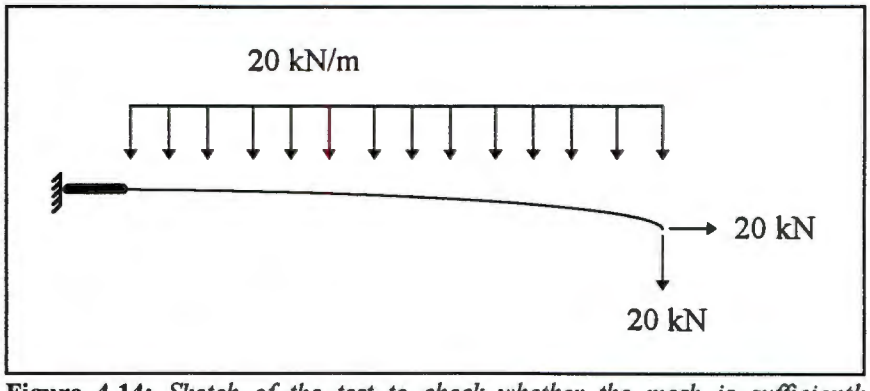

Figure 4.14: *Sketch of the test to check whether the mesh is sufficiently refined. The thick section on the left represents the stiffer section of the clamped conductor.*

As can be seen from the results below, the displacement and rotation along the section are virtually identical when 4 and 40 quadratic elements are used to model the conductor section. Thus 4 elements are sufficient for the first 0.5 metres of the conductor.

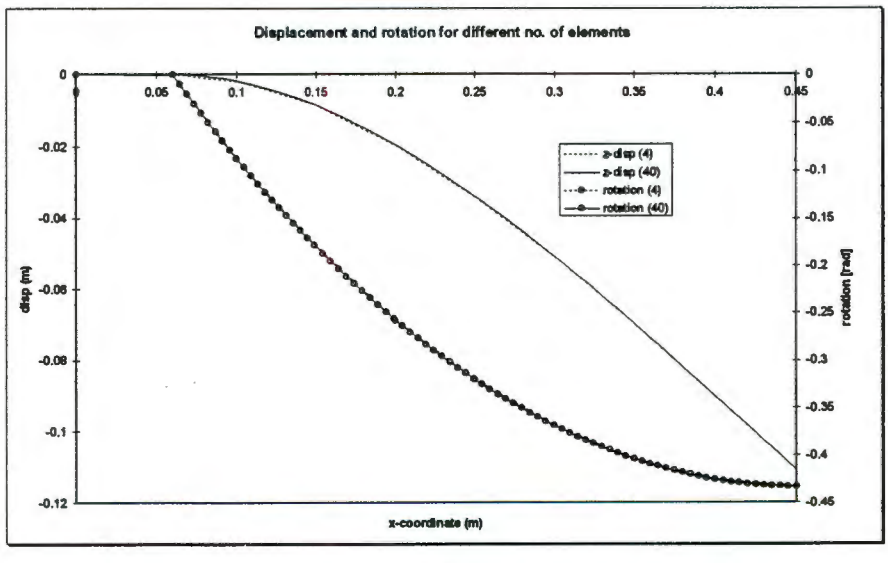

Figure 4.15: *The displacement and Rotation along the length of the 0.5 m long conductor section modelled using 4 and 40 elements respectively.*

4.4.6 Modelling Vibration Dampers

Figure 4.16 shows a typical vibration damper. It consists of two masses which are connected to the clamp bracket by means of a messenger wire. The messenger wire is a stranded cable, usually constructed of 7 or 19 helically wound strands. The dampers are modelled as shown in Figure 4.17 .

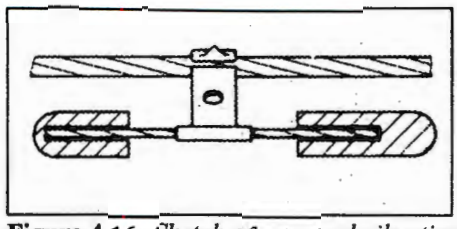

Figure 4.16: *Sketch of a typical vibration damper (Hagedorn, 1986. With Permission from Richard Bergner GmbH + Co.)*

The stiff beam element represents the section of the conductor inside the vibration damper clamp. The clamp body, which joins the messenger wire to the clamp is of solid metal which is very stiff compared to the cable and messenger wires. As such it is modelled as a *beam* type MPC (multiple point constraint). The *beam* MPC constrains the displacement and rotation of one node to the displacement and rotation of a the second node, corresponding to a rigid beam between the two nodes (Hibbitt Karlsson & Sorensen Inc., 1994b). The messenger wire is modelled using a quadratic beam element, with a stiffness equal to EI_{min} as calculated using equation 2.2 . The axial tension in the messenger wires is minimal, and as such the amount of curvature required for slipping between the strands to occur approaches zero, and the bending stiffness takes on its minimum value.

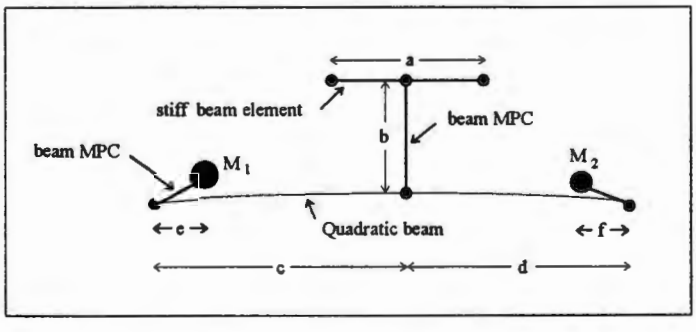

Figure 4.17: *The finite element modelling of a vibration damper.*

The counterweights at the end of the messenger wires are cup shaped and are connected to the messenger wire at the bottom of the "cup" (see Figure 4.16). The centre of mass of the counterweights is thus not necessarily at the point of connection of the messenger wire and the mass. Provision is made for this by connecting the mass elements, used to model the counterweights, to the messenger wire by means of a short *beam* MPC. The implications of this modification are not investigated as part of this project but could have a significant effect on the vibration characteristics of the dampers.

The properties of the vibration dampers modelled are as follows:

No. of strands:	19	*a*:	60 mm
Strand diameter:	2.63 mm	*b*:	100 mm
EI_{min}:	9.2 N.m^2	*c*:	307 mm
M_1:	2.96 kg	*d*:	259 mm
M_2:	2.59 kg	*e*:	35 mm
		f:	40 mm

Table 4.5: *Physical properties of the vibration dampers*

4.4.7 Modelling Adjacent Spans

As the suspension clamp is free to rotate about a pivot point, the aeolian vibrations of a span cause excitation of adjacent spans via the articulation of the suspension clamp. Two adjacent spans with different vibration characteristics (e.g. due to different span lengths), where the conductors of the two spans are coupled by means of the suspension clamp, will thus interact. To accommodate this, an additional span is modelled on either end of the span being subjected to aeolian vibrations, as shown in Figure 4.18

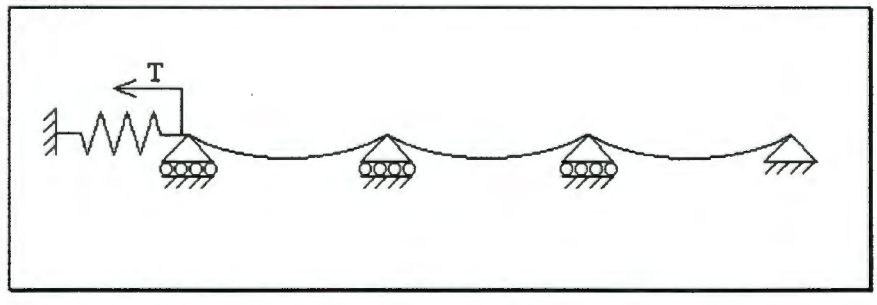

Figure 4.18: *Schematic representation of the finite element model for aeolian vibration*

Additional spans at one end of the line are simulated by means of a non-linear spring and a tensile load (T), corresponding to the tension in the conductor, in parallel. When the model is in static equilibrium, the spring exerts no additional force on the conductor. If the left end of the conductor moves slightly to the left, the span modelled by the spring slackens slightly, and the force exerted on the conductors by this span decreases. When the end of the conductor moves to the right, the opposite occurs.

The force-displacement relationship of the non-linear spring is obtained as follows. The sag geometry of a single span is obtained by means of steps 1 to 3 of the analysis procedure for aeolian vibration as described below. The span length is then increased and decreased in a number of increments, and the change in the reaction force at the end of the span is monitored. A relationship for the change in the force as a function of the change in the span length is then obtained and implemented in the finite element model by means of a non-linear spring.

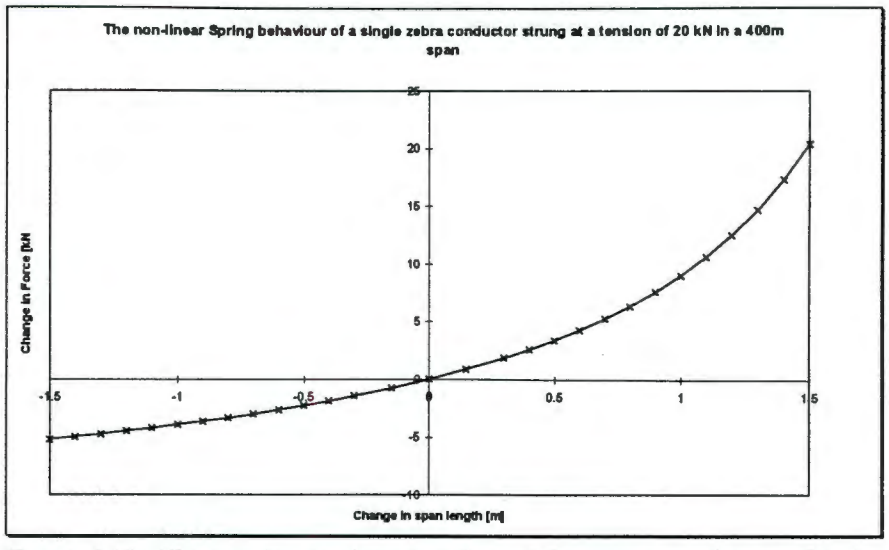

Figure 4.19: *The non-linear characteristics of the spring used to model the behaviour of a 400 m span strung at a tension of 20 kN.*

This relationship is shown for a 400 metre span strung at a tension of 20 kN, in the graph above.

4.4.8 Other Details of the Finite Element Model

i.) Modelling the Problem in Two vs Three Dimensions

As mentioned earlier, the effect of the drag loading on the conductor is negligible in comparison to the gravitational loading, and the additional static stress imposed at the span ends is small compared with the stress imposed due to gravitational loading. Neglecting the drag loading, means that any motion will be in the vertical plane only, and as such the problem may be simplified to a 2-dimensional problem. This reduces the amount of CPU time required for each analysis as the number of degrees of freedom in the problem is reduced. For this type of analysis, where a simulation may take up to 3 days of CPU time, the saving in time due to this simplification makes the simulations more viable for practical design and research purposes, especially as the simplification does not adversely affect the results.

ii.) The Analysis Procedure

The finite element analysis for the aeolian vibration simulations is divided into four steps which may be described as follows (Figure 4.20):

Step1: Apply axial tension to the beam elements of the conductor. This step is required to provide the beam elements with axial stiffness, without which singularities are introduced into the stiffness matrix and convergence does not occur when transverse loads are applied.

Step 2: Apply gravitational load.

Step 3: Displace the ends of the span to obtain the correct sag profile. The total displacement is applied over a number of increments due to

convergence difficulties experienced with the non-linear geometry of the sagging conductor. The amount of displacement is equal to the difference in the unstressed length of the conductor for a specific span length, and the length of the span. The unstressed conductor length is calculated as shown in Appendix B.

Step 4: Apply the aeolian loading by means of the user-defined loading sub-routine.

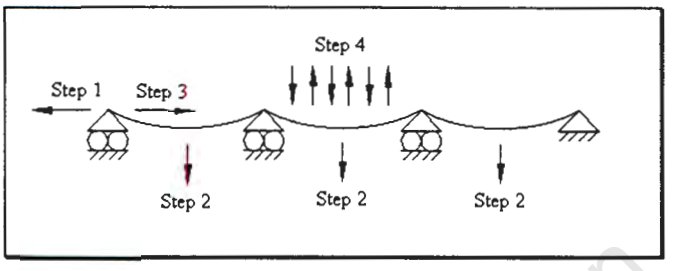

Figure 4.20: *Showing the steps of the analysis for aeolian vibration simulations*

In the simulation of the other types of conductor motion, steps 1 to 3 are identical to the above, with the appropriate loading being applied in step 4.

4.4.9 Details of the Transmission Line Subjected to Aeolian Vibration

Figure 4.21 shows the finite element model of the section of the transmission line modelled for the aeolian vibration simulations.

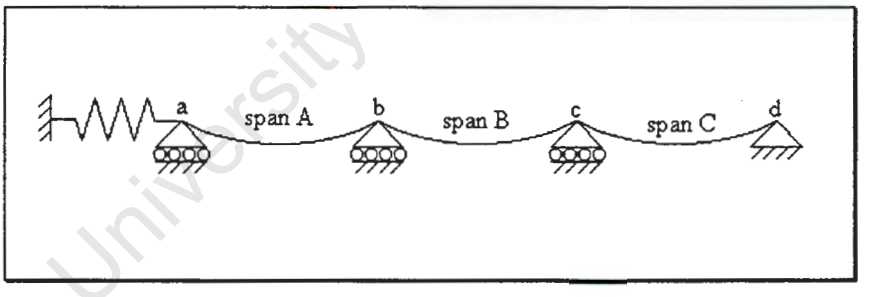

Figure 4.21: *Model of the transmission line section used for the aeolian vibration simulations.*

All three spans are 400m in length, and unless otherwise specified, the aeolian excitation load is applied on the middle span, i.e. span B. The suspension clamp is modelled at suspension points *b* and *c*, and both the bending curvature of the conductor at the interface with the suspension clamp, and the displacement at 89mm from the suspension clamp, are recorded on the left end of span B, i.e. just right of suspension point *b*.

All degrees of freedom of node *d* are restricted, corresponding to a strain tower (described below), while the vertical degrees of freedom at all the other suspension points are restricted. To prevent rigid body modes, the rotation at node *a* is also restricted.

4.5 BOUNDARY CONDITIONS

As shown in this section, the choice of boundary conditions at the ends of the spans may have a significant effect on the results obtained from the model. Different methods of connecting the conductors to the suspension hardware and towers, as used in practice, are described below. A discussion of the validity of the various choices of boundary conditions is followed by a comparison of the finite element results obtained for different options.

4.5.1 Connections Between Conductors and Towers

In a transmission line, the configurations used for the attachment of a conductor to a tower may be classified into two main groups, namely suspension, and strain connections. Strain connections are usually used on the more robust towers where the purpose of the tower is to provide or maintain the necessary axial tension in the conductor to keep it suspended. This type of tower would be used at the terminal point of the line adjacent to a sub-station, at a point along the line where the direction of the transmission line changes, or where a very long span, such as would be used to cross a deep wide valley, requires robust towers at the ends of the span to cope with the weight of such a long span. The strain arrangement is shown in Figure 4.22. The conductor is attached to the insulator string by means of a suspension clamp.

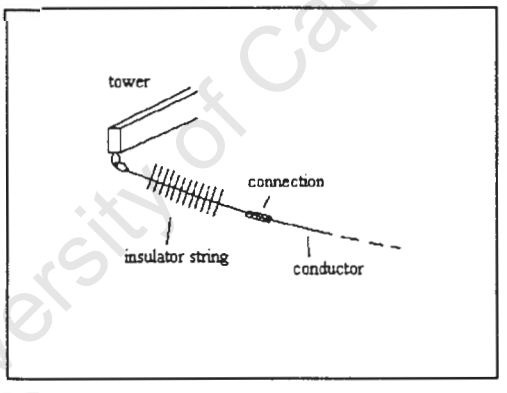

Figure 4.22: *The suspension arrangement for a strain tower.*

The suspension arrangement, which is used in conjunction with suspension tower types is used as a less costly alternative to the strain towers. The purpose of these towers is to provide suspension points for the conductors and relies primarily on the tension of the conductor on either end of the tower to remain upright. Suspension towers are thus lighter, require less material and are therefore more economical, and are thus used as frequently as possible on a transmission line. Limiting factors to the construction of whole transmission lines using suspension towers include mountainous terrain, and the fact that unlike strain towers which are able to maintain much larger horizontal loads, a transmission line constructed solely of suspension towers is more susceptible to cascading failure. Cascading failure occurs where the collapse of one tower results in the subsequent failure of adjacent towers, connected to one another

by the conductors. Suspension towers are thus also interspersed with strain towers to limit the damage of cascading along a line.

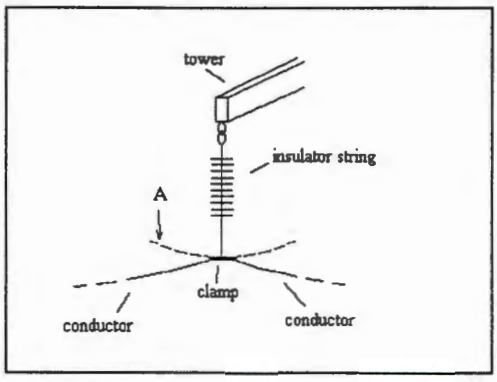

Figure 4.23: *Sketch of a suspension arrangement for the attachment of the conductor to the tower.*

With a suspension tower (see Figure 4.23), the conductor is attached to the insulator string by means of a suspension clamp.

As is to be expected, one of the points along the span of a conductor most susceptible to damage is that where it attaches to the suspension hardware, and the degree of restriction the clamp imposes on the motion of the conductor at this point will have a significant effect on the stresses experienced by the conductor.

4.5.2 Boundary Condition Considerations for a Transmission Line Conductor Model

In the derivation of mathematical models for the vibration of a conductor in a span, a number of different choices have been made by various authors on the boundary conditions at the ends of the span. The assumption of a fully clamped boundary condition is made by Hagedorn (1982), Sturm (1936) and Oliveira et al (1994). Möcks (1989) makes the assumption that the conductor is free to pivot at the one end, while the other is fully clamped. The conductor is usually treated as a taut string or cable.

The types of boundary conditions chosen would be fairly irrelevant when the aim of the model is to investigate the behaviour of a section of the conductor far from the ends of the span. If, however, the aim is to study the behaviour of the conductor nearer to the end points of the span, the boundary conditions chosen will have a significant effect on the results.

In the case of a strain connection, where a string of insulators connects the conductor to the tower, the amount of rotation experienced by the conductor is limited by the rigidity and mass of the insulator string.

For suspension type connections, the suspension clamp is able to rotate about the pivot point. It would however, be incorrect to assume that the rotation is

completely free, as any rotation is restricted by the weight of the conductor in the adjacent span.

Both the assumptions of totally restricted and unrestricted freedom of rotation at the ends are thus strictly speaking incorrect for both the strain and suspension configurations. When considering only the restraining effect of the weight of the adjacent spans on the rotation at the pivot point, and not the inertial effects during vibration, a torsional spring could be used to model the restraining effects of the adjacent spans. Alternatively, the adjacent span could also be included in the model, with the rotational degree of freedom corresponding to the point about which the suspension clamp pivots being unrestricted. In the latter case, provision should also be made for the fact that even though the conductor is continuous between two adjacent spans, the bending and axial behaviour of the conductor section in the clamp is restricted.

Unlike the finite element method, simple mathematical models such as those of Hagedorn, Sturm, Oliviera et al and Möcks which are mentioned above, do not make provision for the limited restriction of the rotation at the clamp. This is a prime example in which the superior modelling capabilities of the finite element method would be expected to give more realistic results.

4.5.3 Results for the Different Boundary Conditions.

To test the effects of different boundary conditions on the behaviour of the conductor, three types of boundary conditions are used and compared on a model for aeolian vibration. The conductor is subjected to aeolian vibration loading at a frequency of 15Hz. The span is 400m in length, and the conductor has a tension of 20kN. The three types of boundary conditions are illustrated in the figures below, and are referred to as cases (i), (ii) and (iii) respectively.

Case (i): The vertical translational and the rotational degrees of freedom are fixed at node O.

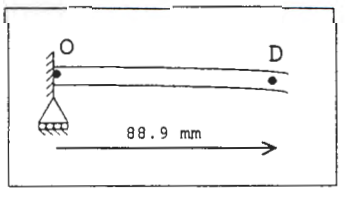

Figure 4.24: *Boundary conditions for* case (i)

Case (ii): The vertical translation of node O is fixed, with rotation and horizontal displacement being unrestricted.

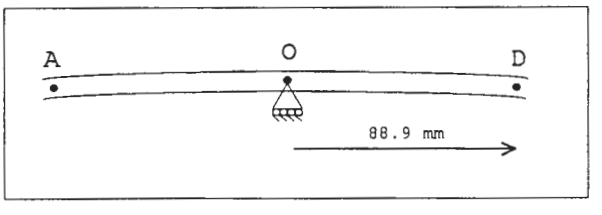

Figure 4.25: *Boundary condition of* case (ii)

Case (iii): Same as case (ii), except that an additional section (section BCO), which is stiffer than the rest of the conductor by a factor of 10^3 is included. This models the suspension clamp and the section of the conductor inside the clamp.

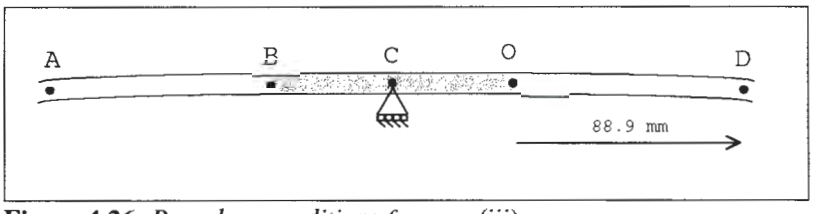

Figure 4.26: *Boundary conditions for* case (iii)

4.5.4 Discussion of the Effects of the Different Boundary Conditions

The results obtained for the three cases are shown and compared in the graphs below.

*i.) **Dynamic Bending curvature.***

The graph of Figure 4.27 shows the change in curvature in the conductor at point O.

As is to be expected, the change in the bending curvature (which, for the purposes of this discussion, will be referred to as the dynamic bending curvature) is greater for case (i), where no rotational freedom is allowed, than in the other two cases. Intuitively, the dynamic stresses in the conductor at the boundary would be expected to be larger for the totally clamped boundary condition, which agrees with the data obtained for the curvature.

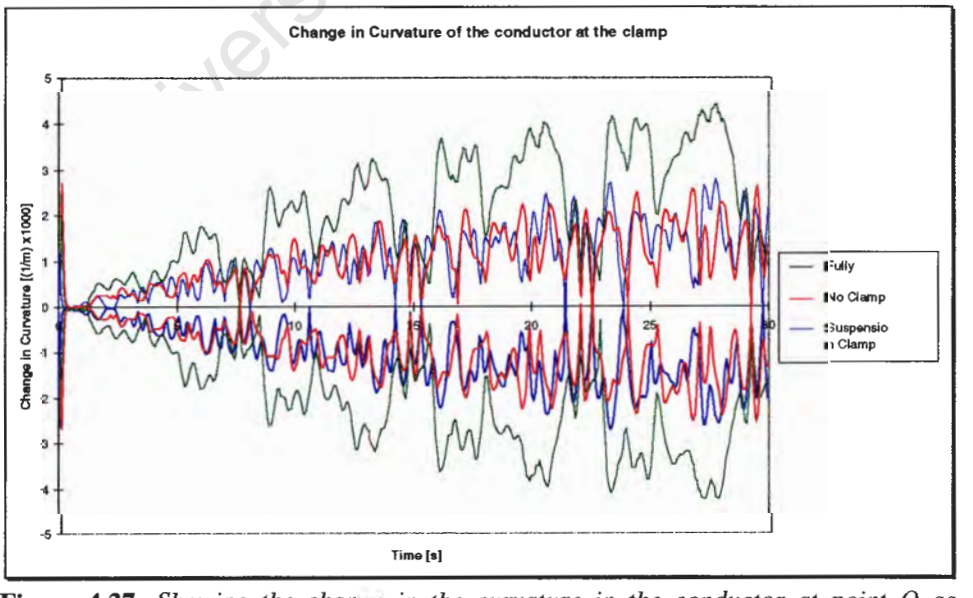

Figure 4.27: *Showing the change in the curvature in the conductor at point O as indicated in the figures above.*

It is quite interesting to note that the traces of the dynamic bending curvature for cases (ii) and (iii) are very similar, with the curvature trace for the

suspension clamp lagging the trace for the no clamp simulation by a small period of time. The estimates of the dynamic curvature and therefore the dynamic stress magnitudes for a specific vibration frequency compare favourably for these two models, implying that the slight simplification of the model by omitting the suspension clamp is an acceptable one. However, when more complicated situations are modelled, such as the vibration of two adjacent spans at different frequencies, it would be better to include the suspension clamp in the model, as it might have a more significant effect on the response of the system.

ii.) Deflection of the Conductor, 88.9 mm from the end of the Clamp

The results obtained for the deflection of the conductor, 89 mm from the last point of contact with the clamp, are shown in Figure 4.29. This point is represented by node D in the diagrams above. When compared with the results of the bending curvature at the interface between the clamp and the conductor, the curves for the three boundary conditions are very similar for the bending curvature and the deflection of node D. This is to be expected, as the deflection and bending curvature, for a linear bending stiffness, are linearly related.

The deflection is calculated by monitoring the rotation (θ) and displacement of node O, and the displacement of node D. Using the data for node O, and knowing the length of the section OD (88.9mm), the position of node D for zero deflection is calculated, and shown as D' in Figure 4.28.

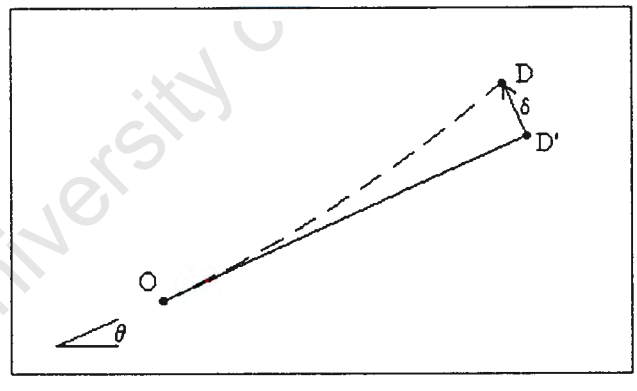

Figure 4.28: *Showing the notation used in calculating the deflection of the conductor at node D.*

The deflection (δ) is then calculated by vector subtraction of the position of D' from the real position of node D. This is done as the vertical displacement of node D alone is meaningless when comparing the different boundary conditions, and gives no direct comparison of the severity of vibration of the conductor.

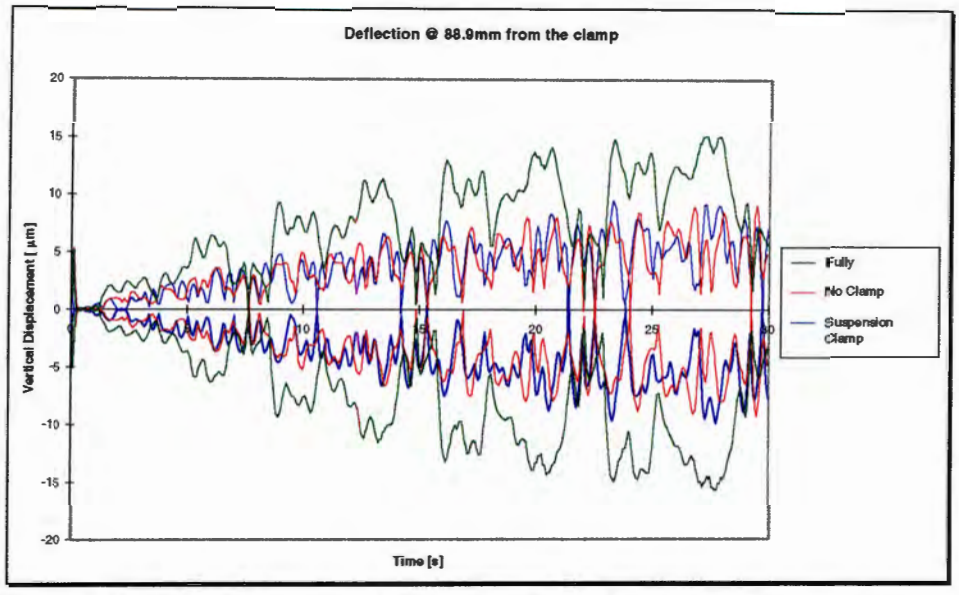

Figure 4.29: *The deflection of node D for the different boundary conditions.*

iii.) Displacement at 100m from the span end

The graph of Figure 4.30 traces the vertical displacement of the conductor, at a point 100m along the span for the three boundary conditions. In each case, the fundamental frequency of the span (about 0.135 Hz) is evident. The displacement histories are very similar for the three cases, with a slightly more irregular vibration pattern being noticed for the no clamp and suspension clamp boundaries. These results show that the effect of the boundary conditions on the behaviour in the free span is not as significant as the effect closer to the suspension points.

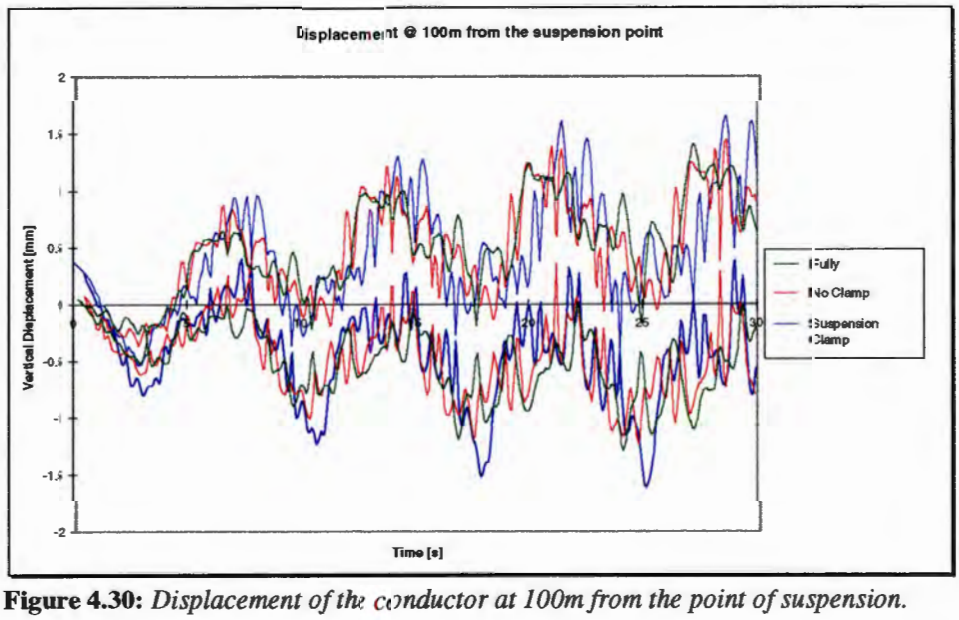

Figure 4.30: *Displacement of the conductor at 100m from the point of suspension.*

From the results given above, it is clear that the choice of boundary conditions has a significant effect on the behaviour of the conductor, especially in the vicinity of the boundary conditions. What this implies, is that care must be

taken when choosing the boundary conditions, so that the results obtained are meaningful and relevant.

4.6 VERIFICATION OF THE MODEL

4.6.1 Static Sag Geometry

In calculating the displacement profile of a conductor span due to gravity, the sag of the conductor is usually calculated according to the catenary relationship (Doocey et al, 1979; Bradbury et al; McDonald et al, 1990). A less accurate but simpler description of the sag geometry is obtained by assuming a parabolic profile, as was the norm before the advent of computers and calculations were performed manually.

The equation for a catenary is given by equation 4.18 below.

$$z(x) = A + B\left(\cosh\left(\frac{x}{B}\right)\right) \qquad (4.18)$$

To obtain values for A and B, the sag in the middle of the span is obtained using equation (B.3). Using this data and the fact that the sag at the end of the spans is zero, a Newton-Raphson procedure is employed to obtain values for A and B.

As seen in the graph of Figure 4.31, the profile for a 400 metre span is identical for the catenary and FEM results. This confirms the validity of the method used in the finite element model in applying the gravitational loads and in accounting for the change in length of the conductor under tension.

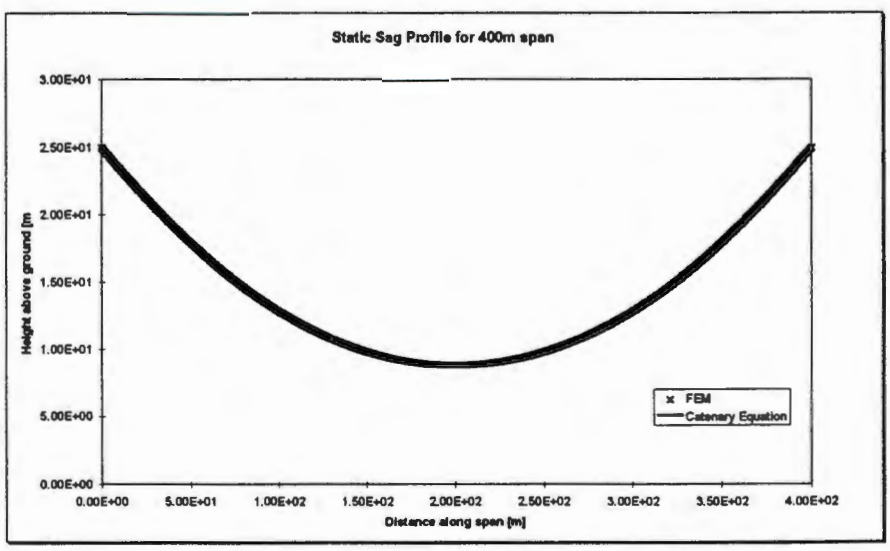

Figure 4.31: *Comparing the static sag profile of the 400m span according to the finite element model, with that predicted by the catenary equation.*

4.6.2 Aeolian Vibration Simulation

To verify the aeolian model, the vibration amplitudes are once again monitored 89mm from the last point of contact with the suspension clamp. The results are compared with those obtained from field observations carried out by Du Plessis (1994). The type of conductor modelled, the ACSR *Zebra* conductor, is the same as used on the test line on which Du Plessis' observations were made.

The data recorded for the vibration amplitudes is presented in Du Plessis' thesis in the form of a matrix, which is shown in Appendix C. The matrix shows the number of times observations were made at a certain frequency and amplitude of vibration. To obtain a meaningful comparison between the Du Plessis' data and the finite element results obtained in this project, the average vibration amplitude at each of the given frequencies is estimated from the field data using the following relationship:

$$A_{ave} = \frac{\sum_{all\_amplitudes} N_i \cdot A_i}{\sum_{all\_amplitudes} N_j} \qquad (4.19)$$

where N_i is the number of occurrences of a certain amplitude A_i at the frequency concerned. The data obtained from the above equation is presented graphically in Figure 4.32 .

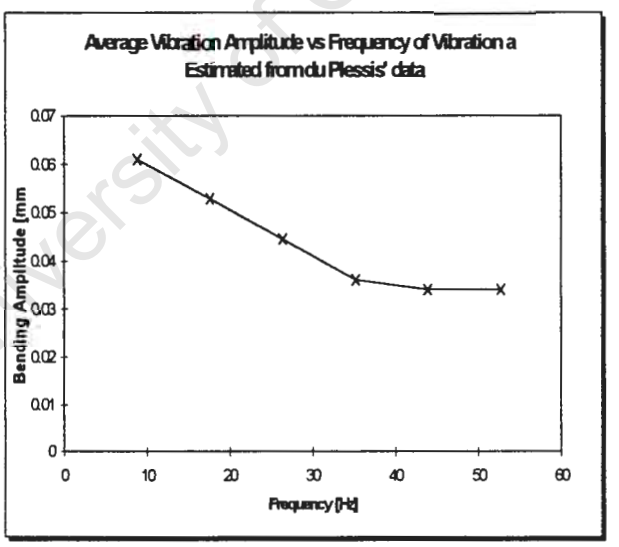

Figure 4.32: *Average amplitude of vibration as a function of the aeolian frequency of vibration as estimated from Du Plessis' (1994) results.*

At the transmission test line in Kroonstad, the single zebra conductor is connected to the support towers by means of two "U" bolts. This essentially corresponds to the model of case (ii) as described in section 4.5. In this model there is no suspension clamp, the conductor is however free to pivot about the point of suspension. In the aeolian vibration simulations a suspension clamp is included in the model, as is encountered in reality on a transmission line. As shown in Figure 4.33 the displacement amplitude measured 89mm from the

clamp is larger for the suspension clamp model than that of the no clamp boundary.

To make a meaningful comparison between Du Plessis' field data and the finite element results, the difference in the boundary conditions must be taken into account. As can be seen from the graph of Figure 4.33, where the displacement amplitude of node D is shown for the two boundary conditions, the displacement for the suspension clamp model is approximately double that obtained for the model with no clamp.

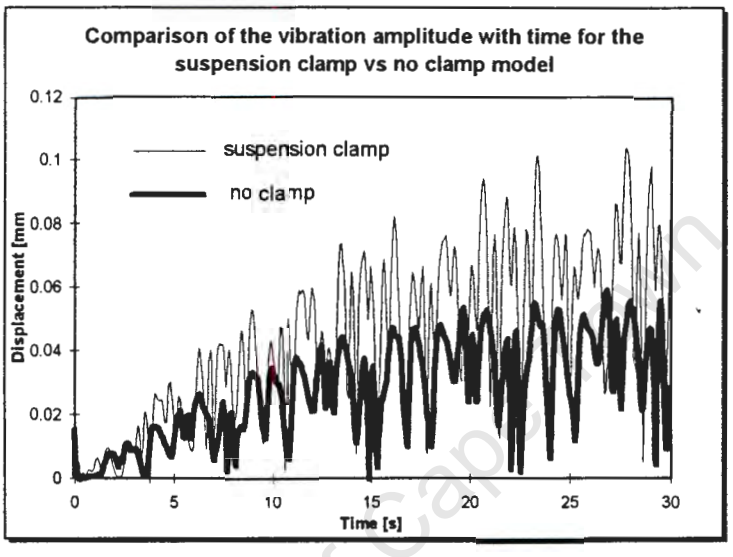

Figure 4.33: *Displacement at node D for suspension clamp and no clamp models*

Figure 4.34 shows the vibration amplitude histories, measured 89 mm from the clamp, for five different aeolian frequencies. The average amplitude as estimated form Du Plessis' data is shown as a dashed line. The latter has been multiplied by a factor of 2 to account (approximately) for the difference in boundary conditions of the test line and the finite element models, as discussed above.

In the finite element models, a tension of 20 kN is applied to the conductor for each of the simulations. In each case the total time of the simulation is equivalent to 450 loading cycles, i.e. the normalised time of 1 corresponds to 450 cycles from the start of excitation.

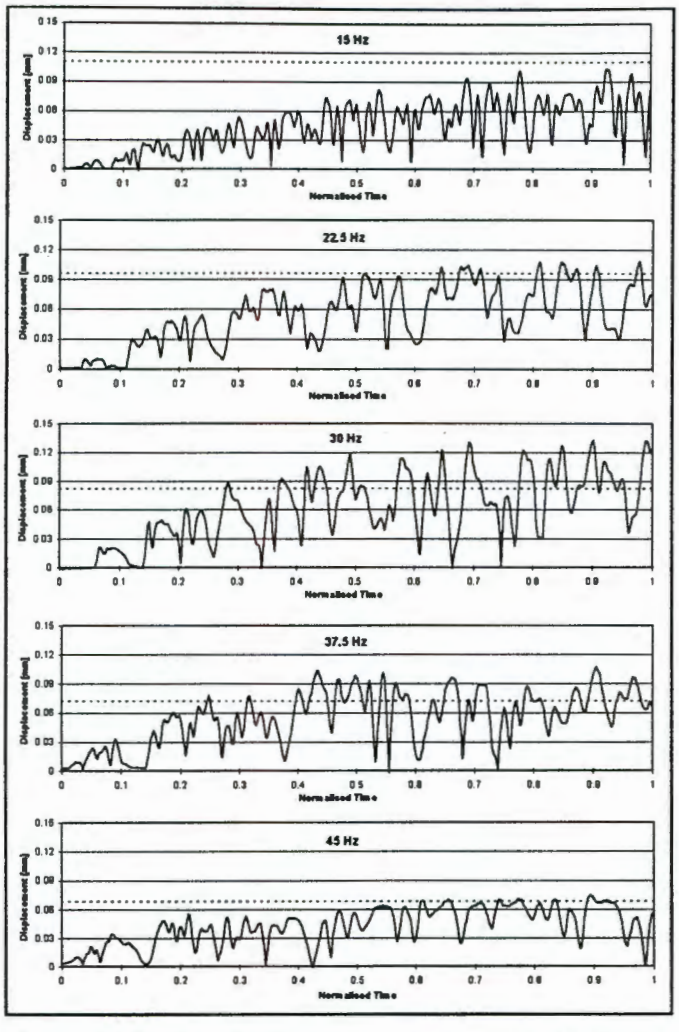

Figure 4.34: *The vibration amplitude histories obtained from the finite element model of the conductor, measured 89 mm from the last point of contact with the suspension clamp. The dashed line indicates the average amplitude of vibration as estimated from Du Plessis' field observations.*

As can be seen from the above, the results obtained from the finite element model compare quite favourably with those obtained from the field observations.

Clearly a more accurate method of comparing the finite element model with the experimental data would have been to run all five simulations with the no clamp boundary condition, to replicate the test rig used by Du Plessis with more accuracy. However, it was decided rather to model the situation which would be encountered on a real transmission line, where suspension clamps are used, than to model the simpler U-bolt assembly of the test line. Time constraints prevented all the simulations being repeated for the simpler boundary conditions.

4.7 OTHER RESULTS

The results of various other simulations are presented and discussed below. These include a comparison of the amplitudes of the axial and bending

alternating stresses during aeolian vibration and the effect of the aeolian vibration frequency and conductor tension on the intensity of vibration. The static stresses in strands of the conductor are given, after which the effect of the vibration of an adjacent span on the stresses experienced on the conductor is discussed. The effects of vibration dampers are then established on both the vibration intensity of the line and the stresses experienced at various locations along the length of the conductor.

4.7.1 Axial vs Bending Alternating Stresses in the Conductor.

To verify that the bending does indeed play an important role in the alternating stresses, the results of the alternating stresses due to bending in the outer strands of the conductor, are compared with the axial stress in the conductor. As the maximum bending occurs at the end of the span, the bending stress is measured here.

Figure 4.35 shows the axial stress in the conductor as monitored for aeolian vibration at 15 Hz, and a conductor tension of 20 kN. The maximum alternating stress amplitude is in the order of 0.06 MPa. The alternating stress amplitude due to bending of the conductor is shown in Figure 4.36. For the same simulation, the maximum alternating stress amplitude due to bending is approximately 2.5 MPa.

It is thus obvious that the bending effects are not only very important when estimating the magnitudes of the alternating stresses in the conductor during aeolian vibration, but also that the axial stress fluctuations are negligible in comparison to the bending stresses.

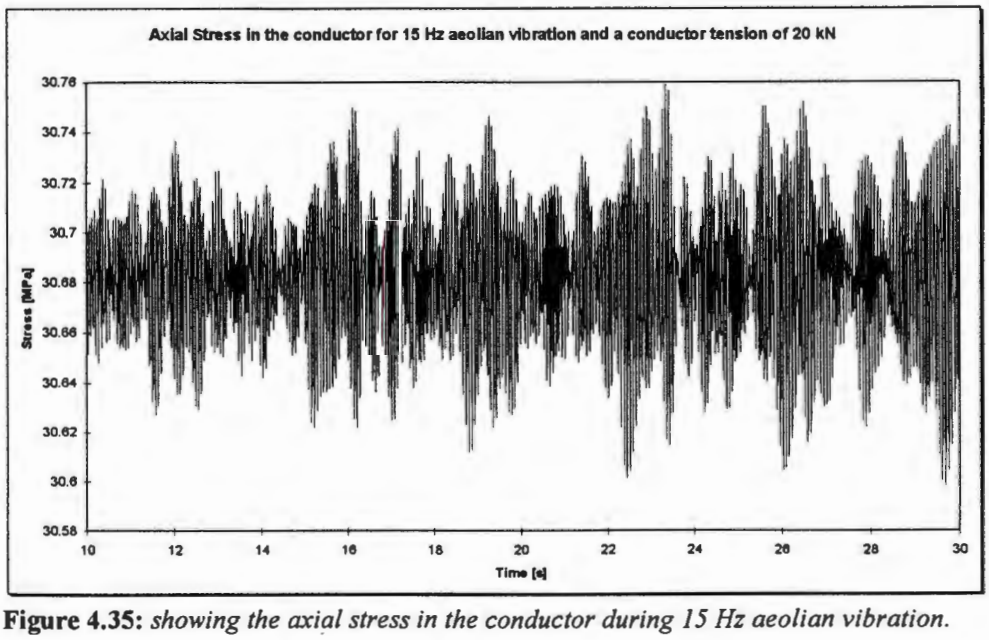

Figure 4.35: *showing the axial stress in the conductor during 15 Hz aeolian vibration.*

4.7.2 Vibration Intensity at Different Frequencies

The results of the alternating stress amplitudes, monitored for frequencies of 15, 22.5, 30, 37.5 and 45 Hz are shown in the graphs below.

The alternating stress amplitudes in the strands of the conductor next to the suspension clamp are calculated using Papailiou's equations as described in chapter 2.

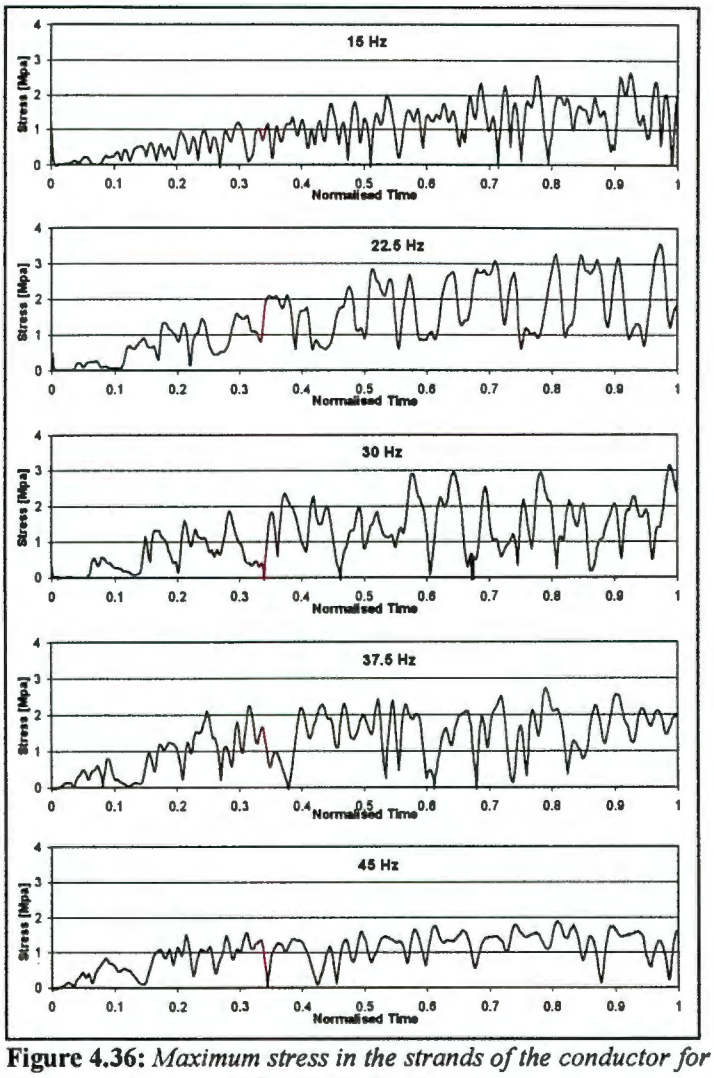

Figure 4.36: *Maximum stress in the strands of the conductor for different frequencies of aeolian vibration.*

From the results, it seems the maximum alternating stress levels occur in the 20 to 30 Hz frequency range. There is a definite reduction of the stress amplitudes as the excitation and vibration frequency increases, with the stress levels at 45Hz being about half that recorded for the 22.5Hz excitation.

From the experimentally obtained fatigue data in figures 2.16 to 2.25 of the EPRI handbook (Doocey et al, 1979) where the number of cycles to fatigue damage as a function of the stress amplitude is given, the minimum stress amplitude at which fatigue damage is likely to occur is approximately 10 MPa after 1000 Megacycles of vibration. The information in the paper by Cigre suggests a similar value (Cigrè Study Committee 22 - Working Group 04, 1988). Comparing the finite element results with this data, it seems that fatigue damage is unlikely to occur under the situations simulated, within 1000 Megacycles.

According to the paper by Cigrè, experimental observations of transmission lines in Europe show that the average number of vibrations experienced by a conductor is approximately 30 million per year. The Cigrè publication also gives the following relationship between the alternating stress amplitude σ_a (MPa) and number of cycles, N:

$$\sigma_a = C \cdot N^z \qquad (4.20)$$

with $C = 263$ and $z = -0.17$ for more than 15.6 Megacycles.

Using this relationship, and a typical value for σ_a of 3.5 as obtained from the finite element simulations, the conductor has a lifetime of about 108 000 Megacycles, or 3 600 years.

It should be realised though that the lifetime would be considerably reduced due to plastic deformation of the conductor at the suspension points. As shown in the section below, the stress magnitudes in the conductor at the suspension points due to gravitational loading are considerable and would be expected to lead to plastic yielding in the strands.

4.7.3 Effect of Conductor Tension

Figure 4.37 shows the vibration amplitudes measured 89 mm from the clamp for three different conductor tensions. The three tensions of 20, 25 and 30 kN correspond to 15%, 18.8% and 22.6% of the UTS[§] of a *Zebra* conductor respectively. As can be seen, the amplitude of vibration is slightly less for 25 kN and 30 kN, than it is for a tension of 20 kN. The same trend is noticed in the alternating stress magnitudes, shown in Figure 4.38.

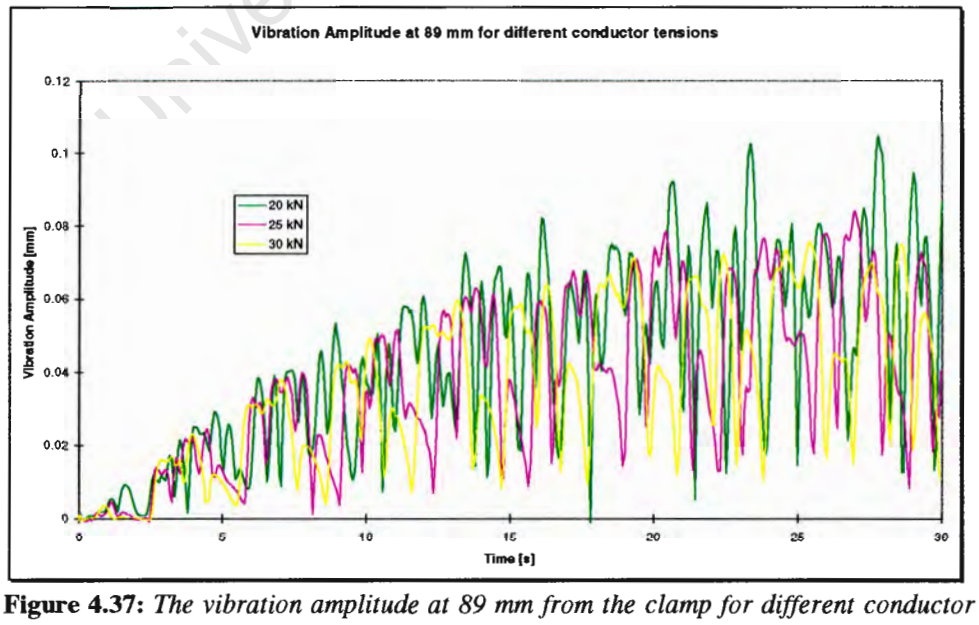

Figure 4.37: *The vibration amplitude at 89 mm from the clamp for different conductor tensions.*

[§] Ultimate Tensile Strength

The data of Table 4.2 shows that an increase in the conductor tension causes an increase in the wavelength. For a given amplitude of vibration, the increase in the wavelength thus decreases the severity of the conductor flexing (Doocey et al, 1979), and as a result the internal damping of the conductor decreases, as demonstrated by the fact that the damping ratio for a tension of 30 kN is less than 50% of the damping for a tension of 20 kN (Table 4.2).

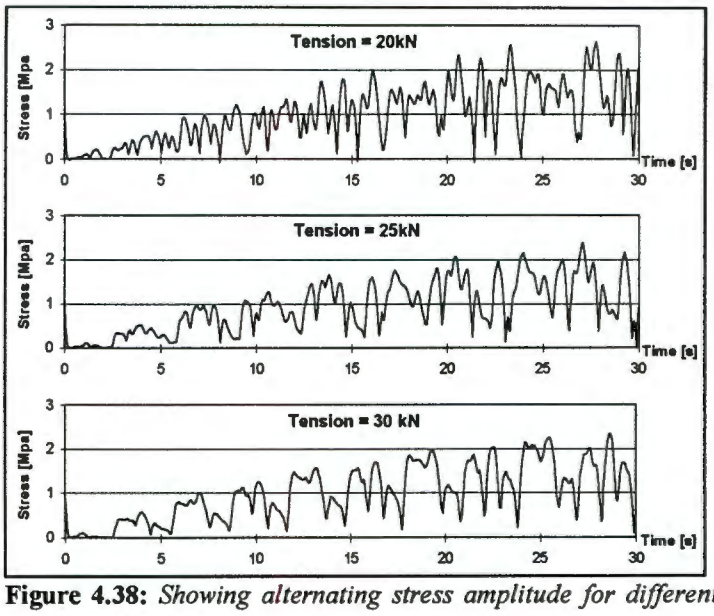

Figure 4.38: *Showing alternating stress amplitude for different conductor tensions.*

Doocey et al (1979) argue that this decrease in the damping causes an increase in the severity of vibration as the conductor tension is increased, contrary to the results obtained below. The range of conductor tensions tested, does not however allow any conclusive decisions to be made about the vibration intensity as a function of the conductor tension. Results for more than one frequency of vibration should also be obtained to provide a better understanding of the dependence of the vibration intensity on the axial tension of a conductor.

Another interesting observation from the results is that the history of the vibration amplitude becomes more regular with an increase in the tension. Definite beat patterns exist in the vibration histories, and the beat period, (the time between successive repetitions of the same vibration pattern), decreases with an increase in the tension. The beat frequency of a beat is equal to the difference in the frequencies of the two modes of vibration participating in a beat (Halliday et al, 1993). A decrease in the beat period with an increase in tension thus suggests that the frequencies of the participating modes tend to approach one another as the tension increases.

4.7.4 Static Stresses in the Conductor

To determine the magnitude of the static stresses in the conductor, the results of a simulation in which the gravitational load is applied on an initially straight conductor are given below.

As the conductor is initially straight, and once-off bending occurs relative to zero bending curvature as the gravitational loads are applied, the variable bending stiffness is implemented as a function of the curvature of the beam elements. This allows the curvature and stress magnitudes experienced at the suspension points, where significant bending occurs, to be modelled with the correct bending stiffness

The maximum bending curvature which occurs at the suspension clamp is equal to 3.5 m^{-1}. The minimum curvature required for the strands of each layer to slip, calculated using equation 2.19 are given in the table below. As can be seen, the curvature of 3.5 m^{-1} exceeds the minimum curvature required for slipping in each of the layers, and as such the additional stress term σ_w^{add} of equation 2.3 is calculated using equation 2.6. These values, together with the minimum stress component, σ_w^{min}, as calculated using equation 2.4, are also shown in the table, along with the total stress in the strand of each layer which is obtained by adding these last two terms.

Strand Layer	κ_i^{slip} [1/m]	σ_w^{add} [MPa]	σ_w^{min} [MPa]	$\sigma_w = \sigma_w^{min} + \sigma_w^{add}$ [MPa]
1	0	0	1151	1151
2	0.089	0.639	1151	1152
3	0.626	0.424	384	384.4
4	0.024	0.222	384	384.2
5	0.0059	0.0808	384	384.1

Table 4.6: *Showing the static stress in the strands of the Zebra conductor next to the suspension clamp. The stress in each of the five strand layers is given.*

For each layer, the stress is calculated on the outer surface of the strand, with the y in equation B equal to the strand radius, thus giving the maximum stresses which would be expected in the strand. The stress values given are the maximum of all the strands in each layer.

The yield stress of aluminium and steel are typically in the order of 150 and 400MPa respectively. The yield stress for both materials is thus exceeded. This is in agreement with what was found by Papailiou (1995a). He mentions that the elastic limit of the conductor strands in the vicinity of the suspension clamps is almost always exceeded.

4.7.5 Vibration Profile of the Span

The shape of span B during aeolian vibration at a frequency of 15Hz and with a conductor tension of 20 kN is shown for different times after the start of vibration in Figure 4.39. In Figure 4.40 the shapes of all three spans are shown at 7.5 and 10 seconds respectively after the start of vibration.

Due to the small amplitude of the vibration, which is in the order of 1mm, the vibration displacement is magnified by a factor of 10 000 and superimposed on the static sag profile of the span.

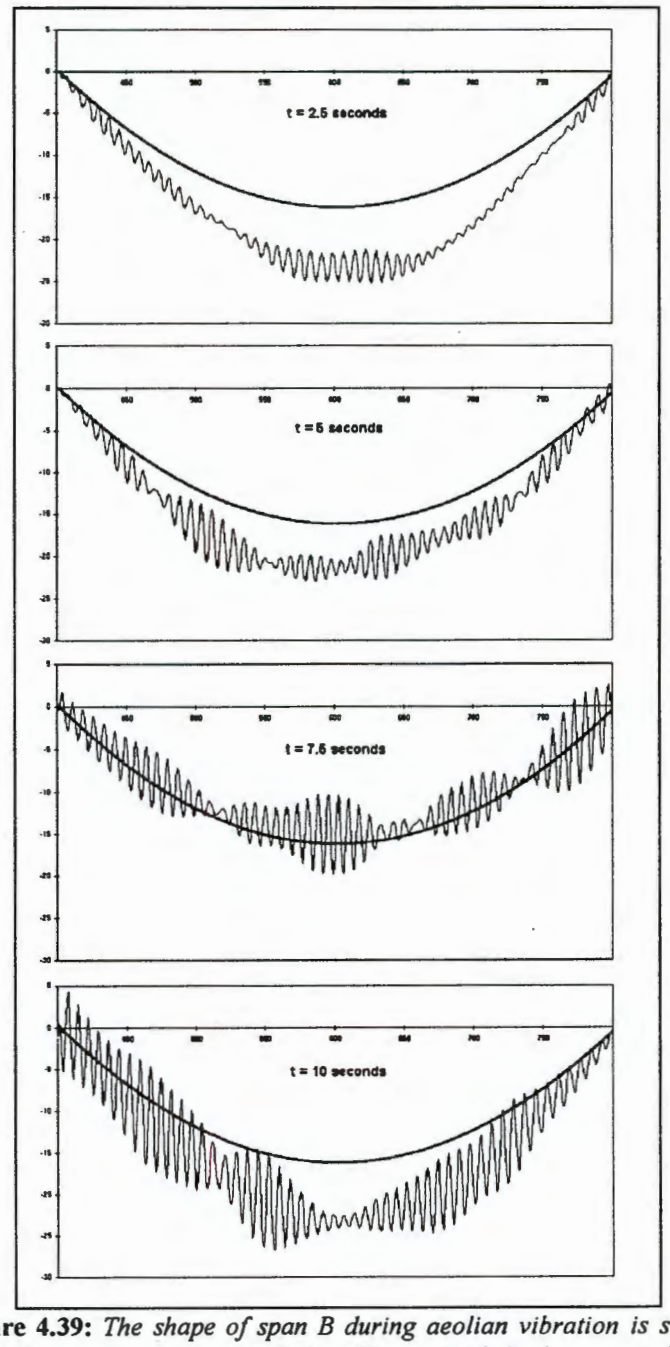

Figure 4.39: *The shape of span B during aeolian vibration is shown for different times in the simulation. The vertical displacements due to the aeolian vibration are magnified by a factor of 10 000 and superimposed on the static displacement profile. All distances are in metres, with the horizontal axis showing the position in the span.*

From the results is evident that the vibration is not necessarily symmetric about the centre of the span. Multiple modes of vibration of the span are excited, including both symmetric and asymmetric modes.

It can also be seen that the number of waves in the span is 52, corresponding to a wavelength of 7.7 metres for the 400m span. This compares very favourably with a wavelength of 7.6 m as predicted by the analytical equations for a taut cable (See Appendix A).

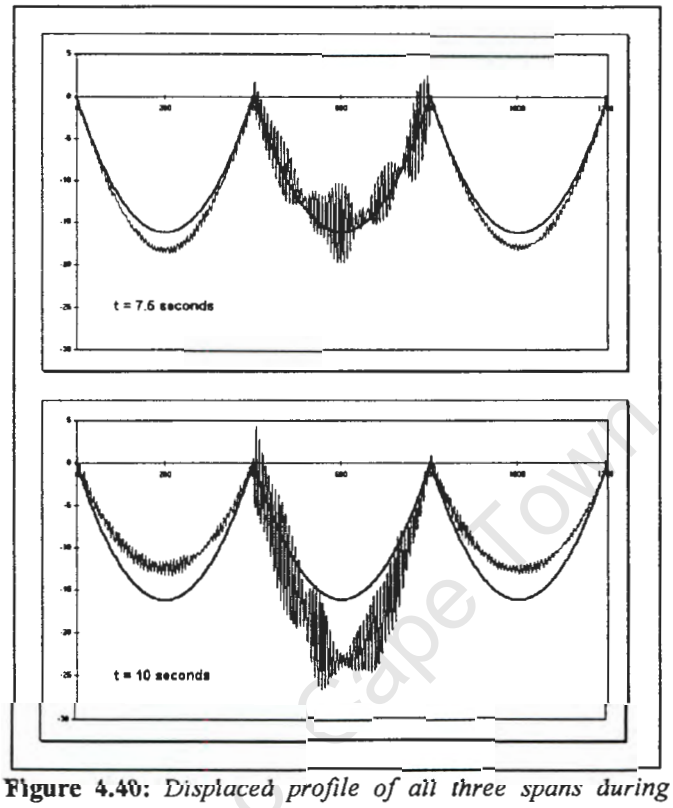

Figure 4.40: *Displaced profile of all three spans during aeolian vibration, after 7.5 and 10 seconds of vibration respectively.*

From the results of Figure 4.40, it is evident that a fundamental mode of vibration of the three spans is excited. As the conductor in the centre span moves downwards, the ends of the spans are pulled closer together, and the two outer spans move up slightly as they are pulled taut. As the centre span drops, the opposite occurs. This explains the lower frequency displacement component which is evident in the displacement history of the conductor 100m from the end of the span, as shown in Figure 4.30 above.

4.7.6 Effect of the Vibration of an Adjacent Span on the Response of the Conductor

In this simulation, the centre span (span B of Figure 4.21) is excited at a frequency of 15 Hz, while the adjacent span (span A) is excited at a frequency of 13 Hz. The axial tension of the conductor is 20 kN.

Figure 4.41 shows the alternating stress amplitudes observed at the end of span B when both spans are excited, compared with that observed when no aeolian excitation is applied to span A.

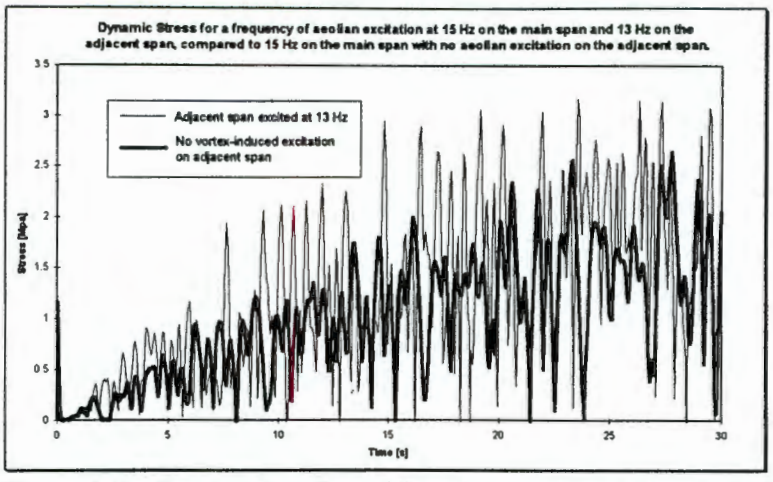

Figure 4.41: *Showing the effect of the vibration of an adjacent span on the amplitude of the alternating stress in the conductor.*

It is evident that the maximum amplitudes in the alternating stress history increase when the two spans vibrate at different frequencies. The peak stresses occur when the conductors on either side of the suspension clamp are simultaneously moving either up or down. When this happens, the motion of the articulating suspension clamp is restricted, and the end of the conductor is effectively subjected to a fixed, or rotationally very stiff, boundary condition. As shown in the section 4.5 dealing with the different boundary conditions, the dynamic bending curvature and therefore the alternating stress amplitude is increased if the articulation of the suspension clamp is limited or prevented.

This example shows the restricted capabilities of an articulating suspension clamp. As stated in the EPRI handbook (Doocey at al, 1979), the assumption that the rocking motion of an articulating suspension clamp reduces the vibration induced dynamic stresses is only valid if the two spans vibrate at exactly the same frequency. This requires not only that the wind velocity is uniform along the length of both spans, but also that the natural frequencies of both spans is identical. It is highly unlikely that both these requirements would be simultaneously fulfilled in practice.

4.7.7 Effect of Dampers on the Conductor

To observe the effects of vibration dampers on the behaviour of the conductor, the results of two simulations of aeolian vibration with vibration dampers at the ends of the spans are given. The frequency of vibration is 15 Hz, while the tension in the conductor is 20 kN.

The dampers are modelled as described in section 4.4.6, and are positioned as shown in Figure 4.42 which shows the location of two dampers at each span end. In the case of only one damper, the damper is located in the position of Damper 1. The distance of 1.45 m between the first damper and the suspension clamp, and between successive dampers, as shown below, is the standard distance used by Eskom on their transmission lines.

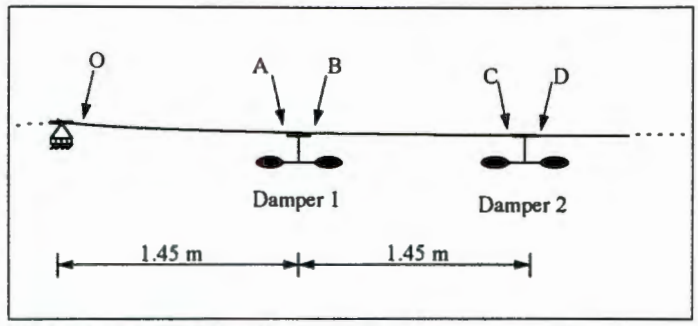

Figure 4.42: *Showing the typical location of vibration dampers on a single conductor on a real transmission line and the finite element model.*

From the results of the stress in the conductor next to the suspension clamp, shown in Figure 4.43 below, it is evident that the inclusion of vibration dampers significantly reduces the stress levels experienced at this point. What is also observed from the results is that the difference in the stress levels experienced at this point for one as opposed to two dampers is not very significant.

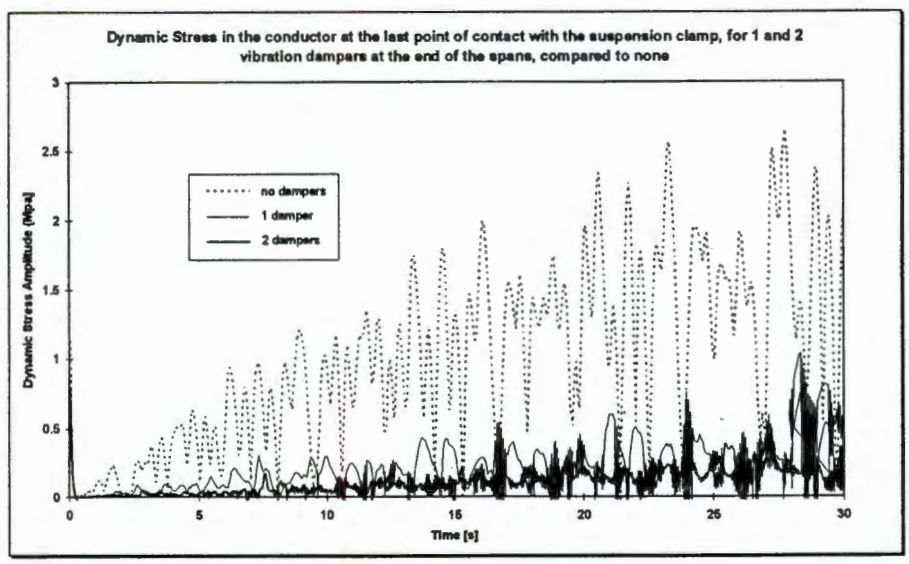

Figure 4.43: *Comparison of the alternating stresses in the conductor immediately next to the last point of contact with the suspension clamp, for none, one and two vibration dampers.*

Figure 4.44 and Figure 4.45 below show the alternating stress amplitudes at the locations as shown in the sketch of Figure 4.42 above, for one and two dampers respectively. A very significant observation which is made from these results, is that even though the inclusion of vibration dampers reduces the dynamic stress levels at the suspension point, it increases the alternating stress levels experienced at other points in the conductor to such an extent that the maximum alternating stress amplitude in the conductor is in fact greater than if no vibration dampers were present.

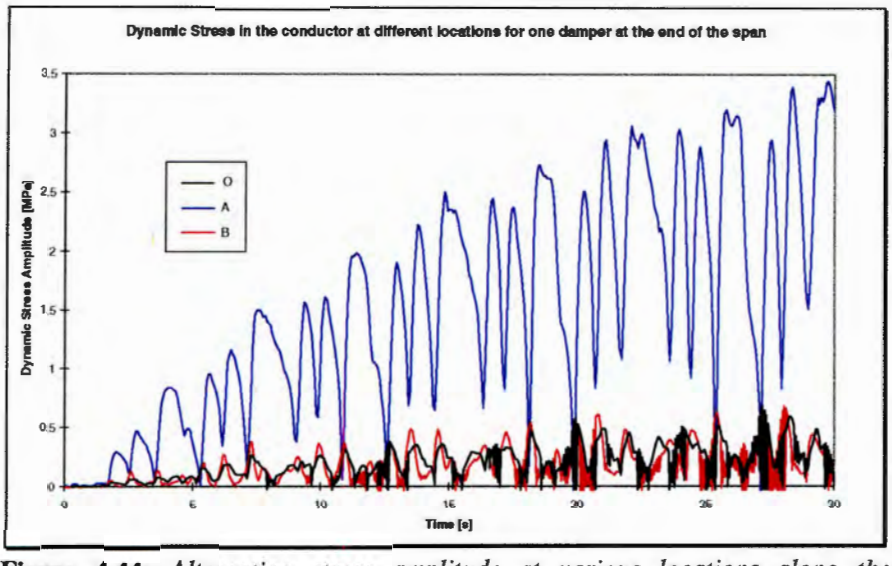

Figure 4.44: *Alternating stress amplitude at various locations along the conductor for one vibration damper at either end of each span.*

As can be seen from these results, the maximum stress in the conductor is observed on the suspension point side of the damper located closest to the middle of the span. (i.e. point C for two dampers, and point A for a single vibration damper). When comparing the maximum dynamic stresses for specific numbers of dampers, it is evident that the maximum dynamic stress in the conductor increases with the number of vibration dampers.

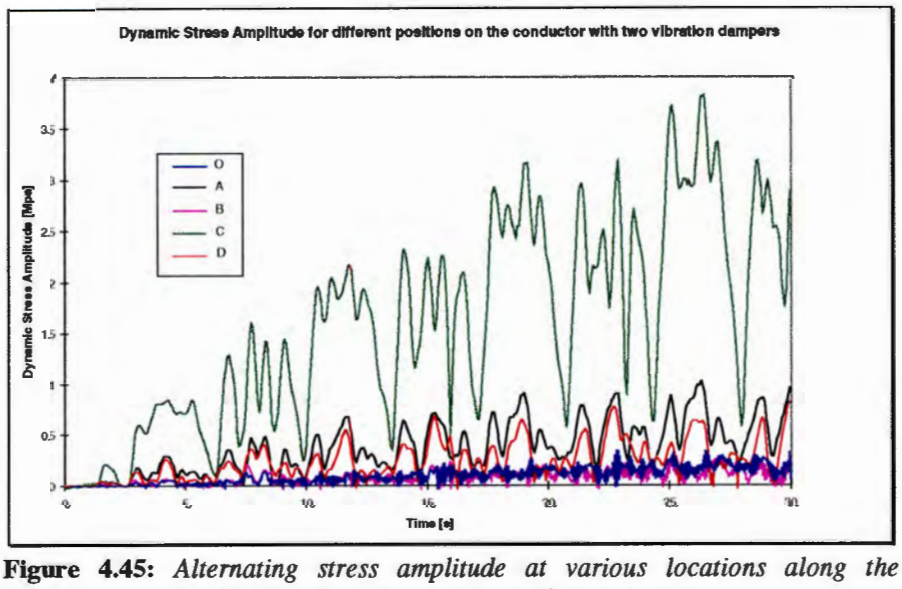

Figure 4.45: *Alternating stress amplitude at various locations along the conductor for two vibration dampers at either end of each span.*

It is important to note, however, that the static stress in the conductor is significantly larger at the end of the span than at the damper attachment points. As the static stress component increases, the maximum amplitude of the dynamic stress component for fatigue failure to occur decreases (Shigley, 1986; Poffenberger). This means that even though the maximum stress in the conductor may be increased with the inclusion of vibration dampers, the possibility and likelihood of fatigue damage of the conductor is reduced. The possibility of damage to the attachment hardware is also reduced.

As mentioned by Gopalan (1991), fatigue failure of insulator strings is possible if the frequency of aeolian vibration of the conductor corresponds to a natural frequency of vibration of the insulator string. The dampers thus also isolate the insulation and other attachment hardware from severe vibrations, and thus prevent them from vibration induced damage.

5. WAKE-INDUCED VIBRATION

This chapter deals the modelling of the wake-induced vibration of bundle conductors. In the short literature review, sources of information which have been found useful are listed. The next section which describes the phenomenon of wake-induced vibration is followed by an explanation of how the wake-induced loads are applied in the finite element model.

A section describing the CFD modelling of the fluid flow around two conductors is followed by the results obtained from the fluid flow simulations and a discussion thereof. The section describing the finite element model used to simulate the wake-induced vibration of a twin conductor bundle is followed by the last section in the chapter which presents and discusses the results obtained from the simulations.

5.1 LITERATURE REVIEW

The behaviour of a cylinder in the wake of another has been studied by various people. Bokaian and Geoola (1985) studied the lift force of two staggered cylinders in a laminar flow. Li et al (1992) carried out a numerical study on the response of a cylinder in the wake of an upstream cylinder while Biazik-Borowa et al (1995) derived mathematical models for the forces acting on both of two in-line cylinders.

In a paper by Zdravkovich and Pridden (1977), the experimental results obtained for the behaviour of two in line cylinders are given and discussed in great detail. In another paper by Zdravkovich (1977), the work and results of various previous authors are reviewed and discussed, and the drag coefficient for stranded cables for various Reynolds numbers and different cable spacings is also given. Other papers that deal with the flow around two cylinders are those by El-Taher (1985) and Gerhardt et al (1981). Du Plessis (1994) discusses the numerical simulation of the fluid flow around two in line conductors for various Reynolds numbers.

The EPRI handbook (Doocey et al, 1979), as in the case of aeolian vibration, is the most useful source of information found regarding wake-induced vibration. It discusses and presents the relevant results of various researchers and gives a detailed discussion of the phenomenon of wake-induced conductor motion and its causes.

5.2 THE PHENOMENON OF WAKE-INDUCED VIBRATION

The causes and different types of wake-induced vibration, together with the nature of the lift and drag forces which give rise to the vibration, are discussed below.

5.2.1 The Causes of Wake-Induced Conductor Motion

Wake-induced vibration is noticed only in conductor bundles where the sub-conductors in the bundle are in close proximity to one another. As the name implies, this type of conductor motion is as a results of the motion of one conductor in the wake of another. Depending on the position of the leeward conductor in the wake of the windward one, the downwind conductor will experience a drag force of a different magnitude to that it would experience on its own in the fluid. It will also experience a lift force for a range of positions (Doocey at al, 1979; Bokaian et al, 1985; Zdravkovich, 1977) due to the pressure and velocity profiles in the first conductor's wake. The drag force experienced by the windward conductor is also reduced as the distance between the two conductors decreases.

Due to the forces on the two conductors which are dependent on their relative positions with respect to one another, only a small perturbation is required to cause the leeward conductor to oscillate in the wake of the windward conductor, if the conditions are favourable. As mentioned by Doocey et al (1979), the occurrence of wake-induced oscillations is dependent on the simultaneous satisfaction of various criteria. These include smooth (laminar) wind conditions, the angle of incidence of the wind to the conductors in the span, and physical properties of the conductor bundle, which include the sub-conductor spacing, type and positioning of spacers and the angle of sub-conductors relative to one another in the bundle.

By means of the spacers which connect the individual sub-conductors in the bundle, the windward conductor is set into motion by the oscillations of the leeward conductor, and as such both windward and leeward conductors participate in the wake-induced oscillations.

5.2.2 Types of Wake-Induced Conductor Motion

Wake-Induced oscillation of conductors can be classified into four categories as illustrated in Figure 5.1 (Doocey at al, 1979). These are the sub-span mode, where the motion occurs within a sub-span (a section of the span between two subsequent spacers) and the rigid body modes of vertical, horizontal and twisting motion which involve the whole length of the span. The last three types of motion are termed "rigid body" as little or no distortion of the bundle cross-section occurs. Even though the wake-induced motion of conductors is broadly classified into these four categories, a particular mode will normally be associated with one or more others. The dominant mode of vibration is however used to describe the motion.

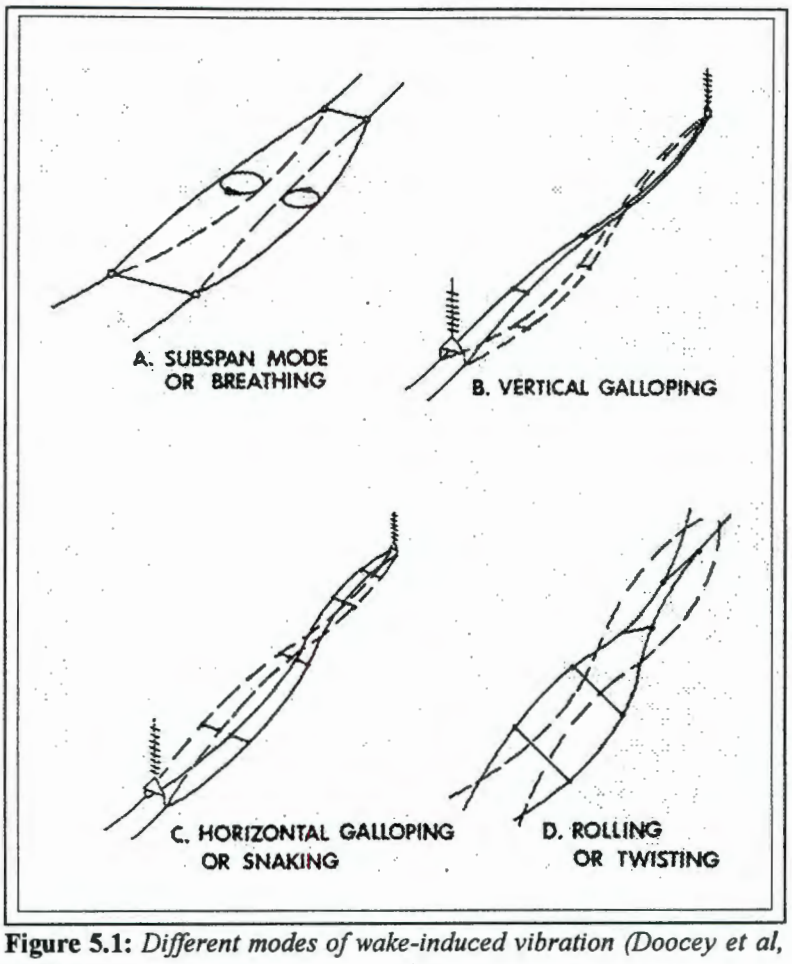

Figure 5.1: *Different modes of wake-induced vibration (Doocey et al, 1979)*

5.2.3 Lift and Drag forces

Data on the lift and drag coefficients on the leeward conductor is available from the EPRI handbook (Doocey et al, 1979) and the paper by Zdravkovich (1977). The data has been found to be a function of the ratio of the distance between the conductors to the cross-sectional diameter of the conductor, and as such is valid for a range of different conductor diameters.

The limitation of the available data however, is that it does not account for a dependence of the drag and lift coefficients on the Reynolds number. The drag coefficient of a conductor is much more dependent on the Reynolds number of the fluid than a smooth cylinder is, as can be seen from Figure 5-8 of the EPRI handbook (Doocey et al) which compares the drag coefficients for a *Chukar* conductor with that of a smooth cylinder for a range of Reynolds numbers. For the smooth cylinder the drag coefficient is fairly constant with a value of 1.1, while for the conductor it changes from about 1.25 for $Re < 20\ 000$, dips to about 0.75 at $Re = 40\ 000$ and then reaches a constant value of about 0.9 for $Re > 70\ 000$. The data from the literature is thus adjusted to match the data obtained from the fluid flow simulations completed as part of this project.

5.3 SIMULATION OF WAKE-INDUCED FORCES

As mentioned previously, the force on the leeward conductor can be described in terms of the lift and drag components respectively, depending on the position of the leeward conductor relative to the windward one. Even though it is not zero, the change in the drag force on the windward conductor is fairly small in comparison to the change in the forces acting on the leeward conductor, and it is thus assumed for the simulations that the windward conductor experiences a constant drag force, no matter what the distance between the two conductors.

The wake-induced loads are implemented in the finite element simulations by means of a user-defined loading subroutine, as in the aeolian vibration and short-circuit current simulations. The loading subroutine monitors the position of each point on a leeward conductor relative to the corresponding point on the windward conductor. A database of lift and drag forces for a grid of relative positions between the two conductors is provided as an array in the subroutine. The lift and drag forces on the leeward conductor are then calculated by interpolating from the database.

Values for the lift and drag coefficients in the database are estimated from the information in the EPRI handbook (Doocey et al, 1979), and from the results of the fluid flow simulations.

5.4 DETAILS OF THE FLUID FLOW MODEL

To obtain values for the lift and drag coefficients on a *Zebra* conductor at a wind velocity of 10 m/s, (the velocity arbitrarily chosen for the modelling of wake-induced vibration), the fluid flow over two conductors in various arrangements is modelled with SPECTRUM, a commercially available finite elements package which has fluid flow modelling capabilities. The details of the finite element mesh and the simulation data are described below.

5.4.1 Element Types

As SPECTRUM does not accommodate two dimensional problems and only provides three dimensional elements for fluid analysis, the essentially 2-D problem is modelled using a single layer of 3-D elements. Six sided brick (Hex) and four sided wedge elements are available.

Name	*no. Hex*	*no. Wedge*	*Other Details*	*Drag Coefficient*
mesh 1	460	540	wedge around cylinder	1.34
mesh 2	1000	0	-	0.91
mesh 3	0	1960	-	1.26
mesh 4	60	7000	Hex around cylinder	0.93
mesh 5	0	1268	-	1.53
mesh 6	630	0	-	1.15

Table 5.1: *Showing the different mesh types used to simulate the air flow around a smooth cylinder.*

The pressure distribution around the cylinder for various mesh arrangements, used in simulations of the fluid flow around a smooth cylinder, is shown in Figure 5.2. The details of each mesh are given in Table 5.1, with the cylinder diameter being 30 mm, the air velocity 10m/s, and the Reynolds number being approximately 20 000.

The drag coefficient (C_d) is calculated from the drag force (D) by means of the following equation:

$$C_d = \frac{D}{\frac{1}{2}\rho A v^2} \qquad (5.1)$$

with ρ being the density of the fluid and A the projected area of the cylinder normal to the direction of the free stream velocity v.

For a Reynolds number of 20 000, the drag coefficient of a smooth cylinder is approximately 1.05 (Doocey et al, 1979; Sayers, 1992; Acheson, 1990).

From the graphs below, it is observed that the pressure distribution around the cylinder is fairly similar for each of the different finite element meshes. What is evident though, is that the pressure distributions predicted by mesh 2, 4 and 6 are more in agreement with one another than for the other three meshes. The drag coefficient predicted by these meshes is also more in agreement with the value obtained from literature.

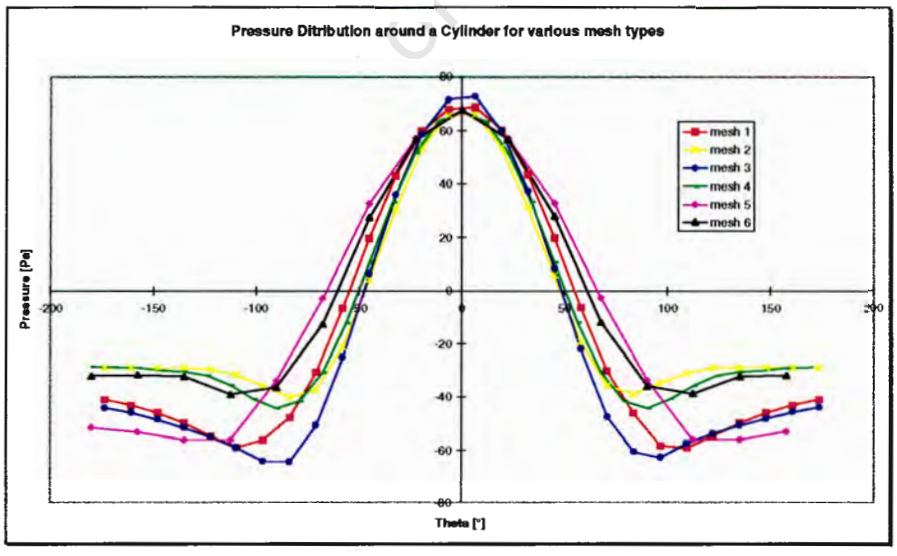

Figure 5.2: *Showing the pressure distribution around the cylinder for different mesh arrangements.*

The angle θ is measured as shown in the sketch below.

From these results, and the results of other similar simulations with slight variations of the above meshes, carried out while testing the different options, it seems that the brick or hex elements model the fluid flow more accurately, with fewer elements being required. One of the more important observations made, is that the modelling of the fluid around the cylinder using hex elements

produces more accurate results than when wedge shaped elements are used. For the simulation of the fluid flow around conductors, a minimal number of wedge elements is thus used only where necessary for purposes of mesh refinement.

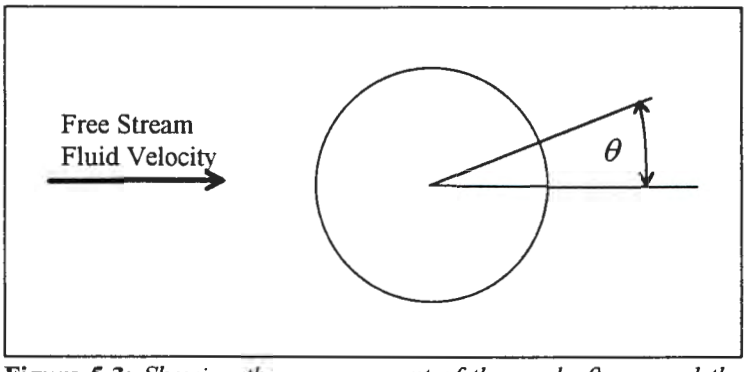

Figure 5.3: *Showing the measurement of the angle θ around the cylinder and conductors*

5.4.2 The Finite Element Mesh

From available literature, it is evident that the surface roughness of a cylinder has an effect on the flow of fluid around the cylinder, and thus on the characteristics of the wake of the cylinder. According to Du Plessis (1994), the wake of a conductor is considerably wider than that for a smooth cylinder of the same overall diameter. As mentioned previously, the drag force on a conductor is also different from that on a smooth cylinder. Doocey et al (1979) state that the difference in the aerodynamic characteristics between stranded conductors and smooth cylinders is fairly significant

To model the air flow over a pair of conductors as accurately as possible, the outer strands on the conductor are thus included in the mesh rather than modelling the conductors as smooth cylinders. This requires a greater degree of refinement of the mesh at the conductors, however the increased effort in generating the meshes and the subsequent increase in CPU time are justified by the greater confidence in the accuracy of the results.

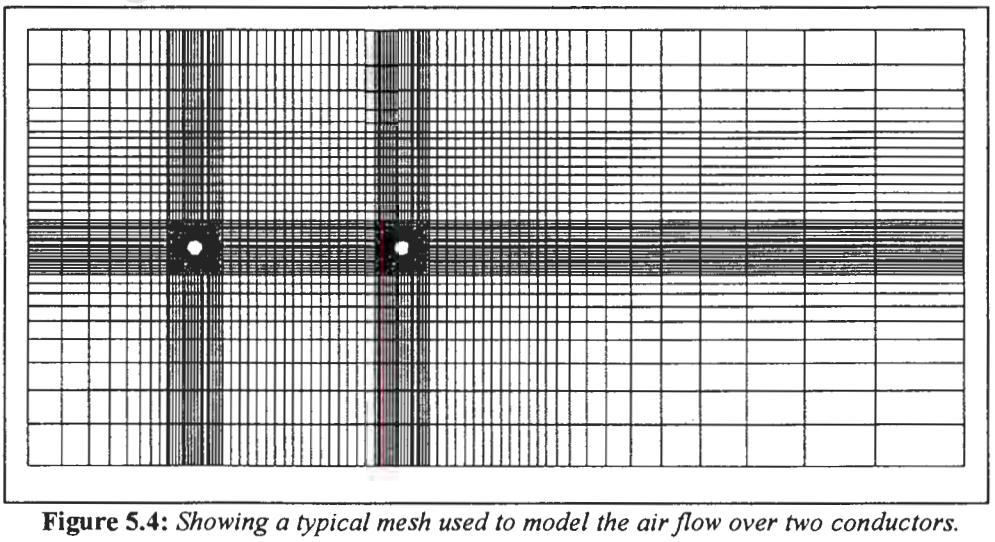

Figure 5.4: *Showing a typical mesh used to model the air flow over two conductors.*

Figure 5.4 shows a typical mesh used in the modelling of the fluid flow over the two conductors. The conductor boundaries are modelled as shown in Figure 5.5 while Figure 5.6 shows how the mesh, consisting of brick elements, accommodates the strands on the outer layer of the conductor.

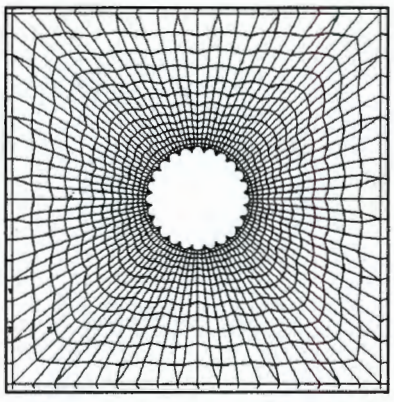

Figure 5.5: *Showing the Mesh refinement around the conductor*

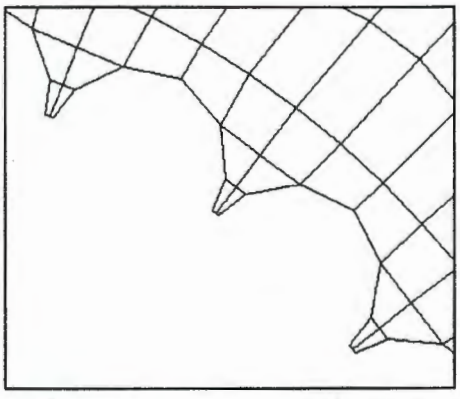

Figure 5.6: *A close-up of the mesh around the strands of the conductor*

The total number of elements in the model is approximately 5000. By refining the mesh as shown above, with a finer mesh around the conductors and fewer elements towards the outer boundaries, the total number of elements is kept as low as possible, while still accommodating more complex fluid flow in the direct vicinity of the conductors.

5.4.3 Details of The Fluid Flow Problems Simulated

i.) Boundary Conditions

The boundary conditions applied in all fluid flow simulations are as follows:

Boundary	Pressure [Pa]	x-velocity [m/s]	y-velocity [m/s]
Left edge	0	10	0
Right edge	0	-	-
Top and bottom	0	10	0
Conductors	-	0	0

Table 5.2: *Boundary Conditions applied in the fluid flow simulations*

The velocity normal to the page is set to zero, effectively reducing the problem to two dimensions as all the degrees of freedom in the third dimension are eliminated from the problem.

ii.) Fluid Properties

The air flowing over the conductors is assumed to be incompressible and isothermal, and is assumed to obey the Navier-Stokes relationship. No turbulence models are activated in the simulations, and the following properties are specified for air at 20 °C (Sayers, 1992):

Dynamic viscosity: 1.8E-5 Pa.s
Density: 1.2 kg/m^3

iii.) Conductor Locations

The drag and lift forces on the conductor are determined for six different locations of the downstream conductor, as indicated on the sketch of Figure 5.7 below. The fluid domain is shown by the shaded area, the upwind conductor is shown in black, and the various locations of the downstream cylinder in white.

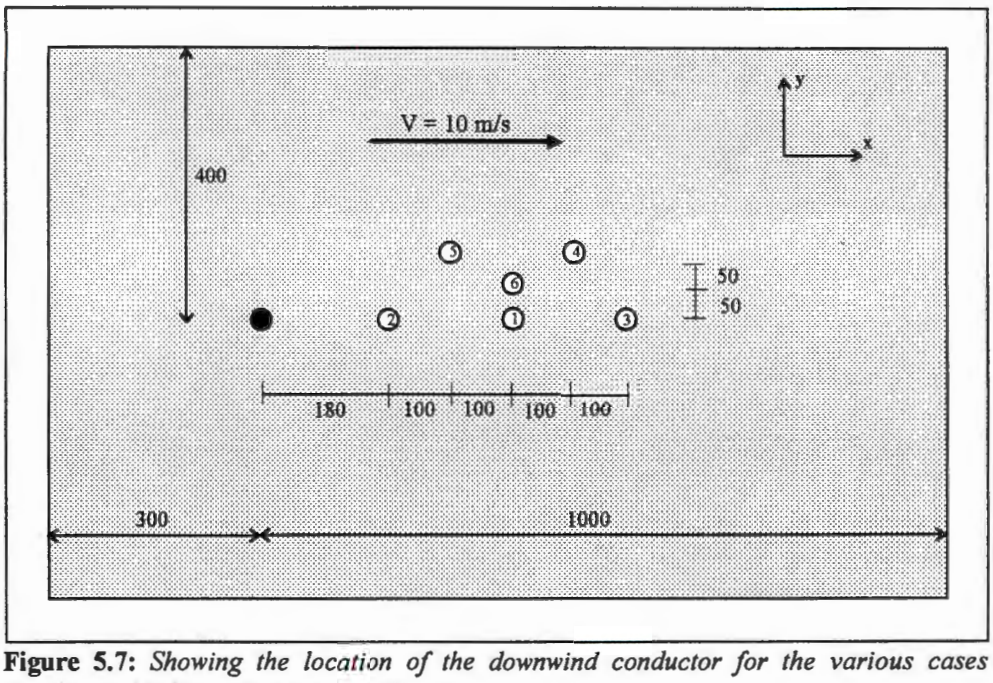

Figure 5.7: *Showing the location of the downwind conductor for the various cases simulated. All dimensions are in millimetres.*

The simulations are referred to by number as shown in the following table, with the positions indicated being those of the downwind conductor relative to the upwind conductor.

Name	x [mm]	y [mm]
Model 1	380	0
Model 2	180	0
Model 3	580	0
Model 4	480	100
Model 5	280	100
Model 6	380	50

Table 5.3: *Showing the position of the leeward conductor with respect for the windward one for the various fluid-flow simulations.*

5.4.4 Calculating the Drag and Lift Forces

The drag and lift force on the conductors are determined from the pressures at the nodes of the cylinder boundary. The cylinder perimeter is modelled as a number of short line segments (see Figure 5.6), corresponding to the element edges which make up the cylinder boundary. The drag force contribution per unit length (of the conductor) which acts on a line segment (F_x^i) is calculated by multiplying the average pressure acting on the line segment by the length of the segment projected onto the y-axis. The total drag force (D) is then

calculated by summing the contribution of the force on each line segment making up the cylinder boundary. The lift force (L) is calculated using the same approach.

Equations 5.2 and 5.3 may be used to calculate the drag and lift forces acting on each line segment respectively, if a local co-ordinate system is used in which the origin is corresponds to the center of the conductor. The notation used is shown in Figure 5.8.

$$F_x^i = -\tfrac{1}{2}\left(y_{n+1} - y_n\right)\left(P_{n+1} + P_n\right) \qquad (5.2)$$

$$F_y^i = \tfrac{1}{2}\left(x_{n+1} - x_n\right)\left(P_{n+1} + P_n\right) \qquad (5.3)$$

The total drag and lift force on the cylinder are calculated using equations 5.4 and 5.5 respectively.

$$D = \sum_{all\_edges} F_x^i \qquad (5.4)$$

$$L = \sum_{all\_edges} F_y^i \qquad (5.5)$$

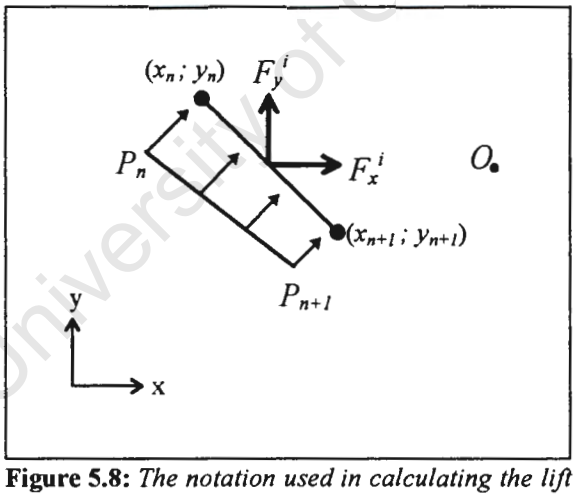

Figure 5.8: *The notation used in calculating the lift and drag forces on a segment of the cylinder boundary*

5.5 RESULTS OF THE FLUID FLOW SIMULATIONS

Typical results of the fluid flow simulations, are presented and discussed below.

5.5.1 The Air Flow around the Conductors

Figure 5.9 below shows the pressure around the downstream cylinder for Model 1 at various stages in the analysis.

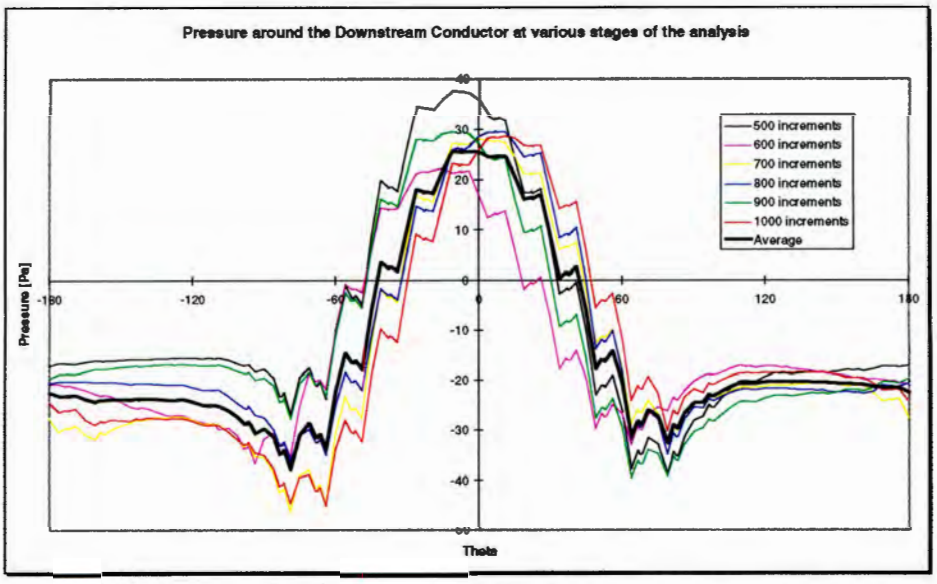

Figure 5.9: *Pressure distribution around the downstream conductor at various increments in the fluid flow simulation. The data is obtained from Model 1.*

The average pressure is calculated using the data from increments 600, 700, 800, 900 and 1000. Disk storage requirements limit the number of increments for which data can be obtained during the analysis, and as such a higher frequency of increments is not used to calculate the average values. Data from earlier increments is disregarded as the change in the pressure values for the fluid regime between the earlier increments is considerably larger than in the second half of the analysis, and it seems that the simulation settles into a steady, though dynamic, solution during the latter half of the analysis.

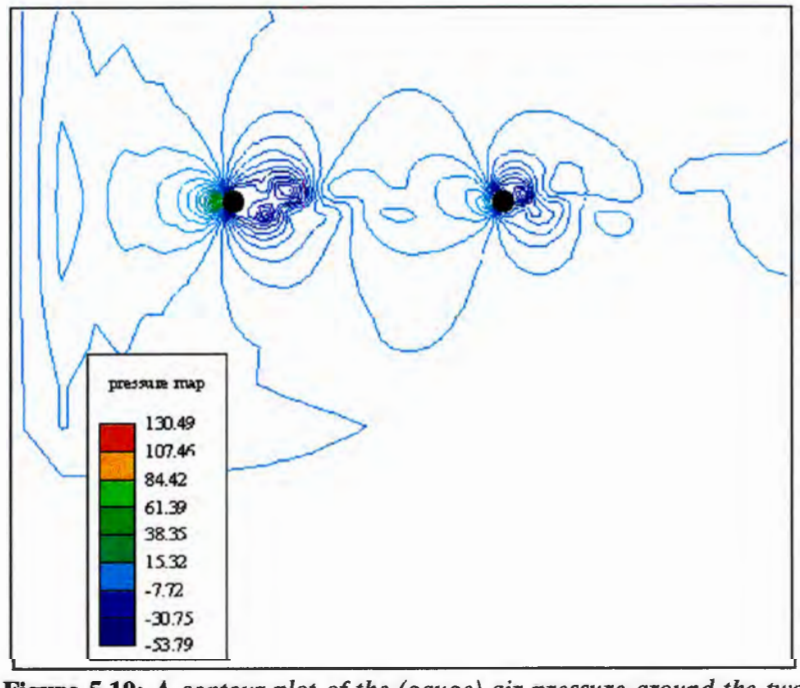

Figure 5.10: *A contour plot of the (gauge) air pressure around the two conductors, for a conductor spacing of 380 mm.*

As can be seen from the results shown in Figure 5.9 above, which are typical for the fluid flow simulations, the pressure distribution around the conductor

does not reach a steady state, even after 1000 time increments (corresponding to a simulated time of 0.5 seconds) of the simulation. This, together with the contour plots of pressure around the two conductors of Figure 5.10, in which the vortices which are shed from the rear of the conductors are evident, suggest that as the problem of air flow around a conductor is essentially a dynamic one, (due to the shedding of vortices and turbulence) it can not be modelled numerically as a steady state fluid flow problem. Du Plessis (1994) mentions that a steady-state solution was also not obtained in his simulations of a similar nature.

Figure 5.11 and Figure 5.12 show contours of the velocity component in the x direction for conductor separations of 380 mm and 180 mm respectively. The velocity for a horizontal (x) separation of 380 mm and a vertical (y) separation of 50 mm is shown in Figure 5.13. Apart from the oscillatory nature of the wake in all cases, it is interesting to note how the fluid flow around the individual conductors is very similar for both conductors with a separation of 380mm, while for a separation of 180 mm, the two conductors seem to act as a single, more streamlined body around which the fluid can flow.

Figure 5.11: *Showing contours of the x-velocity for a conductor separation of 380 mm.*

Taking a closer look at the velocity profile of Figure 5.12 reveals that the air directly in front of the downwind cylinder is actually flowing in the opposite direction to which the wind is blowing. As shown by the results for the drag coefficients below, the second conductor experiences a negative drag force, while the drag on the front conductor is also slightly reduced. This is in accordance with the results given by Zdravkovich and Pridden (1977) and the results of various researchers as reported in the review by Zdravkovich (1977). It also serves to illustrate how effective "slipstreaming" can be in sports such as

motor racing and cycling in reducing the drag force on not only the second, but also the front body in such a tandem arrangement.

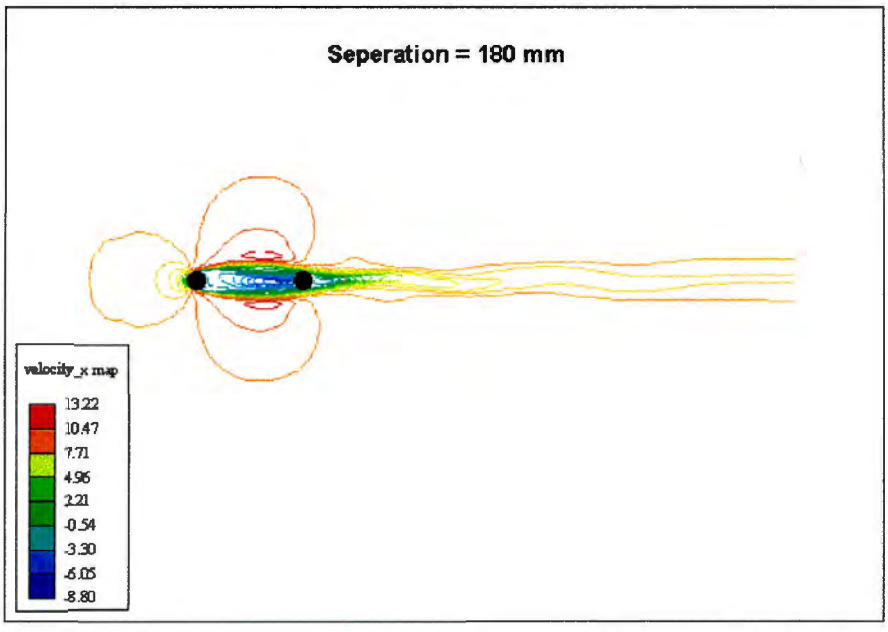

Figure 5.12: *Contours of the x-velocity for a conductor separation of 180 mm.*

More importantly regarding wake-induced vibration, this illustrates how the severity of vibration would be expected to increase considerably if the conductors approach each other to within approximately 5 conductor diameters. If they approach each other to within the distance required for negative drag, they would effectively be pulled together and subsequently clash.

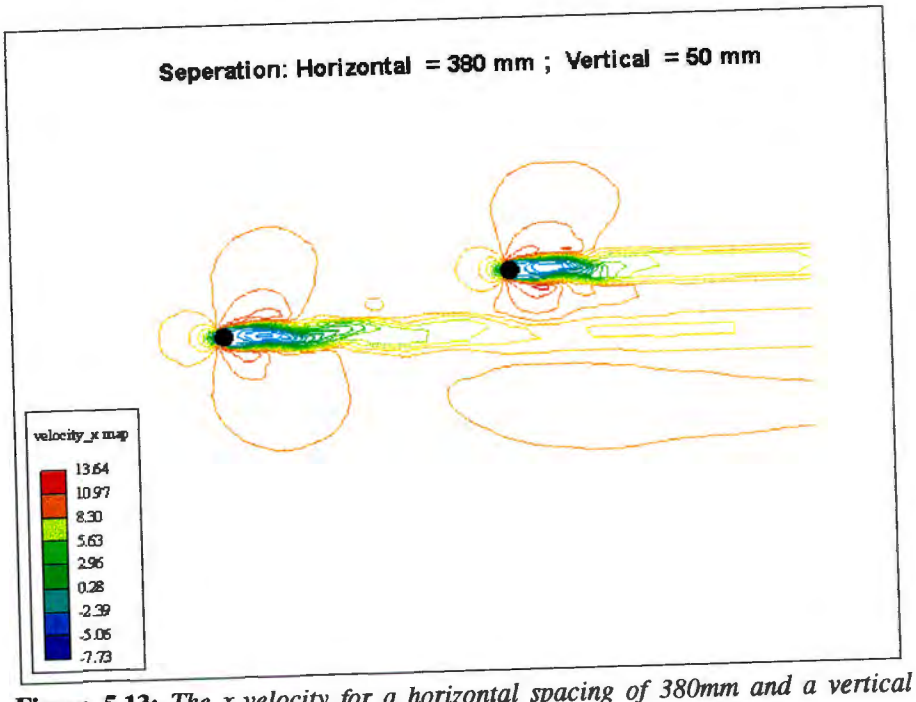

Figure 5.13: *The x-velocity for a horizontal spacing of 380mm and a vertical spacing of 50mm.*

As can be seen from velocity contours above, the wake affects the fluid flow quite far downstream of the conductors, while, on the other hand, the wake is fairly narrow. For a bundle tilt of 7.5 ° (the bundle tilt being the angle between the x-axis and the line joining the centres of the conductors), the second conductor does not appear to be significantly affected by the wake of the upstream conductor. The former does however experience a lift force, in this case in the downward direction, due to the greater velocity of the air in the wake of the upwind conductor. An increase in the velocity causes a drop in pressure, thus a force is experienced which tends to pull the downwind conductor into the wake of the upwind one.

5.5.2 Drag and Lift Coefficients

The drag and lift coefficients, calculated using equations 5.1 to 5.5, and substituting C_L and L for C_D and D in equation 5.1 when calculating the lift coefficient, are shown in the figures below.

i.) Windward Conductor

As can be seen from the results, the drag coefficient is fairly constant for the various positions of the downwind conductor. The only exception with any significance is the slight reduction in the drag on the conductor for Model 2, in which the conductor separation is the least.

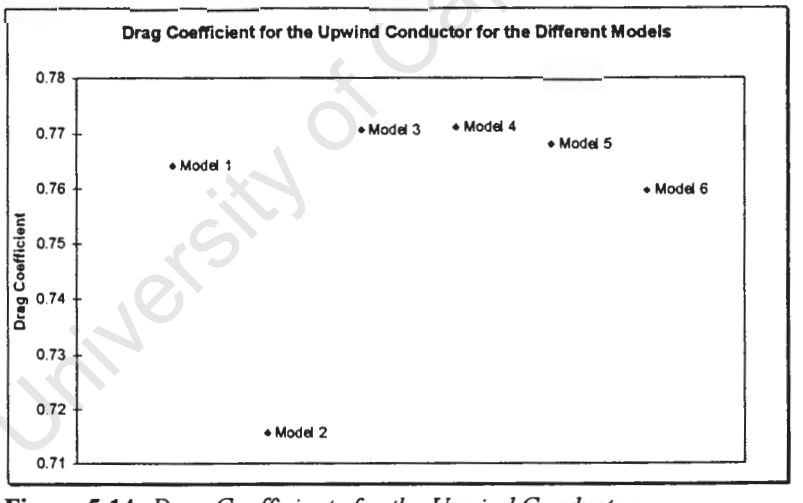

Figure 5.14: *Drag Coefficients for the Upwind Conductor*

With regards to the lift coefficient, the small values below indicate that the lift forces on the front conductor are negligible in comparison with the drag forces and the lift forces acting on the downwind conductor.

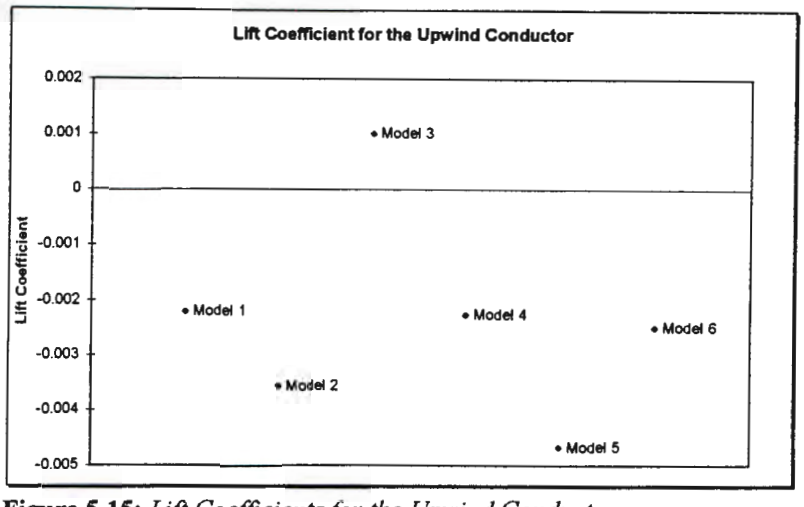

Figure 5.15: *Lift Coefficients for the Upwind Conductor*

ii.) Leeward Conductor

The drag on the downwind conductor is significantly less than on the upwind conductor for the first three models where the two conductors are in line with one another. Even for a spacing of 580 mm, which corresponds to a spacing to diameter ratio of approximately 20, the drag force on the conductor is approximately 40% less than it would be in the free stream.

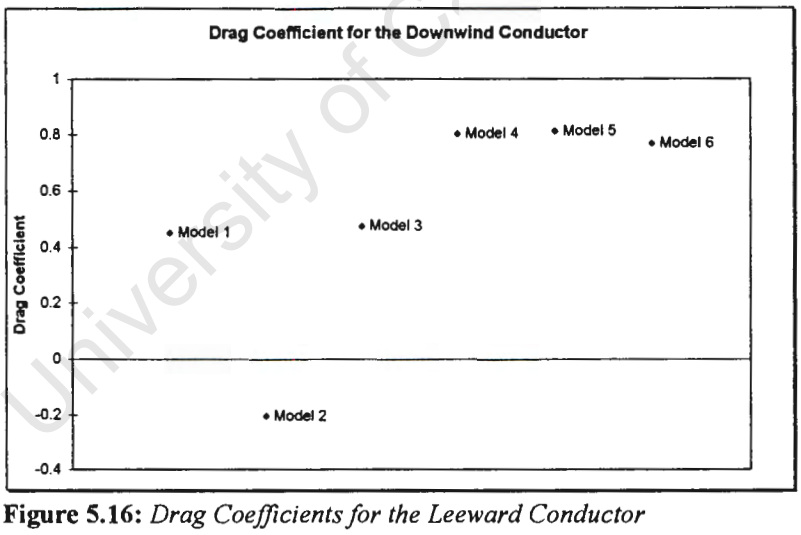

Figure 5.16: *Drag Coefficients for the Leeward Conductor*

As can be seen from the velocity profiles above, the wake behind the conductors is quite narrow. This explains why the drag on the downwind conductor is virtually unaffected by the wake of the upwind conductor for the last three models, which are separated vertically from the front conductor.

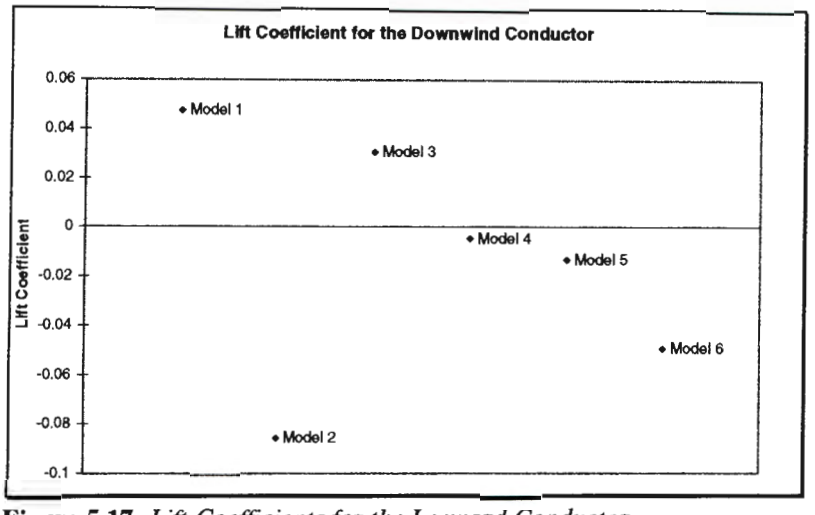

Figure 5.17: *Lift Coefficients for the Leeward Conductor*

It is mentioned above that the higher velocity of the air in the wake of the upwind conductor causes a lift force on the downwind conductor which tends to drag the downwind conductor into the former's wake. The lift coefficients on the downwind conductor, which are calculated as described earlier, are shown in Figure 5.17. What is quite surprising is that the lift coefficient acting on the conductor when it is directly downwind of the first conductor is on average larger than it is when the conductors are separated in the vertical direction.

Figure 5.18, which shows the lift coefficients on the downwind conductor at various stages in the analysis, shows that the dynamic nature of the wake causes a fluctuating lift force to act on the conductor. As mentioned earlier, the real time simulated is only equivalent to about 0.5 seconds, which is not sufficient to get a real idea of the dynamic nature of the lift force. Before any definite conclusions are made about the nature of the lift force from simulations such as these, the simulations should be run for a longer period of time to see how the flow develops, and to study the nature of the lift force in more detail.

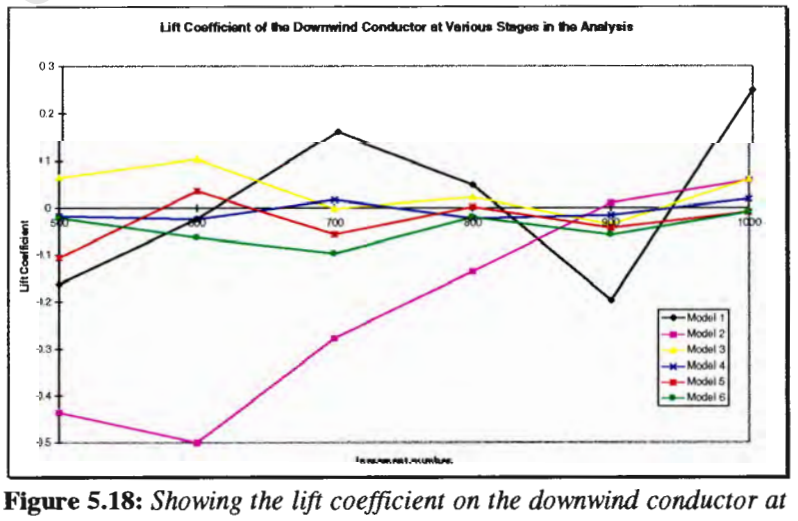

Figure 5.18: *Showing the lift coefficient on the downwind conductor at various stages during the latter half of the simulations.*

5.6 THE FINITE ELEMENT MODEL FOR THE SIMULATION OF WAKE-INDUCED VIBRATION

The details of the finite element model used in the simulation of wake-induced vibration are as described below.

5.6.1 Details of the Simulations

The number of factors which can be varied in a span and which would be expected to have an effect, to a greater or lesser degree, on the onset and severity of vibration, are numerous and include variables such as the sub-conductor separation, bundle tilt, conductor tension and sub-span length. The type and design of the spacers would also be expected to have a considerable effect on the wake-induced vibration of the conductors, depending on the spacer's damping capabilities and stiffness characteristics.

Unless stated otherwise, where relevant, the details of the models as given in Table 5.4 apply to all the models of the span subjected to wake-induced vibration. The implicit integration option is used in all the simulations.

The wake-induced excitation is applied only to the middle sub-span, and all the degrees of freedom are restricted at either end of the span. The steps in applying the wake-induced vibration are similar to those used for the aeolian vibration, with the wake-induced loading being applied in the last step as opposed to aeolian vibration.

Conductor tension:	20 kN
Bundle Type:	Twin, with ACSR *Zebra* sub-conductors
Span Length:	400 m
Sub-Conductor separation:	380 mm
Bundle Tilt:	0°
Number of sub-spans:	9
Length of sub-spans [m]:	48, 48, 44, 40, **40***, 40, 44, 48, 48
Wind Velocity:	10 m/s
Time Simulated:	1000 seconds

Table 5.4: *Details of the Wake-induced Vibration Simulations*

5.6.2 Modelling the Conductor

The conductor is modelled using linear beam elements. Twenty elements are used to model the centre sub-span to which loading is applied. A possible alternative to using beam elements to model the other sub-spans and maybe reducing the CPU time is to model the stiffness and mass of the conductors using spring elements and point masses respectively. Due to the lack of any rotational stiffness at the nodes of the springs, however, rotational rigid body motion is experienced at the junction between the spring elements and the beam elements of the centre sub-spans, which leads to convergence difficulties. The remainder of the sub-spans are thus also modelled by beam elements.

* Centre sub-span to which wake-induced excitation is applied

5.6.3 Modelling the Spacers

Different types and combinations of elements are used to model the spacers:

i.) Spring Elements

Spring elements are used to link the two sub-conductors between sub-spans. The spring stiffness is equivalent to that of an aluminium rod of circular cross-section and with a diameter of 20 mm. The rotation at the ends is unrestricted, thus the rotation of one sub-conductor with respect to the other is unrestricted when using these elements

ii.) Beam Elements

Here the spacers are modelled as linear beam elements, with a circular cross-section of 20mm in diameter, and the material properties of aluminium. The rotation at the junction between a spacer and the conductors is restricted, corresponding to a rigidly clamped joint.

iii.) Spring Elements used in Conjunction with Flexible Joint Elements

Spring elements are once again used to model the spacer, however internal stiffness is provided at the joint between the spacer and conductor nodes by means of flexible joint elements. These elements are used to model joints such as the rubber bushings in car suspension systems and are thus ideal to model the rubber joints used in some currently available spacers. The degrees of freedom of the nodes connected by the joint elements are coupled by means of linear and rotational springs, and optionally dashpots, to provide stiffness and damping respectively for any relative displacement or rotation between the nodes (Hibbitt Karlsson & Sorensen Inc., 1994b).

The values used for the stiffness of the joints are based on data given in an information catalogue for spacers by Karl Pfisterer, a manufacturer of spacer dampers (spacers with internal damping provided by rubber bushing joints). The linear and rotational bending stiffness are estimated from the catalogue as being 5000 N/m and 100 Nm/rad respectively.

Different values for the internal damping of the joints are used and compared, as shown later.

5.6.4 Lift and Drag Forces

The values for the drag and lift coefficients obtained from the fluid flow simulations are used in conjunction with data from the EPRI handbook (Doocey et al, 1979). The drag coefficients obtained from the fluid flow simulations correspond fairly well with those given in the handbook. The main difference, is that the drag coefficients predicted by the simulations are in general approximately 30% less than those given in the handbook. This is probably due to the data given by Doocey et al being valid for a smaller Reynolds number. No mention is made in the handbook for which Reynolds number the data is valid or given.

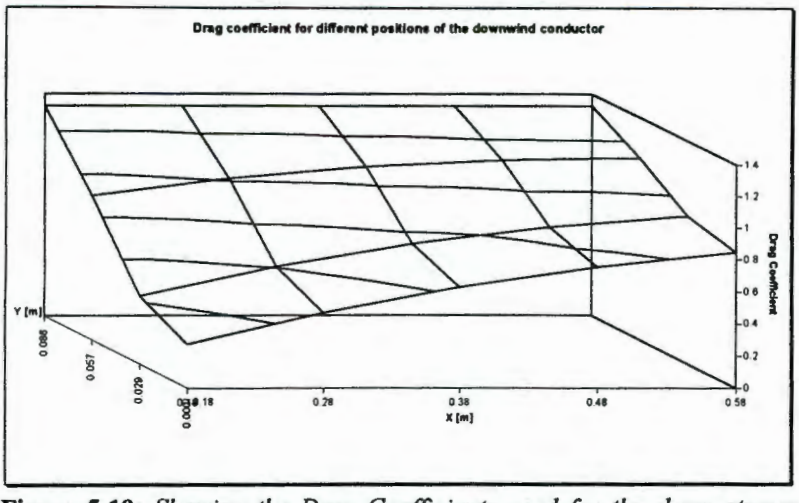

Figure 5.19: *Showing the Drag Coefficients used for the down stream conductor for various positions relative to the upstream conductor*

The values for the drag and lift coefficients given by Doocey et al are thus reduced by 30%. This adjusted data is used as the data-base in the wake-induced loading subroutine. Figure 5.19 and Figure 5.20 show the drag and lift coefficients respectively which are used in the finite element simulations.

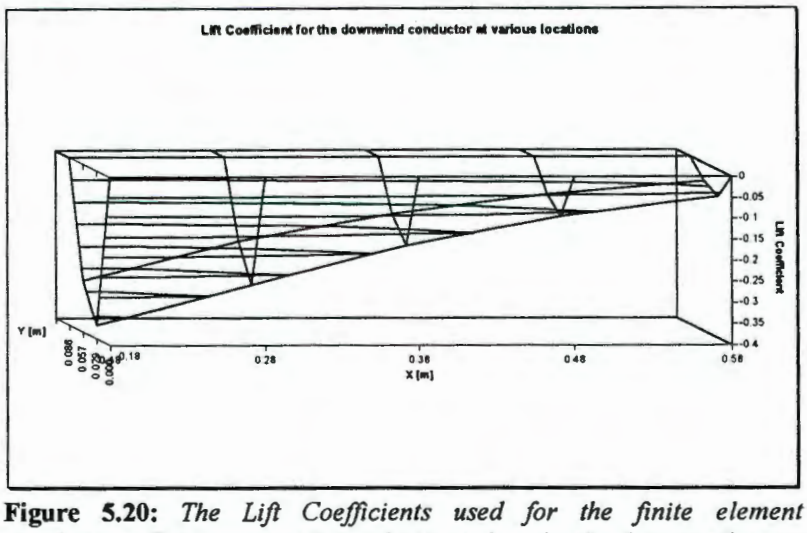

Figure 5.20: *The Lift Coefficients used for the finite element simulations. For negative values of y, the values for the drag coefficients change sign.*

5.7 RESULTS OF THE WAKE-INDUCED VIBRATION SIMULATIONS

The results of the finite element simulations of wake-induced vibration are presented below, and apart from a discussion of typical results obtained, the response of the conductors is also compared for different spacer types, conductor separations, bundle tilt and sub-span lengths.

5.7.1 Typical Response due to Wake-Induced Loading

Figure 5.21 and Figure 5.22 show the vertical and horizontal displacements of the two conductors in the bundle during a typical analysis. The graphs trace the displacement of the centre node in the middle of the excited sub-span with time. What is evident from these results is the beats in the response, which indicate that multiple modes of vibration are activated by the loading.

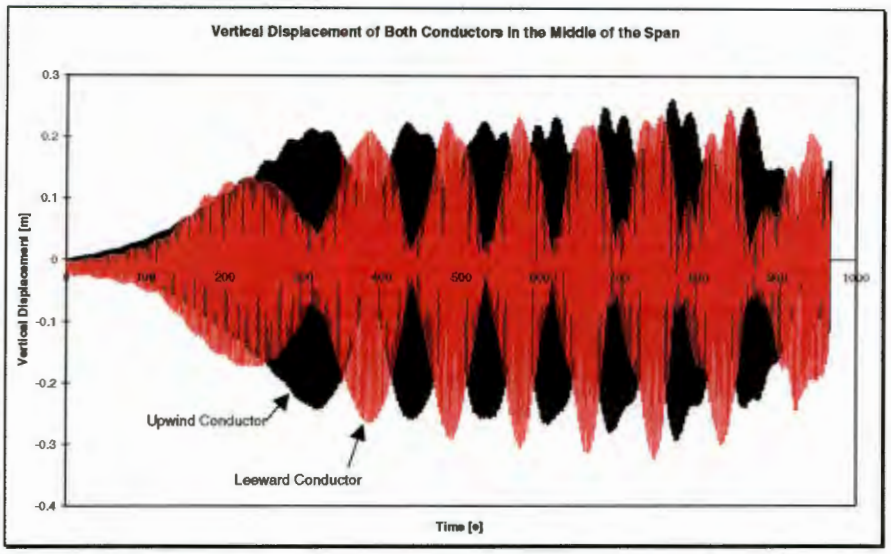

Figure 5.21: *The vertical displacement of both conductors in the middle of the excited sub-span.*

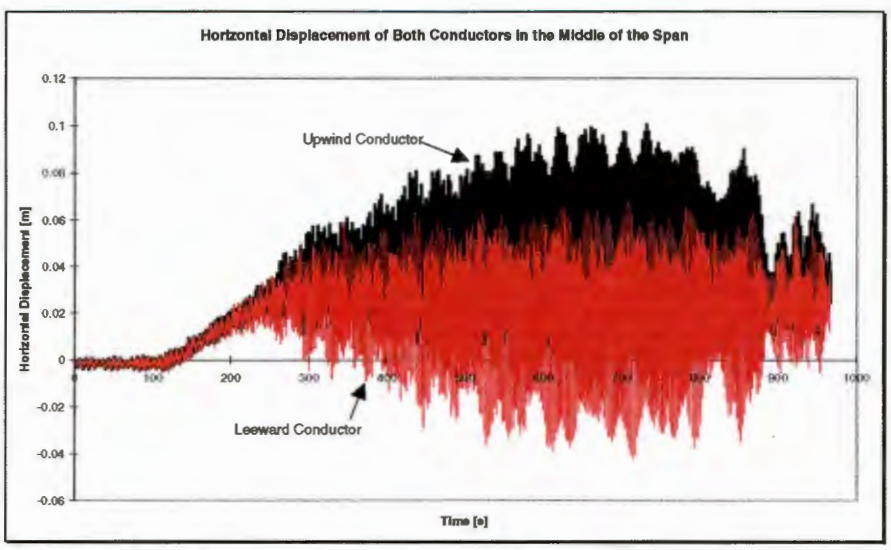

Figure 5.22: *The horizontal displacement of both conductors in the middle of the excited sub-span.*

A very important observation that is made, is that the time taken from the start of the wake-induced loading until any significant vibration occurs is quite substantial. More than a minute of loading is required before the vertical vibration amplitude grows notably, while about four minutes are required before the horizontal vibration becomes substantial. The time required for the

vibration to become noticeable under specific wind conditions would explain why wake-induced vibration is not a very frequently encountered phenomenon (Doocey et al, 1979). The wind speed must remain constant for a relatively long period of time before the onset of significant vibration. It would be interesting to study the effect of a slight or sudden change in the wind conditions on the response of the conductor, to see to what extent the vibration is arrested by the change in the wind speed.

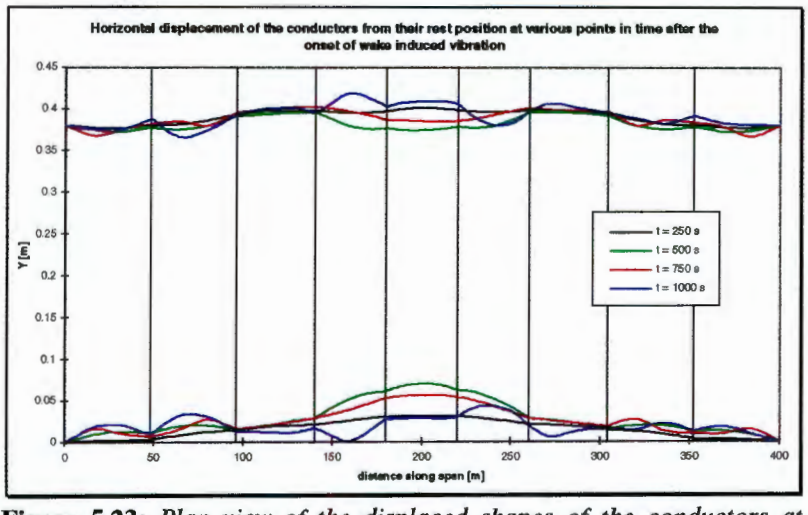

Figure 5.23: *Plan view of the displaced shapes of the conductors at various times. The vertical black lines show the locations of the spacers.*

Figure 5.23 and Figure 5.24 show the horizontal and vertical displacement respectively of the conductors in the span at various times in the analysis. The vertical black lines indicate the locations of the spacers, which in this case are modelled simply as springs. The displacement profiles would suggest that multiple modes of vibration of the span are activated. The rolling mode seems to be dominant however, with sub-span oscillation also being noticeable.

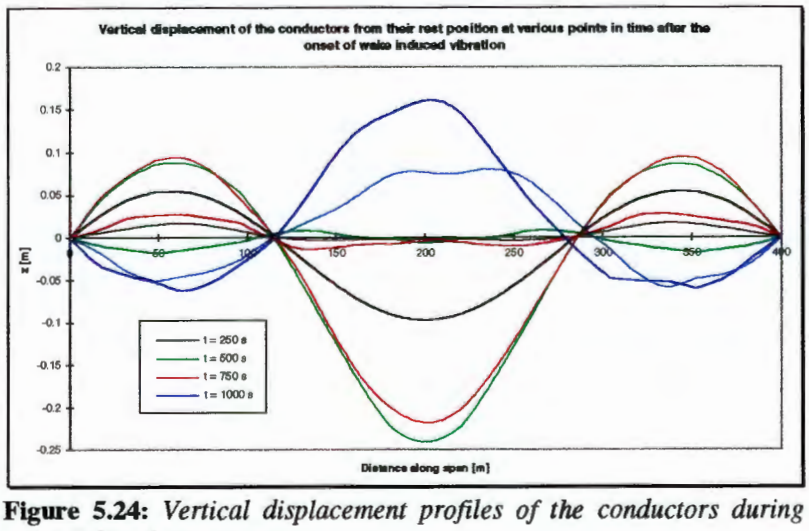

Figure 5.24: *Vertical displacement profiles of the conductors during wake-induced vibration.*

The position in space of the conductors in the middle of the sub-span with time, as seen in cross-section of the bundle, is shown in the figure below. A trace such as this is not very useful in determining the severity of vibration within the sub-span, and gives no indication of the vibration of the conductors relative to one another or with respect to the spacers. The main aim of simulations such as these is to determine the severity of vibration within the sub-span as this is the main source of damage to spacers and the conductors in the far-field of the span. The vibration data is thus presented in a slightly different form, which gives a better indication of the vibration characteristics within the sub-span.

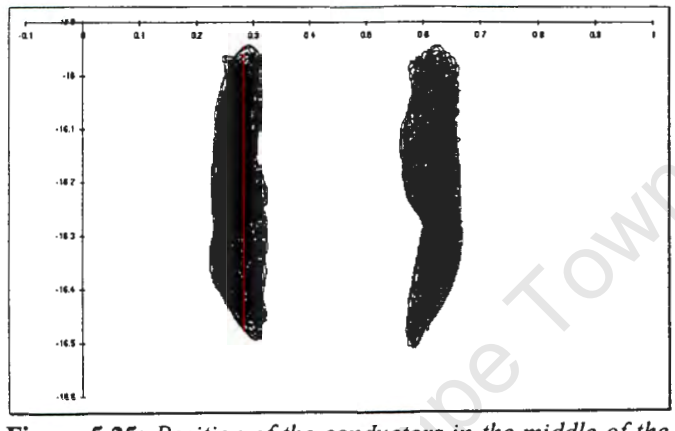

Figure 5.25: *Position of the conductors in the middle of the span as seen in cross-section of the bundle. All dimensions are in metres.*

Figure 5.26 shows the positions of the conductors relative to the centre of mass of the two conductors. It is quite evident from this data that the rolling mode is dominant, with a small amount of sub-span oscillation present.

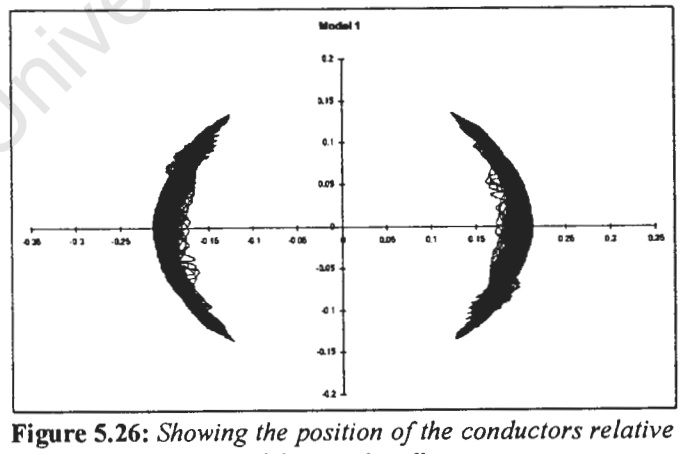

Figure 5.26: *Showing the position of the conductors relative to the centre of mass of the twin bundle.*

To determine the severity of the vibration with respect to the ends of the sub-span, the quantities X and Y are plotted against one another in Figure 5.27. X and Y are calculated using the following two equations:

$$X = \left(x_{2,c} - x_{1,c}\right) - \left(x_{2,s} - x_{1,s}\right) \quad (5.6)$$

$$Y = \left(y_{2,c} - y_{1,c}\right) - \left(y_{2,s} - y_{1,s}\right) \quad (5.7)$$

where $x_{1,c}$ is the x displacement of the upwind conductor, $x_{2,c}$ of the downwind conductor, and, $x_{1,s}$ and $x_{2,s}$ being the displacements of the corresponding conductors at the spacer. The same notations apply for the y values.

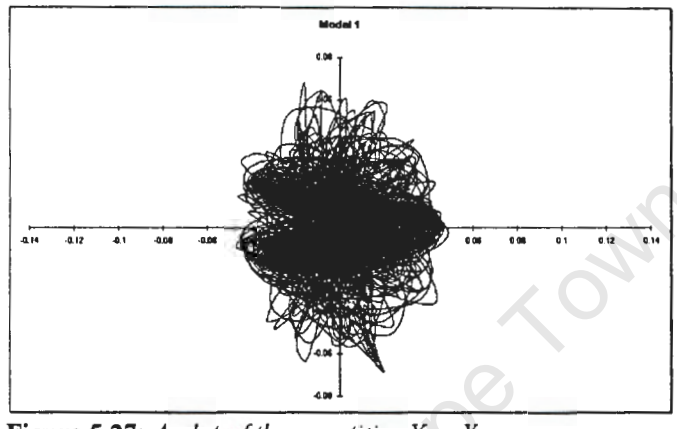

Figure 5.27: *A plot of the quantities X vs Y.*

The data of such a plot essentially gives an indication of the severity of vibration within the sub-span, as it subtracts the displacement in space of the ends of the sub-span from the displacement of the conductors in the centre of the span.

In comparing the results of different simulations below, the displacement of the conductors about the centre of mass of the bundle is used.

5.7.2 Type of Spacer

The results of Figure 5.28 below show the wake-induced vibration for the different spacer models described above. In the case of the spring with flexible joints at the ends, no damping is included in the joint.

In the first case, where the spacer is modelled simply as a spring, the rolling mode of the bundle is fairly unrestricted. Even though the breathing or sub-span mode is evident in the spring and beam models, there is clearly no danger of any clashing of the sub-conductors in the bundle. As mentioned by Doocey et al, the clashing of conductors during sub-span oscillations can lead to damage to the conductors, depending obviously on the severity of the clashing, and the frequency at which it occurs. From the vibration history of the spring with flexible joints, it is quite evident that the breathing mode in the horizontal direction is minimal.

It is quite evident from these results that the type of spacers used has a significant effect on the wake-induced vibration response of the bundle.

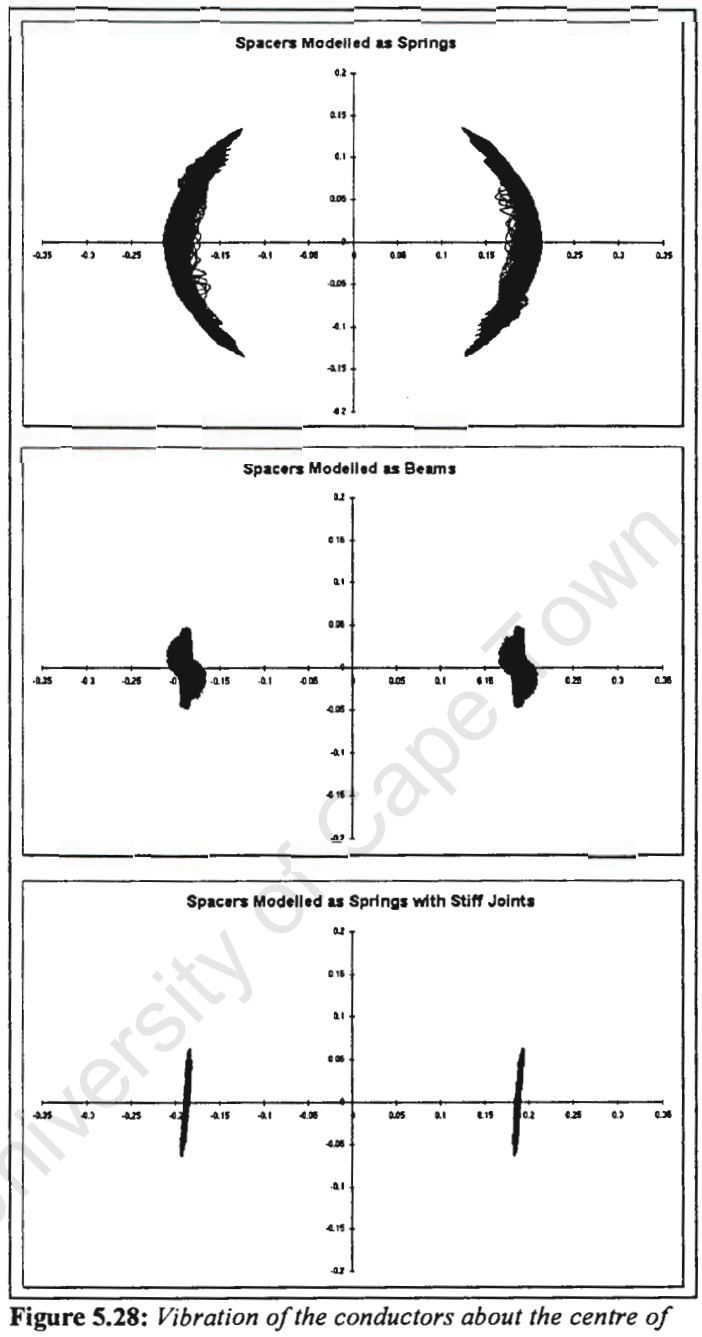

Figure 5.28: *Vibration of the conductors about the centre of mass of the bundle for different spacer types.*

5.7.3 Damping in the Flexible Joints at the Ends of the Spacers

Figure 5.29 compares the vibration characteristics for different amounts of damping in the flexible joints of the spacers. The damping material is assumed to be isotropic, thus all damping coefficients for the translational degrees of freedom are the same, and the damping is identical for all rotational degrees of freedom.

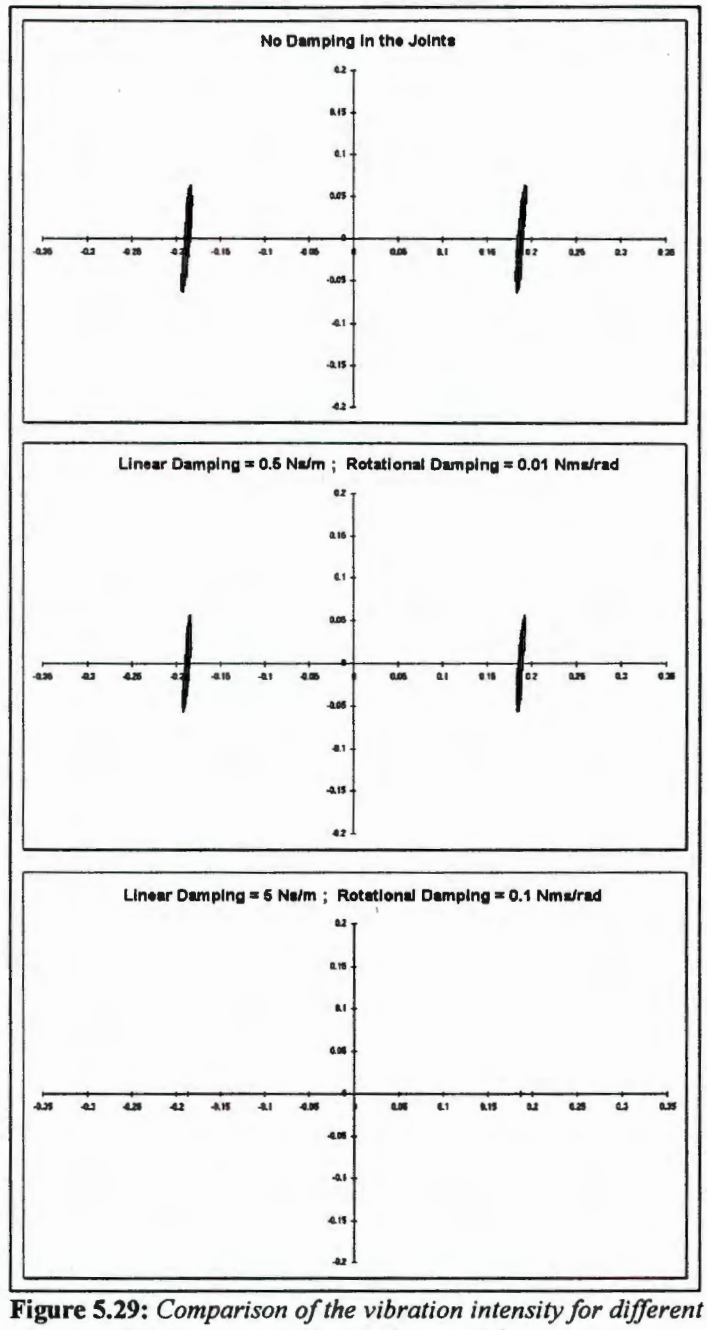

Figure 5.29: *Comparison of the vibration intensity for different amounts of damping in the flexible joints of the spacers.*

The damping coefficients are defined as follows for the translation and rotation degrees of freedom respectively(Hibbitt Karlsson & Sorensen Inc., 1994b):

$$\text{translation:} \quad C_x = \frac{F_{damp}}{\dot{x}} \qquad (5.8)$$

$$\text{rotation:} \quad C_\theta = \frac{\tau_{damp}}{\dot{\theta}} \qquad (5.9)$$

where F_{damp} and τ_{damp} are the damping force and torque respectively, and $\dot{x}$ and $\dot{\theta}$ are the velocities of the respective degrees of freedom.

Even though the results aren't shown above, damping ratios of $C_x = 0.05$ Ns/m and $C_\theta = 0.001$ Nms/rad yield the same results as those with no damping in the joints. Increasing the damping by a factor of 10 reduces the vibration intensity slightly, while an increase of 100, so that $C_x = 5$ Ns/m and $C_\theta = 0.1$ Nms/rad, virtually eliminates all vibration in the span, as can be seen from the results above.

5.7.4 Conductor Separation

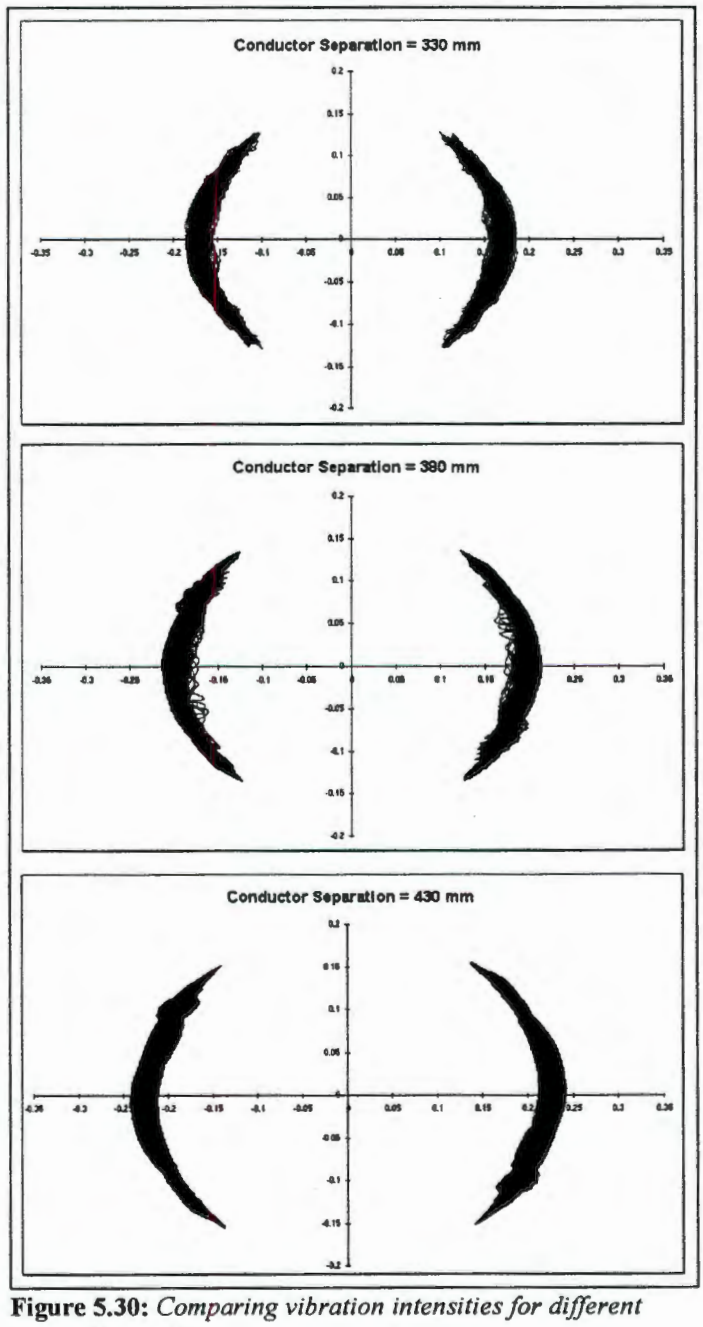

Figure 5.30: *Comparing vibration intensities for different conductor spacings.*

The effect of varying the distance between the conductors in the bundle is shown in the results above.

These results do not show any evidence of any significant effect of the conductor spacing on the intensity of vibration. A more detailed study should however be performed in cases where more severe vibration is obtained such as with a longer sub-span. As shown below, the vibration intensity increases significantly with a longer sub-span, and as such the effects of bundle separation would be expected to be more pronounced for a longer sub-span.

5.7.5 Bundle Tilt

Figure 5.31 shows the vibration characteristics with different amounts of bundle tilt.

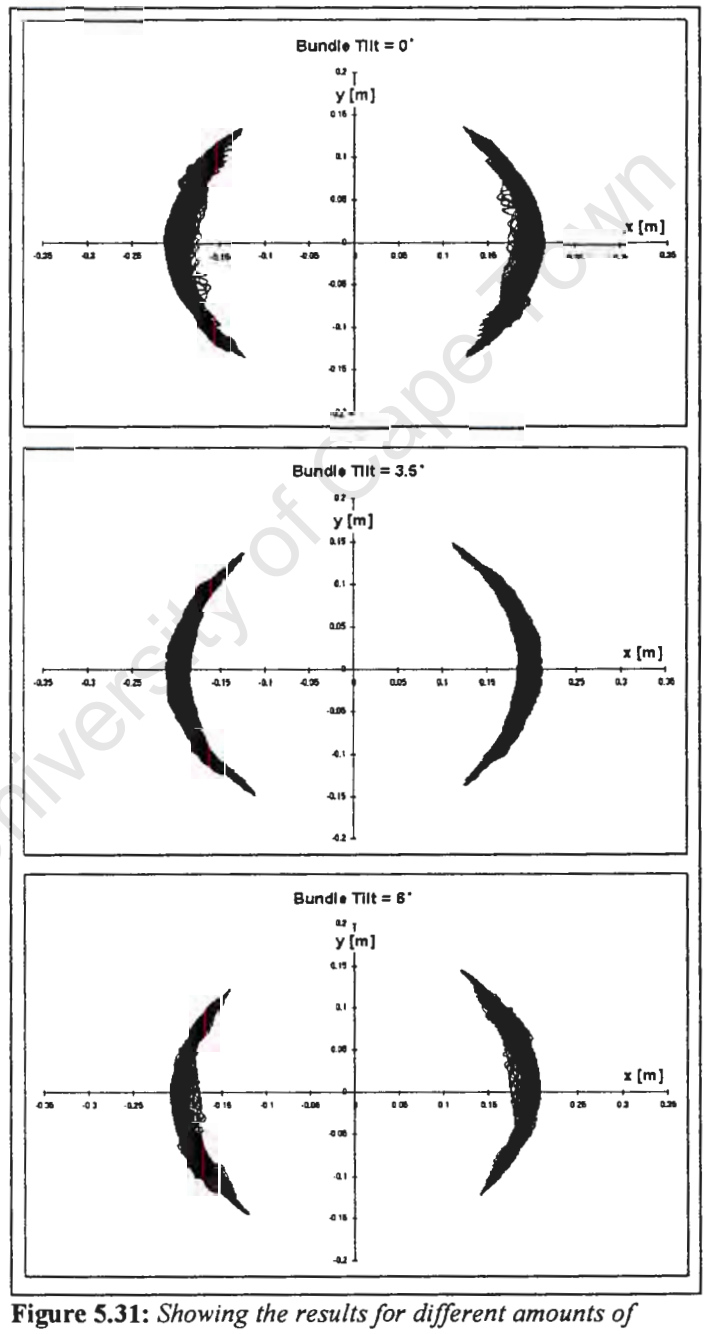

Figure 5.31: *Showing the results for different amounts of bundle tilt.*

Apart from the tilt of the plots which would be expected, no obvious difference exists in these results. The same comments made with respect to a longer sub-span in the previous paragraph apply here though. A more detailed study in which factors such as the sub-span length are varied should thus be performed to obtain a better understanding of the effects of the tilt of the bundle on the intensity of vibration.

5.7.6 Sub-span Length

As mentioned above, the effect of the length of the sub-span on which the wake-induced loading is applied has a significant effect on the severity and type of vibration. Figure 5.32 compares the vibration for a sub-span 40m long to one of 80m in length. For the latter model the lengths of the seven sub-spans are 48, 48, 64, 80, 64, 48 and 48 m respectively. The excitation is again applied only to the centre sub-span.

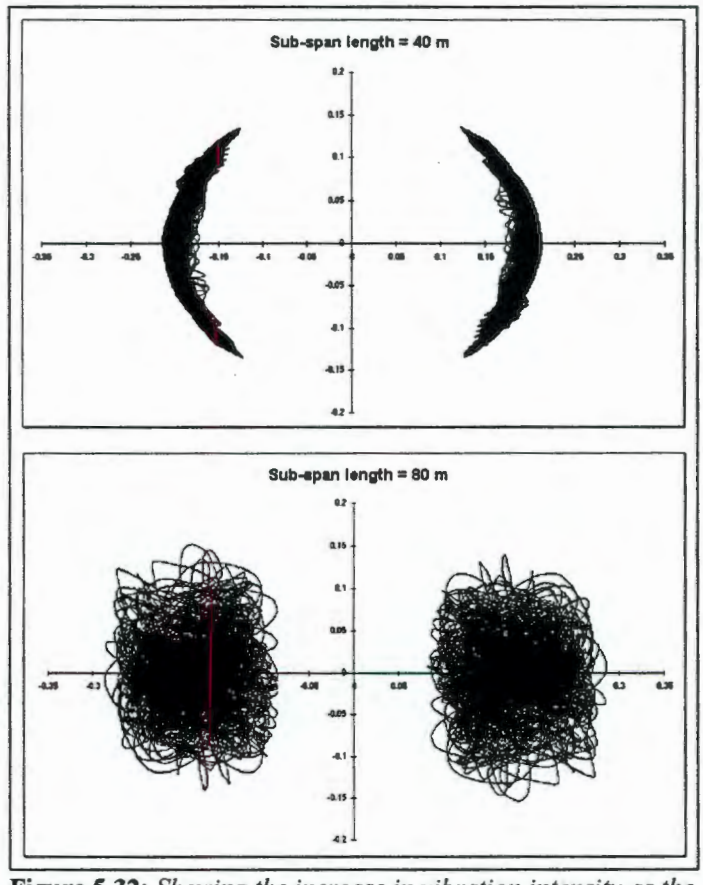

Figure 5.32: *Showing the increase in vibration intensity as the sub-span length is increased from 40 to 80 metres.*

The vibration would be expected to be more intense for a longer sub-span for two main reasons. The first of these is that a longer section of the conductor bundle is subjected to the wake-induced loading, while the second is the increased flexibility as the distance between support points, or between spacers increases.

The most significant observation made from these results is that for the longer sub-span, the rolling mode is no longer dominant, and the sub-span oscillations

are considerably more intense. The danger of clashing between the conductors is also increased substantially, and it could be expected to increase even more with only a slight further increase in the sub-span length.

6. SHORT-CIRCUIT INDUCED CONDUCTOR MOTION

When a short-circuit occurs somewhere along a transmission line, the large currents in the conductors give rise to electromagnetic forces, causing motion of the conductors and conductor bundles. The resultant motion could result in severe damage to conductors and other hardware, as the tensile forces in the conductors, the compressive forces in the spacers, and the reaction loads imposed on the suspension hardware could reach damaging proportions during a short-circuit.

In this chapter, the modelling of the motion of a conductor bundle during a short-circuit fault is described. A short literature review of work which is relevant to short-circuit induced conductor motion is followed by a discussion of typical causes of short-circuits on a transmission line and the dynamic response of the conductors which may be expected during a short-circuit. A discussion of the electromagnetic forces which arise due to the large short-circuit currents in the conductors, together with a description of the loading subroutine written to simulate the loads, constitute the next section. Next, the specific details of the finite element model are presented, and these are followed by a description of the problem used to verify the model. The results of the verification problem are compared with experimental data obtained from literature.

In the last section, the results obtained from a number of different simulations are presented and discussed.

6.1 LITERATURE REVIEW

Work concerned with the behaviour of conductors during the event of a short-circuit has been done by a number of people. In 1987 a document was published by Cigrè which describes analytical methods of estimating the mechanical effects of short-circuit currents (Cigrè Study Committee 23 - Working Group 02, 1987). It also describes how more advanced methods, such as finite element methods could be used to simulate short-circuit effects. An earlier paper by Manuzio (1965) deals with the forces experienced by spacers during short-circuits. She presents analytical methods of estimating the maximum compressive forces experienced by a spacer during a short-circuit, and presents results obtained from experiments conducted on a test rig.

Experimental results obtained by Atwood et.al (1962) have also been published. Apart from the experimental data, they also present an analytical method of determining the peak tension in a conductor during bundle pinch (a consequence of short-circuits which described in more detail later on) of a twin bundle. The peak loads on the spacers can then be determined from the conductor tensions by considering the geometry of the system. The method is known as the *Static Balance Method* (Cigrè Study Committee 23 - Working Group 02, 1987), and involves an iterative solution procedure. The tension in the conductor required by the increase in length of the conductor as it assumes the displaced profile during a short-circuit, and the tension required by a balance of the forces on the system, are equated using this iterative procedure. The displacement profile of the conductor in the direct vicinity

of the spacer, and not in contact with the other conductor, is assumed to be parabolic.

In a more recent paper by Graig and Ford (1980), a method is presented whereby a balance of the energy in the system is used to calculate the peak forces. The work done by the electromagnetic forces is equated to the strain energy in the conductor and the kinetic and potential energies of the support structures at the moment at which the peak loads occur. An iterative procedure is again employed to solve these equations. The attractive feature of this relatively simple method, known as the *Energy Balance Method*, is that it takes not only the number of sub-spans into account, but also the response of the support structures.

Lilien and Dal Maso (1990) carried out numerical simulations of short-circuit effects, and their results compare favourably with the experimental results obtained by them. They simulated both the effects of adjacent phases on one another, and the effects of bundle pinch. In a paper published by Herrmann et al (1989) a method of analysing the mechanical effects of the swinging of the conductor of a particular phase, caused by the short-circuit induced electromagnetic forces between phases, is presented. It takes into consideration the effects of the insulator strings on the behaviour of the system.

In a paper presented at an ABAQUS user's conference, Miri and Sihler (1993) describe their analysis procedures employed in modelling the dynamic response of flexible droppers in a sub-station. Their results obtained for the stress at the insulator-conductor interface agree quite favourably with their measured values.

6.2 THE EFFECTS OF A SHORT-CIRCUIT ON A TRANSMISSION LINE

Before the load on a conductor due to a short-circuit can be implemented in the finite element model, sufficient knowledge of the phenomenon must be available. This section describes possible causes of a short-circuit on a transmission line, followed by a description of the motion introduced into the system by the electromagnetic forces which act on the conductors during a short-circuit.

6.2.1 Causes of Short-Circuits on a Transmission Line

A short-circuit is defined in the IEC publication 909, as "*The accidental or intentional connection, by a relatively low resistance or impedance, of two or more points in a circuit which are nominally at different voltages.*" (IEC Publication 909, 1988). In terms of a three phase transmission line, the points which are at different voltages relative to one another at any point in time are conductors in adjacent phases or a phase and the ground. Thus a short-circuit would occur if any of the phases were electrically connected to one another or to the ground.

Short-circuit currents on a high voltage transmission line could be the result of, amongst others, one of the following faults.

- *Pollution of insulators:* Over a number of years, a coating of dust or other matter builds up on the individual ceramic discs of an insulator string. (See Figure 6.1 below.) This commonly occurs in industrial areas, where pollution in the air is deposited on the insulators, and along coastal regions where salt build-up on the insulators occurs. If sufficient quantities of foreign material are deposited on the insulator, a path for the electric current between the ends of the insulator string is provided and a flash-over occurs. The current is thus free to flow via the polluted insulator, to the steel tower and to ground, providing a path for large short-circuit currents.

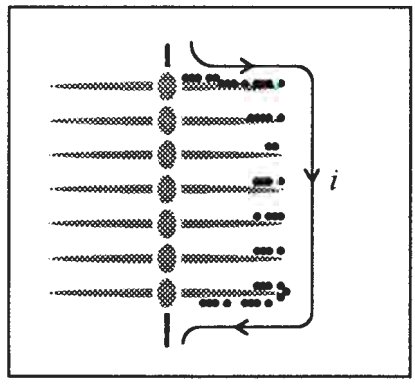

Figure 6.1: *Sketch of a section of a typical insulator string showing a possible path for a short-circuit current provided by pollution (represented as dark spots) on the insulator disks.*

- *The minimum clearance between a conductor and grounded object is violated:* This might occur when a long object on the back of a vehicle, or a branch of a tree comes close to a live conductor.

- *Broken conductors:* When the free end of a broken conductor comes into contact with the ground, a free path for large fault currents is created.

- *Short-circuit between phases:* This would occur if an object had to span two different phases. In the case of a multi-phase transmission line where the phases are located above and below one another, a conductor in one of the upper phases breaking could come into contact with another conductor located below it.

In each of these cases, the mechanical effects of a short-circuit will not only be evident at the exact location of the short-circuit, but also on adjacent spans where an increase in the current will occur. Due to the low resistance of conductors, the large short-circuit currents will occur along a considerable length of the transmission line.

6.2.2 Conductor Motion Resulting From Short-Circuits

For the purposes of long transmission lines, two types of motion govern the behaviour of the conductor during a short-circuit. The first, which applies to one or more of the three phases as a whole, is known as the swing-out effect, and the second which applies to the individual conductors in a conductor bundle, is known as bundle pinch (Cigrè Study Committee 23 - Working Group 02, 1987).

i.) Swing Out Effects

The swing out effect is the resultant motion of a whole phase of the conductor, due to the electromagnetic forces experienced between it and either one or both of the other two phases. A phase could consist of a single conductor or a bundle of conductors, and in the latter case, the bundle may be thought of as a single unit when considering swing out effects.

The forces induced by this type of motion, are an increase in the tension of the conductors, and additional forces in the insulator and suspension hardware. The effects of these forces will be more severe on a short span, of the dimensions encountered in sub-stations, than on longer spans encountered on a typical transmission line. If, for example, the electromagnetic forces between two phases, each consisting of a conductor bundle, cause the two phases to swing together, the increase in the tension in each bundle will be significantly larger for say, a 20 meter span, than it would be for a 400 meter span. As the main aim of this section of the project is to model the effects of short-circuits on the span lengths typically encountered on a transmission line, the stresses introduced as a result of the swing out effects are assumed negligible (Cigrè Study Committee 23 - Working Group 02, 1987) in comparison to those which result from bundle pinch effects described below.

ii.) Bundle Pinch

This occurs only in bundled conductors. For a particular phase, the short-circuit current is shared by the individual conductors in the conductor bundle. The current in each conductor will thus be of the same magnitude and in the same direction as for all the other conductors in the bundle, and as shown by equation 6.1, an attractive force is experienced by two parallel conductors, if the current flows in the same direction. The individual conductors are thus drawn towards one another and may impact with considerable force.

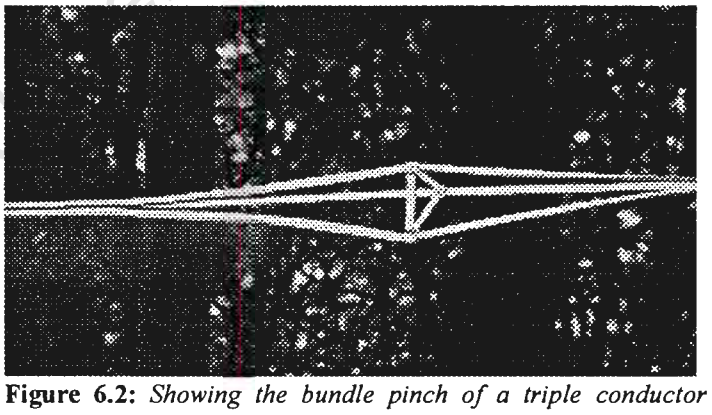

Figure 6.2: *Showing the bundle pinch of a triple conductor bundle. The spacer is also visible. (Möcks, 1972. With Permission of Richard Bergner GmbH + Co.)*

After impact, the conductors usually stay pinched together for the duration of the short-circuit, as shown in Figure 6.2. This results, not only in a significant increase in the tension of the conductors, but also in large compressive forces on the spacer dampers, which connect the conductors in a bundle to one another (see Figure 6.2). The individual strands of the conductor are also likely to be severely

and permanently damaged as they clash, as shown in Figure 6.3, which shows the resultant damage on the conductor of a triple bundle after the occurrence of bundle pinch.

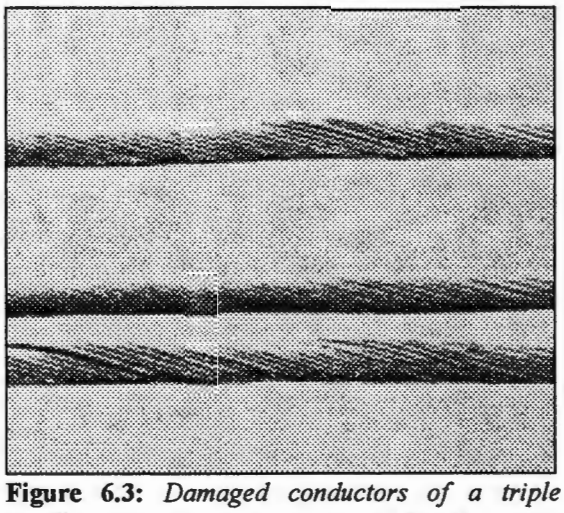

Figure 6.3: *Damaged conductors of a triple bundle after the occurrence of bundle pinch (Möcks, 1972. With permission of Richard Bergner GmbH + Co.)*

As mentioned in the Cigrè Publication (Cigrè Study Committee 23 - Working Group 02, 1987), effects of bundle pinch occur more rapidly than, and are thus virtually independent of, the swing out effects. Bundle pinch effects can thus be analysed separately and independently from the swing-out effects, as is done for this model.

6.3 SIMULATING THE ELECTROMAGNETIC LOADS DUE TO SHORT-CIRCUIT CURRENTS

The equations governing the electromagnetic forces between two current carrying conductors are given below. Next, the equations governing the short-circuit currents in a bundle as a function of time are given. A brief description of the loading subroutine written to implement the loads is then followed by a description of how the loading routine is verified.

6.3.1 The Electromagnetic Force Between Two Current Carrying Wires

When two current carrying wires (*a* and *b*) are parallel, the electromagnetic force experienced by wire *b* is given by the following equation:

$$\vec{F}_{ba} = \frac{\mu_0 L\left(\vec{i}_b \bullet \vec{i}_a\right)}{2\pi\vec{R}} \qquad (6.1)$$

where $\vec{i}_b$ and $\vec{i}_a$ are the current in wires *a* and *b* respectively. The permeability constant, μ_0, has a value of $4\pi \cdot 10^{-7}$ Tm/A, and $\vec{R}$ (see Figure 6.4) is a vector, normal to, and equal in magnitude to the distance between, the two wires (Halliday et al, 1993). The dot product indicates that the force will be attractive when the

current flow is in the same direction in the two wires, and repulsive if in the opposite direction.

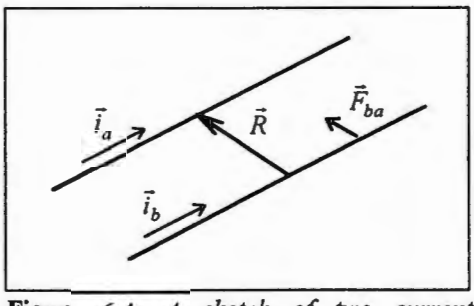

Figure 6.4: *A sketch of two current carrying wires, showing the notation adopted in equation 6.1*

If the wire axes lie along the x-axis, the vector $\vec{R}$ can be written as

$$\vec{R} = R_y\hat{j} + R_z\hat{k} \qquad (6.2)$$

The force $\vec{F}_{ba}$ can then be written in terms of its y- and z-components as

$$\vec{F}_{ba} = F_y\hat{j} + F_z\hat{k} \qquad (6.3)$$

with

$$F_y = \frac{R_y}{|\vec{R}|}\cdot\vec{F}_{ba} \quad \text{and} \quad F_z = \frac{R_z}{|\vec{R}|}\cdot\vec{F}_{ba} \qquad (6.4\text{ a, b})$$

These electromagnetic loads are implemented in the finite element program, as distributed loads per unit length in the y and z directions respectively, by means of the user-defined subroutine which is described later.

6.3.2 Short-Circuit Current in the Conductor of a Transmission Line

The short-circuit current in a phase of a transmission line, far from any generators, is given by the following equation (Cigrè Study Committee 23 - Working Group 02, 1987; IEC Publication 909, 1988):

$$i(t) = \sqrt{2}i_k^*\left[\sin(\omega t + \varphi_u - \gamma_z) + \sin(\gamma_z - \varphi_u)e^{-\frac{t}{\tau}}\right] \qquad (6.5)$$

where $i(t)$ is the time dependent current in the bundle, i^*_k is the initial r.m.s. short-circuit current, ω is the alternating current frequency (in rad/s), φ_u is the voltage phase angle related to the instant at which the short-circuit fault occurs, and γ_z is the impedance angle. The time constant, τ, is defined as

$$\tau = \frac{1}{\omega\cdot\left(R/X\right)} \qquad (6.6)$$

with R and X the resistance and reactance of the conductor bundle respectively.

As the quantity $\gamma_z - \varphi_u$ of equation 6.5 depends on the instant in time at which the fault occurs, it is simply chosen so that sin $(\gamma_z - \varphi_u)$ is maximum, both for simplicity, and so that the worst case scenario is modelled.

The current in each conductor of a phase is calculated by dividing *i(t)*, as calculated using the equation above, by the number of sub-conductors in the bundle.

In calculating the current for the finite element simulations, a frequency of 50 Hz (i.e. $\omega = 100\pi$) is used. A value of 0.082 is used for the ratio $^{R}/_{X}$, as calculated by the Eskom Transmission Line Department for the 400 kV Acacia-Muldersvlei line in the Cape.

6.3.3 The Subroutine used to Simulate the Loads During a Short-Circuit

The subroutine is written in FORTRAN 77, and is shown in Appendix D. A number of conventions are adopted in writing the subroutine, according to which the finite element model making use of the subroutine must be structured. These are discussed below, followed by a description of the loading algorithm and its implementation in the subroutine.

i.) Conventions Adopted for the Subroutine

To enable the subroutine to function with any number of conductors in a sub-conductor, certain conventions, adopted in writing the subroutine, must be followed by the user. These are summarised as follows:

- The axis of the conductor bundle, before gravity is applied, is parallel to the x-axis
- The conductors are numbered so that, when viewing the conductor bundle in cross-section, from the origin along the positive x-axis, conductor 1 is at 3 o'clock. The remaining conductors are then numbered in a counter-clockwise sequence. (Figure 6.5)

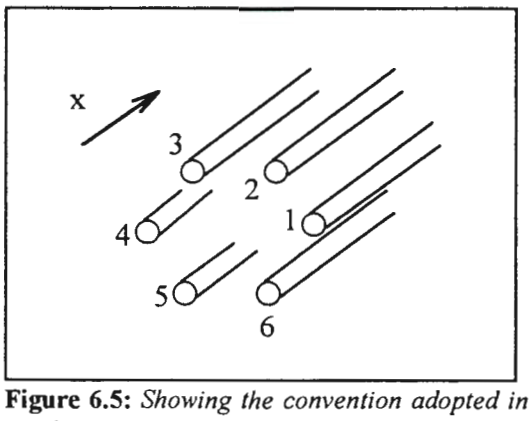

Figure 6.5: *Showing the convention adopted in numbering the sub-conductors of a conductor bundle.*

- The elements of conductor 1 are numbered from 1 to 10 000, those of conductor 2 from 10 001 to 20 000, those of conductor 3 from 20 001 to 30 000, etc.

The user is also required to specify, in the beginning of the code of the subroutine, values for the following variables:

numel: - total number of elements in the model, subjected to short-circuit loads.
numint: - maximum number of integration points in any of the elements in the model.
cond: - number of conductors in the bundle
nelcon: - number of elements per conductor
frq: - frequency (in Hz) of A/C current
istar: - initial r.m.s. short-circuit current, i^*_k
Tau: - exponential decay constant, τ

ii.) A Description of the Loading Algorithm

The process can be described with the help of the flowchart in Figure 6.6 as follows:

The first step in the algorithm is to assign an internal element number, based on the ABAQUS number of the element, the number of conductors in the model, and the number of elements in each conductor, to the element. Due to the convention adopted in the numbering of elements, this is necessary to keep the amount of storage space to a minimum and to make the subroutine as efficient as possible. It is for this reason that the user must specify the values listed above, for the specific problem in hand.

The force per unit length on a specific element is calculated according to the current in the conductors at time t, and the distance of the integration point in relation to the corresponding integration points in the other conductors in the bundle.

The requested load component (F_y or F_z) is then calculated by adding the contribution from all the conductors in the bundle, and this value is then sent back to ABAQUS. As ABAQUS only sends through the current co-ordinates of the integration point for which the load is requested, a common block is used in the subroutine to store the previous co-ordinates of all the integration points. At a time step t_i, the load is calculated using the co-ordinates of the relevant points in the previous time increment t_{i-1}. The error introduced by this assumption is negligible, as the size of the time steps is sufficiently small so that the displacement for subsequent time increments does not change significantly.

The subroutine also does a number of checks, such as whether the amount of space assigned is sufficient to accommodate all the elements in the model, and in the case of a fault being detected, it issues an error message and terminates the analysis.

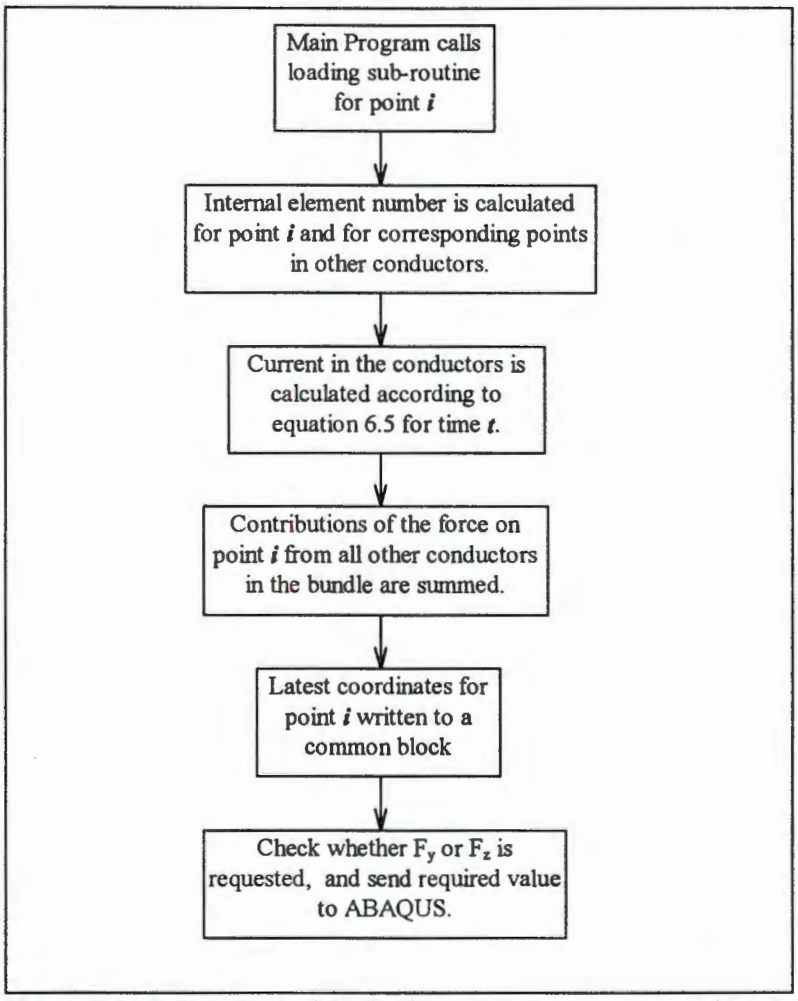

Figure 6.6: *A flow chart of the loading procedure implemented in the loading subroutine.*

6.3.4 Verification of the Loading Subroutine

To verify the problem, a test model consisting of two conductors was set up. The load calculated by the subroutine was then written to a file, along with the time, co-ordinates of the point, and the co-ordinates of the corresponding point on the second conductor for each increment. The recorded data of the force was compared with the forces calculated for the positions of the points relative to one another, and found to agree exactly, thus verifying that the equations had been correctly implemented in the user-subroutine.

6.4 Details of the Finite Element Model

In constructing the finite element model to study the bundle pinch effects in a bundled conductor, a number of different factors must be considered in obtaining a desirable model for the simulation of the bundle pinch effects during a short-circuit. Decisions on element types, mesh densities, time incrementation, integration procedures and contact interface modelling options must be made.

The sections that follow describe some of the factors to be considered in making these decisions. The first section discusses whether the modelling of short-circuit induced motion of conductors is essentially a wave-propagation, or a structural dynamic type problem. Spurious noise generated by the contact definition and encountered in a stress wave propagation problem is then discussed, followed by a comparison of the different types of beam elements available, and their effect on the solution. This is followed by a comparison of results for different mesh densities and a note on the damping introduced. The last section, which deals with the bending stiffness assumptions for the conductor in the short-circuit model follows a discussion of the different contact modelling options.

6.4.1 Wave Propagation vs Structural Dynamic problem ?

Many of the decisions made with respect to the details of the finite element model depend on whether one is modelling a wave propagation or structural dynamics problem. Wave propagation problems are those where the loading consists of frequency components which correspond to the higher natural modes of the structure being excited. The loading and response of a structural dynamics problem on the other hand occur at the lower natural frequencies of the system (Cook et al, 1989; Bathe, 1982; Belytschko, 1983).

Even though most problems can be defined as being either a wave propagation or a structural dynamics one, some problems, such as the one being modelled in this case, may be a combination of both. As mentioned by Belytschko (1983) it often happens that the deformation of the structure is primarily due to the lower frequency components of the load, while peak stresses in a component, such as those which might cause brittle fracture, arise due to propagating waves. For bundle pinch, when considering only the motion of the conductor, the problem could be considered a purely structural dynamic one. However, one of the main aims of the model is to provide the capability of investigating the peak forces in the conductor and the spacers during and immediately after the occurrence of a short-circuit.

At the onset of the short-circuit, the sudden electromagnetic forces on the conductors cause the conductors in a bundle to accelerate towards one another. This results in a reaction wave which is set up at the support points and at the spacers and travels along the length of the conductor. These waves can be assumed to be of sufficient magnitude to have an effect on the maximum loads experienced in the conductor and spacers. The phenomenon of bundle pinch is thus not only a structural dynamic problem, but also a wave propagation one, and as such a viable model for bundle pinch has to consider both these factors.

6.4.2 Noise Generated in the Model

Due to the nature of both a finite element mesh, and the contact modelling between surfaces, noise is generated which would not necessarily be observed in a real continuum (Hibbitt Karlsson & Sorensen Inc., 1994a). The discretized nature of a finite element mesh, which allows loads to be transmitted only at the nodes, results in sporadic stress waves generated when contact occurs in a finite element model which would not be observed in a real continuum. This may result in unrealistic

peak forces being produced when interference occurs between these stress waves, a factor which must be accounted for in the finite element model.

Apart from the noise which may be introduced by the contact between two surfaces in a finite element model, spurious modes are normally encountered in problems involving the propagation of waves (Jiang et al, 1990a & 1990b; Celep et al, 1987; Celep et al, 1983). The contribution of various factors to these spurious modes must also be considered when making decisions on the finite element model. To show the effect that an increase in the number of nodes, and therefore the number of contact points, in a small section of the model can have on the results, a small test simulation is carried out as follows:

The two conductors of a 10m sub-span, which are initially parallel, are subjected to a constant distributed load of 2kN/m so that they accelerate towards one another and subsequently clash. For case A, the element length along the span is uniform at 600 mm. For case B the middle 1.2 m section of the sub-span is modelled using 6 instead of 2 elements, while the remainder of the span is unchanged. As can be seen from the graph below (Figure 6.7), the maximum force in the spacer for case B is considerably more than for case A. This increase for case B is not only due to the fact that there are more nodes in the model at which contact occurs, but also due to spurious modes introduced by the change in adjacent element lengths, a phenomenon described in more detail below.

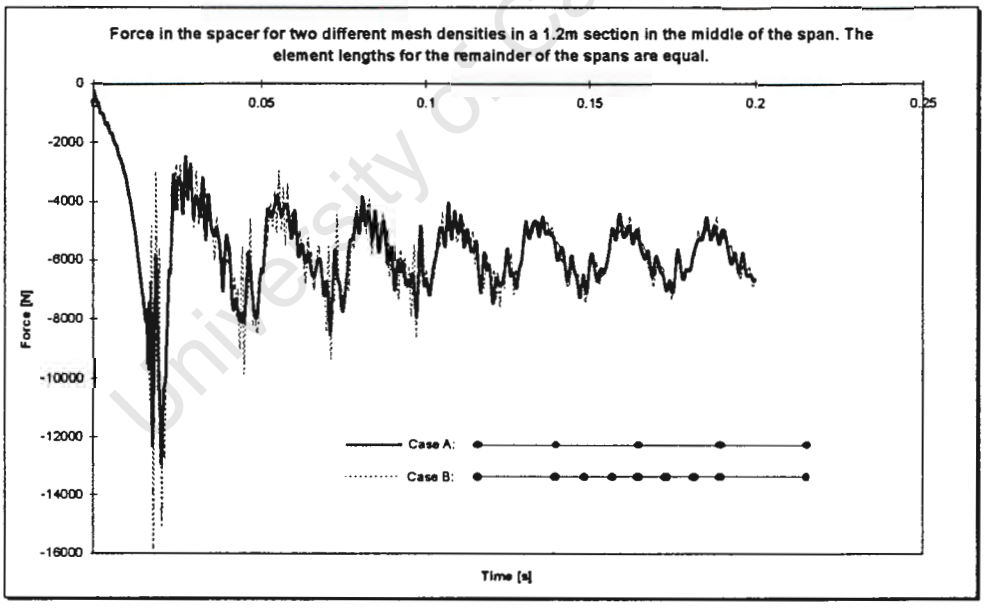

Figure 6.7: *Showing the different results obtained for the force in the spacer due to noise introduced in the system by a change in element length and additional contact points.*

6.4.3 Choice of Element Types

The decision on the choice of elements is based on their contribution to spurious modes, and their ability to model both the dynamic response and the waves propagating through the system with sufficient accuracy.

Cook et al (1989) state that in wave propagation problems, discontinuities of strain (and therefore of stress) propagate throughout the model. He mentions that lower order elements are more capable of modelling these discontinuities than are higher order elements.

With regard to spurious modes being reflected, Celep et al (1983) mention that the reflection is less significant in linear than in constant strain (quadratic) beam elements, but that the difference is not very significant. Jiang et al (1990a) and Celep et al (1983) show that the spurious modes generated during impact are less predominant in a lumped mass matrix formulation, such as that used in the linear 2-noded ABAQUS elements (Hibbitt Karlsson & Sorensen Inc., 1994a) than for consistent mass formulation, which is used for higher order elements.

In a paper by Prathap et al (1990), the authors show that a cubic oscillation of the shear strain is introduced by the reduced integration, employed to relieve locking, in a 3 noded quadratic beam element (such as the quadratic beam elements available in ABAQUS). This could be the reason for the seemingly unrealistic peaks obtained in the history of the force transmitted to the spacer (see Figure 6.8 below), when the conductor is modelled using quadratic beam elements.

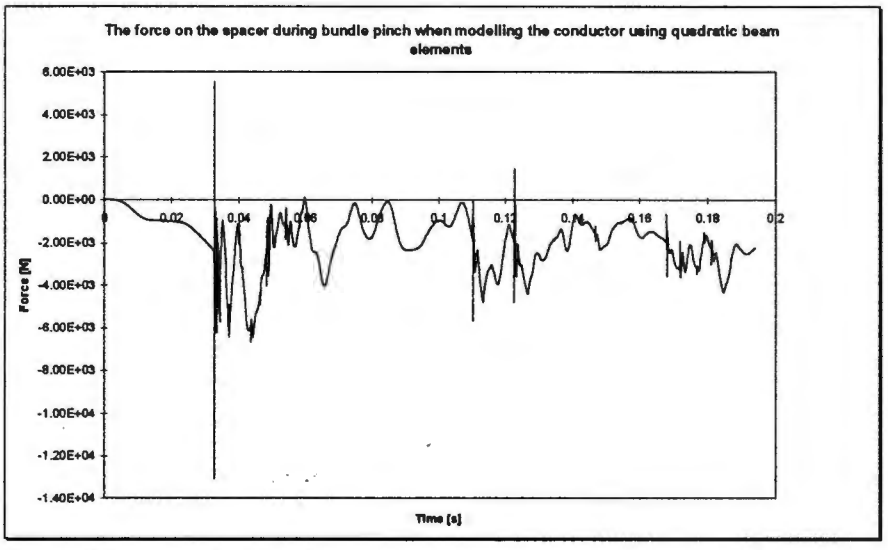

Figure 6.8: *A graph of the force in the spacer when using quadratic elements to model the conductor. The unrealistic peaks in the force obtained are clearly noticeable.*

In a paper compiled by van Wees (1989), he mentions that in terms of beam elements, those based on Euler-Bernoulli beam theory are inaccurate when modelling wave propagation. For the problem in hand, this rules out the 2-noded cubic interpolation beam elements in ABAQUS which are based on Euler-Bernoulli theory.

As far as the use of hybrid beam elements for the bundle pinch model is concerned, it is found that they are not only more expensive computationally, but also result in a very noisy solution in terms of the force history. No literature reference could be found which explained why the solution is as noisy as it is when modelling dynamic situations. It might be however, that the spurious modes introduced by the wave

propagation are amplified by the inclusion of the axial and shear forces in the hybrid elements as additional degrees of freedom. The graph of Figure 6.9 shows the force history in the spacer for a test problem, comparing the results obtained when modelling the conductors with normal linear beam elements, and those obtained for linear hybrid elements.

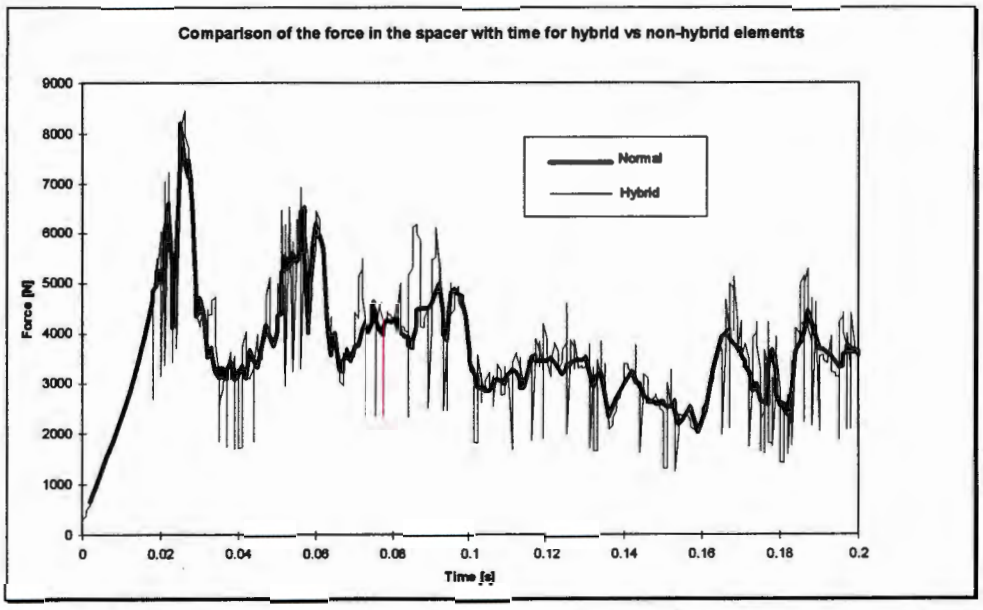

Figure 6.9: *The force in the spacer using hybrid and normal beam elements to model the conductor.*

Unfortunately provision is not made for contact between truss elements in ABAQUS, and as such these elements are not available for the short-circuit simulations.

After considering all these factors it seems that the normal (i.e. non-hybrid) 2 noded beam elements, which are based on linear shape functions are the most favourable when modelling the conductors for bundle pinch. These are referred to in ABAQUS as B31 elements.

6.4.4 Mesh Density and the Size of Adjacent Elements

In the case of an elastic wave propagating through the model, spurious modes are usually noticed in the solution which may have a considerable effect on the results. As mentioned by Jiang and Rogers (1990b), the presence of spurious oscillations is unavoidable. This has to do with the existence of a cut-off frequency corresponding to the highest mode of vibration the mesh is able to model, as well as errors in the higher natural frequencies and mode shapes for the model. It has also been found by Jiang and Rodgers that in the case of one-dimensional problems, a decrease in the size of all the elements in the mesh will not necessarily result in a decrease in the spurious oscillations.

Together with the noise generated by contact, these spurious modes are likely to be amplified with a change in size of adjacent elements in a finite element mesh. As shown by the work of Celep & Turhan (1987) and in the paper by Celep & Bazant (1983), a change in adjacent element dimensions by a factor of 2, which is usually

considered an acceptable factor in mesh refinement, has a significant effect on the spurious modes. For a larger difference in relative element sizes, the error increases further. Thus the element size in the mesh should be kept as uniform as possible.

With regards to the actual size of the elements, a balance must be found so that a sufficient number of modes of vibration of the structure are represented to render the solution accurate, while keeping the computational effort required to solve the problem to an acceptable limit. Bathe (1982) mentions that at most four times the highest loading frequency should be accurately modelled, and that this frequency may be considerably lower in some cases. For a frequency of 50 Hz, which corresponds to the frequency of the A/C current in transmission lines, and a conductor axial tension of 20 kN, the wavelength, according to equations (A.14) and (A.17), is 1.08 metres. Assuming that at least four linear elements are required to approximate the sinusoidal wave, this would mean an element length of about 0.25 metres. The element length required to model the wavelength at a frequency of 50 Hz, using 4 elements per wavelength, would be 0.67 metres, and at 100 Hz (i.e. twice the highest frequency in the loading) would be 0.41 m.

To determine the maximum element size required to model the response with sufficient accuracy, the results of a test problem, set up with different mesh densities, are shown. The graph of Figure 6.10 compares the force in the spacer for a 10m sub-span, where the sub-span is modelled using 14, 26, 38 and 64 elements respectively. The load imposed on each of the conductors is shown in Figure 6.11, and is applied as a uniformly distributed load, acting in the direction of the other conductor. The frequency of loading is 50 Hz, and the magnitude estimated as being slightly higher than that expected during a short-circuit, to represent an extreme case. The spacing between the two conductors is 0.3 metres.

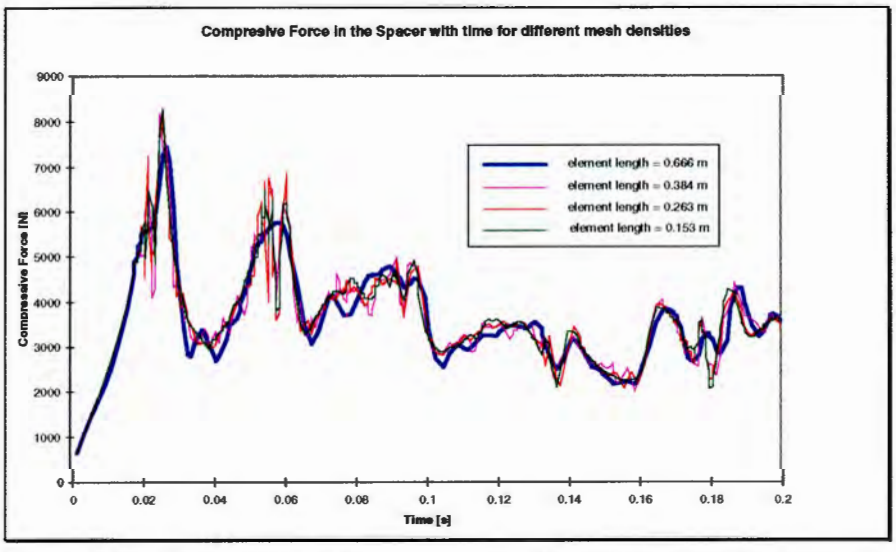

Figure 6.10: *Comparison of the compressive force history in the spacer for different element lengths used to model the conductor.*

As can be seen from the test, the mesh size does not have a significant effect on the results of the spacer force history. It is noticeable, however, that the mesh consisting of 14 elements (element length of 0.67 m), predicts a slightly lower peak force than the other three mesh densities. As the difference in the results for the

three denser meshes is negligible, it is fair to assume that an element length of about 0.4m is sufficient.

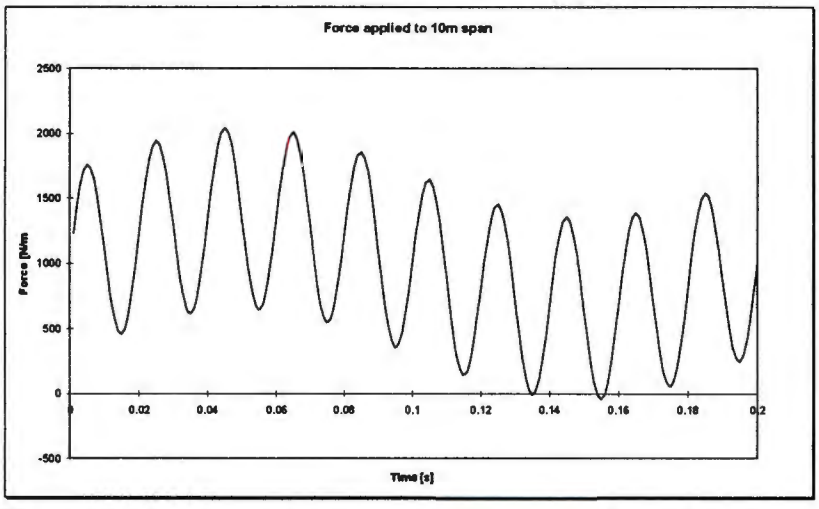

Figure 6.11: *Load applied to the conductors in testing the mesh density*

The main incentive to keep the number of elements to a minimum is the large amount of CPU time required to solve a complex problem of this nature. The approximate CPU time required to run the problem using different numbers of elements is shown in Table 6.1. As can be seen, the time required increases considerably with an increase in the number of elements in the model, justifying the decision to use the minimum number of elements possible, without adversely affecting the results.

No. of elements	approx. CPU time (mins)
14	2
26	11
38	60
64	150

Table 6.1: *Approximate CPU time required for different numbers of elements in the model.*

6.4.5 Including Damping in the Model

As the noise generated by contact and the spurious modes introduced with wave propagation could have quite significant effects on the results obtained, some form of additional damping must be introduced into the solution to dissipate the high frequency noise. Apart from the material damping inherent in the system, the additional damping is justified by the fact that even though the conductor is modelled as being purely elastic, the strands in the conductor are bound to undergo at least a small amount of plastic deformation when the conductors clash (See Figure 6.3). The energy absorbed by the plastic deformation automatically dissipates higher frequencies (Hibbitt Karlsson & Sorensen Inc., 1994a; Timoshenko et al, 1974).

In the modelling of short-circuit effects on the conductors in a sub-station, Miri et al (1993) also experience problems with spurious high frequency noise, which is

eliminated by introducing additional damping into the solution by means of the stiffness proportional Rayleigh damping factor.

In the present model, a value for the stiffness proportional damping of $\gamma = 10^{-4}$ is found to be adequate in damping out any significant noise, while not seriously affecting the solution. The damping ratio introduced by this factor is given by the linear relationship of equation 3.2 with the mass proportional damping factor, α, being given a value of zero. The highest frequency in the loading corresponds to the electrical AC frequency of 50Hz, for which the damping ratio with $\gamma = 10^{-4}$ is 0.016.

6.4.6 Modelling Contact Between the Conductors

A number of different options are available in ABAQUS for dealing with the contact between bodies. In the case of contact between beam elements, two options are available. A third option, which uses the master-slave approach, requires that one of the surfaces be defined as a master, and the other a slave. Unfortunately, ABAQUS only allows beam elements to be modelled as slave surfaces (Hibbitt Karlsson & Sorensen Inc., 1994b), and as no master surface can thus be defined using only beam elements, this option is unavailable for the short-circuit model. As already mentioned, two options are however available, specifically formulated to deal with the contact between beam elements. These are *gap* and *tube-to-tube* contact elements, the details of each being as follows:

i.) Gap Elements (GAPCYL in ABAQUS)

These elements assume that two nodes on parallel cylinders remain in a fixed plane, and come into contact when they approach each other to within a specified distance. There are two problems which make the use of these elements impractical for the modelling of bundle pinch.

Firstly, the direction of the cylinder (or in this case conductor) axis of each element must be specified at the start of the analysis. This pre-defined direction remains constant for the duration of the analysis, while the axes of the conductors do not as the gravitational and short-circuit loads are applied. The second problem is that the plane of contact does not necessarily remain plane during bundle pinch.

Even though these problems are not necessarily very significant, tube-to-tube contact elements which are not restricted in this manner are used.

ii.) Tube-to-Tube Contact Elements (ITT31)

The tube-to-tube contact definition assumes that the contact between two rods or in this case conductors occurs along a curve. The tube-to-tube elements are assigned to the nodes of the one conductor, and a slide line, along which these elements can slide, is defined by the nodes of the second conductor. The minimum distance between the centres of the two conductors is specified, and once a contact element comes to within this specified distance of the slide line, contact at this point is assumed, and the surface interaction algorithm deals with the constraints imposed by the contact.

With regards to modelling the actual interaction of the contact surfaces, two options are available in ABAQUS. These are known as soft and hard contact respectively (Hibbitt Karlsson & Sorensen Inc., 1994b).

iii.) Soft contact

In this case, the surface behaviour is based on the assumption that the force transmitted between the two surfaces is exponentially related to the clearance between the two surfaces (Hibbitt Karlsson & Sorensen Inc., 1994). At a certain clearance c, no pressure is transmitted, while the pressure increases exponentially with a decrease in the clearance, until at zero overclosure, i.e. when contact is made, a pressure p^0 is transmitted, as shown in Figure 6.12.

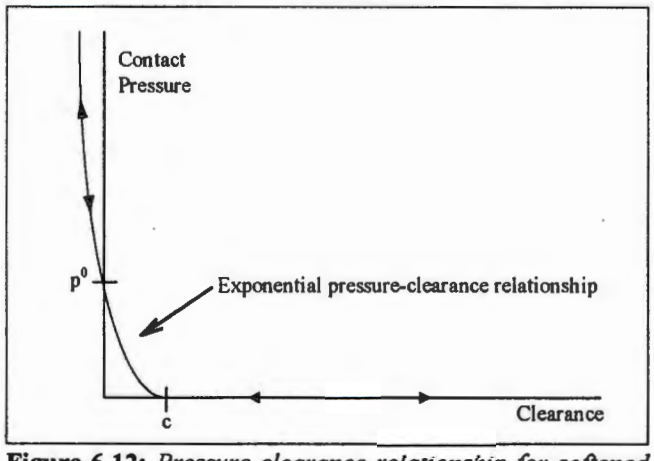

Figure 6.12: *Pressure-clearance relationship for softened contact*

The main disadvantage of this model, even though it does converge easier than the hard contact option described below, is that it assumes totally elastic impact. The assumption that both kinetic energy and momentum are conserved is made, which is not a valid assumption in this case. The conductors are likely to undergo some amount of plastic deformation, as can be seen from Figure 6.3 which shows a section of the conductors of a triple bundle after clashing.

In reality, as can be seen from Figure 6.2, the conductors in the bundle typically stick together after clashing. The elastic impact assumption however, causes the conductors to bounce quite severely off each other immediately after impact (Figure 6.13 below). This causes additional fluctuations in the forces, as is observed when the two contact methods are compared (see Figure 6.14). The user is cautioned in the ABAQUS manuals (Hibbitt Karlsson & Sorensen Inc., 1994b) that severe chatter is likely to occur for the simulation of impact situations when using the soft contact option, which would explain the unrealistic bouncing.

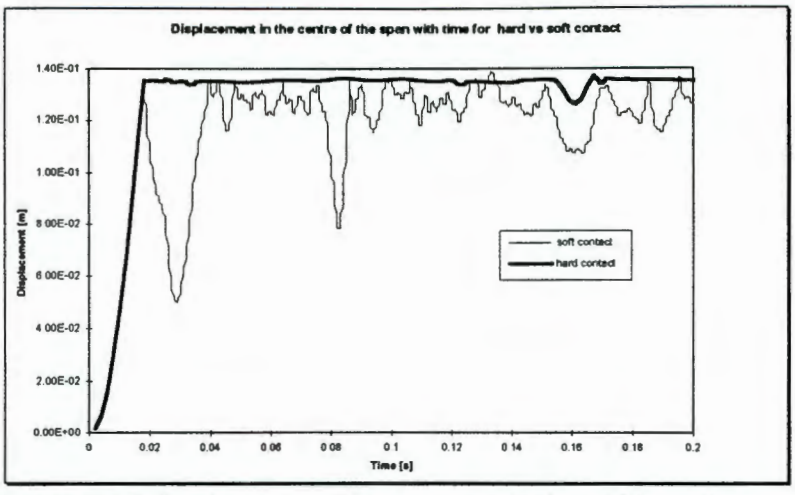

Figure 6.13: *Displacement of the conductor in the middle of the span for soft vs hard contact*

Including additional damping to eliminate the chatter does not resolve the problem, as the amount of damping required to prevent the bouncing significantly and adversely affects the overall behaviour of the conductor.

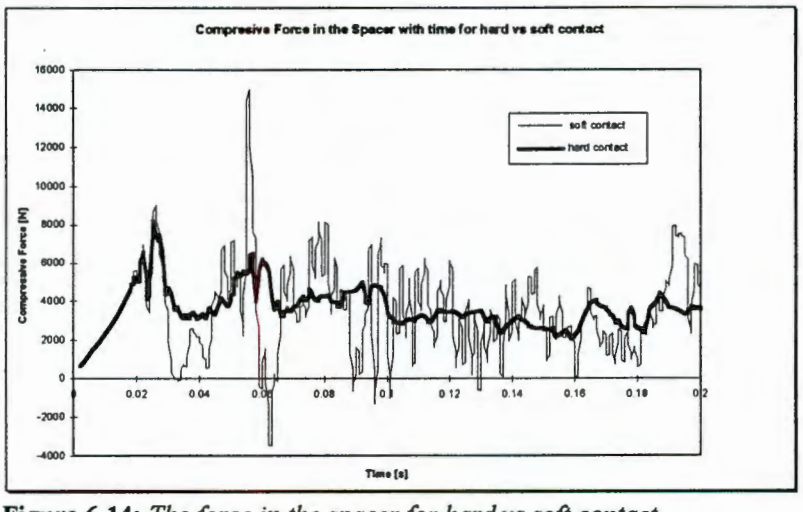

Figure 6.14: *The force in the spacer for hard vs soft contact*

iv.) Hard contact

The pressure relationship for hard contact, shown in Figure 6.15, assumes that no pressure is transmitted between the two surfaces until the closure between the surfaces is zero (Hibbitt Karlsson & Sorensen Inc., 1994b). Once contact is established, a pressure of any magnitude may be transmitted between the surfaces.

This option causes an impact algorithm to be implemented every time contact is established or broken, and as such this option is ideal for relatively high speed impact situations, such as bundle pinching. Even though it is significantly more expensive computationally, it is felt that the additional cost is justified by the improved confidence in the results obtained for the peak force values.

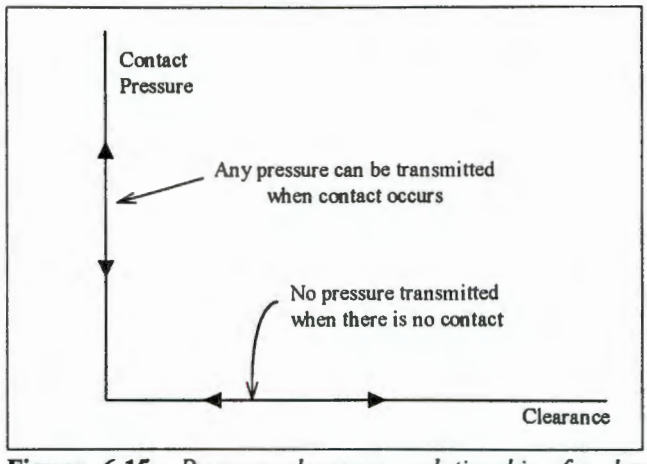

Figure 6.15: *Pressure-clearance relationship for hard contact*

6.4.7 Bending Stiffness of the Conductor

As mentioned in chapter 2, the bending stiffness of a conductor varies as a function of bending curvature. In the event of bundle pinch, a choice between a constant bending stiffness and a curvature dependent bending stiffness would be expected to have an effect on the behaviour of the conductor, especially at the ends of the sub-spans where the bending is most severe. Figure 6.16 compares the tension in the spacer as obtained when the stiffness is assumed to be constant ($EI = EI_{max} = 1605$ Nm^2), with that obtained when the bending stiffness varies as a function of the bending curvature according to Figure 2.2.

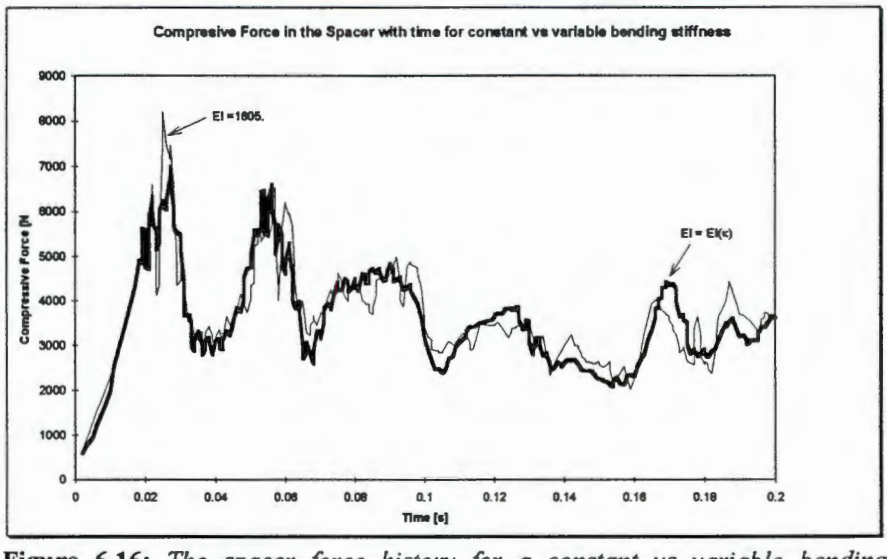

Figure 6.16: *The spacer force history for a constant vs variable bending stiffness*

Neither of these assumptions is strictly speaking correct, the constant bending stiffness not being valid as slipping does occur (If no inter-strand slipping occurred, i.e. the critical curvature was not exceeded, the bending stiffness of the variable stiffness would correspond to EI_{max}, and the curves above would be identical). The limitations of only being able to implement the variable bending stiffness relative to

zero curvature in ABAQUS, as opposed to a change in curvature as discussed in chapter 2, mean that the conductor elements do not have the correct bending stiffness when their direction of bending is reversed as the two conductors move apart. The variable bending stiffness as implemented in ABAQUS does not account for the fact that the bending stiffness increases to it's maximum as soon as the reversal occurs (Papailiou, 1995a,b).

As this test example shows, the difference in the results is not significant for this specific simulation (with the load history of Figure 6.11 once again being applied to the conductors) and for any other simulations where the conductors in the bundle "stick" after impact. If the conductors were however to separate at any stage, as would be the case when the short-circuit is broken, the results could be significantly affected by the variable bending stiffness implemented in ABAQUS.

As mentioned earlier, the bending stiffness should be implemented as a function of the change in curvature of the conductor, rather than the actual bending curvature. However, as this is not possible in ABAQUS, a constant bending stiffness is assumed for the model. This assumption eliminates any error which would be introduced by the ABAQUS implementation of the variable bending stiffness.

6.5 VERIFICATION OF THE MODEL

In the paper compiled by Manuzio (1965), the results of the force experienced in a spacer between the conductors of a twin *Curlew* conductor bundle during a short-circuit test are given. The test span is 130 meters in length, with the spacer being situated midway between the supports, which are of equal height, (i.e. the span is symmetric). The conductors are strung at a tension of 33 kN, the spacing between the conductors is 0.40 meters, and the initial r.m.s short-circuit fault current is 12.5 kA.

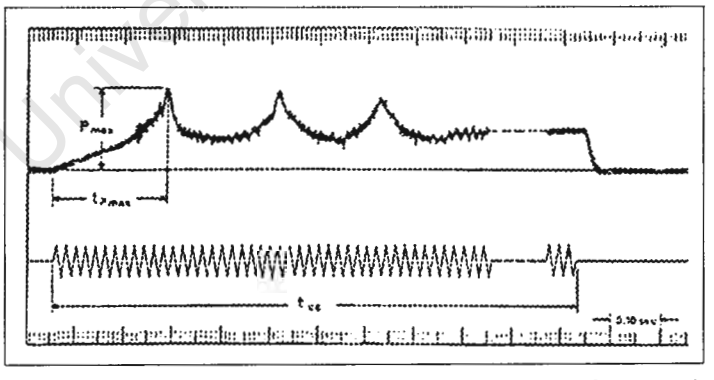

Figure 6.17: *The force in the spacer force as obtained by Manuzio (1965). The bottom curve shows the short-circuit current with time. The value of P_{max} is approximately 4 kN.*

Figure 6.17 shows the force in the spacer obtained by Manuzio, with the value of P_{max} being approximately 4 kN. The spacer force obtained from the finite element simulation of the test is given in Figure 6.18. A few points have been measured from the graph of Manuzio's results and these are shown together with the finite element

results in the graph below. As can be seen, the finite element results agree very favourably with the experimental.

The only real disadvantage of a finite element simulation such as this, is the large amount of CPU time required to obtain a solution. This simulation, for example, requires about 80 hours of CPU time, with the bulk of the processor effort required to deal with the constraints imposed by the contact between the beam elements as the conductors pinch.

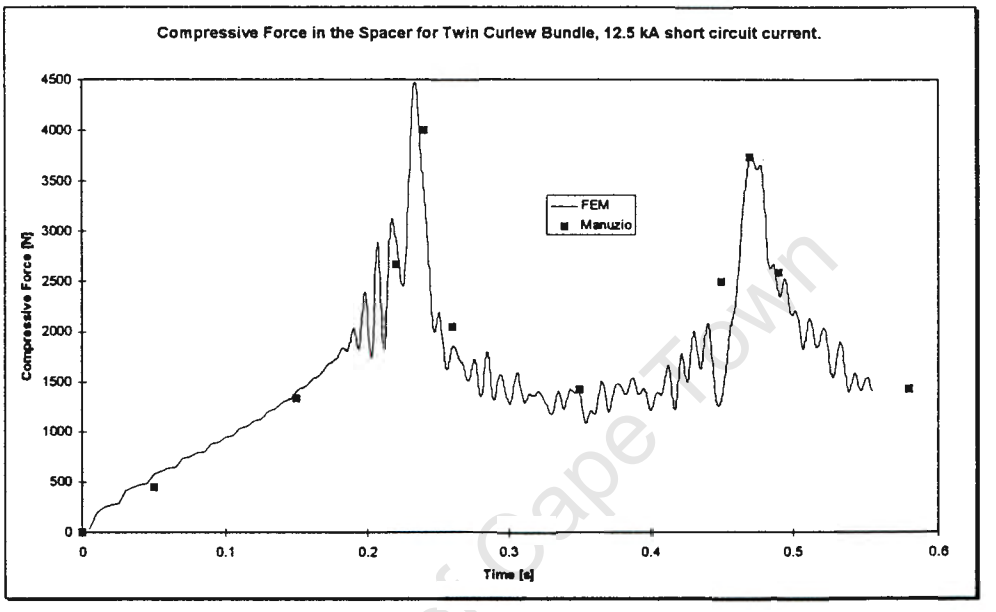

Figure 6.18: *The force in the spacer for one of the tests carried out by Manuzio (1965) as predicted by the finite element model. Selected data points from Manuzio's results, including peak values, are also shown.*

6.6 RESULTS OF THE FINITE ELEMENT SIMULATIONS

To compare the effect of the initial conductor tension, short-circuit current and the number of sub-spans on the forces experienced in the spacer and conductor respectively during a short-circuit, the results of simulations of a simple test span are presented below. The test span is 80 metres long, and consists of a single twin bundle with two *Zebra* conductors, as shown in Figure 6.21. The distance between the conductors is 380 mm, and each of the sub-spans is of equal length. Unless otherwise stated, a single spacer is located in the middle of the span. All degrees of freedom at either end of the span are completely restrained.

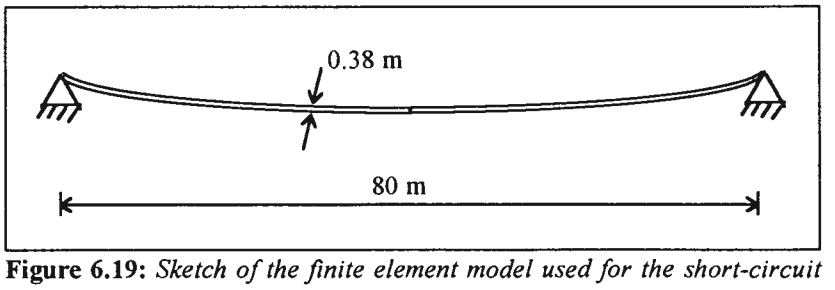

Figure 6.19: *Sketch of the finite element model used for the short-circuit conductor motion simulations.*

Two hundred linear beam elements of equal length are used per conductor. The gravitational loads are applied using the same procedure as with the aeolian vibration simulations.

6.6.1 Initial Short-Circuit Current

An increase in the short-circuit current in the conductors would result in an increase in the electromagnetic forces acting between the conductors, and thus the motion would be expected to be more severe. This is evident in the results for the conductor tension and spacer force which are shown in Figure 6.20 and Figure 6.22 respectively. The values for the short-circuit currents given are the initial r.m.s currents (i^*_k) for the twin bundle, as described earlier.

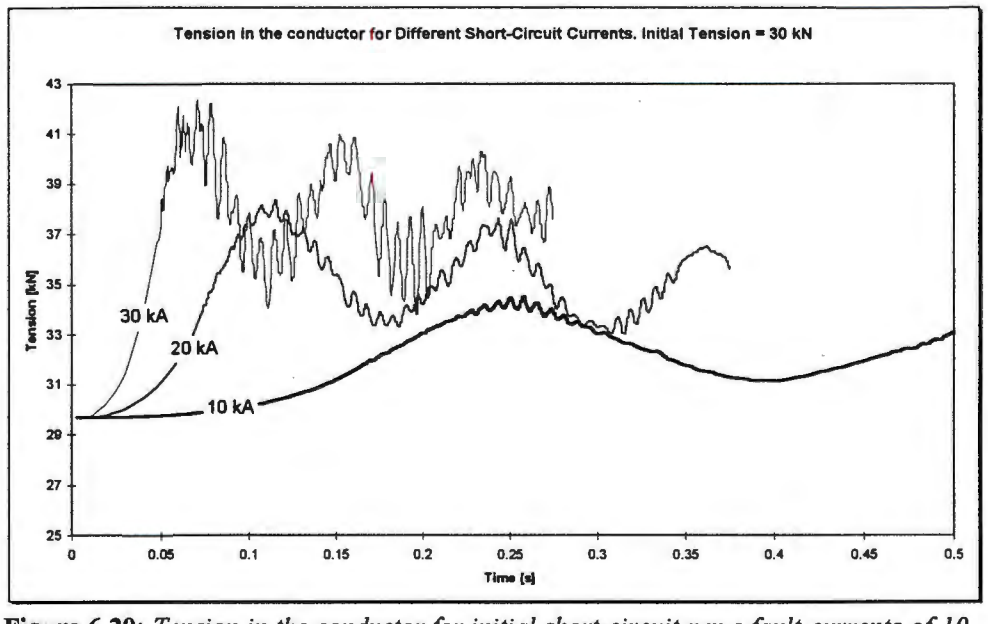

Figure 6.20: *Tension in the conductor for initial short-circuit r.m.s fault currents of 10, 20 and 30 kA. The initial conductor tension is 30 kN.*

It is quite interesting to note that the increase in the maximum force in the spacer is considerably more significant than the increase in the maximum tension of the conductor. Even though the peak tension in the conductor doesn't increase significantly, the slope of the tension curve increases notably due to the higher acceleration of the conductors towards one another. This results in a greater momentum before the conductors clash, and as such the last point of contact between the conductors (as shown in the sketch below) is closer to the spacer. The angle θ thus decreases, and the component of the conductor's tension which must be balanced by the compressive force in the spacer increases. This explains the significant increase in the compressive force of the spacer as shown in Figure 6.22.

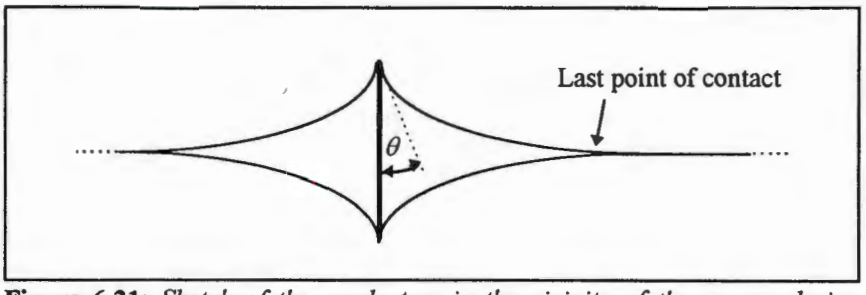

Figure 6.21: *Sketch of the conductors in the vicinity of the spacer during bundle pinch.*

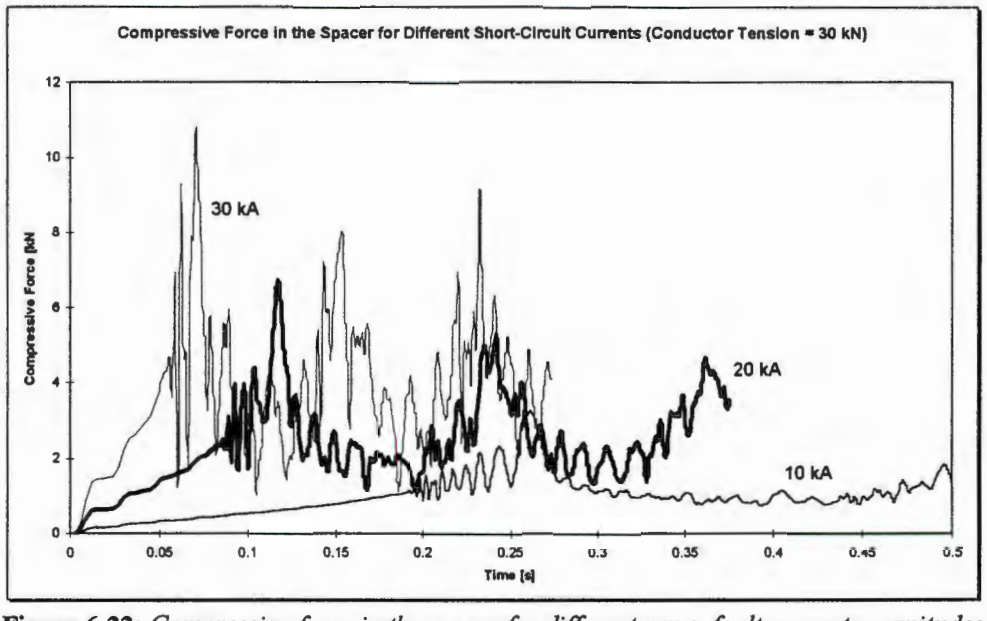

Figure 6.22: *Compressive force in the spacer for different r.m.s. fault current magnitudes.*

6.6.2 Initial Conductor Tension

In the results below (Figure 6.23 and Figure 6.24), the effect of the initial tension in the conductors is shown. With regards to the time dependent tension in the conductors during the short-circuit, not much difference is noted in the graphs. The increase in the tension from the initial value is very similar for each case.

The force in the spacer is affected to a greater extent by an increase in the initial tension than the conductor tension is. It is interesting to note that it is only the first peak force which increases notably. Apart from this peak, the history of the force in the spacer is very similar for all three tensions.

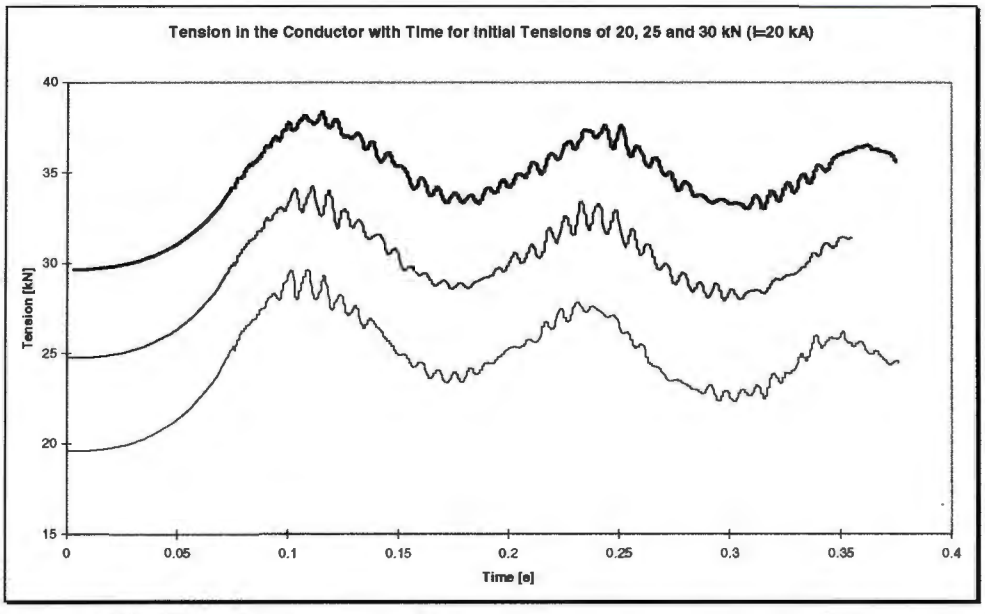

Figure 6.23: *The time history of the tension in the conductor for different initial conductor tensions. The r.m.s fault current for the bundle has a magnitude of 20 kA.*

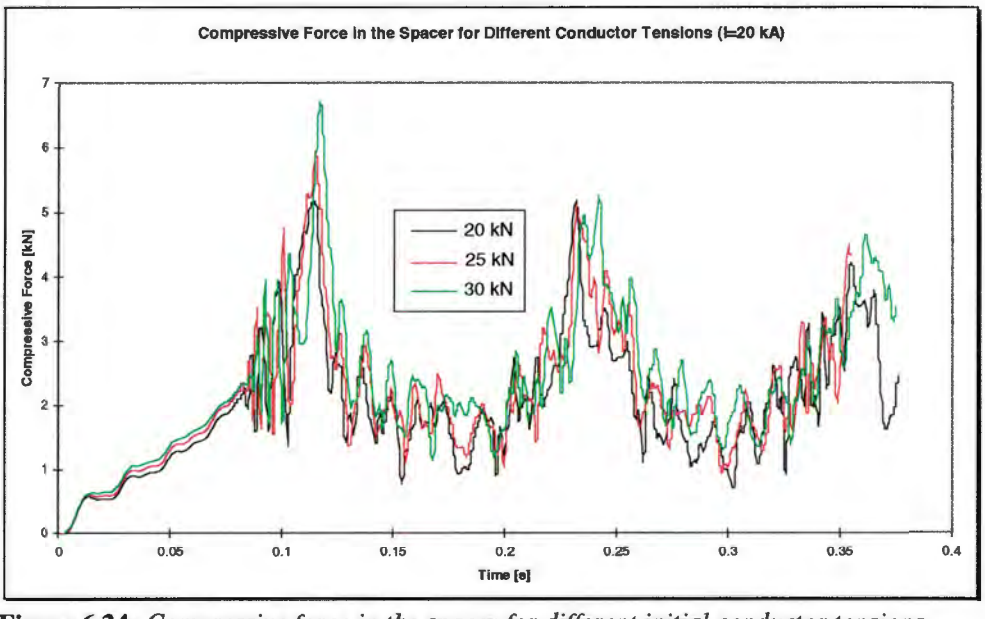

Figure 6.24: *Compressive force in the spacer for different initial conductor tensions*

6.6.3 Number of Spacers in the Span

To determine the effect of the number of sub-spans in the 80 metre span on the forces experienced in the conductor and spacers, the results of simulations for 2, 4 and 6 sub-spans are shown in Figure 6.25 and Figure 6.26 below. Unless stated otherwise, the initial tension in the conductor is 30 kN. The magnitude of the r.m.s. fault current is 20 kA for the bundle.

As can be seen, an increase in the number of sub-spans from 2 to 4 results in an increase of the peak tension in the conductor, while the force in the spacer is virtually unaffected.

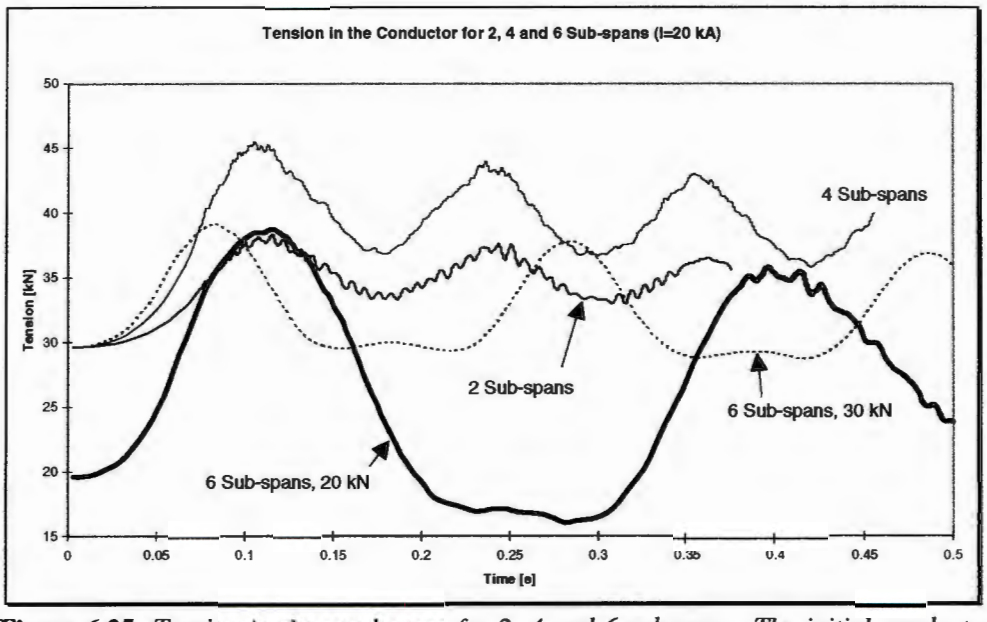

Figure 6.25: *Tension in the conductors for 2, 4 and 6 sub-spans. The initial conductor tension is 30 kN unless otherwise specified, and the short-circuit fault current is 20 kA.*

Increasing the number of sub-spans further, so that 5 spacers separate the 6 sub-spans, causes a decrease in the maximum tension. This is because the conductors do not come into contact with one another, and as the minimum distance reached between the two conductors is greater than it is for 2 and 4 sub-spans, the maximum electromagnetic force between the conductors, being inversely proportional to the distance between the conductors, is less. As the conductors don't clash, the angle θ is always considerably more than it would be if they did, and thus the component of the tension in the conductor which is balanced by the compressive force in the spacer is once again significantly less.

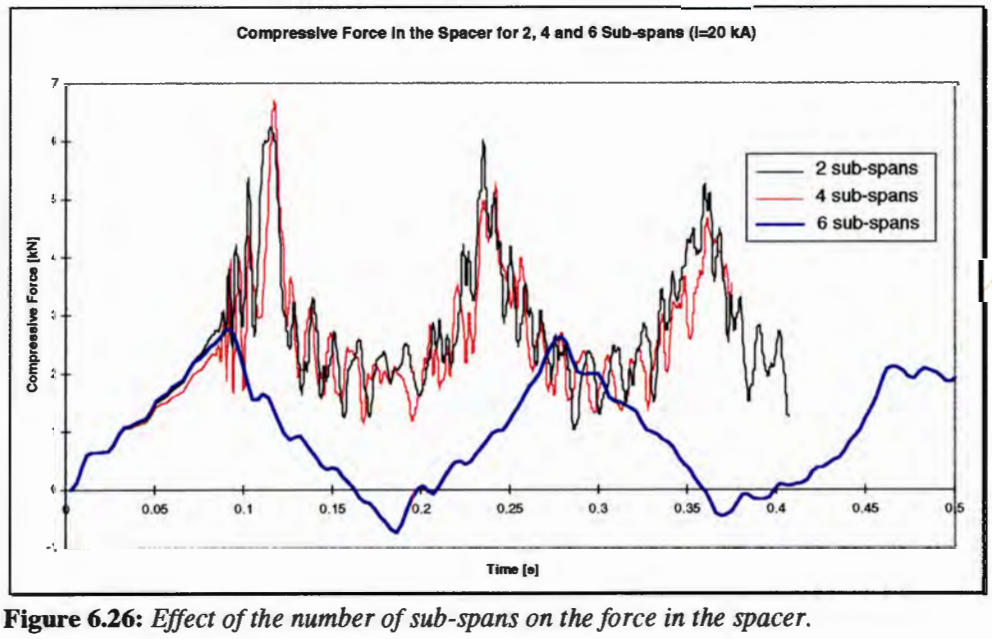

Figure 6.26: *Effect of the number of sub-spans on the force in the spacer.*

Decreasing the initial conductor tension in the 6 sub-span case from 30 kN to 20 kN allows the conductors to clash. It is interesting to note how the peak tension registered in the conductors increases by about 18 kN if the bundles pinch, as opposed to 8 kN when they don't clash, and how the peak tension is approximately the same in both cases.

7. BREAKING CONDUCTORS

In this chapter, the finite element modelling of the motion of a transmission line as a result of a conductor breaking is discussed. After a brief literature review which incorporates a discussion of the problem, the details of a test which is replicated using finite elements are presented. The particulars of the finite element model are then given, after which the model is verified by comparison with experimental and other numerical results. The last chapter presents and discusses results obtained from various finite element simulations.

7.1 LITERATURE REVIEW

When designing transmission towers, including the foundations and any support structures such as guys, one of the design criteria adopted by transmission line engineers is to design the tower to withstand various loads the tower might be subjected to during its lifetime. These include wind loads, where the load imposed on the tower by the drag forces of a strong wind might be sufficient to cause damage to the tower or one of its members. Other load types considered in the design of the towers are those imposed on the tower when one of the conductors or earth wires is suddenly detached from the tower, and the tower is subjected to unbalanced loads (Peyrot et al, 1980; Lummis et al, 1969). A failed insulator string or attachment shackle would cause the sudden removal of a tensile load from the tower. The failure of the conductor (or earth wire) itself, were it to break, would also cause a sudden unbalance in the forces on the tower. A conductor would fail, for example, due to the fatigue failure of a sufficient number of it's strands so that the increased stress in the remaining strands exceeds the tensile strength of the material.

The loading imposed on a tower due to the failure of an adjacent tower is another important consideration when designing towers. Cascading failure of towers has caused severe damage to whole sections of a transmission line in the past (Gupta et al, 1994; Thomas et al, 1982). The sudden increase in the tension of the conductors due to the failure of an adjacent tower causes the subsequent failure of another tower, and so on until the towers of a whole section of a transmission line have collapsed.

Often the loads imposed on the system once it is in a state of static equilibrium after some event, are not significantly large to cause severe damage on their own. The dynamic forces experienced during the failure of a component are, however, usually significantly higher than the quasi-static or static loads, and are thus of more concern than the static loads.

Work has been done by numerous people on the analysis of transmission lines. One of the earlier papers, by Lummis et al (1969) discusses work carried out on the effects of imbalance loads on a transmission line. Their analysis is based on the static equilibrium of forces in the system. Peyrot has been a prominent figure in the large displacement analysis of transmission lines. Peyrot and his colleagues (Peyrot et al, 1978; Peyrot et al, 1981) developed a computer based method for the static analysis of flexible transmission lines under various conditions. Gupta et al (1994) use finite element analysis techniques

to model the dynamic behaviour of a section of a transmission line after the failure of an insulator. They use a single catenary cable element to model the conductor in each span.

In another paper, Peyrot and his colleagues (Peyrot et al, 1980) present results obtained from tests performed on a section of a test line. Numerous broken insulator and broken conductor tests were performed. They then used a modified version of the computer implemented technique of Peyrot et al (1979, 1981), which estimates an impact factor from strain energy considerations, to analytically predict the peak tensions in the system after the failure of a conductor or insulator.

Thomas and Peyrot (1982) published a paper which compares the test results mentioned above with the analytical results obtained from an updated version of their previous analysis techniques which dynamically models the response of the system using numerical methods.

7.2 Details of the Experimental and Numerical Tests by Peyrot and his Colleagues

This section describes the original test by Peyrot et al (1980) which is later replicated using finite elements, and the numerical simulations of the test as carried out by Thomas et al (1982)

7.2.1 Details of the Original Tests (Peyrot et al, 1980)

The finite element model is based on a section of the test line used by Peyrot and his colleagues to study the response of a transmission line in the event of conductor or insulator failure. Various test were performed on the test line, with the one to be simulated using finite elements being referred to as test IIIR1 in the paper by Peyrot et al (1980). In this test, the conductor on one of the spans of the test line was severed, at the location shown in the sketch of Figure 7.1. The insulators used in the test were 2.2m metres in length, and consisted of 10 porcelain insulator discs each.

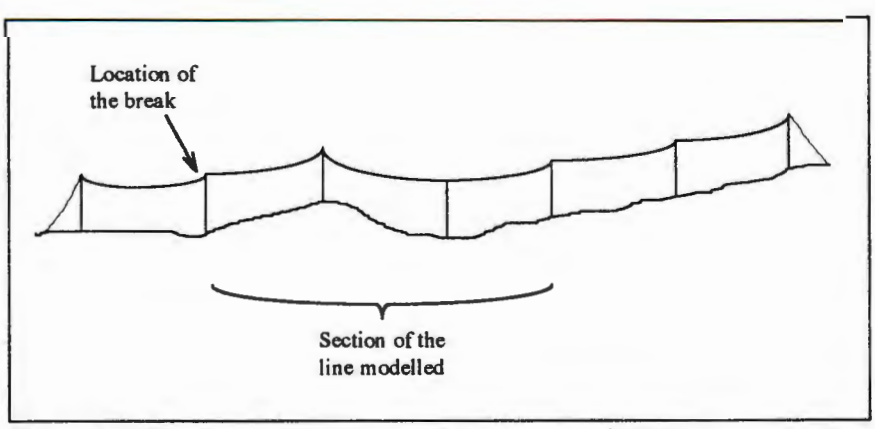

Figure 7.1: *Sketch of the Test Line used by Peyrot et al (1980)*

Unfortunately, detailed results from the original test could not be found, apart from the magnitudes of the first two peaks which are typical in the force history of the insulator adjacent to the break (Insulator A in Figure 7.2). The experimentally obtained tension

magnitudes are 24.6 kN and 32 kN for the first and second peaks respectively. The original tension in the conductor is 19 kN.

The conductor used for the test is a copper and bronze conductor with the following properties (Peyrot et al, 1980):

Designation:	471A copper/bronze
Mass:	1.296 kg/m
Young's Modulus:	105 GPa
Rated Strength:	68.6 kN
Area:	143.8 mm^2

Table 7.1: *Mechanical properties of the conductor used for the broken conductor model.*

7.2.2 The Numerical Simulation of the Test by Thomas & Peyrot (1982)

As mentioned above, only limited results of the original test could be found, however Thomas and Peyrot simulated the experiment numerically, and results of the simulation are available. These results, together with the real peak values given, are used to verify the finite element results.

As can be seen, Figure 7.2 below only shows the three spans directly adjacent to the break location. Thomas and Peyrot (1982) state that three spans are sufficient to model the forces experienced by the tower at which the break occurs with acceptable accuracy. This is the number of spans used in their computer simulations of the test, and to enable a direct comparison to be made with their results, the same number of spans is used in the finite element model.

The spans (in Thomas and Peyrot's model) are modelled using 20, 10 and 5 cable elements for spans A, B and C respectively.

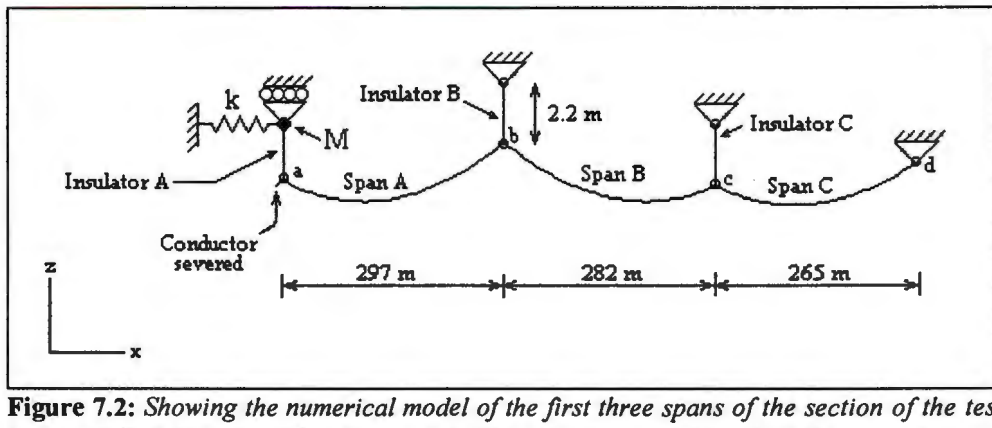

Figure 7.2: *Showing the numerical model of the first three spans of the section of the test line modelled as indicated in Figure 7.1. The elevations at the end of the spans are +0, +8, -1 and +4 metres for nodes a, b, c and d respectively.*

The numerical results obtained by Thomas and Peyrot are shown in Figure 7.9 below. They show the tension in the first insulator (Insulator A) for the two seconds

immediately after the conductor is severed. The magnitudes of the first and second peaks are 26 kN and 30 kN respectively.

7.3 DETAILS OF THE FINITE ELEMENT MODEL.

The details of the various aspects of the finite element model used to simulate the test of Peyrot et al (1980) are discussed below. The modelling of the conductor, insulators and towers is described, and the choice of the explicit and implicit integration options is briefly discussed.

7.3.1 Modelling the Conductor

i.) Number of Elements

In general, the choice of the number and type of elements used to model the conductor does not seem to drastically influence the results. The only notable exception is when approximately 25 or less linear elements are used per span. This can be seen in the results of Figure 7.3, where the tensile force in insulator A is recorded for different numbers of elements per span. Even though the magnitude of the first peak is very similar to that predicted by the other finite element and the experimental results, the second peak tension is exaggerated by the courser model. The history predicted by the different models also varies slightly from one to the next, however that predicted by the 25 element per span model differs to a greater degree from the others.

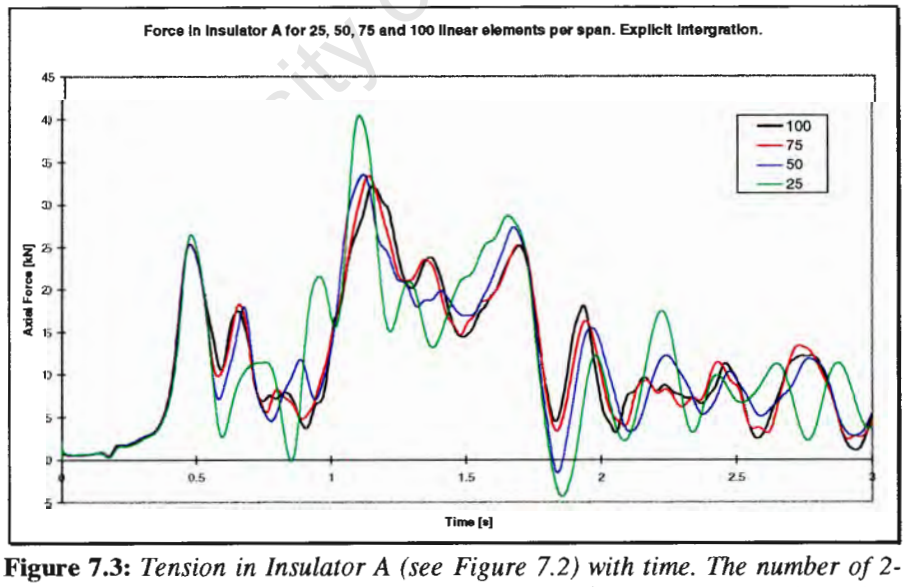

Figure 7.3: *Tension in Insulator A (see Figure 7.2) with time. The number of 2-noded linear beam elements used to model the conductor is compared. Explicit integration is used in all cases.*

Figure 7.4 below compares the force in insulator A for 25, 50 and 75 cubic elements per span. As the number of elements is increased, the second peak approaches the same value as before, the only difference being that fewer cubic elements seem to underestimate the peak tensions, as opposed to over-estimating it in the case of linear elements.

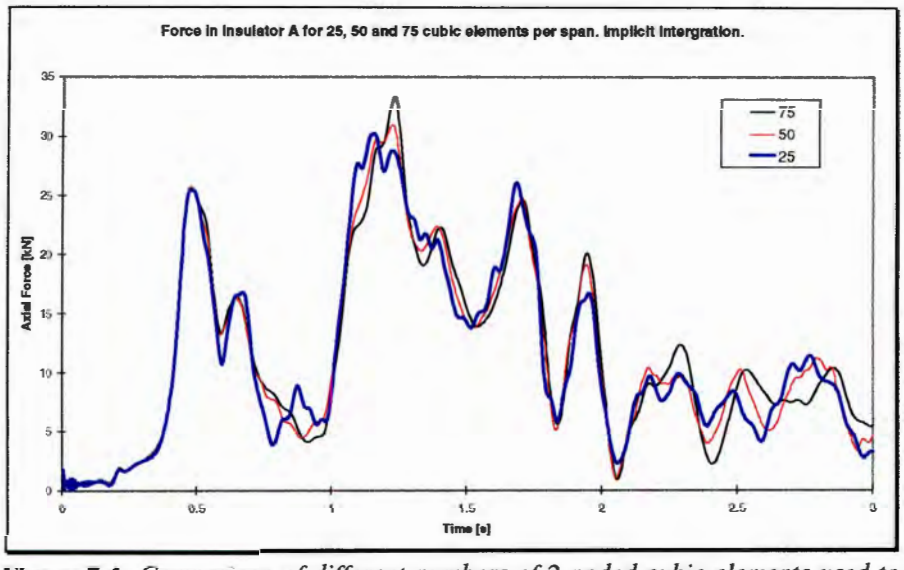

Figure 7.4: *Comparison of different numbers of 2-noded cubic elements used to model the conductor.*

ii.) Element Types

Regarding the type of elements, the ideal choice would once again be the beam elements based on Euler-Bernoulli beam theory. As discussed earlier in the chapter dealing with aeolian vibration, the ratio of the distance between supports to the thickness of the conductor justifies the use of these elements. The 2-noded cubic elements in ABAQUS, being the only ones based on Euler-Bernoulli beam theory, are however not available for the explicit integration option. Linear beam elements are thus used to model the conductor when using explicit integration.

To check whether bending stiffness is negligible for a large displacement problem such as this, the problem is also simulated using linear truss elements.

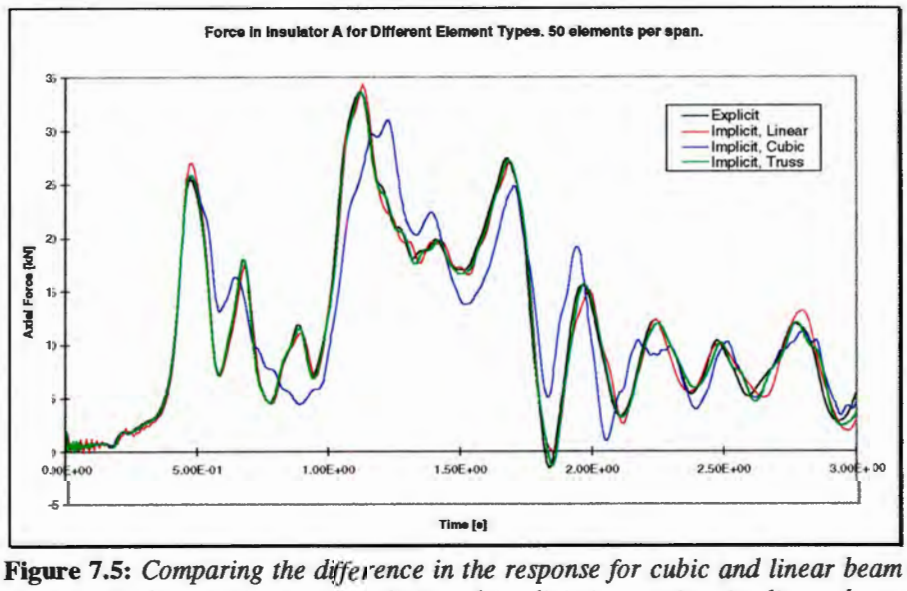

Figure 7.5: *Comparing the difference in the response for cubic and linear beam elements and truss elements. Explicit and implicit integration for linear beam elements are also compared.*

As can be seen from the results of Figure 7.5, there is a slight difference between the results of the linear and cubic elements. The cubic elements predict the conductor's response more accurately, as the peak tension values obtained are more in agreement with the experimental values than are those predicted by the linear elements. The higher order cubic elements would be expected to yield more accurate results in a structural dynamics problem such as this, as mentioned by Cook et al (1989). The difference, between the results are however not very substantial.

Regarding the truss elements, the results obtained using implicit integration are very similar to those obtained using linear beam elements with explicit integration, as can be seen from the results below. Truss elements can thus also be used with a fair degree of confidence, and the results show that bending effects are negligible when analysing the dynamics of a transmission line due to a broken conductor.

iii.) Damping in the conductor

The effect of the internal damping of the conductors is shown in Figure 7.6. The results are shown for different values of the Rayleigh stiffness proportional damping constant (γ of equation 3.2). The overall response is fairly similar with $\gamma = 0.0001$ to what it is with $\gamma = 0.001$, with the only difference being that the curve is more ragged for the lower damping constant. For $\gamma = 0.01$ however, there is a more significant effect on the response of the system, and the peak values are less than those reported by Thomas and Peyrot (1982).

A value of 0.001 for γ is thus used in the finite element model, as it smoothes out the response and removes noise, without excessively damping the response.

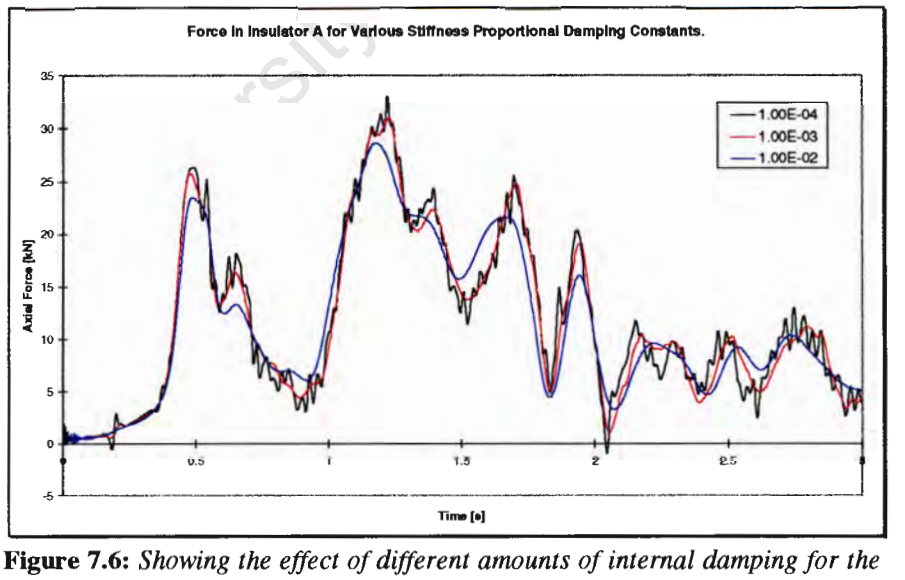

Figure 7.6: *Showing the effect of different amounts of internal damping for the conductor.*

7.3.2 Modelling the Insulators

The insulators are modelled using truss elements, the reason being that the nodes at the ends of the elements are pinned joints, similar to the real joints at the end of an insulator string. Unfortunately, no data on the physical properties of the insulators used in the tests is available, so arbitrarily chosen values of 0.01 m^2 and 5000 kg/m^3 for the

cross-sectional area and density respectively are used to give the insulators a mass of 50 kg per metre.

Figure 7.7 shows the force in Insulator A when the insulators are modelled using 2 vs 10 truss elements, and as is clearly evident, the history is much more noisy for the 10 element version. The magnitude of the first peak is also significantly greater than the value of 24.6 kN reported by Peyrot et al (1980).

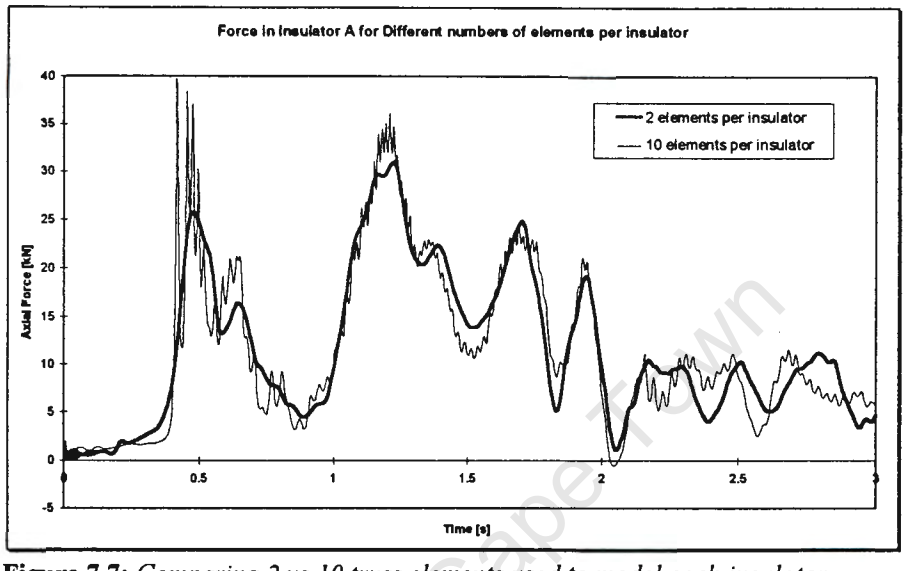

Figure 7.7: *Comparing 2 vs 10 truss elements used to model each insulator.*

As the two element version gives results which agree more favourably with those obtained in the literature, two elements are used per insulator in all the models.

An interesting observation, from the above comparison however, is that the initial increase in the tension at the base of the first peak is much more gradual for two than for ten elements per insulator. The peak tension has been measured in each case in the element closest to the tower connection. This may be due to the fact that the top element of the insulator string is unaffected by the dynamic effects of the broken conductor for a longer period of time in the ten element model, and that the velocity of the bottom of the insulator string is higher by the time the top element is affected than in the two element model.

7.3.3 Modelling the Towers

The same technique used by Thomas and Peyrot is used in the present finite element model to include the effects of the tower on the response of the system. The horizontal stiffness of the tower at the point of attachment of the top of the insulator string is assumed to be linear, and as such is modelled by means of a spring element (shown in Figure 7.2). The inertial effects of the tower are included by means of a mass element (M) which is attached to the node at the top of the insulator string. The top of the insulator is unrestrained only along the axis of the span, and as such the spring and mass elements are free to move only along the horizontal x-axis.

The tower stiffness may be obtained by applying a load at the relevant point on the tower, and monitoring the displacement as a function of the load applied. The force-

displacement data could be obtained for certain towers from reports on tower tests such as those carried out by Eskom's Tower Test Station in Rosherville, South Africa.

As shown below, the value chosen for the mass of the mass element does not have a significant effect on the response of the system. If the tower is assumed to act as a mass-spring system, a value for the mass may be calculated from equation 7.1 (Halliday and Resnick, 1993) which relates the period of vibration (T) of a mass-spring system to the mass and the spring stiffness respectively.

$$T = 2\pi\sqrt{\frac{M}{k}} \qquad (7.1)$$

The period of the tower would have to be obtained experimentally, or alternatively from a finite element eigenvalue analysis of the tower.

The value used by Thomas and Peyrot for the tower stiffness is 392.4 kN, while the mass element ranges from 100 to 1000 kg.

7.3.4 Explicit vs Implicit Integration

The choice of the integration method does not have a significant effect on the results. As can be seen in Figure 7.5 above, the histories of the insulator force are virtually identical for the explicit and implicit integration techniques, where linear beam elements are used. The two main differences between these two methods, are firstly that the explicit scheme does not support any beam elements other than the 2-noded linear versions, and secondly, that the explicit scheme is significantly faster in terms of computational effort. When 50 linear beam elements are used to model each span, the amount of CPU time required is 4 and 20 minutes for the explicit and implicit techniques respectively, while 50 cubic elements with implicit integration take about 60 minutes.

The choice of integration techniques thus depends strongly on the time available for the analyses. If each of the problems can be left to run for a few hours and forgotten about, the implicit technique is ideal, especially as cubic elements would be expected to yield the most accurate results. If, on the other hand, the aim of the simulations is to obtain a number of comparative results and time is of the essence, explicit integration should be used when solving the problem.

7.4 VERIFICATION OF THE MODEL

Figure 7.8 and Figure 7.9 show the tension in insulator A for the finite element model and the numerical simulation of Thomas et al (1982) respectively. As mentioned previously, the values for the first two peaks as obtained from the experiments by Peyrot et al (1980) are 24.6 and 32 kN.

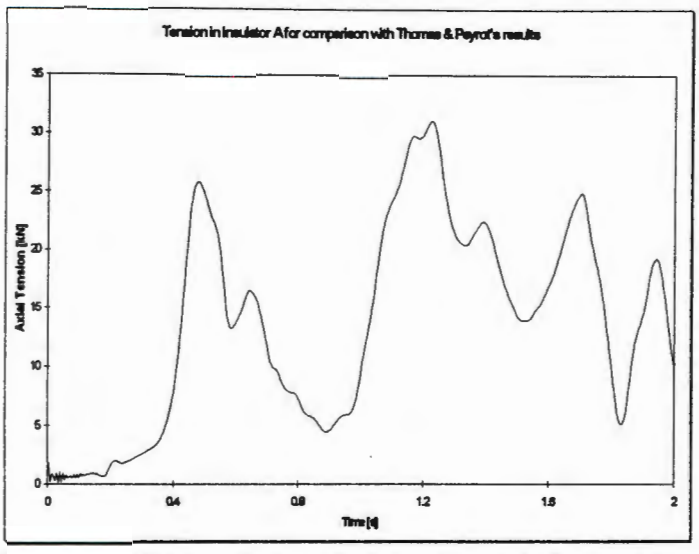

Figure 7.8: *Showing the tension in Insulator A as obtained from the finite element simulation of the experimental test performed by Peyrot et al (1980).*

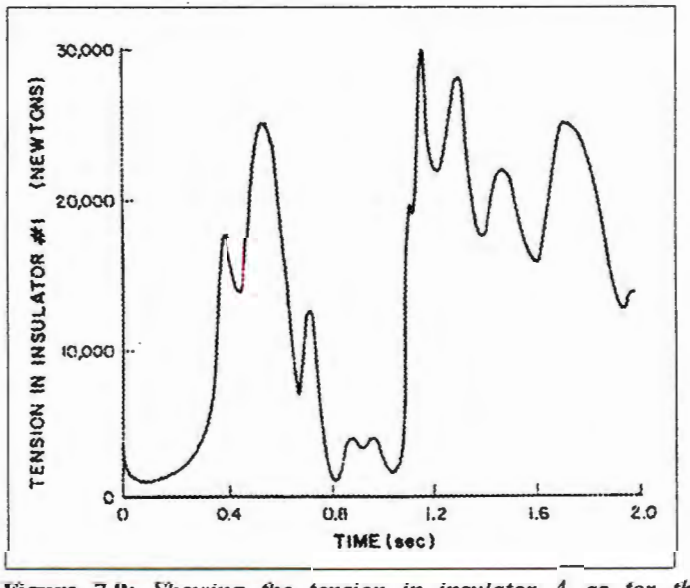

Figure 7.9: *Showing the tension in insulator A as for the numerical simulation of the test by Peyrot et al (1980) as obtained by Thomas et al (1982).*

Thomas et al state that the high frequency component superimposed on their results, with a period of 0.15 seconds, is due to the discretized masses used in their model, and should thus be ignored. They state that the second peak does not appear as a single well defined peak in their computational results as in the experimental results, which they attribute to the discretized nature of the problem.

Comparing the two figures with one another, and the peak values obtained with the experimental results, it may be concluded that the finite element model is capable of modelling the response of a transmission line after a conductor breakage with sufficient accuracy for design and research purposes.

7.5 RESULTS

The results of various finite element simulations of the breaking of a conductor are shown below. They are all based on the original test by Peyrot et al (1980), and the effects of varying the tower mass, stiffness and initial conductor tension are discussed below. Additional results of the finite element simulation of the original test are also presented and discussed.

7.5.1 Tower Mass

The reason for the inclusion of mass in the tower model is to simulate the inertial effects of the tower. The mass used, and the tower mass referred to in this chapter, is thus not the total mass of the tower but rather a mass which would have the same equivalent inertial effect as the tower.

According to Thomas and Peyrot (1982), the value chosen for the mass element does not significantly affect the response of the system, and the results obtained by Thomas et al were virtually identical for a mass of 100 and 1000 kg respectively.

From equation 7.1 above, an increase in the mass would result in an increase in the period of vibration of the tower. As can be seen from the results of shown in Figure 7.10, however, a change in the mass does not drastically affect the response of the system, in agreement with the results of Thomas and Peyrot.

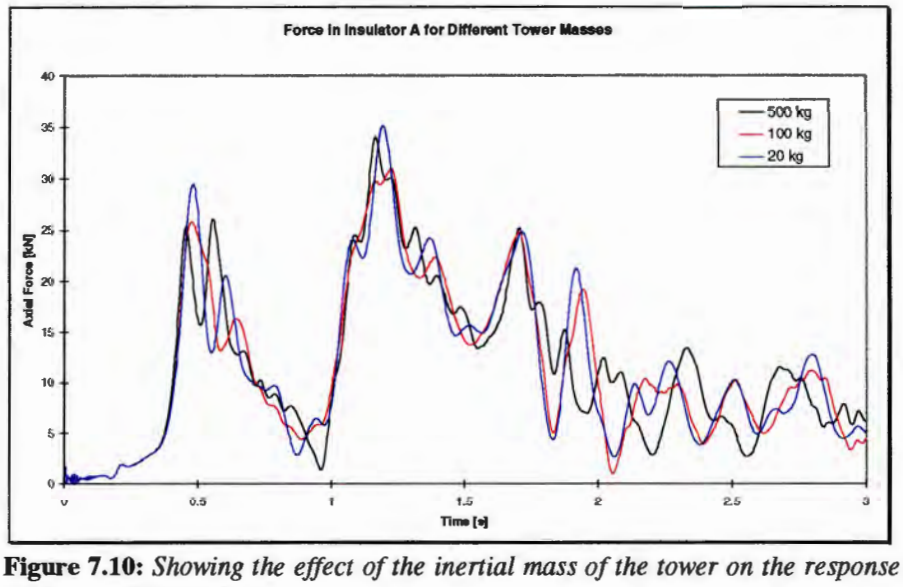

Figure 7.10: *Showing the effect of the inertial mass of the tower on the response of the transmission line.*

7.5.2 Tower Stiffness

Unlike the magnitude of the mass element, the stiffness of the tower seems to have a more significant effect on the response of the system.

As can be seen from the results of Figure 7.11, an increase in the tower stiffness causes a substantial increase in the first tension peak in the insulator. The increase in the value for the second peak is not quite as pronounced. Another difference in the results which is noticed, is that the rate of tension increase is greater as the tower becomes stiffer.

The rate at which the tension increases is probably not large enough though for rate dependent effects of the insulator material to be significant.

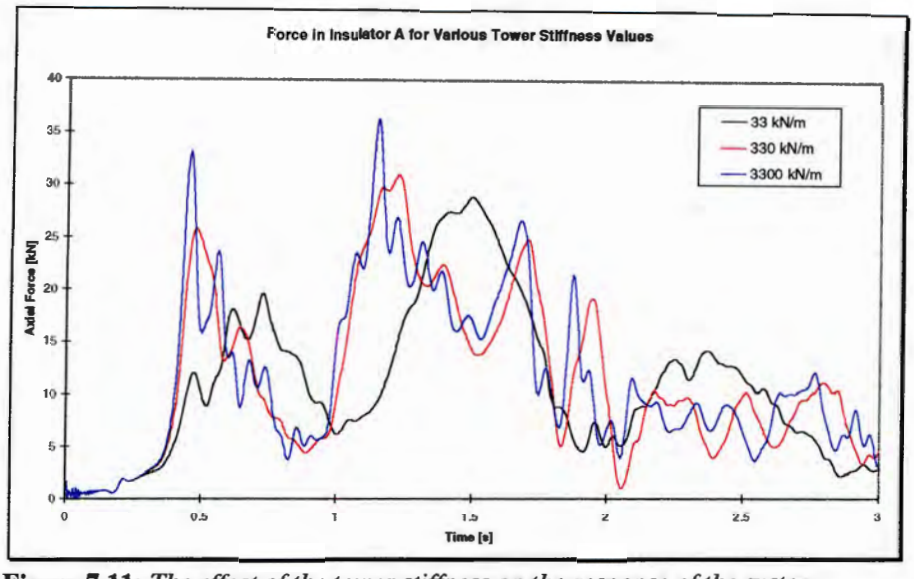

Figure 7.11: *The effect of the tower stiffness on the response of the system.*

7.5.3 Initial Conductor Tension

As expected, the peak forces in the insulator increase with an increase in the original tension of the conductor (Figure 7.12). What is interesting though, is that the impact factor, which has been used in the past (Peyrot et al, 1980, Borges et al, 1968) to quantify peak dynamic loads in terms of the initial or final conductor tensions, decreases with an increase in the initial conductor tension. The impact factor is defined as the ratio of the peak force in the insulator to the static tension in the conductor before the conductor breaks.

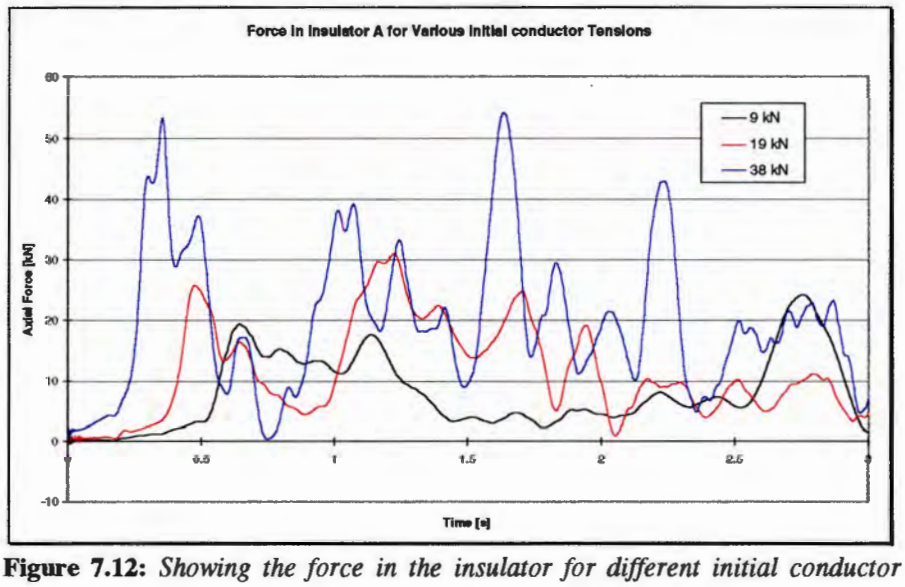

Figure 7.12: *Showing the force in the insulator for different initial conductor tensions.*

The impact factors calculated from the finite element results are given in the table below, together with values estimated from a chart of data, given by Borges et al (1968), which is shown in the paper by Peyrot et al (1980).

	Impact Factors		
Tension [kN]	FEM (3 spans)	Borges et al (2 spans)	Borges et al (1 span)
9	2.7	2.4	2.3
19	1.7	1.7	1.6
38	1.4	1.2	1.15

Table 7.2: *Showing the impact factor as obtained from the finite element simulations in comparison with those estimated from the data of Borges et al (1968), for various initial conductor tensions.*

The data by Borges et al is given only for one and two spans, whereas the finite element model has three spans. The impact factor is reported by Borges et al to increase by about 8% for each additional span

7.5.4 Displacement Profiles

Figure 7.13 shows the shape of the three spans at ½ second intervals after the conductor breaks. After 0.5 seconds the sag has increased along all three spans and a wave originates on the left hand side. This wave is set up as the insulator is pulled up, and can be seen travelling along the span during the next few intervals.

The maximum vertical displacement during the motion following the break of the conductor is approximately 6.3 metres.

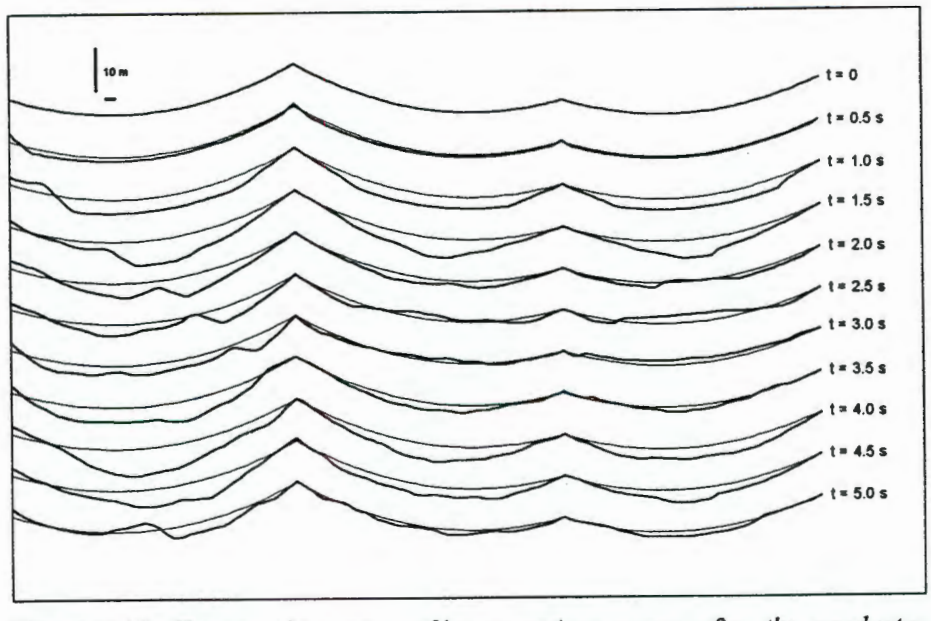

Figure 7.13: *Showing the span profiles at various stages after the conductor breaks. To give an indication of the scale, the two lines in the top left corner represent a length of 10 metres in the vertical and horizontal directions respectively.*

7.5.5 Forces at Various Locations on the Transmission Line

The force in the conductor at either end of span A and the tensions in insulators A and B are shown in Figure 7.14. The tension histories in insulator A and in the conductor at the left hand side of the span are very similar, showing that the insulator string essentially becomes part of the conductor span, and thus experiences the same tensile

loads. The force curve for the conductor at the right of span A shows a delay before the motion reaches this point in the span. What is also interesting is the small amount of compression experienced in the conductor and the insulator at the left of the first span. The peak tensions experienced in the conductor at the right of the span and in insulator B are 25 kN and 16 kN respectively.

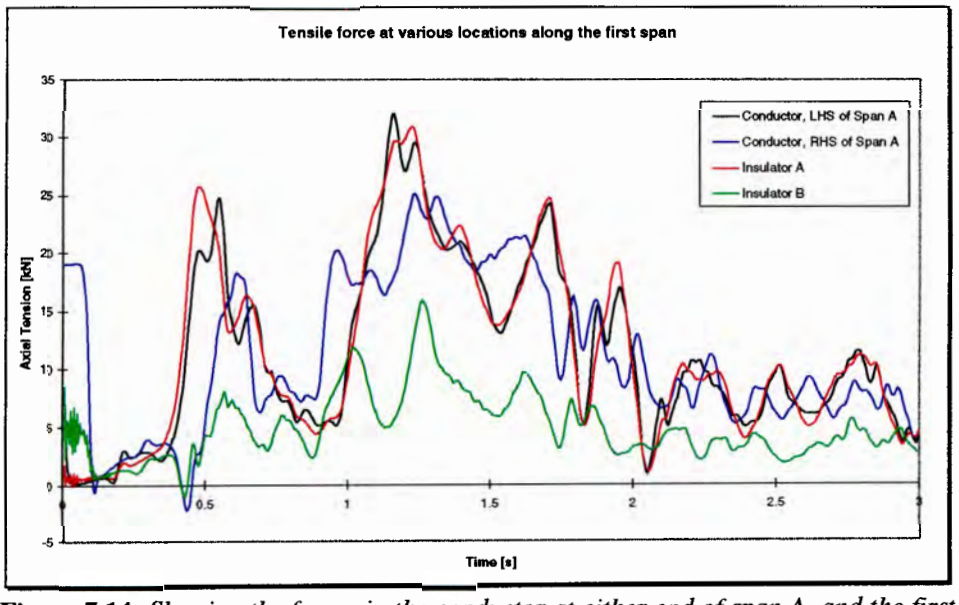

Figure 7.14: *Showing the forces in the conductor at either end of span A, and the first two insulators, A and B, respectively.*

8. CONCLUSIONS

Based on the information discussed and the results presented and analysed in this thesis, the following conclusions are drawn:

8.1 CONDUCTOR MATERIAL PROPERTIES

- The choice of bending stiffness has a significant effect on the stresses predicted by the EPRI and Poffenberger-Swart formulas.
- Even though the curvature dependent bending stiffness can be implemented by means of Papailiou's equations, it should be modified to be dependent on the change in curvature rather than the absolute curvature, to make provision for initially curved elements, as is the case with a sagging conductor.
- For aeolian vibration, the damping can be implemented by means of Rayleigh damping, with the stiffness proportional damping being estimated from existing data for the frequency of aeolian vibration, and the mass proportional damping being zero.

8.2 AEOLIAN VIBRATIONS

- Aeolian vibration of a conductor in a transmission line can be successfully modelled with the use of finite elements and the algorithm used to simulate vortex-induced loading. It has been found that 2-noded cubic elements are preferable for modelling the conductor, and that 15 elements per wavelength, corresponding to the mode of vibration for the frequency of excitation, are sufficient to model aeolian vibration.
- The effects due to drag are negligible in comparison to the gravity loads, and aeolian vibration can thus be modelled in two dimensions.
- With regards to the intensity of vibration as encountered for a single *Zebra* conductor at the Kroonstad test station, the change in curvature of the conductor is less than the minimum required for a decrease in the bending stiffness. The assumption of a maximum bending stiffness for bending relative to the static sag position is thus correct.
- The choice of boundary conditions has a significant effect on the stresses in the conductor at the end of the span, while the axial alternating stresses in the conductor strands are virtually insignificant in comparison with the alternating stresses which are caused by bending.
- The vibration amplitude of a *Zebra* conductor is a maximum in the 20 to 30 Hz frequency range, while the conductor tension does not have a significant effect on the vibration intensity for the range of tensions tested (20 to 30 kN tension).

- The mode of aeolian vibration of a symmetric span is not necessarily symmetric, and the alternating stresses in the conductor are increased if the adjacent span vibrates at a slightly different frequency.
- Dampers effectively reduce the intensity of vibration at the end of the span, however the alternating stresses are significantly increased at the points of attachment of the dampers to the conductor.

8.3 WAKE-INDUCED VIBRATIONS

- The drag force on the downwind conductor varies significantly depending on it's location relative to the upwind conductor, while the drag force on the upwind conductor does not change significantly. The lift force on the upwind conductor is negligible, while it is more significant, and varies with time, on the downwind conductor.
- The type of spacers used has a significant effect on the intensity of vibration of the whole span, and the use of flexible joints at the ends of the spacers, particularly if they include some form of internal damping, significantly reduces the intensity of wake-induced vibration.
- The conductor separation and bundle tilt do not have a significant effect on the intensity of vibration for the range of values tested, while an increase in the sub-span length significantly increases the sub-span mode of oscillation. The rolling mode is the predominate wake-induced mode of vibration in the shorter sub-spans.
- As shown, constant excitation for a number of minutes is required before significant wake-induced oscillations occur. This would be a possible explanation for the relative infrequent occurrence of wake-induced vibrations.

8.4 SHORT-CIRCUIT INDUCED CONDUCTOR MOTION

- The finite element method, including the loading sub-routine written to simulate the short-circuit current induced loads, has been successfully used to reproduce existing experimental results. The modelling of bundle pinch more complex than it seems as it is both a wave propagation and structural dynamics problem.
- Due to contact and the discretized nature of a finite element model, noise is introduced into the solution. A change in the size of adjacent elements aggravates noise and spurious oscillations into the solution, while quadratic, cubic and hybrid beam elements increase the presence of spurious modes. Linear beam elements are most adept at modelling the stress waves that propagate through the conductor, and are thus the favourite elements for the modelling of bundle pinch. A small amount of damping is however still required to eliminate spurious noise.
- It has been found that tube-to-tube contact elements are best suited to model the contact between conductors, and that the hard contact algorithm is preferable to

soft contact as the latter causes the conductors to bounce unrealistically off each other.

- With regards to the bending stiffness of the conductors, it has been found that the value chosen does not have a significant effect on the results for bundle pinch.
- An increase in the short-circuit current from 10 to 30 kA significantly increases the peak forces in the spacer, while the increase in the peak conductor tension is not quite as drastic, though still significant. Even though an increase in the initial conductor tension does not have a significant effect on the increase in the conductor tension, it does cause a noticeable increase in the maximum force in the spacer.
- For the problem modelled, an increase in the number of sub-spans from 2 to 4 increases the maximum tension in the conductor, while increasing the number of sub-spans to 6 actually reduces the peak conductor tension. The difference in the spacer force for 2 and 4 sub-spans is negligible, while the force decreases significantly with 6 sub-spans, because the conductors do not clash in this case.

8.5 MOTION RESULTING FROM A BROKEN CONDUCTOR

- The dynamic behaviour of a section of a transmission has been successfully simulated using the finite element method. Results obtained from experiments and previous numerical simulations have been satisfactorily reproduced.
- The choice of elements and integration technique (explicit vs implicit) has a negligible effect on the results and it has been found that 50 elements per span are sufficient for modelling the conductor. A small amount of damping is required to simulate internal material damping and remove spurious higher frequency noise.
- The inertia of the tower has a negligible effect on the response of the system, while a change in the tower stiffness has a more pronounced effect. The initial conductor tension significantly increases the peak force in the insulator which is located directly next to the break.

8.6 FURTHER RESEARCH

From the results shown, it can be concluded that the finite element models developed can be used with confidence for more detailed and in-depth research and design purposes. The more important constraints and limitation of the models, which the designer should be aware of, are as follows:

- Time requirements for the simulations are fairly demanding, especially for the aeolian vibration and bundle pinch simulations.
- Information on the internal damping of conductors is limited and sometimes difficult to obtain.

- As the conductor is modelled as a continuum, local effects in the strands of the conductor in the vicinity of the suspension clamps, such as plastic damage to the strands due to the conductor being clamped, are not accounted for.
- Until a material model is developed which accommodates the variable bending stiffness as a function of the change in curvature, as opposed to the actual curvature, the variable bending stiffness can not be implemented in the models.
- In the case of aeolian and wake-induced vibration, the effect of the conductor motion on the fluid characteristics is neglected due to the excessive computational effort which would be required for an interactive fluid-structural finite element model.
- Data on the wake-induced lift and drag forces is limited and the lift coefficients are assumed to be constant over time, while they would be expected to change as shown by the fluid flow simulations.

9. RECOMMENDATIONS

The following recommendations on the finite element models, which are thought to be the most important and relevant to future research, are made along with a few recommendations on practical considerations for the construction of a transmission line.

Conductor Material Properties

- A material model should be generated to accommodate the variable bending stiffness of a conductor, not only for initially straight, but also initially curved elements.

Aeolian Vibration

- The effect of conductor tensions should be evaluated for a range of vibration frequencies.
- The effect of vibration of the adjacent spans should be studied for a greater range of vibration frequencies.
- The increase in the alternating stresses introduced in the conductor at the point of attachment of the dampers should be studied in more detail.

Wake-Induced Vibration

- The fluid flow simulations should be carried out for a longer period of time to study the development of the flow over two conductors over a longer period of time.
- A larger data-base of lift and drag forces for a range of wind velocities should be generated by carrying out more fluid flow simulations.
- Spacers with flexible joints with inherent damping should be used to limit vibration intensity.
- Sub-spans should be kept as short as possible to limit sub-span oscillations.

Bundle Pinch

- Linear beam elements should be used to model the conductor, and the length of elements should be constant.

Breaking Conductors

- The model for breaking conductors should be extended to include failure criteria of towers and other hardware. The finite element model can be used to obtain estimates of the load histories on towers and insulators. These force histories can then be applied to finite element models of towers during the design stages to monitor their response to the loading.
- Care should be taken with conductor spacing when bundle pinch is of concern. Depending on the magnitude of the short-circuit fault current expected and the tension in the conductor, the peak forces in the spacers and in the conductor

during a short-circuit could be more severe for some sub-span lengths than others.

REFERENCES

Aberdare Power Cables Division, Aberdare Cables (Pty) Ltd South Africa, *Catalogue of Conductors.*

Acheson, D.J., *Elementary Fluid Dynamics*, Oxford University Press, New York, 1990

Agelink, G., "Results of Overhead Line Conductor Self-Damping Measurements", *Cigre Symposium paper*, no. 22-81, 1981

Atwood, A.T., et al, "Dynamic Behaviour of a 220-kV Dead-End Suspension Bus During Short-circuit", *Transactions of the American Institute of Electrical Engineers Part III:PAS*, vol.81, pp. 153-169, June 1962

Bathe, K.J., *Finite Element Procedures in Engineering Analysis*, Prentice-Hall, Englewood Cliffs, New Jersey, 1982

Belytschko, T., "An Overview of Semidiscretization and Time Integration Procedures", *Computational Methods for Transient Analysis*, vol.1, edited by Belytscko and Hughes, Elsevier Publishers, Netherlands, 1983

Biazak-Borowa, E., Flaga, A., "Quasi-Static Models of Aeorodynamic Loads on Two Circular Cylinders in Staggered Arrangement", *9ICWE*, pp.95-106, 1995

Bokaian, A., Geoola, F., "Wake Displacement as Cause of Lift Force on Cylinder Pair", *Journal of Engineering Mechanics*, vol.111, no.1, pp.92-99, January 1985

Borges, J.F., Marecos, J., Castanheta, M., " Estudo Experimental dos Esforcos Originados Pela Rotura de Conductores em Linhas de Alta Tensao", *The National Civil Engineering Laboratory*, Lisbon, Portugal, November 1968, cited by Peyrot et al (1980).

Bradbury, J., Kuska, G.F., Tarr, D.J., "Sag and Tension Calculations in Mountainous Terrain", *IEEE Conference Publication,* no.176, Date unknown

Celep, Z., Turhan, D., "Transient Wave Propagation in Constant and Linear Strain Elements", *Journal of Sound and Vibration*, vol.116, pp.12-23, 1987

Celep, Z., Bazant, Z.P., "Spurious Reflection of Elastic Waves due to Gradually Changing Finite Element Size", *International Journal for Numerical Methods in Engineering*, vol.19, pp.631-646, 1983

Chi, M., & Vossoughi, J., "Response of Slender Structural Members in Self-Excited Oscillation", *Journal of Sound and Vibration*, vol.101, no.1, pp.75-83, 1985

Chilukuri, R., "Incompressible Laminar Flow Past a Transversely Vibrating Cylinder", *Journal of Fluids Engineering*, vol.109, pp.166-171, June 1987

Cigrè Study Committee 22 - Working Group 01, "Report on Aeolian Vibration", *Electra*, no.124, pp.42-101, May 1989

Cigrè Study Committee 22 - Working Group 04, *Endurance Capability of Conductors - Final Report*, July 1988

Cigrè Study Committee 23 - Working Group 02, *The Mechanical Effects of Short-Circuit Currents in Open-Air Substations*, Paris, 1987

Claren, R., Diana, G., "Dynamic Strain Distribution on Loaded Stranded Cables", *IEEE Transactions on Power Apparatus and Systems*, vol. 88-PAS, no.11, pp. 1678-1690, Nov. 1969

Cook, R.D., D.S.Malkus, Plesha, M.E., *Concepts and Applications of Finite Element Analysis 3rd ed.*, John Wiley & Sons,USA, 1989

Craig, D.B., Ford, G.L., "The Response of a Strain Bus to Short-Circuit Currents", *IEEE Transactions on Power Apparatus and Systems*, vol.99, pp.434 - 442, March 1980

Diana, G., & Falco, M., "On the Forces Transmitted to a Vibrating Cylinder by a Blowing Fluid", *Meccanica*, vol.6, pp.9-22, 1971

Doocey, E.S., et al, *Wind-Induced Conductor Motion - Transmission Line Refernce Book*, Electric Power Research Institute, USA, 1979

Douglas, J.F., Gasiorek, J.M., Swaffield, J.A., *Fluid Mechanics 2nd ed.*, Longman Scientific & Technical, Singapore, 1985

Du Plessis, P., *Mechanical Oscillations on Overhead Transmission Lines*, Dr.(Eng.) Thesis, Johannesburg, July 1994

El-Taher, R.M., "Flow Around Two Parallel Circular Cylinders in a Linear shear Flow", *Journal of Wind Engineering and Industrial Aeorodynamics*, vol.21, pp.251-272, 1985

Feng, C.C, *The measurement of Vortex-induced effects in Flow Past Stationary and Oscillating Circular and D-section cylinders*, MSc thesis, University of British Columbia, 1968

Gerhardt, H.J, Kramer, C., "Interference Effects for Groups of Stacks", *Journal of Wind Engineering and Industrial Aeorodynamics*, vol.8, pp.195-202, 1981

Gopalan, T.V., "Fatigue Failure of Insulator String of Overhead Transmission Line", *Journal of Engineering Mechanics*, vol 117, no 1, pp 88-99, January 1991

Goswami, I., Scanlan, R.H, & Jones, N.P., "Vortex-Induced Vibration of Circular Cylinders. I: Experimental Data", *Journal of Engineering Mechanics*, vol.119, no.11, pp.2270-2287, Nov 1993

Gupta, S., et al, "Structural Failure Analysis of 345 kV Transmission Line", *IEEE Transactions on Power Delivery*, vol.9, no.2, pp.894-903, April 1994

Hagedorn, P., "On the Computation of Damped Wind-Excited Vibrations on Overhead Transmission Lines", *Ribe Mitteilungen*, Richard Bergner GmbH + Co. internal publication, Germany, no 16e, pp 5-26, 1986

Hagedorn, P., Kraus, M., "Aeolian Vibrations: Wind Energy Input Evaluated from Measurements of an Energised Transmission Line", *IEEE Transactions on Power Delivery*, vol.6, no.3, pp.1264-1269, July 1991

Halliday, D., Resnick, R., Walker, J., *Fundamentals of Physics 4th ed.*, John Wiley & Sons, USA, 1993

Herrmann, B., Stein, N., Kiessling, G., "Short-Circuit Effects in HV Substations with Strained Conductors. Systematic Full Scale Tests and a Simple Calculation Method", *IEEE Transactions on Power Delivery*, vol.4, no.2, pp. 1021-1028, April 1989

Hibbitt Karlsson & Sorensen Inc., *ABAQUS V5.4 Theory Manual*, USA, 1994a

Hibbitt Karlsson & Sorensen Inc., *ABAQUS V5.4 Standard User Manual*, USA, 1994b

Hibbitt Karlsson & Sorensen Inc., *ABAQUS V5.4 Explicit User Manual*, USA, 1994c

Hurlbut, S.E., Spaulding, M.L., White, F.M., "Numerical Solution for Laminar Two Dimensional Flow about a Cylinder Oscillating in a Uniform Stream", *Journal of Fluids Engineering*, vol.104, pp.214-222, June 1982

IEC Publication 909. *Short-circuit Current Calculation in Three Phase AC-Systems*. Geneva, 1988

IEEE Committee report, "Standardisation of Conductor Vibration Measurements", *IEEE Transactions on Power Apparatus and Systems*, vol 85, , pp 10-22 no 1, January 1966

Jiang, L., Rogers, R.J., "Spurious Wave Reflection at the Contact Interface for Finite Element Impact analysis", *Journal of Sound and Vibration*, vol.143, pp. 221-230, 1990a

Jiang, L., Rogers, R.J., "Effects of Spatial Discretization on Dispersion and Spurious Oscillations in Elastic Wave Propagation", *International Journal for Numerical Methods in Engineering*, vol. 29, pp.1205-1218, 1990b

Karl Pfisterer, *Spacer Damper Catalogue on AV Spacer Dampers*, publication date and other details unknown

Kommenda, R.A., Swart, R.L., "Interpretation of Field Vibration Data", *IEEE Transactions on Power Apparatus and Systems*, vol. PAS-87, no.4, pp.1, April 1968, cited by Papailiou (1995a)

Li, J., Sun, J., Roux, B., "Numerical Study of an Oscillating Cylinder in Uniform Flow and in the Wake of an Upstream Cylinder", *Journal of Fluid Mechanics*, vol.237, pp.457-478, 1992

Lilien, J.L., Dal Maso, F., "Contribution to the Line Design by Accurate Predetermination of Severe but Occasional Stresses", *Cigre Conference Paper*, no. 22-103, Paris, August 1990

Lummis, J., "Effect of Conductor Imbalance on Flexible Transmission Structures", *IEEE Transactions on Power Apparatus and Systems*, vol.PAS-88, no.11, pp.1672-1678, November 1969

Manuzio, C., "An investigation into the Forces on Bundle Conductor Spacers under Fault Conditions", *IEEE Transactions on Power Apparatus and Systems*, vol. PAS-86, no.2, pp.166-184, 1965

McConnell, K.G, Zemke, W.P., "The Measurement of Flexural Stiffness of Multistranded electrical Conductors while under Tension", *Experimental Mechanics*, vol., pp.198-20420, June 1980

McDonald, B., Peyrot, A., "Sag-Tension Calculations Valid for Any Line Geometry", *Journal of Structural Engineering*, vol.116, no.9, pp. 2374-2387, 1990

McGill, P.B., Ramey, G.E., "Effect of Suspension Clamp Geometry on Tranmsisison Line Fatigue", *Journal of Energy Engineering*, vol. 112, no.3, pp.168-185, December 1986

Miri, A.M., Sihler, C., Stein, N., "Influence of Electromagnetic Forces on Flexible Conductors in High Voltage Substations", *ABAQUS Users' Conference Proceedings*, Aachen, Germany, pp. 453-466, June 1993

Möcks, L., "On the Calculation of Alternating Bending Strain in an Oscillating Conductor", *Ribe Mitteilungen*, Richard Bergner GmbH + Co. internal publication, Germany, no. 16e, pp.45-54, 1986

Möcks, L., "Subspan length of Bundle conductors", *Ribe Mitteilungen* (Richard Bergner GmbH + Co internal company publication), no 9e, 1972

Möcks, L., "Damping of High-Voltage Overhead Conductor Vibrations", *ETZ-Report 15e*, VDE-Verlag, Berlin, 1984

Möcks, L., "Die Beanspruchung und Lebensdauer von Leiterseilen unter dem Einfluß winderregter Schwingungen", *Ribe Mitteilungen*, Richard Bergner GmbH + Co. internal publication, Germany, no 17, pp 3-10, 1988

Noiseux, D.U., "Similarity Laws of the Internal Damping of Stranded Cables in Transverse Vibrations", *Proceedings of the 1991 IEEE Power Engineering Society Transmission and Distribution Conference*, September 1991

Oliveira, R.E, & Freire, D.G., "Dynamic modelling and Analysis of Aeolian Vibrations of Single Conductors", *IEEE Tansactions on Power Delivery*, vol 9, no 3, pp 1685-1693, July 1994

Papailiou, K.O., *Die Seilbiegung mit einer durch die innere Reibung, die Zugkraft und die Seilkrümmung veränderlichen Biegesteifigkeit*, Diss. ETH Nr. 11057, 1995a

Papailiou, K.O., *On the Bending Stiffness of Transmission Line Conductors*, Switzerland, 1995b

Peyrot, A., et al, "Analysis of Flexible Transmission Lines", *Journal of the Structural Division*, vol.104, no. ST5, pp.763-779, May 1978

Peyrot, A., et al, "Longitudinal Loads from Broken Conductors and Broken Insulators and their Effect on Transmission Lines", *IEEE Transactions on Power Apparatus and Systems*, vol.PAS-99, no.1, pp.222-231, Jan/Feb 1980

Poffenberger, J.C., *Conductor Fatigue in Overhead Lines*, Published by Preformed Line Products, U.S.A.

Prathap, G., Naganarayana, B.P., "Analysis of Locking and Stress Oscillations in a General Curved Beam element", *International Journal for Numerical Methods in Engineering*, vol. 30, pp.177-200, 1990

Ramey, G.E., Duncan, R.R., Brunair, R.M., "Experimental Evaluation of S-N Curves for Drake ACSR Conductor", *Journal of Energy Engineering*, vol. 112, no.2, pp.138-151, August 1986

Raoof, M., Huang, Y.P., "Axial and free bending analysis of spiral strands made simple"., *Journal of Engineering Mechanics*, vol. 118, no. 12, pp.2335 - 2351, Dec. 1992

Sarpkaya, T., & Kline, H.K., "Impulsively-Started Flow about four types of bluff-Body", *Journal of Fluids Engineering*, vol.104, pp.207-213, June 1982

Sayers, A.T., *Fluid Mechanics: An Introduction*, Oxford University Press, Cape Town, 1992

Scanlan, R.H., Swart, R.L., "Bending Stiffness and Strain in Stranded Cables", *IEEE conference paper* C68 43-PWR, 1968

Schäfer, B., "Dynamic Modelling of Wind-Induced Vibrations of Overhead Lines", *International Journal of Non-Linear Mechanics*, vol.19, no.5, pp.455-467, 1984

Seppa, T.O., "Measurements of Bending Stiffness of Transmission Conductors in the Free span and Near the Ends of the Span", *Presentation to Cigre SC 22*, WG 11, September 1995

Shigley, J.E., *Mechanical Engineering Design 1st metric ed.*, McGraw-Hill Inc., Singapore, p 268, 1986

Simmons, J.M., Cleary, P.M., "Measurement of Aeorodynamic Power Associated with Vortex-Induced Vibration of Electrical Transmission Lines", *IEEE Transactions on Power Apparatus and Sytems*, vol.PAS -99, no.1, pp.158-164, Jan/Feb 1980

Staubli, T., "Calculation of the Vibration of an elastically mounted cylinder using experimental Data from Forced oscillation", *Journal of Fluids Engineering*, vol. 105, pp. 225-229, June 1983

Sturm, R.G., "Vibration of Cables and Dampers - Part I", *Journal of the American Institite of Electrical Engineers*, vol 55, pp 455-465, May 1936

Thomas, M.B., Peyrot, A., "Dynamic Response of Ruptured Conductors in Transmission Lines", *IEEE Transactions on Power Apparatus and Systems*, vol.PAS-101, no.9, pp.3022-3027, September 1982

Timoshenko, S., Young, D.H., Weaver, W., *Vibration Problems in Engineering 4th edition.*, John Wiley and Sons Inc., USA, 1974

van Wees, "Simulation of the Dynamic Response of Structures for very Short Load Durations", *ABAQUS Users' Conference Proceedings*, Italy, pp.267-274, May 1989

Zdravkovich, M.M., "Review: Review of Flow Interference Between Two Circular Cylinders in Various Arrangements", *Journal of Fluids Engineering*, pp.618-633, December 1977

Zdravkovich, M.M., Pridden, D.L., "Interference Between Two Circular Cylinders - Series of Unexpected Discontinuities", *Journal of Industrial Aeorodynamics*, vol.2, pp.255-270, 1977

APPENDIX A

The Equation of Motion of a Taut Cable (Möcks, 1988)

The equation governing the motion of a taut cable in a plane, with its axis in the x-direction, and vertical movement limited to a plane, is governed by the following fourth order differential equation:

$$EI\frac{\partial^4 w}{\partial x^4} - T\frac{\partial^2 w}{\partial x^2} + m\frac{\partial^2 w}{\partial t^2} = 0 \qquad \text{(A.1)}$$

where

T - tension (N)
EI - bending stiffness (N.m^2)

Assuming the above equation can be written as a product of a function which is only dependent on time, and another which is totally dependent on x, i.e.

$$w(x,t) = W(x)\cdot f(t) \qquad \text{(A.2)}$$

the differential can be separated and rewritten as two separate equations:

$$EI\frac{d^4 W(x)}{dx^4} - T\frac{d^2 W(x)}{dx^2} - \omega^2 m W(x) = 0 \qquad \text{(A.3)}$$

$$\frac{d^2 f(t)}{dt^2} + \omega^2 f(t) = 0 \qquad \text{(A.4)}$$

The general solution of equation A.3 has the following form:

$$W(x) = A\cdot e^{-\alpha\cdot x} + B\cdot e^{\alpha\cdot x} + C\cdot\sin(\beta\cdot x) + D\cdot\cos(\beta\cdot x) \qquad \text{(A.5)}$$

with
$$\alpha = \sqrt{\frac{T}{2EI} + \sqrt{\left(\frac{T}{2EI}\right)^2 + \frac{m\omega^2}{EI}}} \qquad \text{(A.6)}$$

and
$$\beta = \sqrt{-\frac{T}{2EI} + \sqrt{\left(\frac{T}{2EI}\right)^2 + \frac{m\omega^2}{EI}}} \qquad \text{(A.7)}$$

A, B, C and D are constants to be determined for the relevant boundary conditions.

For the case where both ends are clamped, the following boundary conditions hold:

$$W(0) = W(S) = \left.\frac{dW}{dx}\right|_{x=0} = \left.\frac{dW}{dx}\right|_{x=S} = 0 \qquad (A.8)$$

Substituting these boundary conditions into equation A.5 and its derivative with respect to x yields the following equation after elimination of the constants A, B, C and D:

$$\left(\cos\beta L - \frac{\alpha}{\beta}\sin\beta L\right)\cdot\left(\alpha e^{\alpha L} + \beta\sin\beta L - \alpha\cos\beta L\right) + \left(\beta\sin\beta L + \alpha\cos\beta L\right)\cdot\left(e^{\alpha L} - \cos\beta L - \frac{\alpha}{\beta}\sin\beta L\right) = 0 \qquad (A.9)$$

having assumed that L is large compared to α, i.e. $e^{-\alpha L} \Rightarrow 0$

Simplifying equation A.9 yields the following:

$$\tan\beta L = \mu \qquad (A.10)$$

where

$$\mu = \frac{4EI(m\omega^2)}{T^2} \qquad (A.11)$$

Assuming $\mu << 1$, which according to Möcks (1989) is a valid assumption for almost all conductors, equation A.10 reduces to

$$\sin\beta L = 0 \qquad (A.12)$$

which has the solution

$$\beta = \frac{n\pi}{L} \qquad n = 1,2... \qquad (A.13)$$

Substituting (A.7) into (A.13) yields the following equation for the natural frequency of vibration of the conductor span:

$$f = \frac{n}{2L}\left(\sqrt{\frac{T}{m}}\right)\left(\sqrt{1+\left(\frac{n\pi}{L}\right)^2\frac{EI}{T}}\right) \qquad (A.14)$$

which can also be rewritten as

$$f = \frac{c}{\lambda} \qquad (A.15)$$

where the transverse wave velocity c is

$$c = \left(\sqrt{\frac{T}{m}}\right)\left(\sqrt{1+\left(\frac{n\pi}{L}\right)^2 \frac{EI}{T}}\right) \qquad (A.16)$$

and the wavelength λ is

$$\lambda = \frac{2L}{n} \qquad (A.17)$$

APPENDIX B

Calculation of the Unstressed Length of a Conductor

The following equations governing the catenary shape of the conductor are given in the EPRI handbook (Doocey et al, 1979):

$$T = mgC \qquad (B.1)$$

$$C = a \cdot \cosh\frac{S}{2a} \qquad (B.2)$$

$$D = C - a \qquad (B.3)$$

$$l = 2a \cdot \sinh\frac{S}{2a} \qquad (B.4)$$

where

- T - Tension in conductor at the supports (N)
- C - distance of support from the directrix of the catenary (m)
- m - mass per unit length of conductor (kg/m)
- g - gravitational constant (m/s^2)
- a - catenary constant (m)
- S - span length (m)
- D - sag in the middle of the span (m)
- l - length of the tensioned conductor (m)

For demonstrative purposes, the original unstressed length of the conductor is calculated using the following data:

$S = 400$ m
$g = 9.81$ m/s^2
$m = 1.63$ kg/m
$T = 20$ kN.

From equation B.1, the value for C is calculated as 1250.8 metres. The constant a is then found by finding the roots of equation B.2, giving a value of $a = 1234.56$ m.

The sag in the centre of the span is thus 16.24 metres. Equation B.4 then gives the length of the conductor as 401.75 m.

The axial strain in the conductor (ε) is

$$\varepsilon = \frac{l - l_0}{l_0} \qquad (B.5)$$

and

$$\varepsilon = \frac{\sigma}{E} = \frac{T}{A \cdot E} \qquad (B.6)$$

with the cross-sectional area of the conductor given by A, and the axial elastic modulus by E.

Substituting the appropriate values into equation B.6, and solving for l_0 in equation B.5, the original unstressed length of the conductor is calculated as $\boldsymbol{l_0 = 401.28}$ **m.**

APPENDIX C

Vibration Field Data

The following tables show data obtained from Du Plessis Thesis (1994) for the vibration data of a single *Zebra* conductor as recorded at the Kroonstad test station. The vibration amplitude of the conductor is measured 89mm from the last point of contact with the suspension point, and the data is given as the peak to peak amplitude of vibration.

Frequency	Vibration Amplitude (μm peak to peak)							
[Hz]	68	135	203	270	338	405	473	540
8.8	3632	3450	1333	231	24	12	1	0
17.6	18906	3335	1898	1744	228	95	43	20
26.4	24722	2087	961	922	140	69	43	6
35.2	20605	408	158	110	19	7	0	1
43.9	17962	0	0	0	0	0	0	0
52.7	9177	0	0	0	0	0	0	0

Frequency	Vibration Amplitude (μm peak to peak)							
[Hz]	608	675	743	810	878	945	1013	1080
8.8	0	0	0	0	0	0	0	0
17.6	12	9	6	0	2	0	3	17
26.4	7	10	17	7	0	36	8	0
35.2	11	1	0	0	0	0	0	0
43.9	0	0	0	0	0	0	0	0
52.7	0	0	0	0	0	0	0	0

APPENDIX D

Code for ABAQUS User-Defined Loading Subroutines

The FORTRAN 77 code for the loading subroutines used in the ABAQUS finite element simulations is given below. The code is given for the aeolian vibration, short-circuit current, and wake-induced vibration subroutines respectively.

Aeolian Vibration

```
      subroutine DLOAD(f,kstep,kinc,time,noel,npt,layer,kspt,coords,
     &                 jltyp)
************************************************************************
*  Program:       subroutine for use in ABAQUS to specify aeolain wind  *
*                 loading of a HV transmission line conductor.          *
*  Developer:     G.C.Kruse, Cerecam, UCT                               *
*  Date:          February, 1996                                        *
*                                                                       *
*  variables in common block CBLOCK:                                    *
*        numel:          no. of elements                                *
*        numint:         no. of load intergration points per element    *
*        lasttime:       previous time increment                        *
*        theta:          phase adjustment angle for loading             *
*        frqcount:       number of cycles since theta was last adjusted *
*        kinclast:       previous increment number                      *
*                                                                       *
*  variables to be defined by the user:                                 *
*        phi:      phase difference between loading and displacement    *
*        w:        freqeuncy (rad/s) of vortex shedding                 *
*        F0:       magnitude of load from lift equation                 *
*        adjfreq:  number of cycles until new theta is calculated       *
*        firstel:  lowest element no. of loaded elements                *
*        elmon:    element number to be monitored                       *
************************************************************************
c
      include 'ABA_PARAM.INC'
c
      integer     numel,numint,frqcount,elmon,orind
      Parameter   (numel=900,numint=3)
      real*8      ulast,lasttime,theta,flast,dulast
c
      integer     ind,adjfreq,istat,kinclast,firstel
      real*8      u,du,dt,phi,pi,w,F0,mu,div
      parameter   (pi = 3.14159)
c
      common/CBLOCK/  lasttime(numel,numint,2),
     &      frqcount(numel,numint,2),ulast(numel,numint,2),
     &      theta(numel,numint,2),kinclast(numel,numint),
     &      flast(numel,numint,2),orind(numel,numint),
     &      dulast(numel,numint,2)
c
      dimension   time(2),coords(3)
```

```
c
c---  check loading type,number of elements, no. of intergration points.
c
      if(noel.gt.numel) goto 97
      if(npt.gt.numint) goto 98
      if(jltyp.ne.42) goto 99
c
c---  !!!!!!!!!!       ASSIGN PROBLEM DATA        !!!!!!!!!!
c
      phi = pi/2.0
      w = 14.805*2.0*pi
      F0 = 0.024
      adjfreq = 2
      firstel = 1
      elmon = 900
c
c---  initialise variables
c
      ind = 0
      u = coords(2)
c
c---  initialise variables in common block if first increment
c
      if((time(1).lt.(0.01)).and.(orind(noel,npt).ne.1)) then
         ulast(noel,npt,2) = coords(2)
         theta(noel,npt,2) = phi
         frqcount(noel,npt,2) = 0
         kinclast(noel,npt) = 0
         orind(noel,npt) = 1
         goto 80
      endif
c
c---  update control values if new increment
c
      if(kinc.gt.kinclast(noel,npt)) then
         lasttime(noel,npt,1) = lasttime(noel,npt,2)
         ulast(noel,npt,1) = ulast(noel,npt,2)
         frqcount(noel,npt,1) = frqcount(noel,npt,2)
         theta(noel,npt,1) = theta(noel,npt,2)
         dulast(noel,npt,1) = dulast(noel,npt,2)
         flast(noel,npt,1) = flast(noel,npt,2)
      endif
      dt = time(1) - lasttime(noel,npt,1)
      du = u-ulast(noel,npt,1)
c
c---  check whether previous displacement was maximum
c
      ind = 0
      if((du.lt.0).and.(dulast(noel,npt,1).gt.0)) ind = 1
c
c---  if maximum then update phase difference
c
      if(ind.eq.1)
     &   frqcount(noel,npt,2) = frqcount(noel,npt,1) + 1
c
      if(frqcount(noel,npt,2).lt.adjfreq) goto 90
      frqcount(noel,npt,2) = 0
      div = ABS(du/dulast(noel,npt,1))
      if(div.lt.(0.01)) then
         mu = 1.5
      elseif(div.gt.100) then
         mu = 0.5
      else
         mu = 1.0 - (0.25*LOG10(div))
```

```
      endif
      theta(noel,npt,2) = (phi+(w*((mu*dt) - time(1)))+(pi/2.0))
      if(abs(theta(noel,npt,2)).gt.(2.0*pi))
     &      theta(noel,npt,2) = mod(theta(noel,npt,2),(2.0*pi))
      goto 90
c
c---  update info for time = 0
c
 80   continue
      ulast(noel,npt,1) = ulast(noel,npt,2)
      theta(noel,npt,1) = theta(noel,npt,2)
      frqcount(noel,npt,1) = frqcount(noel,npt,2)
      f = F0*sin(w*time(1) + theta(noel,npt,2))
      if ((noel.eq.elmon).and.(npt.eq.1)) then
       open(unit=99,file='/k2/gckruse/clamp/res.dat',status=
     &       'NEW',iostat=istat,access='SEQUENTIAL')
         if(istat.ne.0) then
            write(6,*) '***error no. ',istat,'opening file'
            call xit
         endif
c
c---  write data to file for first increment
c
         write(99,490) 'inc','time','disp','load'
         write(99,490) '---','----','----','----'
         write(99,500) kinclast(noel,npt),lasttime(noel,npt,1),
     &   ulast(noel,npt,1),flast(noel,npt,1)
 490  format(1x,a3,2x,a4,5x,a4,6x,a4)
      endif
c
c---  calculate load and update ulast
c
 90   continue
      f = F0*sin(w*time(1) + theta(noel,npt,2))
      lasttime(noel,npt,2) = time(1)
      ulast(noel,npt,2) = coords(2)
c
c---  write data to file 'res.dat' for subsequent increments
c
      if ((kinc.gt.kinclast(noel,npt)).and.(noel.eq.elmon).and.
     &             (npt.eq.1)) then
         if (kinc.ne.1) then
          open(unit=99,file='/k2/gckruse/clamp/res.dat',status=
     &      'old',iostat=istat,access='sequential')
         endif
c
         if(istat.ne.0) then
            write(6,*)'*** error no. ',istat,' opening file again'
            call xit
         endif
         if(kinc.gt.1) then
            write(99,500) kinclast(noel,npt),lasttime(noel,npt,1),
     &      ulast(noel,npt,1),flast(noel,npt,1)
         endif
 500    format(i4,1x,f6.4,1x,10(f10.7,1x))
        close(unit=99)
      endif
c
c---  update variables
c
      dulast(noel,npt,2) = du
      flast(noel,npt,2) = f
      kinclast(noel,npt) = kinc
      goto 100
```

```
c
c---  error messages and escape
c
 97   continue
      write(6,*) '*** Number of elements numel needs to be',
     &           ' increased ***'
      call xit
 98   continue
      write(6,*) '*** Number of intergration points per element',
     &           ' exceeds that specified in numint ***'
      call xit
 99   continue
      write(6,*) '*** Incorrect loading specified for dload subrouti',
     &           'ne ***'
      call xit
c
100   continue
      return
      end
```

Short-circuit Loading

```
      Subroutine DLOAD(f,kstep,kinc,time,noel,npt,layer,kspt,coords,
     &                 jltyp)
************************************************************************
*   Program:    subroutine for use in ABAQUS to specify short-circuit  *
*               current loading on a HV transmission line bundle.      *
*   Developer:  G.C.Kruse, Cerecam, UCT                                *
*   Date:       April, 1996                                            *
*                                                                      *
*   variables:                                                         *
*         cond:       number of the conductor in the bundle            *
*         numel:      no. of elements                                  *
*         numint:     no. of load intergration points per element      *
*         cordlast:   array containing the previos coordinates of each *
*                       point                                          *
*         kinclast:   last increment number                            *
*         elincond:       element no ... of the conductor ncond        *
*         ncond:      current conductor for which force is being calc. *
*         noelnew:    internal element number assigned to reduce common*
*                       block size                                     *
*         find:       force component indicator:                       *
*                     -1: y component (jltyp=42)                       *
*                     -2: z component (jltyp=43)                       *
*         mu0:        permetivity constant                             *
*           R:          distance between conductors A anb B            *
*           ia,ib:      current in condutcors a,b repectively          *
*                                                                      *
*   variables to be defined by user:                                   *
*         frq:        freqeuncy (Hz)of AC current                      *
*         istar:  initial symmetrical short circuit current            *
*         Tau:        Time decay constant                              *
*         elmon:      element number to be monitored                   *
*         cond:       number of conductors in the bundle               *
*         nelcon:     number of elements making up each conductor      *
*                                                                      *
*   remarks:                                                           *
*   ========                                                           *
*   orientation of the bundle: The FEM should be generated so that     *
*      the conductor span runs along the x-axis.                       *
*                                                                      *
*   numbering of conductors: When viewing the conductor bundle in      *
*      cross-section, from the origin outwards along the positive      *
*      x-axis, then conducor 1 is at the 3 o'clock position. The       *
*      remaining conductors are numbered in a counter-clockwise        *
*      sequence.                                                       *
*                                                                      *
*   element numbering: The element numbers making up conductor no.1    *
*      should range from 1 to 10 000, for conductor no. 2 from 10 001  *
*      to 20 000, etc.                                                 *
************************************************************************
c
      include 'ABA_PARAM.INC'
c
      integer     numel,numint,elmon,istat,ncond,kinclast,nelcon,
     &            noelnew,find,elincond,partB
      real*8      cordlast,pi,frq,w,cond,lasttime,ia,ib,mu0,istar,Tau
      parameter   (numel=700,numint=3,elmon=15 ,cond=2,nelcon=320)
      parameter   (pi=3.14159,frq=50.,istar=15000.,Tau=0.06)
c
      common/CBLOCK/    cordlast(numel,numint,3,2),
     &                  kinclast(numel,numint),
     &                  lasttime(numel,numint,2),
```

```
     &                    flast(numel,numint,2,2)
c
      dimension   time(2),coords(3)
c
c---  determine conductor number
c
      ncond = 0
      do i=1, cond
         if((noel.gt.((i-1)*10000)).and.(noel.lt.(i*10000))) ncond = i
      enddo
      if(ncond.eq.0) goto 96
c
c---  assign internal element number
c
      elincond = noel - ((ncond-1)*10000)
      partB = (ncond-1)*nelcon
      noelnew = elincond + partB
c
c---  check loading type,number of elements, no. of intergration points.
c
      if(noelnew.gt.numel) goto 97
      if(npt.gt.numint) goto 98
      if((jltyp.ne.42).and.(jltyp.ne.43)) goto 99
      if(jltyp.eq.42) find = 1
      if(jltyp.eq.43) find = 2
c
c---  convert frequency from Hz to rad/s, calculate mu0
c
      w = frq*2.0*pi
      mu0 = 4.0*pi*1.0E-7
c
c---  if zero'th increment, set indicator, update cordlast etc.
c
      if(time(1).lt.(1.E-7)) then
         kinclast(noelnew,npt) = 0
         lasttime(noelnew,npt,1) = 0
         flast(noelnew,npt,find,1) = 0
         do i=1, 3
            cordlast(noelnew,npt,i,1) = coords(i)
         enddo
         if ((noel.eq.elmon).and.(npt.eq.1).and.(jltyp.eq.43)) then
            open(unit=198,file='/k2/gckruse/sc/scl.mon',status=
     &           'new',iostat=istat,access='SEQUENTIAL')
            if(istat.ne.0) then
               write(6,*) '***error no. ',istat,'opening file'
               call xit
            endif
c
c---  write data to file for first increment
c
            write(198,*) cordlast(noelnew,npt,2,1),
     &        cordlast(noelnew+200,npt,2,1)
         endif
         close(unit=198)
         goto 92
      endif
c
c---  update control values if new increment
c
      if((ncond.eq.1).and.(kinc.gt.kinclast(noelnew,npt))) then
         lasttime(noelnew,npt,1) = lasttime(noelnew,npt,2)
         flast(noelnew,npt,find,1) = flast(noelnew,npt,find,2)
         do i=1, cond
            nel = ((i-1)*nelcon) + elincond
```

```
            do j=1, 3
               cordlast(nel,npt,j,1) = cordlast(nel,npt,j,2)
            enddo
         enddo
      endif
c
c---  calculate current in conductor, load
c
 90   continue
        ia = SQRT(2.)*istar*(SIN((w*time(1))-
     &         (pi/2.0))+((2.718)**(-time(1)/Tau)))
        ib = ia
c
        f = 0.
        fy = 0.
        fz = 0.
      do i=1, cond
c
c---    no contribution to force on conductor from itself
c
           if(ncond.eq.i) goto 91
c
c---    internal element number of element in conductor i
c
           noelB = ((i-1)*nelcon) + elincond
c
c---    a,b: coordinates of conductor experiencing, and
c---         contributing to, the load respectively
c
         ya = cordlast(noelnew,npt,2,1)
         za = cordlast(noelnew,npt,3,1)
         yb = cordlast(noelB,npt,2,1)
         zb = cordlast(noelB,npt,3,1)
c
           y = yb - ya
           z = zb - za
           R = SQRT((y**2) + (z**2))
           Fab =(ia*ib*mu0)/(2.0*pi*R)
c
           fy = fy + ((y*Fab)/R)
           fz = fz + ((z*Fab)/R)
 91        continue
        enddo
        goto 93
 92     continue
        fy = 0
        fz = 0
 93     continue
        if(jltyp.eq.42) f = fy
        if(jltyp.eq.43) f = fz
c
c---  write data to file 'result' for subsequent increments
c
      if ((kinc.gt.kinclast(noelnew,npt)).and.(noel.eq.elmon).and.
     &              (npt.eq.1).and.(jltyp.eq.43)) then
         if (kinc.ge.1) then
            open(unit=198,file='/k2/gckruse/sc/sc1.mon',status=
     &      'old',iostat=istat,access='sequential')
         endif
c
         if(istat.ne.0) then
            write(6,*)'*** error no. ',istat,' opening file again'
            call xit
         endif
```

```
          if(kinc.ge.1) then
             write(198,*) cordlast(noelnew,npt,2,1),
     &        cordlast(noelnew+200,npt,2,1), fy, fz
          endif
           close(unit=198)
        endif
c
c---    update variables
c
        lasttime(noelnew,npt,2) = time(1)
        do i=1, 3
           cordlast(noelnew,npt,i,2) = coords(i)
        enddo
        flast(noelnew,npt,find,2) = f
        kinclast(noelnew,npt) = kinc
        goto 100
c
c---    error messages and escape
c
 96     continue
        write(6,*) '*** Element numbering and number of conductors',
     &             ' specified in bundle dont correspond ***'
        call xit
 97     continue
        write(6,*) '*** Number of elements numel needs to be',
     &             ' increased ***'
        call xit
 98     continue
        write(6,*) '*** Number of intergration points per element',
     &             ' exceeds that specified in numint ***'
        call xit
 99     continue
        write(6,*) '*** Incorrect loading specified for dload subrouti',
     &             'ne ***'
        call xit
c
100     continue
        return
        end
```

Wake-Induced Vibration

```
      Subroutine DLOAD(f,kstep,kinc,time,noel,npt,layer,kspt,coords,
     &                 jltyp)
************************************************************************
*   Program:    subroutine for use in ABAQUS to specify the loads on a *
*               leeward conductor in the wake of a wind ward one.      *
*   Developer:  G.C.Kruse, Cerecam, UCT                                *
*   Date:       July, 1996                                             *
*                                                                      *
*   variables:                                                         *
*         cond:       number of the conductor in the bundle            *
*         numel:      no. of elements                                  *
*         numint:     no. of load intergration points per element      *
*         cordlast:   array containing the previos coordinates of each *
*                       point                                          *
*         kinclast:   last increment number                            *
*         elincond:       element no ... of the conductor ncond        *
*         ncond:      current conductor for which force is being calc. *
*         noelnew:    internal element number assigned to reduce common*
*                       block size                                     *
*         find:       force component indicator:                       *
*                     -1: y component (jltyp=42)                       *
*                     -2: z component (jltyp=43)                       *
*         R:          distance between conductors A anb B              *
*                                                                      *
*   other variables to be defined:                                     *
*         elmon:      element number to be monitored                   *
*         cond:       number of conductors in the bundle               *
*         nelcon:     number of elements making up each conductor      *
*         numinfox:   number of x values for which data is available   *
*         numinfoy:   number of y values for which data is available   *
*         xinfo:      array of x values for which interpolation        *
*                     data is available                                *
*         yinfo:      array of y values for which interpolation        *
*                     data is available                                *
*         finfo:      array of force values                            *
*                                                                      *
*   remarks:                                                           *
*   ========                                                           *
*   orientation of the bundle: The FEM should be generated so that     *
*      the conductor span runs along the x-axis.                       *
*                                                                      *
*   numbering of conductors: The windward conductor is conductor       *
*      number 1, and the leeward is conductor number 2.                *
*                                                                      *
*   element numbering: The element numbers making up conductor no.1    *
*      should range from 1 to 10 000, for conductor no. 2 from 10 001  *
*      to 20 000.                                                      *
************************************************************************
c
      include 'ABA_PARAM.INC'
c
      integer     numel,numint,elmon,istat,ncond,kinclast,nelcon,
     &            noelnew,find,elincond,partB,numinfoz,numinfoy,
     &            nel,i,j,noelB,y1i,y2i,z1i,z2i
      parameter   (numinfoy=7,numinfoz=9)
      real*8      cordlast,frq,pi,w,cond,lasttime,yinfo(numinfoy),
     &            zinfo(numinfoz),finfo(2,numinfoy,numinfoz),ftemp1,
     &            ftemp2,z,y,z1,z2,y1,y2,flast,ya,yb,za,zb
      parameter   (numel=200,numint=3,elmon=1,cond=2,nelcon=20)
      parameter   (pi=3.14159)
c
```

```
      common/CBLOCK/    cordlast(numel,numint,3,2),
     &                  kinclast(numel,numint),
     &                  lasttime(numel,numint,2),
     &                  flast(numel,numint,2,2)
c
      dimension   time(2),coords(3)
c
c---  assign x, y and force data
c
      yinfo(1) = -10.
      yinfo(2) = 0.018
      yinfo(3) = 0.028
      yinfo(4) = 0.038
      yinfo(5) = 0.048
      yinfo(6) = 0.058
      yinfo(7) = 10.
      zinfo(1) = -10.
      zinfo(2) = -0.086
      zinfo(3) = -0.057
      zinfo(4) = -0.029
      zinfo(5) = 0.03
      zinfo(6) = 0.029
      zinfo(7) = 0.057
      zinfo(8) = 0.086
      zinfo(9) = 10.
c---  drag force info
      do i=1,numinfoy
     do j=1, numinfoz
        finfo(1,i,j) = 1.32
        finfo(2,i,j) = 0.
     enddo
      enddo
      finfo(1,2,5) = 0.27
      finfo(1,2,6) = 0.42
      finfo(1,2,7) = 0.90
      finfo(1,3,5) = 0.47
      finfo(1,3,6) = 0.60
      finfo(1,3,7) = 1.01
      finfo(1,4,5) = 0.63
      finfo(1,4,6) = 0.75
      finfo(1,4,7) = 1.08
      finfo(1,5,5) = 0.75
      finfo(1,5,6) = 0.85
      finfo(1,5,7) = 1.13
      finfo(1,6,5) = 0.84
      finfo(1,6,6) = 0.92
      finfo(1,6,7) = 1.14
      do i=2, 6
         finfo(1,i,3) = finfo(1,i,7)
         finfo(1,i,4) = finfo(1,i,6)
      enddo
c
c---  lift force info
c
      finfo(2,2,3) = 0.28
      finfo(2,3,3) = 0.18
      finfo(2,4,3) = 0.12
      finfo(2,5,3) = 0.07
      finfo(2,6,3) = 0.04
      finfo(2,2,4) = 0.37
      finfo(2,3,4) = 0.27
      finfo(2,4,4) = 0.18
      finfo(2,5,4) = 0.11
      finfo(2,6,4) = 0.06
```

```
      do i=2, 6
         finfo(2,i,6) = -finfo(2,i,4)
         finfo(2,i,7) = -finfo(2,i,3)
      enddo
c
c---  determine conductor number
c
      ncond = 0
      do i=1, cond
         if((noel.gt.((i-1)*10000)).and.(noel.lt.(i*10000))) ncond = i
      enddo
      if(ncond.eq.0) goto 96
c
c---  assign internal element number
c
      elincond = noel - ((ncond-1)*10000)
      partB = (ncond-1)*nelcon
      noelnew = elincond + partB
c
c---  check loading type,number of elements, no. of intergration points.
c
      if(noelnew.gt.numel) goto 97
      if(npt.gt.numint) goto 98
      if((jltyp.ne.42).and.(jltyp.ne.43)) goto 99
      if(jltyp.eq.42) find = 1
      if(jltyp.eq.43) find = 2
c
c---  if zero'th increment, set indicator, update cordlast etc.
c
      if(time(1).lt.(1.E-7)) then
         kinclast(noelnew,npt) = 0
         lasttime(noelnew,npt,1) = 0
         flast(noelnew,npt,find,1) = 0
         do i=1, 3
            cordlast(noelnew,npt,i,1) = coords(i)
         enddo
         if ((noel.eq.elmon).and.(npt.eq.1).and.(jltyp.eq.43)) then
            open(unit=198,file='/k2/gckruse/wake/wake1.mon',status=
     &           'new',iostat=istat,access='SEQUENTIAL')
            if(istat.ne.0) then
               write(6,*) '***error no. ',istat,'opening file'
               call xit
            endif
c
c---  write data to file for first increment
c
            write(198,*) cordlast(noelnew,npt,2,1),
     &        cordlast(noelnew+200,npt,2,1)
         endif
         close(unit=198)
         goto 92
      endif
c
c---  update control values if new increment
c
      if((ncond.eq.1).and.(kinc.gt.kinclast(noelnew,npt))) then
         lasttime(noelnew,npt,1) = lasttime(noelnew,npt,2)
         flast(noelnew,npt,find,1) = flast(noelnew,npt,find,2)
         do i=1, cond
            nel = ((i-1)*nelcon) + elincond
            do j=1, 3
               cordlast(nel,npt,j,1) = cordlast(nel,npt,j,2)
            enddo
         enddo
```

```
      endif
c
c---  calculate force
c
 90   continue
        f = 0.
c
c---  constant force on conductor one specified in this sub-routine
c
      if(ncond.eq.1) then
         if(find.eq.1) f=1.32
         if(find.eq.2) f=0.
         goto 93
      endif
c
c---  internal element number of element in conductor 1
c
      noelB = elincond
c
c---  a,b: coordinates of leeward, windward conductors respectively
c
      ya = cordlast(noelnew,npt,2,1)
      za = cordlast(noelnew,npt,3,1)
      yb = cordlast(noelB,npt,2,1)
      zb = cordlast(noelB,npt,3,1)
c
      y = (ya - yb)
      z = (za - zb)
c
c---  determine interpolation quantities
c
      y1 = 0.
      y2 = 0.
      y1i = 0
      y2i = 0
      z1 = 0.
      z2 = 0.
      z1i = 0
      z2i = 0
      do i=2, numinfoy
         if((y.gt.yinfo(i-1)).and.(y.le.yinfo(i))) then
           y1 = yinfo(i-1)
           y2 = yinfo(i)
           y1i = i-1
           y2i = i
         endif
      enddo
      do i=2, numinfoz
         if((z.gt.zinfo(i-1)).and.(z.le.zinfo(i))) then
           z1 = zinfo(i-1)
           z2 = zinfo(i)
           z1i = i-1
           z2i = i
         endif
      enddo
c
      ftemp1 = ((y-y1)*(finfo(find,y2i,z1i)-finfo(find,y1i,z1i))/
     &          (y2-y1)) + finfo(find,y1i,z1i)
      ftemp2 = ((y-y1)*(finfo(find,y2i,z2i)-finfo(find,y1i,z2i))/
     &          (y2-y1)) + finfo(find,y1i,z2i)
c
      f = ((z-z1)*(ftemp2-ftemp1)/(z2-z1)) + ftemp1
c
      goto 93
```

```
 92   continue
      f = 0
 93   continue
c
c---  write data to file 'result' for subsequent increments
c
      if ((kinc.gt.kinclast(noelnew,npt)).and.(noel.eq.elmon).and.
     &              (npt.eq.1).and.(jltyp.eq.43)) then
         if (kinc.ge.1) then
            open(unit=198,file='/k2/gckruse/wake/wake1.mon',status=
     &      'old',iostat=istat,access='sequential')
         endif
c
         if(istat.ne.0) then
            write(6,*)'*** error no. ';istat,' opening file again'
            call xit
         endif
         if(kinc.ge.1) then
            write(198,*) cordlast(noelnew,npt,2,1),
     &       cordlast(noelnew+200,npt,2,1)
         endif
          close(unit=198)
       endif
c
c---  update variables
c
       lasttime(noelnew,npt,2) = time(1)
       do i=1, 3
          cordlast(noelnew,npt,i,2) = coords(i)
       enddo
       flast(noelnew,npt,find,2) = f
       kinclast(noelnew,npt) = kinc
       goto 100
c
c---  error messages and escape
c
 96    continue
       write(6,*) '*** Element numbering and number of conductors',
      &           ' specified in bundle dont correspond ***'
       call xit
 97    continue
       write(6,*) '*** Number of elements numel needs to be',
      &           ' increased ***'
       call xit
 98    continue
       write(6,*) '*** Number of intergration points per element',
      &           ' exceeds that specified in numint ***'
       call xit
 99    continue
       write(6,*) '*** Incorrect loading specified for dload subrouti',
      &           'ne ***'
       call xit
c
100    continue
       return
       end
```

APPENDIX E

Example Input File for SPECTRUM

An example input data file for the air flow simulations is given below.

```
DEFINE_PROBLEM \
   name = "Twin1" \
   title = "Air flow over two conductors" \
   type = "nonlinear" \
   solid = "off" \
   fluid = "on" \
   static = "on" \
   dynamic = "off" \
   vibration = "off" \
   buckling = "off"
DEFINE_REGION \
      name = "air" \
      type = "fluid" \
      state_law_model = "air"
      DEFINE_EQUATION \
         type = "incompressible_isothermal" \
         subtype = "navier_stokes"
      COORDINATE \
         file = "/home/uct/gckruse/twin1/coords.dat.prn"
   DEFINE_REGION \
      name = "air"
      DEFINE_ELEMENT_SET \
         name = "wedge elemens" \
         type = "continuum" \
         shape = "six_node_wedge" \
         material_model = "air"
         ELEMENT_NODES \
            file = "/home/uct/gckruse/twin1/elements.dat.prn"
   DEFINE_MATERIAL_MODEL \
      name = "air" \
      type = "fluid"
      STRESS_MODEL \
         type = "constant_viscosity" \
         viscosity = 1.8e-05
         name = "air"
   DEFINE_REGION \
      name = "air"
      DEFINE_ELEMENT_SET \
         name = "hexagonal elemens" \
         type = "continuum" \
         shape = "eight_node_hex" \
         material_model = "air"
         ELEMENT_NODES \
            file = "/home/uct/gckruse/twin1/elements2.dat.prn"
      DEFINE_NODAL_BOUNDARY_CONDITION_SET \
```

```
    name = "left"
    INCLUDE_BOUNDARY_CONDITION_NODE \
      file = "/home/uct/gckruse/twin1/left.dat.prn"
    DEFINE_NODAL_BOUNDARY_CONDITION \
      type = "zero" \
      variable = "pressure" \
      mode = "on"
    DEFINE_NODAL_BOUNDARY_CONDITION \
      type = "constant" \
      variable = "x_velocity" \
      mode = "on" \
      value = 10
    DEFINE_NODAL_BOUNDARY_CONDITION \
      type = "zero" \
      variable = "y_velocity" \
      mode = "on"
  DEFINE_NODAL_BOUNDARY_CONDITION_SET \
    name = "right"
    INCLUDE_BOUNDARY_CONDITION_NODE \
      file = "/home/uct/gckruse/twin1/right.dat.prn"
    DEFINE_NODAL_BOUNDARY_CONDITION \
      type = "zero" \
      variable = "pressure" \
      mode = "on"
  DEFINE_NODAL_BOUNDARY_CONDITION_SET \
    name = "sides"
    INCLUDE_BOUNDARY_CONDITION_NODE \
      file = "/home/uct/gckruse/twin1/sides.dat.prn"
    DEFINE_NODAL_BOUNDARY_CONDITION \
      type = "zero" \
      variable = "y_velocity" \
      mode = "on"
    DEFINE_NODAL_BOUNDARY_CONDITION \
      type = "zero" \
      variable = "pressure" \
      mode = "on"
    DEFINE_NODAL_BOUNDARY_CONDITION \
      type = "constant" \
      variable = "x_velocity" \
      mode = "on" \
      value = 10
  DEFINE_NODAL_BOUNDARY_CONDITION_SET \
    name = "flats"
    INCLUDE_BOUNDARY_CONDITION_NODE \
      file = "/home/uct/gckruse/twin1/allnodes.dat.prn"
    DEFINE_NODAL_BOUNDARY_CONDITION \
      type = "zero" \
      variable = "z_velocity" \
      mode = "on"
  DEFINE_NODAL_BOUNDARY_CONDITION_SET \
    name = "cyl1"
    INCLUDE_BOUNDARY_CONDITION_NODE \
      file = "/home/uct/gckruse/twin1/cyl1.dat.prn"
    DEFINE_NODAL_BOUNDARY_CONDITION \
      type = "zero" \
      variable = "x_velocity" \
      mode = "on"
    DEFINE_NODAL_BOUNDARY_CONDITION \
```

```
        type = "zero" \
        variable = "y_velocity" \
        mode = "on"
    DEFINE_NODAL_BOUNDARY_CONDITION_SET \
      name = "cyl2"
      INCLUDE_BOUNDARY_CONDITION_NODE \
        file = "/home/uct/gckruse/twin1/cyl2.dat.prn"
      DEFINE_NODAL_BOUNDARY_CONDITION \
        type = "zero" \
        variable = "x_velocity" \
        mode = "on"
      DEFINE_NODAL_BOUNDARY_CONDITION \
        type = "zero" \
        variable = "y_velocity" \
        mode = "on"
DEFINE_REGION \
  name = "air"
  DEFINE_NODAL_INITIAL_CONDITION \
    type = "zero" \
    variable = "pressure"
DEFINE_STATE_LAW_MODEL \
  name = "air" \
  type = "constant_density" \
  density = 1.2
DEFINE_REGION \
  name = "air"
  VISUALIZATION_OUTPUT \
    time_step_frequency = 100 \
    pressure = "on" \
    velocity = "on" \
SOLUTION_STRATEGY \
  automatic_time_increment_selection = "on" \
RUN_SOLVER
TRANSLATE \
source_format = "centric_vis" \
source_file = "Twin1" \
destination_format = "vis_ascii" \
destination_file = "Twin1ascii" \
begin_timestep = 1 \
end_timestep = 1000
```

APPENDIX F

Example ABAQUS Input Deck

The following is a typical input deck, used to specify the problem details for a finite element simulation in ABAQUS.

```
*HEADING
Aeolian Vibration Simulation: 15 Hz, 20 kN
*PREPRINT, ECHO=NO, MODEL=YES, HISTORY=NO
*NODE
1,      -401.58,    25.
387,    -4.439,     25.
388,    -2.920,     25.
389,    -1.907,     25.
390,    -1.232,     25.
391,    -0.782,     25.
397,    -0.1489,    25.
398,    -0.1045,    25.
399,    -0.06,      25.
400,     0.,        25.
401,     0.06,      25.
402,     0.1045,    25.
403,     0.1489,    25.
409,     0.7357,    25.
410,     1.129,     25.
411,     1.699,     25.
1191,    399.94,    25.
1192,    400.511,   25.
1193,    400.904,   25.
1199,    401.491,   25.
1200,    401.536,   25.
1201,    401.58,    25.
1202,    401.624,   25.
1203,    401.669,   25.
1209,    402.302,   25.
1210,    402.752,   25.
1211,    403.972,   25.
1212,    404.440,   25.
1213,    405.96,    25.
1601,    803.16,    25.
5001,   -410.,      25.
5002,    811.58,    25.
6001,    0.,        25.
*NGEN, NSET=NALL
1, 387
411, 1191
1213, 1601
*NSET, NSET=N391
391
*NSET, NSET=N397
```

```
397
*NSET, NSET=N403
403
*NSET, NSET=N409
409
*NSET, NSET=N1193
1193
*NSET, NSET=N1199
1199
*NSET, NSET=N1203
1203
*NSET, NSET=N1209
1209
*NFILL, NSET=NALL, BIAS=1.5, TWO STEP
N391, N397, 6
*NFILL, NSET=NALL, BIAS=0.69, TWO STEP
N403, N409, 6
*NFILL, NSET=NALL, BIAS=1.45, TWO STEP
N1193, N1199, 6
*NFILL, NSET=NALL, BIAS=0.667, TWO STEP
N1203, N1209, 6
*ELEMENT, TYPE=B22H, ELSET=ALLCOND
1, 401, 402, 403
2, 403, 404, 405
3, 405, 406, 407
4, 407, 408, 409
789, 1193, 1194, 1195
790, 1195, 1196, 1197
791, 1197, 1198, 1199
792, 1199, 1200, 1201
1702, 391, 392, 393
1703, 393, 394, 395
1704, 395, 396, 397
1705, 397, 398, 399
2001, 1201, 1202, 1203
2002, 1203, 1204, 1205
2003, 1205, 1206, 1207
2004, 1207, 1208, 1209
*ELEMENT, TYPE=B22H, ELSET=CLAMP
1706, 399, 400, 401
*ELEMENT, TYPE=B23H
1501, 1, 3
1698, 387, 388
5, 409, 410
2005, 1209, 1210
2009, 1213, 1215
*ELGEN, ELSET=ALLCOND
5, 784
1501, 193, 2
1698, 4
2005, 4
2009, 194, 2
*ELSET, ELSET=COND, GENERATE
1, 792, 1
*ELSET, ELSET=INFOEL
1, 2
*NSET, NSET=INFONOD
397, 400, 401, 403, 604, 605, 801
```

```
**
** Define non-linear spring for adjacent spans
**
*ELEMENT, ELSET=ENDS, TYPE=SPRING2
5001, 5001, 1
5002, 1601, 5002
*SPRING, ELSET=ENDS, NONLINEAR
1, 1
-2.282E3, -.5
-1.886E3, -.4
-1.463E3, -.3
-1.010E3, -.2
-0.524E3, -.1
0.    , 0.
0.565E3, .1
1.1179E3, .2
1.848E3, .3
2.579E3, .4
3.382E3, .5
**
** Define mechanical properties of the conductor
**
*BEAM GENERAL SECTION, ELSET=ALLCOND, DENSITY=2534,
SECTION=NONLINEAR GENERAL
6.433E-4, 3.293E-8, 0., 3.293E-8, 6.587E-8
*DAMPING, ALPHA=0., BETA=1.55E-5
*AXIAL, LINEAR
46.5E6
*M1,LINEAR
1605.
*M2,LINEAR
1605.
*TORQUE, LINEAR
10.E9
**
** Define the properties of the clamped conductor section
**
*BEAM GENERAL SECTION, ELSET=CLAMP, DENSITY=2534, SECTION=NONLINEAR
GENERAL
6.433E-4, 3.293E-8, 0., 3.293E-8, 6.587E-8
*AXIAL, LINEAR
46.5E9
*M1,LINEAR
1.E6
*M2,LINEAR
1.E6
*TORQUE, LINEAR
10.E9
**
** define boundary conditions
**
*MPC
PIN, 400, 6001
*BOUNDARY
5001, 1, 2
5002, 1, 2
1, 2, 2
6001, 2, 2
```

```
1201, 2, 2
1601, 1, 4
**
** Specify name of the user-defined loading subroutine
**
*USER SUBROUTINE, INPUT=kload152d.for
**
** tension conductor
**
*STEP
*STATIC
*CLOAD
1, 1, -20.E3
*END STEP
**
** apply gravity
**
*STEP, NLGEOM, INC=100
*STATIC
*DLOAD
ALLCOND, GRAV, 9.81, 0., -1.
*END STEP
**
** release tension
**
*STEP, NLGEOM, INC=1000
*STATIC
*BOUNDARY, TYPE=DISP
5001, 1, , 1.58
5002, 1, , -3.16
1601, 1, 1, -3.16
*END STEP
**
** apply aeolian loading
**
*STEP, NLGEOM, INC=10000
*DYNAMIC, HAFTOL=1.E6
0.005, 30.0, 0.000001, 0.005
*DLOAD
COND, PYNU
*MONITOR, NODE=403, DOF=2
*NODE FILE, NSET=INFONOD, FREQ=1
U
*EL FILE, ELSET=INFOEL, FREQ=1
SE
*ENERGY FILE, FREQ=5
*RESTART, WRITE, OVERLAY
*END STEP
```

APPENDIX G

Internal Damping of a *Zebra* Conductor

The following graph shows the power dissipated by a vibrating ACSR *Zebra* conductor for different frequencies and bending angles. The data was obtained from Richard Bergner GmbH + Co.